

Die approbierte Originalversion dieser  
Dissertation ist in der Hauptbibliothek der  
Technischen Universität Wien aufgestellt und  
zugänglich.

<http://www.ub.tuwien.ac.at>



The approved original version of this thesis is  
available at the main library of the Vienna  
University of Technology.

<http://www.ub.tuwien.ac.at/eng>



TECHNISCHE  
UNIVERSITÄT  
WIEN  
Vienna University of Technology

Diese Dissertation haben begutachtet:

---

Priv.-Doz. Dr. Johann Marton

---

Assoc.-Prof. Dr. Catalina Curceanu

D I S S E R T A T I O N

## **Studies of SiPM photosensors for time-of-flight detectors within PANDA at FAIR**

Ausgeführt zum Zwecke der Erlangung des akademischen Grades eines Doktors der  
technischen Wissenschaften unter Leitung von

**Priv.-Doz. Dr. Johann Marton**

Stefan-Meyer-Institut für subatomare Physik  
der Österreichischen Akademie der Wissenschaften  
und Atominstitut der Technischen Universität Wien

eingereicht an der Technischen Universität Wien Fakultät für Physik von

**Dipl.-Ing. Lukas Gruber**

Matrikel Nr. 0326092  
Kaiserstraße 90/24, A-1070 Wien

---

Ort, Datum

---

Unterschrift



# Kurzfassung

PANDA ist ein Experiment auf dem Gebiet der Teilchenphysik, welches sich derzeit in Planung befindet und am Beschleunigerzentrum FAIR in Betrieb gehen wird. Das Experiment widmet sich der Untersuchung der starken Wechselwirkung mit Hilfe von Annihilationen zwischen Protonen und Antiprotonen. Ein wesentlicher Teil des Experiments ist der Flugzeitdetektor, da dieser für eine möglichst genaue Zeitmessung und damit für die zeitliche Trennung von aufeinanderfolgenden Ereignissen sowie die Identifikation verschiedener Teilchenarten von großer Bedeutung ist. Der Detektor besteht aus einer regelmäßigen Anordnung von kleinen Plastiksintillatorplättchen mit einer Größe von ungefähr  $30 \times 30 \times 5 \text{ mm}^3$  und wird deshalb auch als Szintillatorkachel-Hodoskop oder kurz SciTil-Hodoskop bezeichnet. Um die Szintillationsphotonen nachzuweisen, werden an jedem Szintillator sogenannte Silizium-Photoelektronenvervielfacher (SiPM) angebracht. Der gesamte Detektor besteht aus insgesamt 5760 einzelnen Plastiksintillatoren und erstreckt sich über eine Gesamtfläche von rund  $5.2 \text{ m}^2$ . Die wichtigste Anforderung an den Detektor ist das Erreichen einer Zeitauflösung im Bereich von 100 ps ( $\sigma$ ). Des Weiteren sollte die Menge an benötigtem Detektormaterial minimiert werden, um einerseits die vorgegebenen Dimensionen hinsichtlich des gesamten PANDA Detektors erfüllen zu können, und andererseits andere Detektorsysteme nicht zu beeinträchtigen.

Die bereits erwähnten SiPM haben sich als extrem vielseitige Alternative zu traditionellen Vakuum-Photoelektronenvervielfachern (PMT) etabliert und werden bereits in vielen Bereichen der Teilchenphysik, aber auch in bildgebenden Verfahren der Medizin verwendet. Aufgrund ihrer Eigenschaften, wie zum Beispiel gute Zeitauflösung und Effizienz, kompakter Aufbau, niedrige Betriebsspannung, Strahlungsresistenz oder geringer Kostenaufwand, eignen sich SiPM für den Einsatz in Experimenten der Hochenergiephysik, wie beispielsweise PANDA. Ein wesentlicher Unterschied im Vergleich zu herkömmlichen PMTs ist die Unempfindlichkeit gegenüber teils hohen Magnetfeldern. Diese relativ

neue Detektortechnologie befindet sich in ständiger Weiterentwicklung und so wurde vor kurzem der erste digitale SiPM (DPC) von Philips auf den Markt gebracht. Bei dieser neuen Entwicklung ist die Ausleseelektronik in den Photosensor integriert, wodurch ermöglicht wird, die gewissermaßen digitale Funktionsweise des SiPM besser umzusetzen. Konventionelle analoge SiPM und der Philips DPC wurden für den Großteil der hier vorgestellten Untersuchungen und Resultate verwendet.

Um die verwendeten Photodetektoren zu charakterisieren und deren Funktionsweise bestmöglich zu verstehen, wurde eine detaillierte experimentelle Studie unter Verwendung von gepulsten Lasern durchgeführt. Die Pulsbreite lag dabei im Bereich von einigen Picosekunden oder Femtosekunden. Speziell im Hinblick auf Detektoranwendungen in der Hochenergiephysik, wie zum Beispiel im PANDA Flugzeitdetektor, wurden Parameter wie die interne Verstärkung der SiPM, die Dunkelzählrate, Zeitauflösung, die benötigte Zeit zur Wiederherstellung nach dem Detektieren von Photonen und das dynamische Verhalten sowie deren Abhängigkeit von Temperatur- und Betriebsspannungsänderungen untersucht. Im Zuge der Messungen wurde unter anderem speziell auf die intrinsische Zeitauflösung von analogen und digitalen SiPM Wert gelegt. Es zeigte sich, dass SiPM welche mit neuen Technologien zur Reduktion von optischem Übersprechen zwischen benachbarten Zellen oder der Emission verzögerter Ladungsträgern ausgestattet sind, allgemein bessere Resultate liefern und auch größere Bereiche der Betriebsparameter zulassen, da sie weniger stark auf Temperatur- oder Spannungsschwankungen reagieren. Solch eine Neuheit ist beispielsweise der Einsatz von speziellen optischen Begrenzungen zwischen den einzelnen Zellen. Wie die dargelegten Ergebnisse zeigen sind SiPM in jedem Fall für die vorgesehene Anwendung als Photodetektoren für das SciTil-Hodoskop geeignet.

Zur weiteren Entwicklung eines geeigneten Szintillationsdetektors mit ausreichender Zeitauflösung für das PANDA Experiment wurde eine weitere detaillierte Studie durchgeführt, deren Ziel es war, die einzelnen Faktoren, welche die Zeitauflösung beeinflussen, genauer zu untersuchen und zu verstehen. Der erste Teil dieser Untersuchung konzentrierte sich auf die theoretische Behandlung der Zeitauflösung von Plastikszintillatoren, welche durch die Statistik der Emission von Szintillationsphotonen als auch durch

den Einfluss der Lichtausbreitung im Szintillator limitiert ist. Des Weiteren wurden verschiedene Materialien und Versuchsdetektoren unter gleichbleibenden experimentellen Bedingungen getestet und verglichen, um verschiedenste Parameter wie beispielsweise das Szintillatormaterial und die Szintillatorgeometrie, die Photodetektorposition sowie die Anzahl der Detektoren oder den Auslöseschwellwert der Elektronik zu untersuchen. Beim Vergleich von verschiedenen Szintillatormaterialien zeigte sich wie die Zeitauflösung von den Zeitkonstanten des Szintillationsprozesses und der Lichtausbeute beeinflusst wird. Das Experiment bestätigte die theoretischen Überlegungen, nämlich dass Szintillatoren für hohe Zeitauflösung möglichst kurze Zeitkonstanten und maximale Lichtausbeute vorweisen sollten. Die Geometrie des Szintillators verändert den Einfluss der Lichtausbreitung und damit auch die Zeitauflösung. Eine Vergrößerung der Seitenlänge der Szintillatorplättchen wirkte sich deshalb negativ auf die Zeitauflösung aus. Durch die Verwendung einer  $^{90}\text{Sr}$ -Quelle und die Auslese eines EJ-228 Plastikszintillators mit Hilfe des Philips DPC konnte schließlich eine Zeitauflösung von  $\sigma = 62.3 \pm 0.8$  ps erzielt werden.

Schlussendlich war es das Ziel die erforderliche Zeitauflösung von  $\sigma \sim 100$  ps nicht nur im Labor sondern auch in einem hochenergetischen Teilchenstrahl an einer Beschleunigeranlage zu erreichen. Aus diesem Grund wurde ein Prototyp des SciTil-Detektors konstruiert und in einem 2.7 GeV/c Protonenstrahl am Forschungszentrum Jülich getestet. Die Resultate dieses Experiments werden in der vorliegenden Arbeit ausführlich besprochen. Im Zuge der Messung wurden zahlreiche SiPM von verschiedenen Anbietern mit einer sensitiven Fläche von  $3 \times 3$  mm<sup>2</sup> und ebenso der Philips DPC mit unterschiedlichen Plastikszintillatoren kombiniert, um die beste Abstimmung zu finden. Die Ergebnisse zeigen in erster Linie, dass Variationen der Energiedeposition im Szintillator und der Anzahl der detektierten Photonen einen gravierenden Einfluss auf die Zeitauflösung haben, da dadurch die erhaltenen Zeitstempel einer erheblichen Schwankung unterliegen. Korrigiert man jedoch für diese Fluktuationen, kann die Zeitauflösung drastisch verbessert werden, und Werte deutlich unter 100 ps (sigma) sind möglich. Unter Verwendung von zwei SiPM der Firma KETEK (PM3360TS) in Kombination mit einem EJ-232 Plastikszintillator konnte eine Zeitauflösung von  $\sigma = 82.5 \pm 1.7$  ps erzielt werden. Mit dem Philips DPC

als Photodetektor wurde ein Wert von  $\sigma = 35.4 \pm 0.4$  ps erreicht.

Um die Optimierung der Szintillationsdetektoren für PANDA noch weiter voranzutreiben und die Grenzen der Zeitauflösung zu erreichen, wurde ein auf Geant4 basierendes Simulationsprogramm entwickelt. Die Simulation wird dabei behilflich sein die physikalischen Prozesse noch genauer zu untersuchen und experimentelle Daten noch genauer zu verstehen. Des Weiteren kann das Programm dazu verwendet werden verschiedenste Szintillatorgeometrien einfach zu vergleichen, um den endgültigen Detektoraufbau zu fixieren. Erste Simulationen eines einfachen Szintillationsdetektors, bestehend aus einem Szintillator und zwei Photodetektoren, zeigten bereits, dass experimentelle Tendenzen zur Anzahl der detektierten Photonen und Zeitauflösung gut wiedergegeben werden können. So wurde beispielsweise durch die Simulation bestätigt, dass ein Szintillationsdetektor der auf höchste Zeitauflösung abzielt, nach Möglichkeit eine Vielzahl von Zeitstempeln desselben Ereignisses verwenden sollte, um den Zeitpunkt des Auftretens dieses Ereignisses möglichst genau bestimmen zu können.

# Abstract

The PANDA experiment at FAIR is a planned particle physics experiment dedicated to strong interaction studies using proton-antiproton annihilations. The PANDA time-of-flight (TOF) system is foreseen as a Scintillator Tile (SciTil) Hodoscope, which will deliver valuable input for event timing and particle identification. The proposed detector is based on small plastic scintillator tiles with a size of about  $30 \times 30 \times 5 \text{ mm}^3$ , which are read-out with directly attached Silicon Photomultipliers (SiPMs). The whole system is composed of 5760 scintillator tiles and twice the number of photodetectors, covering an area of about  $5.2 \text{ m}^2$  in total. The requirements for the detector are a time resolution in the order of 100 ps sigma and a minimum use of material due to the limited space inside the PANDA spectrometer.

SiPMs are extremely versatile photodetectors which tend to successively replace the ordinary vacuum Photomultiplier Tubes (PMTs) in many of the photosensing demands ranging from particle physics to medical imaging. Due to many advantages like good time resolution, high photon detection efficiency (PDE), compactness, low operating voltage, radiation hardness, low cost and, in contrast to PMTs, insensitivity to magnetic fields, SiPMs are well suited for applications in high energy physics like PANDA. Recently, Philips invented the first fully digital SiPM (DPC), which allows to exploit the quasi digital nature of single photon detection. The analog and digital SiPM, respectively, are the main detector technologies used within this work.

This thesis describes a detailed study of SiPM properties in order to characterize the new devices and get a profound understanding of their functionality. The characterization studies have been carried out using various experimental setups employing pulsed pico- and femtosecond lasers. With regard to applications in high energy physics experiments, e.g. the PANDA TOF system, parameters like SiPM gain, dark count rate, time resolution, dynamic range and recovery time as well as their temperature dependence have

been investigated. In this context, the time resolution of conventional analog SiPMs and of the digital SiPM is discussed. Using SiPMs with some technology against cross-talk and after-pulses, e.g. trenches between pixels, led to larger operating ranges and better overall performance. The presented results show that SiPMs are well suited for usage in the SciTil system.

For the further development of a scintillator based detector suitable for PANDA, a detailed optimization study including parameters like the scintillator material and size, the photodetector position, type and quantity as well as the electronics threshold has been carried out. The aim was to find out how the individual parameters contribute to the time resolution of a scintillator based TOF detector and to finally achieve the goal of a time resolution below 100 ps sigma. In this context, also the statistics of photon emission as well as the photon propagation in a plastic scintillator are studied. Comparing different types of plastic scintillators showed that the scintillation time constants as well as the intrinsic light yield influence the time resolution. In this context, it was shown that scintillators for highest time resolution should provide short rise- and decay times and highest light output, as expected from theory. The geometry of the scintillator affects the time resolution as it defines the impact of photon propagation. Increasing the scintillator size led to reduced time resolution. In a basic measurement setup using a  $^{90}\text{Sr}$  source and an EJ-228 plastic scintillator read-out with the Philips DPC, a time resolution of  $\sigma = 62.3 \pm 0.8$  ps could be eventually achieved.

To finally proof the feasibility of reaching a time resolution of 100 ps sigma with the proposed scintillator tiles, a prototype SciTil detector based on the optimization studies has been developed and tested in a 2.7 GeV/c proton beam. Results of the beam test experiment at Forschungszentrum Jülich are presented. In course of the measurement, various commercially available SiPMs with  $3 \times 3$  mm<sup>2</sup> sensitive area as well as the Philips DPC have been employed in combination with different types of fast plastic scintillators. The data analysis showed that energy deposit fluctuations and variations in the number of detected photons have a big influence on the time resolution due to the time slewing effect. It is shown that applying appropriate corrections leads to drastic improvement in



time resolution and values well below 100 ps sigma can be achieved. Using two KETEK SiPMs (PM3360TS) attached to an EJ-232 plastic scintillator, a time resolution of  $\sigma = 82.5 \pm 1.7$  ps was obtained. Employing the Philips DPC, a value of  $\sigma = 35.4 \pm 0.4$  ps was found.

In order to further optimize the scintillation counters for the SciTil system, a simulation tool for scintillator based detectors using Geant4 has been developed. The simulation aims to provide a deeper understanding of the physical processes and will help to push the time resolution towards the limits and finalize the detector layout. Preliminary results on the detected number of photons and time resolution of a scintillator tile read-out with two photodetectors show that the simulation can already reproduce the trend of experimental results. In this context, the simulation confirms that a scintillation detector aiming at highest time resolution should make use of multiple time stamps.



# Acknowledgments

First of all I want to thank my supervisor Dr. Johann Marton for his help and support during my work at the Stefan Meyer Institute (SMI). He provided the opportunity to do my PhD thesis at the SMI and introduced me to the institute as well as to the PANDA collaboration and to the PANDA time-of-flight group. I particularly appreciate his valuable input to this research work and his guidance throughout the past four years, supporting my work and ideas whenever possible. Without his help this doctoral thesis would not have been possible. My thanks also go to Dr. Catalina Curceanu for reviewing this thesis and for her careful proofreading. I also wish to thank Prof. Eberhard Widmann and Dr. Johann Zmeskal for their support and for sharing their expertise. Thanks also to the colleagues from the PANDA group for the interesting discussions. Here, I would like to point out Dr. Herbert Orth and thank him for his ideas and help and for the financial support. Furthermore I want to thank Dr. Thomas Frach and Dr. Ralf Schulze for the help during the test beam experiment.

Next, I wish to mention some of my colleagues and friends. In this context, I would like to take the opportunity to express my gratitude to Dr. Ken Suzuki. Working together with him, I could learn a lot about scientific work and gained a lot of skills and competences for my future career. With passage of time he became a kind of second supervisor to me, who was never getting tired answering my questions. Whenever I did not understand the outcome of some simulation or measurement, he found a way how to solve the problem and carry on. During the last four years he also became a friend to me. I will not forget the evenings when we were sitting together with others at the institute, or beside some experiment, or at some pub, discussing about any scientific or non-scientific stuff. I also want to thank him for organizing a test beam experiment which delivered very nice results and is an important part of this thesis, and of course for his careful proofreading.

Furthermore I would like to express my thanks to my colleagues and friends Silvester,

Lukas, Stefan, Andreas, Sebastian, Martin, Dominik, Martin Simon, Clemens, Susanne, Oswald, Paul, ... for their help, support and the useful discussions. Thanks to all of you for the enjoyable hours we spent together, whether it be while playing tennis or soccer, going hiking or simply having a beer and chatting. I really sometimes needed that times to relax and recharge the batteries for new challenges.

At this point, but ahead of all others, I want to express my deepest gratitude to my family and to my girlfriend Tanja. I would like to thank my parents for their persistent support, not only during the last four years, but throughout the long journey from schooldays and studies till the present day. Without your help all these things would not have been possible. Furthermore I want to thank Tanja for her huge patience during the past years and especially during the last few months of thesis writing. Thank you for all your love and all the sacrifices you make to support me.

# Contents

<b>Kurzfassung</b>	<b>iii</b>
<b>Abstract</b>	<b>vii</b>
<b>Acknowledgments</b>	<b>xi</b>
<b>1 Introduction</b>	<b>1</b>
<b>2 The PANDA experiment at FAIR</b>	<b>5</b>
2.1 The FAIR accelerator complex . . . . .	5
2.2 The PANDA spectrometer . . . . .	7
2.2.1 Target system and beamline . . . . .	10
2.2.2 Magnet system . . . . .	11
2.2.3 The tracking system . . . . .	12
2.2.4 Particle identification . . . . .	15
2.2.5 Electromagnetic calorimeter . . . . .	20
2.2.6 Hypernuclear detector . . . . .	21
2.2.7 Luminosity detector . . . . .	21
2.2.8 Data acquisition system . . . . .	22
<b>3 The Scintillator Tile Hodoscope</b>	<b>23</b>
3.1 Physics motivation . . . . .	24
3.1.1 Hypernuclear physics . . . . .	24
3.1.2 Overall particle identification . . . . .	24

3.1.3	Software triggering . . . . .	25
3.2	Technical motivation . . . . .	25
3.2.1	Event timing . . . . .	25
3.2.2	Relative time-of-flight . . . . .	30
3.2.3	Charge discrimination . . . . .	30
3.2.4	Conversion detection . . . . .	30
3.2.5	Track finding . . . . .	31
3.3	Detector requirements . . . . .	31
3.4	Detector layout . . . . .	32
<b>4</b>	<b>Semiconductor photodetectors</b>	<b>35</b>
4.1	Photodiodes . . . . .	36
4.2	Avalanche Photodiodes . . . . .	37
4.3	Silicon Photomultipliers . . . . .	37
4.4	The Digital Photon Counter . . . . .	39
4.4.1	Sensor layout . . . . .	40
4.4.2	Data acquisition scheme . . . . .	41
<b>5</b>	<b>Silicon Photomultiplier characterization studies</b>	<b>43</b>
5.1	Characterization of analog SiPMs . . . . .	43
5.1.1	SiPM gain . . . . .	44
5.1.2	Photon Detection Efficiency . . . . .	49
5.1.3	Dark-noise, cross-talk and after-pulsing . . . . .	50
5.1.4	Dynamic range . . . . .	52
5.1.5	Recovery Time . . . . .	70
5.1.6	Time resolution . . . . .	80
5.1.7	Position sensitive SiPM detector . . . . .	81
5.2	Characterization of the Digital Photon Counter . . . . .	83
5.2.1	Dark count rate . . . . .	83
5.2.2	Time resolution . . . . .	85

5.3	Discussion of results . . . . .	88
<b>6</b>	<b>Time resolution of plastic scintillators</b>	<b>91</b>
6.1	The influence of photon counting statistics . . . . .	92
6.2	The influence of photon propagation . . . . .	95
<b>7</b>	<b>Timing performance study for the SciTil detector</b>	<b>99</b>
7.1	Test measurements using the Philips Digital Photon Counter . . . . .	101
7.1.1	Setup . . . . .	101
7.1.2	Optimization of parameter settings . . . . .	102
7.1.3	Measurement of the time resolution . . . . .	109
7.2	Test measurements using conventional SiPM . . . . .	112
7.3	Detector optimization . . . . .	115
7.3.1	Optical coupling between scintillator and photodetector . . . . .	116
7.3.2	Photodetector position . . . . .	116
7.3.3	Photodetector type . . . . .	120
7.3.4	Number of photodetectors . . . . .	122
7.3.5	Electronics threshold . . . . .	123
7.3.6	Scintillator material . . . . .	129
7.3.7	Scintillator geometry . . . . .	130
7.3.8	Scintillator wrapping . . . . .	132
7.4	Discussion of results . . . . .	133
<b>8</b>	<b>Beam test at COSY</b>	<b>135</b>
8.1	The JESSICA beam line at COSY . . . . .	135
8.2	The SciTil-SiPM prototype . . . . .	139
8.2.1	Data acquisition . . . . .	140
8.2.2	Data analysis . . . . .	140
8.2.3	Results . . . . .	154
8.3	The SciTil-DPC prototype . . . . .	161
8.3.1	Data acquisition . . . . .	162

8.3.2	Data analysis . . . . .	163
8.3.3	Results . . . . .	171
8.4	Discussion of results . . . . .	177
<b>9</b>	<b>Simulation of the timing properties of a scintillator tile detector</b>	<b>179</b>
9.1	Detector construction . . . . .	180
9.2	Number of detected photons . . . . .	182
9.3	Time resolution . . . . .	183
9.4	Discussion of results . . . . .	187
<b>10</b>	<b>Summary and outlook</b>	<b>189</b>
<b>A</b>	<b>Time-of-flight resolution and intrinsic time resolution</b>	<b>195</b>
A.1	Time-of-flight with two identical detectors . . . . .	195
A.2	Time-of-flight with three detectors . . . . .	198
A.2.1	Calculation of intrinsic time resolution . . . . .	198
A.2.2	Chi-square minimization . . . . .	200
A.2.3	Example . . . . .	201
	<b>List of Tables</b>	<b>203</b>
	<b>List of Figures</b>	<b>205</b>
	<b>List of abbreviations</b>	<b>211</b>
	<b>Bibliography</b>	<b>215</b>
	<b>Curriculum vitae</b>	<b>221</b>



# Chapter 1

## Introduction

Highest time resolution and efficiency in scintillation based detectors is becoming more and more important for many applications ranging from particle physics to medical imaging. Especially in the field of high energy physics (HEP), where almost all experimental systems rely on such detectors for particle identification purposes, e.g. time-of-flight (TOF) systems, the requirements are steadily growing. Better time resolution allows to achieve higher precision or to build more compact detectors due to shorter flight paths needed. For medical applications like Positron Emission Tomography (PET) and in particular TOF-PET, a higher timing precision in the detection of annihilation gamma photons can lead to better image quality, shorter examination times and therefore lower doses for patients [1].

Nowadays, a tremendous effort is placed on the improvement of scintillation based detectors, in particular on the advancement in the field of photodetectors. In recent years, the introduction of new semiconductor photodetectors, e.g. the SiPM, led to a progressive replacement of conventional PMTs in many of the photosensing applications in particle physics, astrophysics and medicine. The main advantages of SiPMs are good time resolution, high photon detection efficiency (PDE), compactness and radiation hardness. Furthermore, the devices are almost insensitive to magnetic fields, which is a basic ingredient for the use in HEP experiments, where usually high magnetic fields are present. The transparency to gamma photons offers new possibilities for detector design, especially for

medical applications like PET [2]. Since this new technology is still in an early phase, there is a lot of room for improvements and many groups in science as well as industry are working on this interesting topic to characterize and further optimize the new devices. In this context, the recent invention of the first fully digital SiPM (DPC) by Philips has been an important milestone [3].

Because of many advantages, a variety of large experiments and collaborations in particle physics already use or plan to use SiPMs on a large scale, e.g. CALICE [4], T2K [5], CMS at CERN [6], BELLE II at KEK [7] or PANDA at FAIR [8]. The PANDA TOF system is planned as a Scintillator Tile (SciTil) Hodoscope [9], which foresees to use small plastic scintillator tiles read-out with SiPMs. The barrel TOF system is extremely important for event timing in PANDA, since it serves as a trigger detector in the otherwise trigger less data acquisition scheme. Furthermore, it provides PID below the momentum threshold of the Cherenkov detectors. The requirements are a minimum use of material and a time resolution in the order of 100 ps sigma.

The objective of this work is to fully understand and characterize the SiPM device and to develop a prototype scintillation detector based on SiPMs for the SciTil system, reaching a time resolution below 100 ps sigma. In this context, several types of commercially available SiPMs from different vendors (Hamamatsu, KETEK, Zecotek, AdvanSiD and Philips) have been tested. In course of the studies, a special focus has been placed on the timing performance and applications in HEP. Combining the photodetector with a scintillator and dedicated read-out electronics, a first test setup has been built. Starting from a basic detector layout, the prototype has been developed further by performing test measurements using radioactive sources. To finally proof the feasibility of reaching a time resolution in the order of 100 ps sigma, the proposed detector has been tested in a proton beam at a test beam facility. Last but not least, a simulation based on Geant4 [10] has been developed, which aims to further improve the SciTil detector and to provide input for experiments, to push the time resolution towards its limits.

The present thesis is organized in the following way. The next chapter gives a general

introduction about FAIR and the PANDA experiment, to get an overview about physics goals, requirements and the individual detector systems. The barrel TOF system of PANDA is motivated in Chapter 3, by demonstrating the main benefits for the PANDA experiment. The basic detector layout as well as the requirements posed on the SciTil system are discussed in detail.

The second and main part of the thesis concentrates on the research studies that have been carried out during this doctoral work. Chapter 4 introduces the conventional SiPM and the fully digital Philips DPC and shortly explains the basic functionality. Extensive experimental studies have been performed in order to characterize and understand the SiPM devices. Experimental implementation, analysis and outcome of these studies are described and discussed in Chapter 5. The obtained information is used as input for development and optimization of a SciTil prototype detector, as explained in the subsequent chapters.

Chapter 6, Chapter 7 and Chapter 8 deal with the development and testing of a prototype detector for SciTil. Starting from theory, the statistics of the scintillation process and the parameters limiting the time resolution of a scintillation detector are studied. Experimental tests using radioactive sources, leading to an optimized detector layout, are summarized and interpreted. Finally, the results of test beam measurements are shown to demonstrate the applicability of the proposed detector for the SciTil system.

Chapter 9 shortly introduces a Geant4 based simulation tool, which is currently being developed to further optimize the SciTil detector and fully understand experimental data. First results of the simulation, including studies on an alternative detector layout employing bar-shaped scintillator geometries, are presented and discussed. Ways to improve the agreement between measurement and simulation are given.

The thesis ends with Chapter 10, which summarizes the results and outcome of this work and gives final remarks as well as a short outlook about ongoing and future research on the SciTil project.



## Chapter 2

# The PANDA experiment at FAIR

The PANDA (Antiproton Annihilations in Darmstadt) experiment [8, 11] will be installed at the Facility for Antiproton and Ion Research (FAIR) [12, 13], which is currently being constructed in Darmstadt, Germany. PANDA will allow to reach a new level of precision in the study of fundamental questions of hadron and nuclear physics by investigating interactions of antiprotons with protons and nuclei.

The study of the strong interaction and its underlying theory of Quantum Chromo Dynamics (QCD) are central topics of modern physics research. Phenomena like quark confinement and the origin of hadron masses are still one of the great puzzles of physics and not yet fully understood. Past experiments at FNAL, USA or LEAR at CERN have shown that antiproton-proton annihilations are an effective way to study such fundamental questions. Within this context, FAIR and PANDA will be able to deliver beams of unprecedented quality and intensity and will allow to perform spectroscopy measurements with precision way beyond the one of other experiments.

### 2.1 The FAIR accelerator complex

Within the next years, the GSI Helmholtz Centre for Heavy Ion Research in Darmstadt [14] will be expanded to form a new international accelerator facility called FAIR,

at the moment one of the largest research projects worldwide. The FAIR accelerators will be able to deliver high quality primary beams of protons and ions, as well as secondary beams of antiprotons and stable and unstable nuclei to several experiments, dedicated to different topics in hadron and nuclear physics. A schematic view of the whole accelerator complex is shown in Fig. 2.1.

The work horse of FAIR is a double ring accelerator, consisting of two synchrotrons with 1.1 km circumference (SIS-100 and SIS-300) and respective magnetic rigidities of 100 Tm and 300 Tm, which is intended to accelerate protons and other ions up to uranium. The SIS-100 will provide intense pulsed beams of  $U^{28+}$  ions and protons with intensities of  $5 \times 10^{11}$  ions per pulse at an energy of 2.7 GeV/nucleon and  $4 \times 10^{13}$  protons per pulse at an energy of 29 GeV, respectively. The goal of the SIS-300 is to deliver high energy ion beams up to 35 GeV/nucleon for  $U^{92+}$  ions with an intensity of about  $3 \times 10^{11}$  ions per second. The presently existing Universal Linear Accelerator (UNILAC) and the SIS-18 synchrotron will be used to accelerate the ions prior to the injection into the synchrotron.

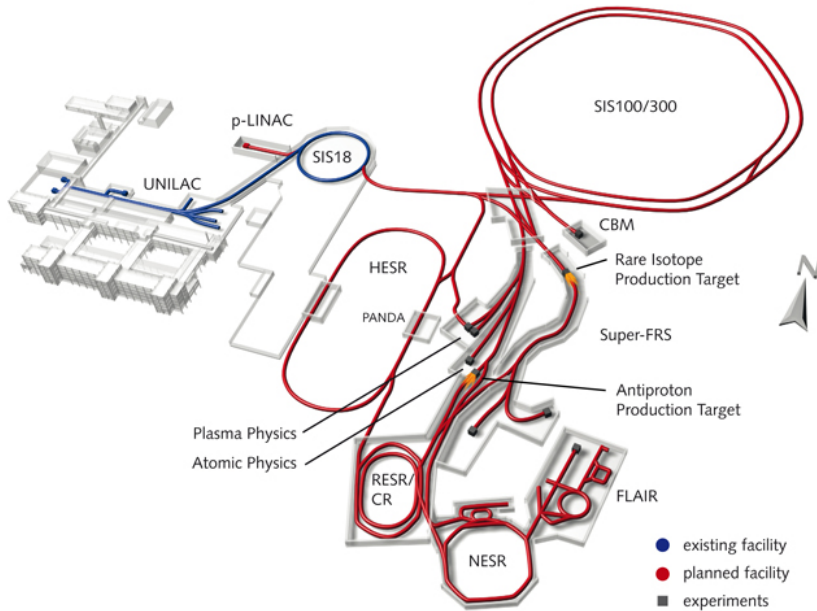


**Figure 2.1:** Schematic view of the FAIR accelerator complex, showing the position of the main experiments [14]. The existing and new facilities are indicated by the colors blue and red, respectively.

In addition, a new linear accelerator (p-LINAC) will be built in order to provide high intensity proton beams of 70 MeV for injection.

After acceleration within the synchrotrons, the antiprotons are produced within a Cu target and the beams are guided to a complex system of storage rings, where the bunches are stored, cooled and prepared to fulfill the requirements of the different experiments. At present it is planned to have four subsequent rings: the Collector Ring (CR), the Recirculation Experimental Storage Ring (RESR), the New Experimental Storage Ring (NESR) and the High Energy Storage Ring (HESR). The main experiments which are located along the various storage rings can be grouped into four topics of research:

- **Nuclear Structure and Astrophysics (NuSTAR):** study of physics of atomic nuclei, new aspects of nuclear structure, nuclear astrophysics, fundamental interactions and symmetries using secondary beams of radioactive nuclei.
- **Compressed Baryonic Matter (CBM):** investigations of extreme nuclear matter states and the phase transition to the quark-gluon plasma at high baryon density with nuclear-nuclear collisions.
- **Antiproton Annihilations in Darmstadt (PANDA):** study of basic hadronic and nuclear problems and fundamental symmetries, hadron spectroscopy, search for new forms of matter and gluon excitations in the physics of charmed and strange quarks by investigating the interaction of antiprotons with nucleons and atomic nuclei.
- **Atomic, Plasma Physics and Applications (APPA):** superdense plasma physics, atomic physics, applied research in material science and biology.

## 2.2 The PANDA spectrometer

PANDA is a fixed target experiment located at the HESR with its circumference of 574 m, which can provide antiprotons in the momentum range of 1.5 GeV/c to 15 GeV/c and acts as an accelerator as well as a storage ring for the antiprotons. The HESR is equipped with

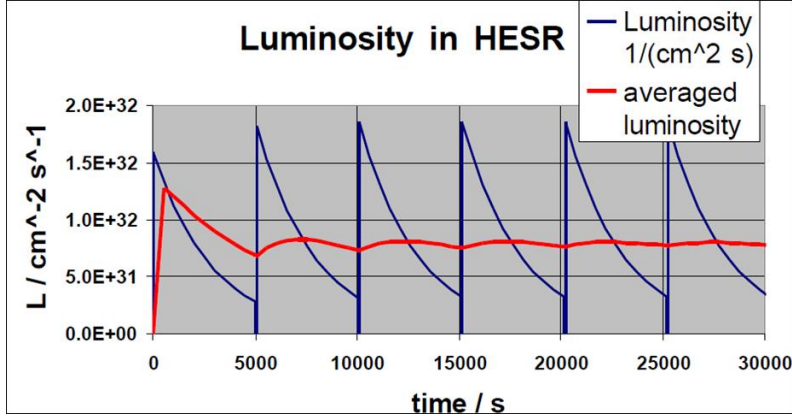


**Figure 2.2:** Time dependence of the beam related luminosity in the HESR [15]. In between the refills of the ring the beam current is reduced due to collisions with the target and the rest gas.

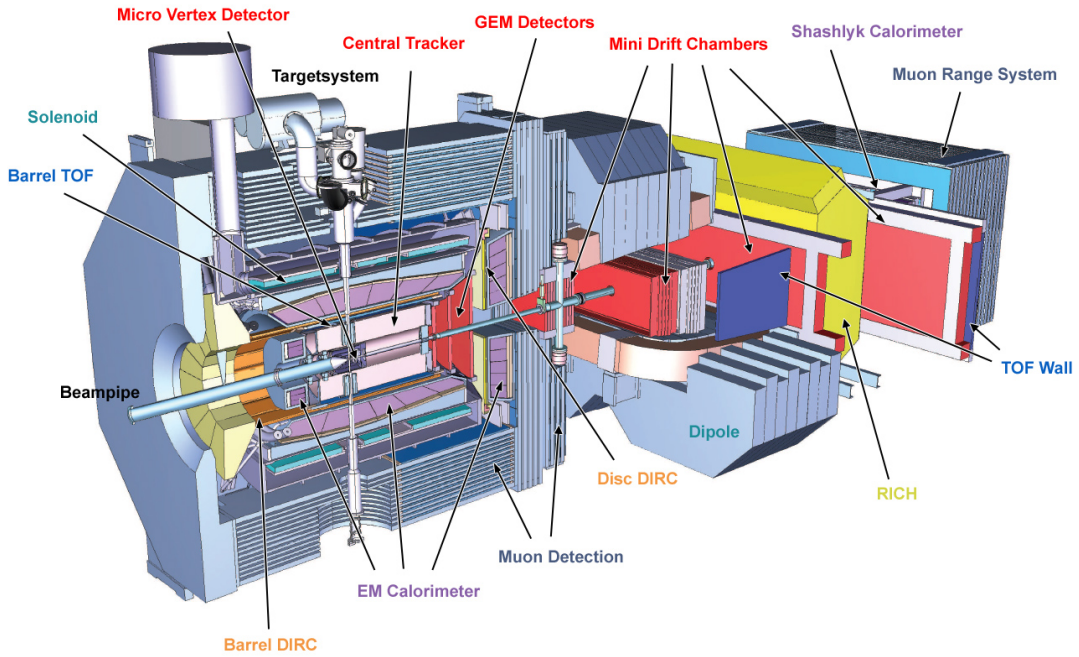
an electron cooler and a system for stochastic cooling and can be operated in two modes: the high luminosity mode, with a maximum luminosity of  $L = 2 \times 10^{32} \text{ cm}^{-2} \text{ s}^{-1}$  and a beam momentum resolution of  $\delta p/p < 10^{-4}$ , and the high resolution mode, with an order of magnitude lower luminosity but better momentum resolution of  $\delta p/p < 4 \times 10^{-5}$ . Fig. 2.2 is taken from Ref. [15] and shows the time dependence of the luminosity. Depending on the operation mode (high luminosity or high resolution), there are in total  $10^{11}$  or  $10^{10}$  antiprotons stored in the ring.

The physics program of PANDA imposes challenging requirements on the detector systems. The main tasks of the PANDA detector are:

- full angular acceptance
- high rate capability up to  $2 \times 10^7$  interactions per second
- good angular resolution for charged and neutral particles
- good particle identification for  $\gamma$ -rays, leptons, muons, kaons, protons, etc.
- high momentum resolution in the order of  $\sim 1\%$
- efficient event selection (continuous acquisition)

In order to fulfill the requirements, the PANDA detector is composed of two magnetic spectrometers, namely the target spectrometer surrounding the interaction region and the forward spectrometer for detection of particles emitted in forward direction at small angles

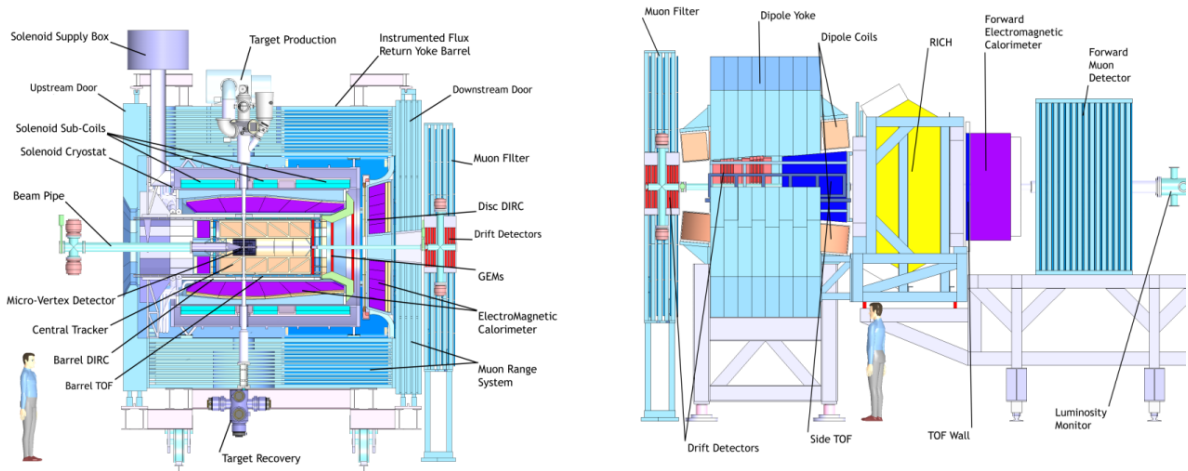




*Figure 2.3: 3D-view of the PANDA detector. The picture is taken from Ref. [16].*

with respect to the beam axis. The target spectrometer is planned to detect particles which are emitted with angles greater than  $5^\circ$  and  $10^\circ$  in the vertical and horizontal plane. The combination of both systems allows almost  $4\pi$  angular acceptance. Fig. 2.3 shows a 3D-view of the PANDA detector with all its main subsystems, as there are:

- the target system and beamline
- the magnet system: solenoid and dipole magnets
- the tracking system: Micro Vertex Detector, Central Tracker, Gas Electron Multiplier (GEM) detectors and Forward Tracker (drift chambers)
- the particle identification system: DIRC detectors, time-of-flight (TOF) detectors, RICH, Muon Range System
- the electromagnetic calorimetry: EMC and Shashlyk calorimeter
- the hypernuclear detector
- the luminosity detector
- the data acquisition system



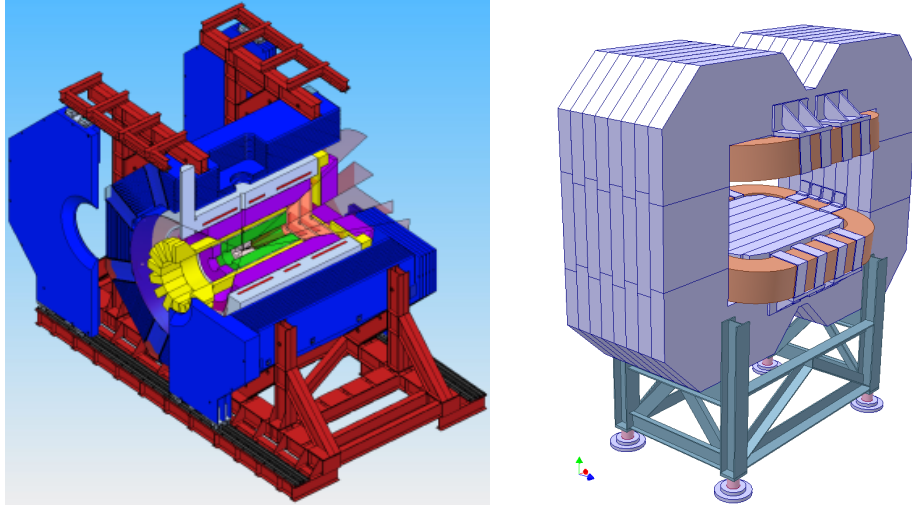
**Figure 2.4:** Side view of the PANDA target spectrometer (left) and forward spectrometer (right). All sub-detector systems are labeled. The pictures are taken from Ref. [16].

Fig. 2.4 shows a side view of the target spectrometer surrounding the interaction region and the forward spectrometer, which is located further downstream.

### 2.2.1 Target system and beamline

The target material is inserted into the PANDA detector in vertical direction, perpendicular to the beam pipe, as it can be seen in Fig. 2.4. In order to achieve the design luminosity of  $2 \times 10^{32} \text{ cm}^{-2} \text{ s}^{-1}$ , a target density of about  $4 \times 10^{15}$  hydrogen atoms per  $\text{cm}^2$  is necessary. Depending on the experimental requirements, two different target systems are foreseen for PANDA [17].

**Pellet target.** The pellet target consists of a stream of frozen hydrogen microspheres (pellets), which is traversing the antiproton beam in vertical direction. The typical pellet size ranges between  $20 \mu\text{m}$  and  $40 \mu\text{m}$ . Other typical parameters are a pellet fall speed of about  $60 \text{ m/s}$  and a pellet rate of  $10\text{--}15 \text{ kHz}$ . With the pellet option it is easier to reach high target densities and a tracking of the individual pellets allows to reconstruct the interaction point. One disadvantage of the pellet option is the possible time structure of the target, since there may be times without any pellet in the beam. This results in a time dependent luminosity and higher instantaneous event rates.



**Figure 2.5:** The target solenoid magnet together with the inner detectors (left). The cryostat is shown in light blue, with embedded coils in red, surrounded by the magnet yoke colored in blue. The cones indicate the acceptance of the individual detectors. On the right: the forward dipole magnet. The pictures are reprinted from Ref. [18].

**Cluster jet target.** The cluster jet beam is produced by expansion of a pre-cooled gas into the vacuum. The size of a cluster amounts to typically  $10^3$  to  $10^5$  atoms per cluster. The big advantage of a hydrogen cluster beam is the homogeneous density distribution without any time structure, resulting in a luminosity without time structure.

### 2.2.2 Magnet system

Magnetic fields in PANDA are needed for momentum reconstruction as prerequisite for successful particle identification (PID). The PANDA magnet system [18] consists of two superconducting magnets, a solenoid for the target spectrometer and a dipole within the forward spectrometer (see Fig. 2.4). Fig. 2.5 shows a picture of the two magnet systems used in PANDA. The solenoid magnet for the target region has to provide a magnetic field of 2 T over a length of about 4 m and a diameter of 1.9 m. Within this space all the detector systems are placed. In order to insert the warm target pipe in vertical direction into the detector, the coil has to be split leaving a hole of 100 mm in diameter. As a consequence of the asymmetric design, it becomes very challenging to reach the desired field homogeneity of less than 2% over the whole region of the inner and outer tracker.

The return yoke of the magnet is also part of the muon range system by putting mini drift tubes in between the 13 iron layers. For maintenance and commissioning it's possible to move the whole magnet system of about 300 tons outside of the beam.

In order to reconstruct momenta of particles emitted in forward direction at angles  $\leq 5^\circ$  vertically ( $\leq 10^\circ$  horizontally), a large aperture dipole magnet with a bending power of 2 Tm is used in the forward spectrometer. One special challenge of the magnet is to fulfill the requirements on stray fields with a large aperture of 1 m $\times$ 3 m and a relatively short length of 2.5 m. Antiprotons with the highest momenta of 15 GeV/c are deflected in the magnetic field by an angle of about  $2^\circ$ , thus, an additional magnet system is installed behind the PANDA detector for compensation.

### **2.2.3 The tracking system**

In order to provide high resolution track reconstruction of charged particles at all solid angles, the PANDA tracking system is composed of four individual sub-detectors, three of them located in the target spectrometer (Micro Vertex Detector, Central Tracker and GEMs), and the Forward Tracker (drift detectors) for very forward tracks in the forward spectrometer, as shown in Fig. 2.4.

#### **Micro Vertex Detector**

The Micro Vertex Detector (MVD) [19] is the innermost tracking device of the PANDA target spectrometer, located very close to the beam pipe (see Fig. 2.4). Its main duty is to provide vertex information of primary interaction vertices and secondary vertices in order to reconstruct decays of short lived particles, like D-mesons, with high precision. Therefore, a vertex resolution better than 100  $\mu$ m is needed. Due to its position very close to the interaction region, the MVD system requires radiation hard detectors and front-end electronics.

The detector technology of choice is the silicon detector with two different types, silicon

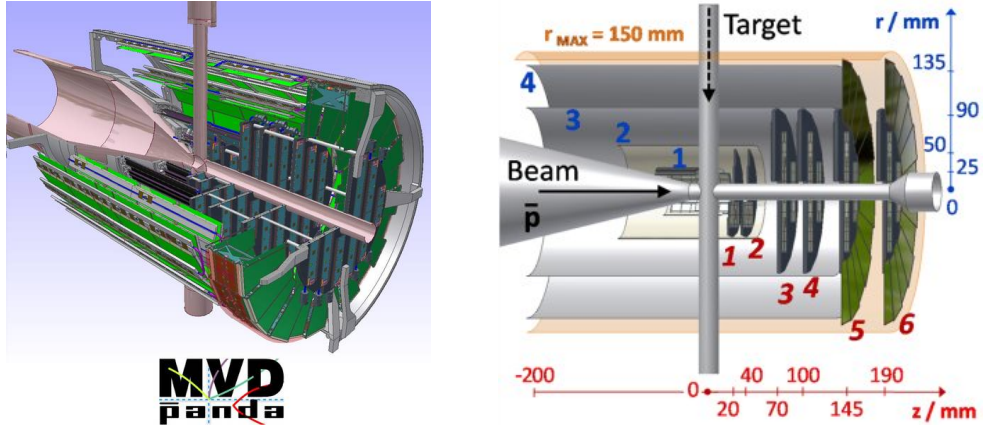


**Figure 2.6:** The left picture shows a 3D-view of the Micro Vertex Detector [19], which consists of four barrel layers and six disk layers. The inner part is equipped with silicon pixel detectors, while the outer regions use double-sided silicon strip detectors. On the right, the dimensions of the detector are indicated.

pixel detectors and double-sided silicon strip detectors. The MVD is composed of four barrel layers surrounding the interaction point and six disk layers in forward direction, as shown in Fig. 2.6. The inner parts are equipped with pixel detectors, while for the outer parts strip detectors are used.

### Central tracker

The cylindrical Central Tracker (CT) or Straw Tube Tracker (STT) [20] with an internal (external) radius of 15 cm (42 cm) surrounds the MVD and is composed of 27 layers of straw tubes, as shown in Fig. 2.7. A straw tube can be seen as a small single channel drift chamber. The cylindrical tubes of 10 mm diameter are 150 cm long and are arranged in basic modules of planar double-layers. The straw tubes use gold-coated tungsten or rhenium electrodes of  $27\ \mu\text{m}$  diameter and are filled with an Ar/CO<sub>2</sub> gas mixture at 1 bar overpressure, which is acceptable for the  $27\ \mu\text{m}$  thick tube walls made of aluminized mylar film.

By measuring the drift time in the tubes, the radial distance from the wire ( $\rho/\phi$  plane) can be determined better than  $150\ \mu\text{m}$ . The collected charge defines the energy loss. The

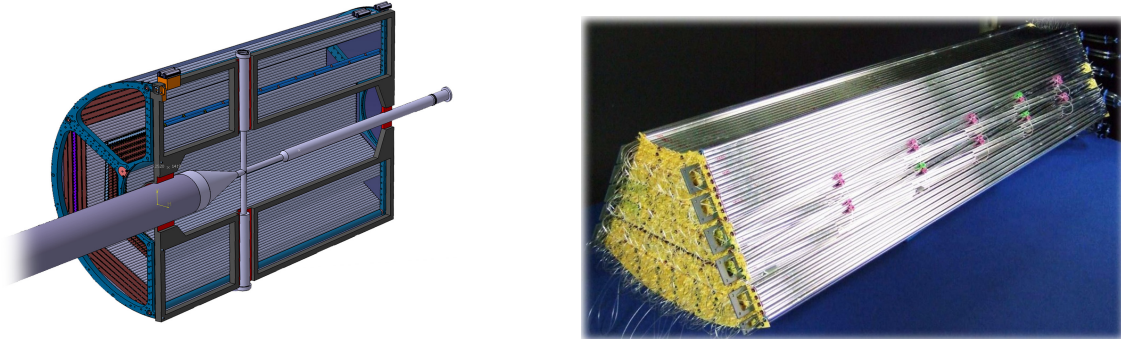


**Figure 2.7:** A drawing of the Straw Tube Tracker, which consists of 27 layers of cylindrical straw tubes (left). On the right: assembled straw tubes. Pictures taken from Ref. [21].

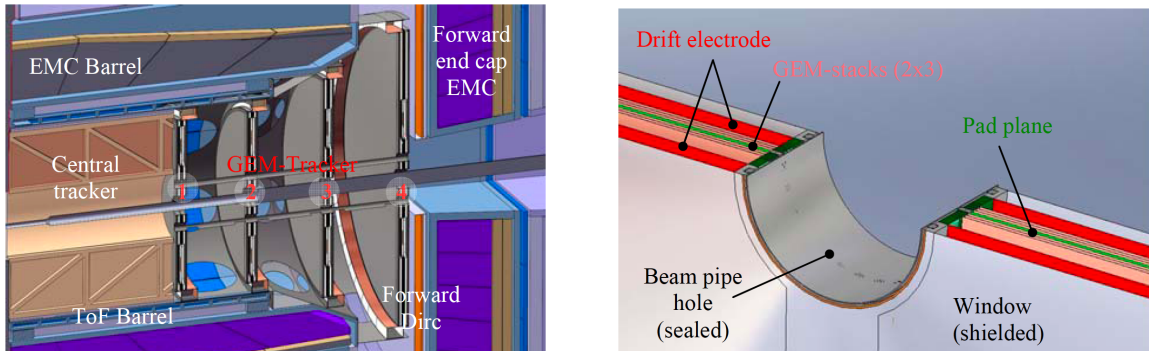


**Figure 2.8:** The left picture shows the location of the GEM disks downstream of the CT. In the current design only three GEM disks are foreseen. On the right one can see the internal structure of a single GEM disk. Pictures are taken from Ref. [21].

position in longitudinal ( $z$ ) direction can be determined better than 1 mm by placing some tubes with a small skew angle of about  $3^\circ$  with respect to the other tubes. Under these conditions, a momentum resolution in the order of 1% can be expected from the CT system. In addition, the  $dE/dx$  measurement can be used as an input for PID.

### Gas Electron Multiplier stations

Three planar disks of Gas Electron Multiplier (GEM) detectors [8] complete the tracking system of the target spectrometer by detecting particles emitted at angles  $< 22^\circ$  to the axis, which is beyond the acceptance of the CT. The location of the GEM trackers is shown

in Fig. 2.8. The GEM disks with a diameter of 90 cm, 112 cm and 148 cm are mounted downstream of the CT at distances of 1.17 m, 1.53 m and 1.89 m from the interaction point. Each disk consists of a double-sided read-out pad plane, two stacks with three GEM foils each, a cathode plane and a window foil per side (see Fig. 2.8). This setup allows track position measurements in four projections, which results in a position resolution better than  $100\ \mu\text{m}$ . The GEM disks have to stand a high particle flux of about  $3 \times 10^4\ \text{cm}^{-2}\text{s}^{-1}$  very close to the beam pipe.

### **Forward tracker**

The Forward Tracker (FT) [8] is used for momentum reconstruction of particles deflected by the magnetic field of the dipole magnet in the forward spectrometer. The acceptance of the FT is defined by the aperture of the dipole magnet, which is equal to  $\pm 10^\circ$  and  $\pm 5^\circ$  with respect to the beam axis in horizontal and vertical direction, respectively. The whole detector is based on cylindrical straw tubes of comparable material and geometry as used for the CT in the target spectrometer (see section 2.2.3).

In total, the FT consists of about 13 000 straw tubes, which are arranged in three pairs of planar tracking stations with a material budget of 0.3% of one radiation length per station. One pair is placed in front of the dipole, the second pair is located inside the magnet gap and the third one is placed behind the dipole magnet (see Fig. 2.4). Each tracking station consists of four double-layers of straw tubes, which are mounted on special support frames, as shown in Fig. 2.9. With a position resolution of 0.1 mm per detection layer, the expected momentum resolution of the FT is better than 1%.

### **2.2.4 Particle identification**

One of the main prerequisites needed to reach the challenging physics goals of the PANDA experiment is an efficient way of identifying particles of different species in a momentum range from 200 MeV/c up to 10 GeV/c. Therefore, PANDA is making use of several dedicated PID systems, as can be seen in Fig. 2.4.

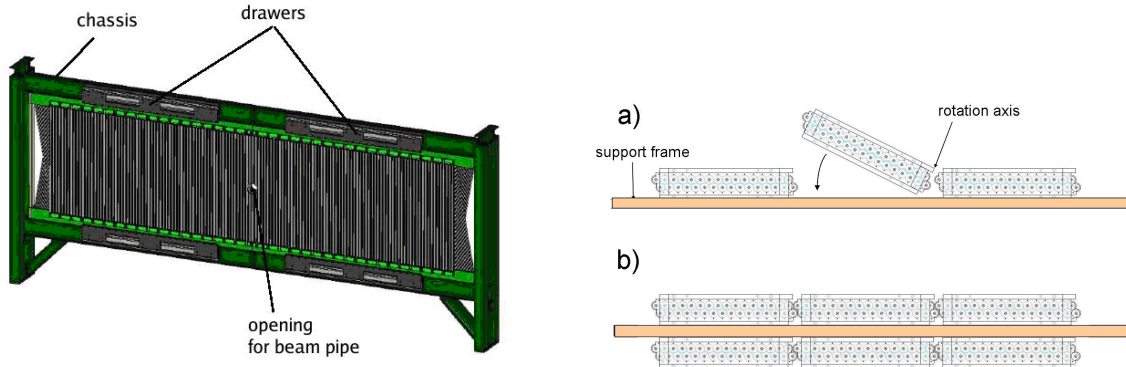


**Figure 2.9:** Left: a single tracking station of the FT. In total, the FT consists of six stations, arranged in three pairs. Each station is composed of four double-layers of straw tubes. On the right: mounting of a single double layer (a) and two double-layers mounted on a support frame (b). Pictures are reprinted from Ref. [21].

Within the target spectrometer the identification of particles with momenta  $> 1 \text{ GeV}/c$  is done by using Cherenkov counters based on the Detection of Internally Reflected Cherenkov Light (DIRC) principle. For identification of hadrons in forward direction a Ring Imaging Cherenkov Counter (RICH) is installed in the forward spectrometer. In order to successfully identify slow particles in the target region, a TOF system is installed, consisting of a TOF barrel detector. Within the forward spectrometer, an additional TOF wall is foreseen as a stop detector for measuring the transit time. Furthermore, the magnet yokes are instrumented with a Muon Range System (MRS) in order to efficiently identify muons.

## DIRC detectors

The PANDA DIRC detectors [22, 23] are divided into two sub-detectors, which are both installed within the target spectrometer. A barrel DIRC detector [24, 25, 26], similar to the one realized at the BaBar facility [27], surrounds the beam at a distance of about 48 cm and covers the polar angle range between  $22^\circ$  and  $140^\circ$ , while the angular range between  $5^\circ$  and  $22^\circ$  is covered by an end-cap disc DIRC detector. Both systems are based on the same principle of reflecting the Cherenkov light produced by a charged particle in a medium onto an array of photodetectors, and determining the Cherenkov angle to define



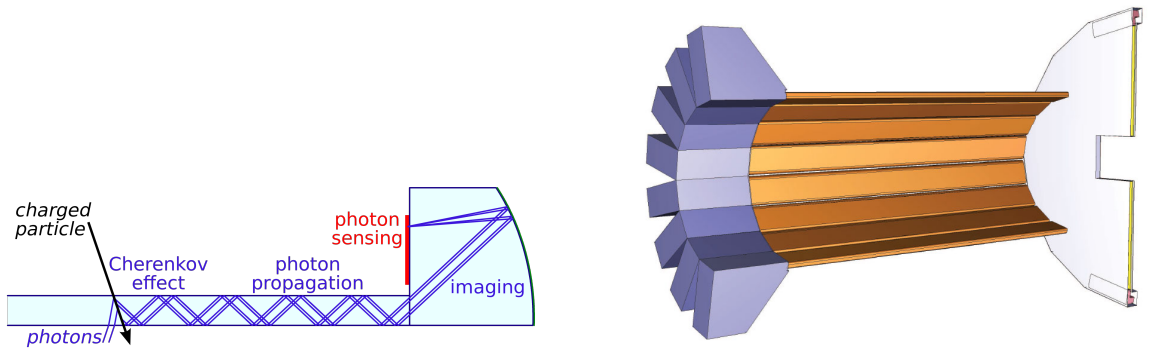


**Figure 2.10:** Left: basic principle of a DIRC detector. The picture on the right shows a drawing of the PANDA barrel DIRC and disc DIRC detectors [21].

the particle velocity. In combination with tracking information the particle can then be identified via its mass. The basic DIRC principle is illustrated in Fig. 2.10, together with a picture of the PANDA DIRC detectors.

The expected performance of the DIRC detectors is a  $\pi/K$  misidentification  $< 2\%$  for momenta up to  $3.5 \text{ GeV}/c$  for the barrel and momenta up to  $4 \text{ GeV}/c$  for the disc DIRC. For the barrel DIRC a single photon Cherenkov angle resolution of about  $8\text{--}9 \text{ mrad}$  is expected.

For both detectors, fused silica either in form of thin slabs for the barrel DIRC or a disc in case of the end-cap DIRC detector is used as Cherenkov radiator and light guide at the same time. For the barrel, in total 80 silica bars of  $1.7 \text{ cm}$  thickness,  $3.3 \text{ cm}$  width and  $250 \text{ cm}$  length are foreseen. In case of the disc DIRC, an octagonal disc of  $2 \text{ cm}$  thickness and about  $2 \text{ m}$  diameter is used. At the end of the light guides special focusing optics are used to guide the light into an expansion volume and finally onto an array of suitable photodetectors.

Because of the challenging requirements posed on the photodetectors, e.g. single photon sensitivity, low dark count rate, high Photon Detection Efficiency (PDE), fast timing ( $\sigma \sim 100 \text{ ps}$ ), long lifetime ( $0.5 \text{ C}/\text{cm}^2/\text{yr}$  for the barrel,  $4\text{--}10 \text{ C}/\text{cm}^2/\text{yr}$  for the disc), high rates (up to  $2 \text{ MHz}/\text{cm}^2$ ) and possibility of operation in a magnetic field of up to  $1.5 \text{ T}$ , it was for a long time not clear which detector technology to use. Therefore, several types

of photodetectors, e.g. the Micro-Channel Plate Photomultiplier Tube (MCP-PMT), the Multi-Anode Photomultiplier Tube (MAPMT) or the Silicon Photomultiplier (SiPM), have been under investigation [28, 29]. Currently, it is foreseen to use MCP-PMTs as photodetectors, with a total number of 10–15 k read-out channels.

### **Time-of-flight system**

As mentioned before, the PANDA TOF system [8] consists of a barrel TOF detector located within the target spectrometer and a TOF wall in forward direction (see Fig. 2.3 and Fig. 2.4). In the latest design [9] it is foreseen to install the TOF barrel in between the DIRC barrel and the EMC, and not as shown in the picture, inside of the DIRC barrel. The barrel TOF detector, or so-called Scintillator Tile (SciTil) Hodoscope, allows to identify slow charged particles (below 700 MeV/c) in combination with the CT [30]. Providing a fast time response, the detector is also very useful as an input for event timing and trigger algorithms [15].

Requirements for the barrel TOF detector are a time resolution of  $\sigma \sim 100$  ps and, due to the limited space in between the barrel DIRC and EMC, a minimum use of material. It is therefore planned, to equip the detector with small plastic scintillator tiles ( $\sim 30 \times 30 \times 5$  mm<sup>3</sup>) read-out with directly attached SiPMs. In total, the detector is composed of about 5800 scintillator tiles and twice the number of photodetectors. The TOF detector could be easily expanded using a forward disc made up of about 1000 additional tiles just in front of the disc DIRC. The SciTil detector is described in more detail in Chapter 3.

As shown in Fig. 2.4, the TOF wall is placed at a distance of 7 m from the interaction point and uses larger plastic scintillator plates, which are read-out with PMTs from both sides. With an expected time resolution of about 50 ps, the TOF wall can serve as a precise stop counter for measuring the transit time to other start detectors near the target. Under this condition a pion/kaon ( $\pi/K$ ) separation as well as a kaon/proton ( $K/p$ ) separation at a level of three standard deviations should be possible.

## Ring Imaging Cherenkov Counter

A Ring Imaging Cherenkov Counter (RICH) is foreseen in the forward spectrometer [8] (see Fig. 2.4) to enable PID also at the highest momenta between 2 GeV/c and 15 GeV/c. The planned RICH uses two different radiator materials (aerogel and C<sub>4</sub>F<sub>10</sub>) with refractive indices of 1.0304 and 1.00137, respectively, in order to provide reliable  $\pi/K$  and  $K/p$  separation over this broad momentum range. Mirrors are used to focus the Cherenkov light onto an array of PMTs, which are located outside of the active volume.

## Muon range system

In PANDA, many processes of interest have muons in their final state, e.g. originating from  $J/\psi$  and D-mesons. Therefore, an efficient muon identification system is mandatory for the PANDA detector. The muon detection system of PANDA [8] is planned as a Muon Range System (MRS), using a series of iron layers as absorbers with interleaved layers of Mini Drift Tubes (MDTs) for detection.

Within the target spectrometer, the muon system can be divided into two parts, namely the barrel and the forward end-cap, as shown in Fig. 2.4. For the barrel part, the laminated yoke of the solenoid magnet acts as a detection system for muons. In total, 13 sensitive layers alternate with 3 cm thick iron absorbers. In the forward end-cap, more material is needed because of higher momenta of particles. Therefore, five iron layers of 6 cm thickness each are used in combination with six detection layers. In addition, a removable muon filter consisting of another five 6 cm thick iron layers with corresponding detection layers is used downstream the end-cap.

At the very end of the forward spectrometer there is another muon detector for high momentum particles which is similar to the muon system used within the target spectrometer (see Fig. 2.4). The detectors are located 9 m from the interaction point in between several layers of iron absorbers in order to successfully discriminate between muons and other particles like pions.

### 2.2.5 Electromagnetic calorimeter

The PANDA calorimetry [8, 31] comprises an Electromagnetic Calorimeter (EMC) in the target spectrometer and a Shashlyk Calorimeter located in the forward region, as shown in Fig. 2.3 and Fig. 2.4. Fig. 2.11 shows a picture of the EMC, which consists of 15 552  $\text{PbWO}_4$  crystals read-out with large area Avalanche Photodiodes (APDs). Using fast and radiation hard  $\text{PbWO}_4$  crystals with short radiation length and decay time seems to be the optimal choice with regard to the high count rates expected at PANDA and the compact design required for the EMC. The crystals are 20 cm long ( $\sim 22$  radiation lengths  $X_0$ ) with a front size of  $2.1 \times 2.1 \text{ cm}^2$  and are cooled to  $-25^\circ\text{C}$  to increase the light yield.

The EMC barrel with 57 cm inner radius consists of 11 360 crystals, the forward end-cap of 3600 crystals and the backward end-cap comprises 592 crystals. The expected performance of the EMC combines an energy resolution better than 2% at an energy of 1 GeV and an electron/pion ( $e/\pi$ ) discrimination of  $10^3$ . Furthermore, a moderate intrinsic time resolution in the order of a few ns can be expected.

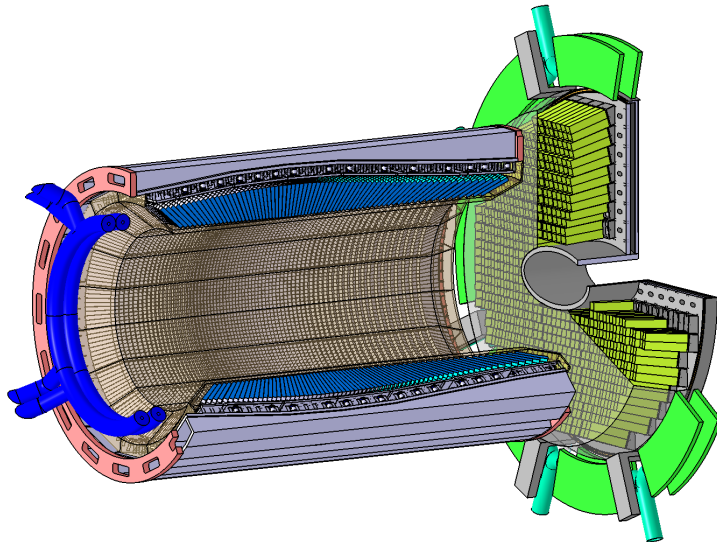


**Figure 2.11:** The PANDA EMC located in the target spectrometer [21], consisting of the barrel EMC, the forward end-cap EMC and the backward end-cap EMC (not shown).

The forward calorimeter is foreseen as a Shashlyk-type calorimeter with the purpose to detect electrons and photons in forward direction at 7.5 m from the target with high efficiency and resolution. The calorimeter is based on modules of alternating layers of scintillators and lead, read-out with wavelength shifting fibers passing through the modules and coupled to PMTs. The front size of one module is 110 mm×110 mm and the length is 680 mm, which corresponds to about 20  $X_0$ . In order to achieve a better spatial resolution each module is divided into 4 separate units of 55 mm×55 mm. The modules are arranged in 27 columns and 13 rows, resulting in 351 modules in total. An energy resolution of 4%/√ $E$  is expected for this type of calorimeter.

### 2.2.6 Hypernuclear detector

In order to perform hypernuclear studies with the PANDA detector, the experiment will make use of a dedicated hypernuclear detector [8] which can be inserted into the target region in place of the MVD and the backward end-cap EMC. This dedicated target station serves as a secondary target of about 25 mm to 30 mm thickness to produce double hypernuclei as well as a detector for high precision  $\gamma$ -spectroscopy. The target itself consists of alternating layers of absorbers and silicon micro-strip detectors, while a germanium detector array is used to measure the decays of produced hypernuclei.

### 2.2.7 Luminosity detector

A luminosity monitor [8] is installed at the very end of the forward spectrometer (see Fig. 2.4) in order to measure the elastic scattering of antiprotons and deduce the absolute luminosity at PANDA. The luminosity detector consists of four layers of HV-MAPS (High-Voltage Monolithic Active Pixel Sensor) with 50  $\mu\text{m}$  thickness and 80  $\mu\text{m}$  × 80  $\mu\text{m}$  pixel size, placed in vacuum and separated by 10 cm to 20 cm along the beam pipe.

### 2.2.8 Data acquisition system

In contrast to many other recent experiments, the PANDA data acquisition system [8] is based on continuous digitization of all detector channels without any dedicated hardware trigger. In order to allow an event rate of at least  $2 \times 10^7$  events/s, each subsystem is configured as an autonomous self-triggering unit, also responsible for data preprocessing at the read-out stage, including valid hit detection, intelligent data reduction by clustering or signal shape analysis. The gathered information of physical relevance is marked with a precise time stamp and buffered for further processing and event building at a later stage. The final trigger selection is done at computer nodes which access the buffers via network. The main advantage of this concept is the high flexibility, e.g. in the choice of trigger algorithms.

## Chapter 3

# The Scintillator Tile Hodoscope

The barrel TOF detector placed within the PANDA target spectrometer is motivated by physical as well as technical considerations. Such a system is not only beneficial for the overall PID performance of the PANDA experiment [30] but also provides important input to event building and software triggering [15]. As a consequence, several different detector concepts have been proposed in the past years. However, most of them have been criticized because of too much material budget in front of the EMC, or could not be realized simply because of the extremely limited space within the target spectrometer.

The Scintillator Tile (SciTil) Hodoscope is a new detector concept for the barrel TOF system and is based on small plastic scintillator tiles read-out with directly attached SiPMs. The current design foresees a fast timing detector of about 2 cm radial thickness (less than 2% of a radiation length) with a time resolution better than 100 ps sigma. Large effort is currently taken to prove the feasibility of the new design and optimize the detector parameters in order to finalize the R&D phase. This chapter briefly discusses the main benefits of the new barrel TOF system and describes the detector layout as proposed by the PANDA TOF group [9].

## 3.1 Physics motivation

### 3.1.1 Hypernuclear physics

The study of single and in particular double hypernuclei is one of the main physics topics of the PANDA experiment. As already described in Chapter 2, the hypernuclei program requires a dedicated target and detector station inside the target spectrometer. In PANDA, the double hypernuclei are produced in a multi-stage process with a primary reaction  $\bar{p} + p \rightarrow \Xi^- \bar{\Xi}^+$ . The  $\Xi^-$  undergo further reactions which may result in the production of hypernuclei, whereas a large fraction ( $\sim 85\%$ ) of the anti-hyperons annihilate directly inside the target and produce two kaons, leaving the interaction region in forward direction. Hence, identifying these kaons with a suitable detector gives a hint for the production of hypernuclei and is mandatory for background suppression. The kaon momentum distribution is peaked around 500 MeV/c. The barrel DIRC detector is able to identify approximately half of these kaons, while the other half is beyond its momentum threshold. A positive kaon identification with the SciTil detector can therefore increase the trigger rate by a factor of 2.

### 3.1.2 Overall particle identification

In addition to dedicated physics topics and channels, it can be expected that the SciTil detector in combination with the CT can provide valuable input to the overall PID of the PANDA experiment. In order to evaluate the benefit of a barrel TOF detector, the Technical Assessment Group on Particle Identification (TAG PID) released a report, dealing with the expected performance of individual PID sub-detectors as well as the combination of detector systems [32]. Though this report was still based on previous design concepts for the barrel TOF (other detector technology, no end-cap TOF, different location), an improvement, especially concerning  $\pi/K$  and  $K/p$  separation power and misidentification among several physics channels, was reported. From the proposed SciTil design with reduced material budget, longer flight path from the target, closer distance



to the EMC and larger solid angle coverage, one can expect a further improvement in performance.

### 3.1.3 Software triggering

The SciTil detector can be used for software triggering at PANDA. The PANDA experiment does not have any hardware trigger but continuously digitizes the hits from all sub-detectors. Event selection and data reduction happens at a later stage by software triggering, based on the input of one or more detector systems. During the first phase of data taking this software triggering is based on simple signatures from well understood and reliable detectors, as it is expected from the SciTil system.

## 3.2 Technical motivation

### 3.2.1 Event timing

Apart from improved PID performance, the barrel TOF system can also provide an important input for any event building algorithm, as reported in detail in Ref. [15]. When looking at the event rates present at PANDA, it becomes obvious that a fast timing detector is desirable in order to disentangle signals belonging to multiple events. As already mentioned in the previous chapter, there are two modes of operation foreseen for the PANDA experiment: the high precision mode with an average luminosity of  $L = 2 \times 10^{31} \text{ cm}^{-2}\text{s}^{-1}$  and a high luminosity mode with  $L = 2 \times 10^{32} \text{ cm}^{-2}\text{s}^{-1}$ . By multiplying with the total cross section for  $p\bar{p}$  interactions  $\sigma_{tot} \approx 100 \text{ mb}$ , one can derive the average event rate in high luminosity mode of  $\dot{N}_{avg} = 20 \text{ MHz}$ . The value for the high precision mode is a factor 10 smaller. For the following explanations only the high luminosity mode is taken into account, as this reflects the maximum expected load for the experiment.

Due to the time dependent beam current in the HESR and the time structure of the target (see section 2.2), the maximum instantaneous event rate, however, is higher. Taking this

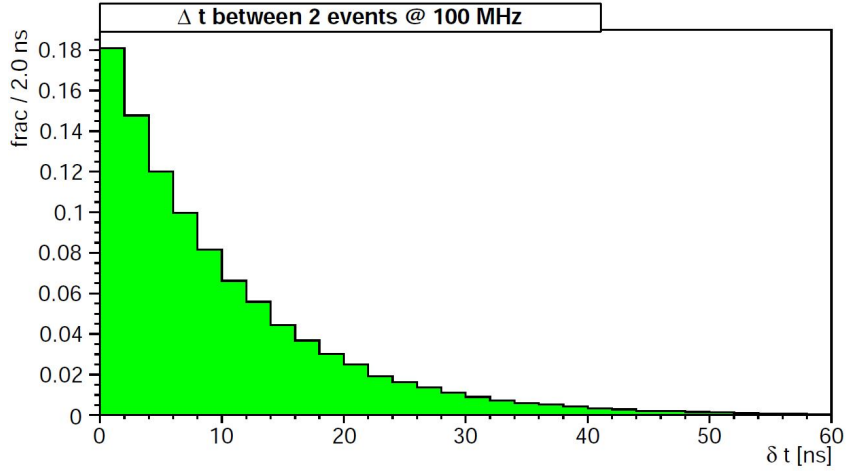


**Figure 3.1:** Time difference between two successive events at an instantaneous event rate of  $\dot{N}_{max} = 100$  MHz. Reprinted from Ref. [9].

into account, the maximum event rate in high luminosity mode is given by  $\dot{N}_{max} = 50$  MHz for the cluster jet target and  $\dot{N}_{max} = 100$  MHz for the pellet target. At an event rate of 100 MHz, the time difference between two events follows an exponential distribution with a mean  $\overline{\delta t} = 1/\dot{N}_{max} = 10$  ns. This means that for 63 % of all events the  $\delta t$  is smaller than the mean value. Fig. 3.1 is taken from Ref. [9] and shows this behavior.

From these considerations it becomes clear that a fast timing detector is desired to identify signals from different events. Furthermore, it is obvious that the time resolution of the timing detector directly affects the measurement precision of particle hit times  $t_i$  and creation times  $t_{0,i}$ , and hence determines the efficiency for finding non-overlapping events.

Fig. 3.2 is taken from Ref. [15] and shows the time distribution of events for different time resolutions at an event rate of 100 MHz and 6 charged particles per track. Subsequent events are colored cyclically in black, red and blue. The time resolution values of 100 ps, 1–2 ns and 5 ns are chosen as typical values for the SciTil system, EMC and tracking detectors of PANDA. It has to be noted that these values are meant to represent total time resolutions  $\sigma_t$ , since the determination of the time  $t_0$  an event occurred requires the combination of several detector systems, e.g. SciTil, CT and EMC. However, if the momentum resolution is sufficiently good one can assume that the total time resolution

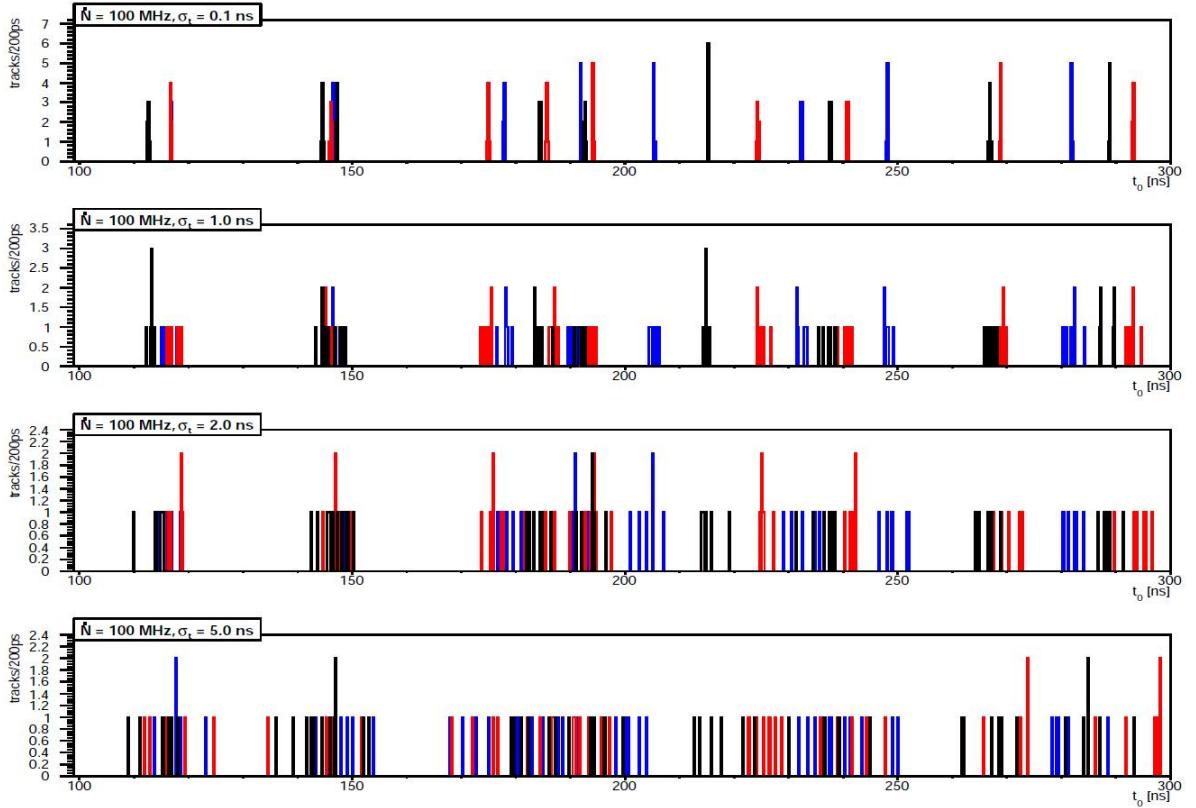


**Figure 3.2:** Distribution of particle creation times  $t_{0,i}$  for multiple events with 6 charged particles ( $N_c = 6$ ) for different time resolutions at an instantaneous event rate of  $\dot{N}_{max} = 100$  MHz. Subsequent events are colored cyclically in black, red and blue. Reprinted from Ref. [15].

will be determined by the timing detector with the smallest time uncertainty. One can see that for the best time resolution of  $\sigma_t = 100$  ps, most of the events can be separated, while for values  $\sigma_t \geq 1$  ns the time signals of different events start to overlap, which results in a loss of separation efficiency.

In this simple event building approach one can define an efficiency as the fraction of non-overlapping events. Fig. 3.3(a) is taken from Ref. [9] and shows the rate dependence of the efficiency for different time resolutions for events with 6 charged ( $N_c = 6$ ) and no neutral ( $N_n = 0$ ) particles.  $\sigma_{t,n}$  is the time resolution for neutral particles, i.e. the time resolution of the EMC. Since neutral particles are not considered here,  $\sigma_{t,n} = 0$ . The plot clearly shows a large improvement for the best time resolution. Assuming a time resolution of  $\sigma_t = 100$  ps the efficiency is greater than 95% for all event rates.

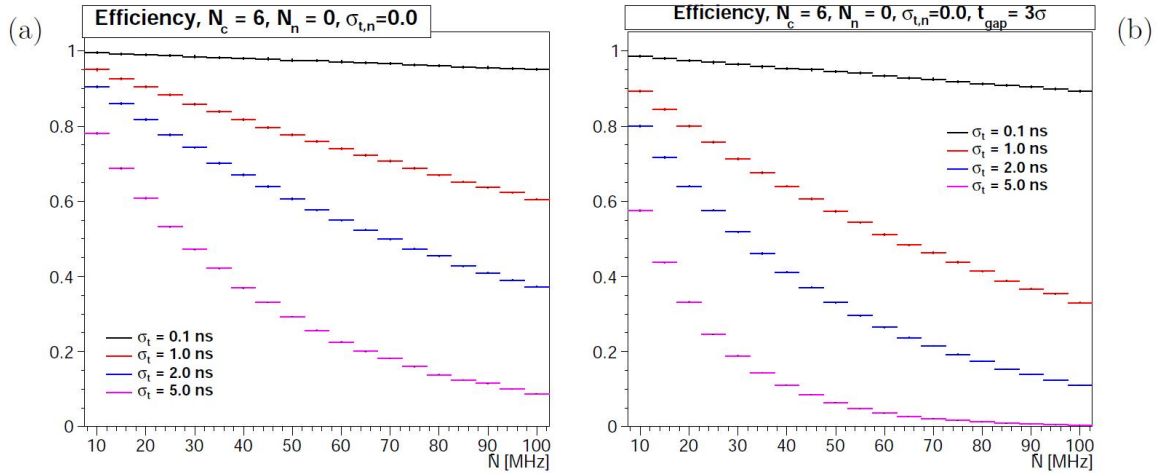


**Figure 3.3:** Event building efficiency as a function of the instantaneous event rate for different time resolutions  $\sigma_t$  based on pure overlap approach (a) and on a simple event building algorithm (b). Only events with six charged particles ( $N_c = 6$ ) are considered, no neutral particles are taken into account ( $N_n = 0$ ,  $\sigma_{t,n} = 0$ ). Reprinted from Ref. [9].

It has to be noted that the values for the efficiency may not be equivalent with the results obtained with a realistic event building algorithm, which is not just based on selecting the non-overlapping events. In order to achieve a slightly more realistic situation one could think of an algorithm that considers all creation times  $t_{0,i}$  as belonging to an event, if they are separated by a certain time  $t_{gap} = 3\sigma_t$  from another bunch of  $t_{0,i}$ . As a result the efficiency decreases, as it can be seen in Fig. 3.3(b). However, the efficiency is still above 90% for all event rates, considering only charged particles that can be identified in the SciTil detector.

Of course, many interesting physics channels also have photons in their final states, which can be reliably detected only in the EMC. This results in different time resolutions for different particle species. Assuming a time resolution for neutral particles of  $\sigma_{t,n} = 1$  ns combined with a time resolution for charged particles of 100 ps, the efficiency given in Fig. 3.3(b) drops to about 60% at an event rate of 50 MHz and 40% at an event rate of 100 MHz, respectively [15].

The results shown so far concentrate on the efficiencies for instantaneous event rates  $\epsilon(\dot{N})$ . The interesting quantity to look at is now the efficiency for all events recorded within a

longer time of data taking  $t_{run}$ , i.e. the time-averaged efficiency  $\bar{\epsilon}$ . Therefore, the time dependence of the event rate has to be modeled. As shown in Ref. [15], this can be done using the sum of an exponential and a constant:

$$\dot{N}(t) = a_0 \cdot \exp(-a_1 \cdot t) + a_2 \quad (3.1)$$

with a peak rate  $\dot{N}_{max} = a_0 + a_2 = 50$  MHz in case of the cluster jet or  $\dot{N}_{max} = 100$  MHz for the pellet target, respectively, and an average rate  $\dot{N}_{avg} = 20$  MHz. The time weighted efficiency is then given by:

$$\bar{\epsilon}_{50} = \frac{1}{N} \int_0^{t_{run}} \dot{N}(t) \cdot \epsilon(\dot{N}) dt \quad \text{with } N = \int_0^{t_{run}} \dot{N}(t) dt \quad (3.2)$$

and

$$\bar{\epsilon}_{100} = \frac{1}{N} \int_0^{t_{run}} \dot{N}(t) \cdot \epsilon(2 \cdot \dot{N}) dt \quad (3.3)$$

The results for the time-weighted efficiencies are given in Table 3.1, together with the relative gain of having a precise timing detector, which is defined as:

$$G_{0.1} := \frac{\bar{\epsilon}(0.1 \text{ ns})}{\bar{\epsilon}} \quad (3.4)$$

It quantizes how many more events can be successfully reconstructed. The above discussion shows the advantage of having a precise barrel timing detector like the proposed SciTil system in terms of event building at PANDA. A more detailed analysis of the influence of precise particle timing on the event building can be found in Ref. [15].

**Table 3.1:** Time weighted efficiencies and relative gain when having a fast timing detector with  $\sigma_t = 100$  ps for two different peak event rates and four different time resolutions [9].

$\sigma_t$ [ns]	0.1	1.0	2.0	5.0
$\bar{\epsilon}(50 \text{ MHz})$ [%]	97	75	58	29
$\bar{\epsilon}(100 \text{ MHz})$ [%]	94	58	36	12
$G_{0.1}(50 \text{ MHz})$	1.0	1.3	1.7	3.3
$G_{0.1}(100 \text{ MHz})$	1.0	1.7	2.6	7.8

### 3.2.2 Relative time-of-flight

The SciTil detector can provide valuable input in PID that is based on relative TOF measurements, as it is planned in the forward spectrometer using the TOF wall. This becomes particularly important in cases where an event contains only one charged particle track reaching the forward region. In such cases a start time signal from a charged particle detector inside the target spectrometer can help to identify the events correctly. At best, this start signal should be of comparable precision as the stop signal. Table 3.2 lists some physics channels with a higher fraction of events containing only a single charged particle track in forward direction.

**Table 3.2:** *Some physics channels with a higher fraction of events containing only a single charged particle track in forward direction [9]. These events may be identified by relative TOF.*

Physics channel	Beam momentum (GeV/c)	Single forward event fraction
$D^{*+}D^{*-}$	4.1	18 %
$\Omega_c^0\bar{\Omega}_c^0$	15	36 %
$\eta_c1\eta$	5.5	17 %
$\Omega^-\bar{\Omega}^+$	5.7	16 %
$\Lambda_c^+\bar{\Lambda}_c^-$	11.15	15 %
$D_s(2317)D_s^-$	4.3	12 %

### 3.2.3 Charge discrimination

A TOF system like the SciTil detector which is sensitive to charged particles and located in front of the EMC can serve as an input for the latter in order to discriminate between charged and neutral particles. In the stage of software triggering this can be extremely helpful since the full track information is not yet available.

### 3.2.4 Conversion detection

Similar to the discrimination of charged and neutral particles, the SciTil detector can be used to identify photon conversions happening inside other detectors. Since the SciTil barrel is placed just in between the barrel DIRC detector and the EMC, photon conver-

sions inside the DIRC system may be detected. Due to the thick DIRC radiator these conversions are supposed to be rather frequent. With a reasonable spatial resolution of the TOF barrel one may correct for these photon conversions.

### 3.2.5 Track finding

A barrel TOF detector located outside the CT can be used as a seed for track finding in the latter. This requires that the TOF detector is able to measure both  $\Phi$  and  $z$  with reasonable precision. Using this information could speed up the whole process of pattern recognition and reduce the formation of ghost tracks. This procedure does not require the very best time resolution but a fast and easy available detector signal without extensive processing or calibration. Therefore, the SciTil detector is well suited for this action, contrary to the EMC.

## 3.3 Detector requirements

As shown in the last sections, the SciTil detector can enhance the performance of the PANDA spectrometer. In order to fully exploit the technical and physical benefits as outlined above, the barrel TOF system has to fulfill several requirements which can be summarized as following:

- **time resolution of  $\sigma \sim 100$  ps:** in order to provide useful input to event building and software triggering a precise time information is needed. The same holds for TOF measurements. With regard to relative TOF, the time resolution should be in the order of other TOF detectors (e.g. TOF wall).
- **minimum use of material:** the main concern of the barrel TOF detector is its influence on other detector systems mainly due to its material but also due to heat generation, which may result in a deterioration of the performance of these systems. Secondly, the radial space inside the target spectrometer is limited to about

2 cm. The current design foresees a mechanically independent detector with minimal thickness and material budget corresponding to 2% of one radiation length, placed in between the DIRC system and the EMC.

- **large angular acceptance:** in order to ensure best performance in combination with other detector system, the SciTil detector should match the angular acceptance of the CT and DIRC barrel, i.e. a solid angle between  $22^\circ$  and  $140^\circ$ .

### 3.4 Detector layout

The SciTil detector is planned as a barrel TOF system with approximately 50 cm radius located just outside the DIRC volume. The basic layout of the detector has been proposed by the PANDA TOF group in Ref. [9] and foresees small plastic scintillators read-out with directly attached SiPMs.

The smallest unit of the SciTil detector is the scintillator tile in combination with two SiPMs, as shown on the left in Fig. 3.4. Two SiPMs positioned on two different sides of the scintillator are used to increase the number of detected photons and improve the time resolution. The current layout is based on tiles with dimensions of  $28.5 \times 28.5 \times 5 \text{ mm}^3$ ,

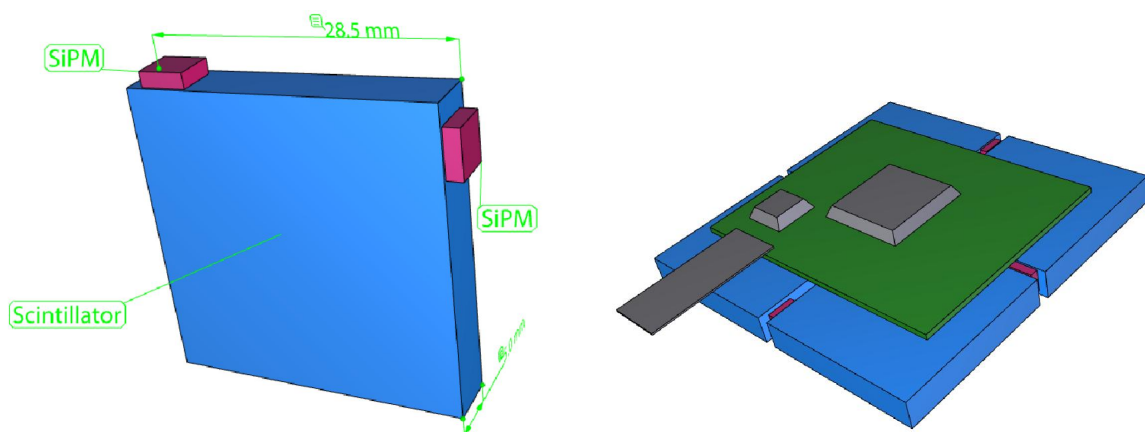


**Figure 3.4:** The basic SciTil layout as proposed in Ref. [9]. The basic unit of the SciTil detector is the scintillator tile readout with two SiPMs (left). Four tiles are arranged in quad-modules with front-end electronics at the back (right).



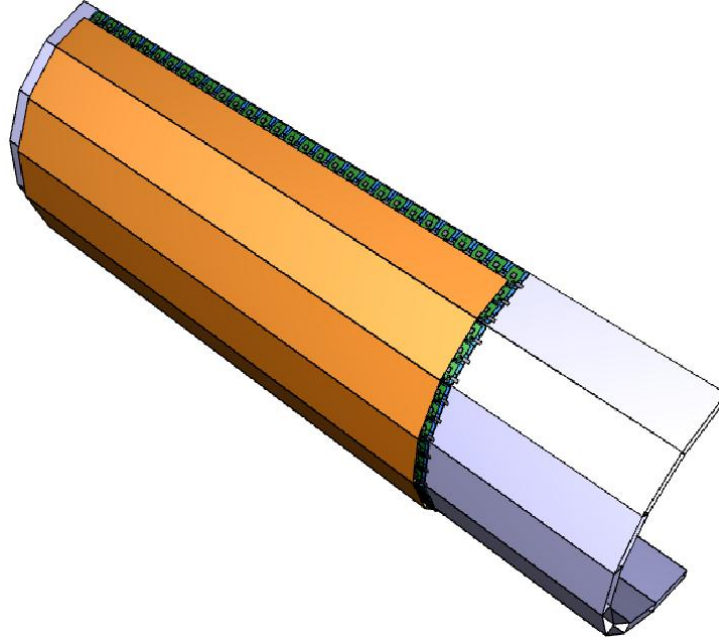


**Figure 3.5:** A half barrel of the SciTil detector [9], consisting of 8 super-modules with  $3 \times 30 = 90$  quad-modules each.

arranged in quad-modules consisting of four tiles and corresponding front-end electronics (see Fig. 3.4 right). 90 quad-modules are combined to form a super-module. The whole barrel is composed of 16 super-modules, as shown in Fig. 3.5.

The use of plastic scintillators for the SciTil detector is motivated by a couple of factors. Plastic scintillators offer short rise- and decay times and deliver high light output. Typical numbers are rise times in the order of 500 ps to 1 ns and decay times of about 2 ns. The absolute light yield is about 10 000 scintillation photons per MeV of energy loss. Therefore, a thickness of 5 mm is enough to produce about 10 k photons for a minimum ionizing particle (MIP). In addition, plastic scintillators are easy to handle and cheap. Typical scintillators used for TOF application are BC-404 and BC-408 from Saint-Gobain Crystals<sup>1</sup> or EJ-200 and EJ-204 from Eljen Technology<sup>2</sup> with similar physical properties.

The SiPM seems to be the optimal choice to detect the light produced inside the scintillator tile. SiPMs offer several advantages like good time resolution, high PDE, compactness,

---

<sup>1</sup><http://www.detectors.saint-gobain.com/>

<sup>2</sup><http://www.eljentechnology.com/>

robustness, low cost and possibility of operation in magnetic fields, to state the most important ones for the proposed SciTil detector. It is planned to use SiPMs with an active area of  $3 \times 3 \text{ mm}^2$ . There are efforts by different companies to develop SiPMs with larger active area or matrices of SiPMs to increase the sensitive area. At the moment SiPMs from Hamamatsu<sup>3</sup> and KETEK<sup>4</sup> are considered as the most promising candidates to be used for the SciTil system. However, it may be also an option to use the Digital Photon Counter (DPC), which was introduced recently by Philips as the first fully digital SiPM [3, 33].

Concerning the read-out electronics for the SciTil detector it is most important that the good intrinsic time resolution of the SiPM is maintained. Besides, the total power consumption is another important parameter. At the moment, the use of an ASIC to amplify and discriminate the SiPM signal is foreseen. As an alternative, it might be an option to employ the DPC from Philips, where the electronics is already integrated into the SiPM chip, as explained in the next chapter.

All numbers and dimensions are taken from Ref. [9], which can be seen as the basic and most promising concept for the barrel TOF system. However, the SciTil detector is a recent topic in PANDA which is currently still in the R&D phase. Parameters like the scintillator material, the size of the scintillator tile, the position of the SiPMs on the tile, the SiPM type or the number of attached SiPMs are subject of current investigations and part of optimization studies. Results of these ongoing studies concerning the optimization and finalization of the detector layout are described in great detail in the following chapters.

---

<sup>3</sup>Hamamatsu Photonics K.K., <https://www.hamamatsu.com/>

<sup>4</sup>KETEK GmbH, <http://www.ketek.net/>

## Chapter 4

# Semiconductor photodetectors

The advances in the field of semiconductor photodetectors led to a progressive replacement of the conventional PMT in many applications, ranging from particle and nuclear physics to astrophysics or medical imaging. The commercial evolution of solid state detectors started in the 1960s with the development of the photodiode, continued with the invention of the Avalanche Photodiode (APD) and recently reached a new level with the progress in the field of the Geiger-mode APD (G-APD), also called Silicon Photomultiplier (SiPM).

With the development of the SiPM, being a highly sensitive photodetector, the solid state devices became competitive and, in some applications, even superior to vacuum photodetectors. Because of many advantages of this detector, many groups in science as well as industry are placing huge effort in R&D to further improve the device.

The principle of semiconductor photodetectors is similar to the one of other ionization detectors, however, semiconductor devices are based on the collection of electrons and holes which are produced in crystalline semiconductor material by ionizing radiation. The energy required to create such electron-hole pairs is about a factor 10 smaller compared to detectors based on gas ionization, resulting in better energy resolution. Other advantages are high stopping power due to higher density, fast time response, compact size, low power consumption or insensitivity to magnetic fields. Drawbacks are high noise or the sensitivity to radiation damage due to the crystalline structure. Most semiconductor

photodetectors are based on Silicon material.

## 4.1 Photodiodes

The photodiode is based on a simple p-n junction or in most cases on a PIN junction, which is an intrinsic semiconductor region in between a p-type and n-type semiconductor region, as shown on the left in Fig. 4.1. The absorption of a photon leads to the generation of an electron-hole pair by the inner photoelectric effect, with the electron in the conduction band and the hole in the valence band. The electric field inside the diode leads to separation of the charges and movement to the electrodes and thus to a detectable photocurrent.

The photodiode is typically operated at low reverse bias. Since the PIN photodiode is a linear device without any internal gain it cannot be used to measure very low light levels. Therefore, the device is mainly used in applications where high light yields are expected, e.g. crystal calorimeters in HEP.

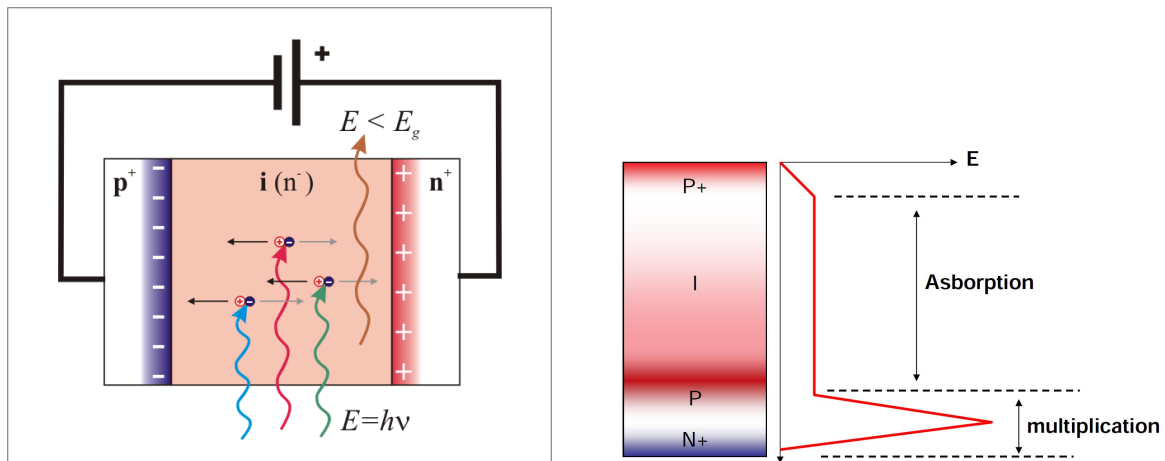


**Figure 4.1:** Schematic of a PIN photodiode operated in reverse bias (left). Photons with energy  $E = h\nu$  create electron-hole pairs. If the photon energy is smaller than the bandgap energy  $E_g$  the material becomes transparent. Right: schematic of a PIPN junction as used for APDs. Holes drift to the p+ layer and recombine, thus, do not contribute to the avalanche multiplication. Electrons move towards the p-n+ junction where they are accelerated and start impact ionization. Reprinted from Ref. [34].

## 4.2 Avalanche Photodiodes

In order to increase the sensitivity of the photodiode, the device can be operated at a higher reverse bias voltage, like it is done in APDs. Due to the high electric field in an APD, the photoelectrons can gain enough energy to produce further electron-hole pairs by impact ionization, thus, starting an avalanche. However, the applied voltage should be not too high in order to prevent holes from impact ionization and avoid an uncontrolled breakdown of the diode. Therefore some APDs are based on PIPN diodes in order to separate the absorption region from the multiplication region, as shown on the right in Fig. 4.1. The typical gain of APDs is in the order of 50 to 200. APDs are very versatile photodetectors and are used in many fields, e.g. HEP (CMS and PANDA Electromagnetic Calorimeters), medical applications like Positron Emission Tomography (PET).

## 4.3 Silicon Photomultipliers

The SiPM consists of an array of Single Photon Avalanche Diodes (SPADs), also called (micro-)cells or pixels, operated in Geiger-mode, i.e. above the breakdown voltage, which makes the device sensitive to single photons, just like a PMT. SiPMs have a gain of typically  $10^5$  to  $10^7$ , the typical size of a single microcell is ranging from  $10 \times 10 \mu\text{m}^2$  to  $100 \times 100 \mu\text{m}^2$ .

The SPADs work similar to APDs and are all connected in parallel and read-out at a common output (cathode or anode). However, in contrast to conventional APDs the electric field inside the diode is high enough that both electrons and holes can contribute to the avalanche generation by impact ionization. The result is an uncontrolled and self-sustaining multiplication process (breakdown) and a large current flow (in the order of  $\mu\text{A}$ ) in the diode. As a consequence, the avalanche has to be quenched, which is usually done by using a high-ohmic resistor (in the order of a few 100 k $\Omega$ ) in series to each SPAD or by an active quenching circuit.

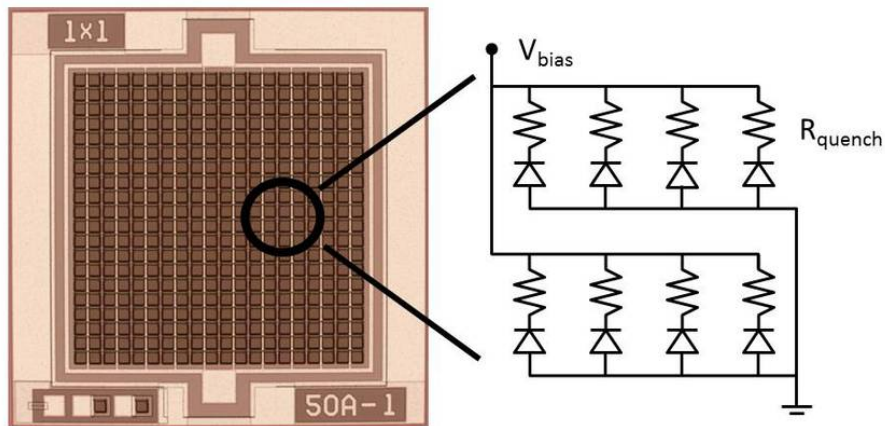


**Figure 4.2:** Top view (left) and schematic (right) of a SiPM from KETEK<sup>1</sup> with  $1 \times 1 \text{ mm}^2$  sensitive area and  $50 \times 50 \mu\text{m}^2$  pixel size, thus  $20 \times 20 = 400$  pixels connected in parallel. Each pixel works as an individual SPAD with a quenching resistor  $R_{\text{quench}}$  in series. The device is operated at reverse bias  $V_{\text{bias}}$ , above the breakdown voltage.

Fig. 4.2 shows the basic layout of a SiPM from KETEK<sup>1</sup>. Since the avalanche process is self-sustaining the device only needs the first photo-generated carriers to trigger a breakdown. The charge carriers can be generated by a single photon or by the interaction of multiple photons inside the diode. This makes the SiPM sensitive to single photons, with each pixel acting as a quasi-digital device detecting only whether or not one or more photons have entered.

Nowadays, many different SiPM models with different names, e.g. SiPM, Multi-pixel Photon Counter (MPPC), Multi-pixel Avalanche Photo Diode (MAPD), are available from a large variety of vendors, e.g. Hamamatsu<sup>2</sup>, KETEK, AdvanSiD<sup>3</sup>, Zecotek<sup>4</sup>, SensL<sup>5</sup>. Philips<sup>6</sup> recently invented the first fully digital SiPM, called Digital Photon Counter (DPC), by putting active electronics aside to each cell, exploiting the quasi-digital nature of the SiPM device.

<sup>1</sup>KETEK GmbH, <http://www.ketek.net/>

<sup>2</sup>Hamamatsu Photonics K.K. (HPK), <https://www.hamamatsu.com/>

<sup>3</sup>Advanced Silicon Detectors, <http://advansid.com/>

<sup>4</sup>Zecotek Photonics Inc., <http://www.zecotek.com/>

<sup>5</sup>SensL, <http://sensl.com/>

<sup>6</sup>Philips Digital Photon Counting, <http://www.digitalphotoncounting.com/>

## 4.4 The Digital Photon Counter

Recently, the so-called Digital Photon Counter (DPC) has been introduced by Philips as the first fully digital SiPM [3, 33, 35]. So far, the main field of application for this device is medical imaging, e.g. PET, however, the new detector is gaining more and more attention also in the field of HEP.

The difference to an analog SiPM can be explained employing Fig. 4.3. In a conventional SiPM, the single cells (diodes) with serial quenching resistors are all connected in parallel and the electrical pulses generated by the detection of photons are combined into a single analog output signal, which is usually quite small. To retrieve the digital information like time or energy, the signal is further processed using conventional electronics like an amplifier, discriminator, TDC and ADC, which may be combined into an ASIC. In case of the DPC, CMOS electronics is directly integrated into the SiPM, meaning that each cell has a separate ADC which produces a digital output signal and in addition all cells are connected to a TDC also integrated into the SiPM chip. The resulting output is a digital time stamp and a digital sum of trigger bins (photon count). An additional circuit

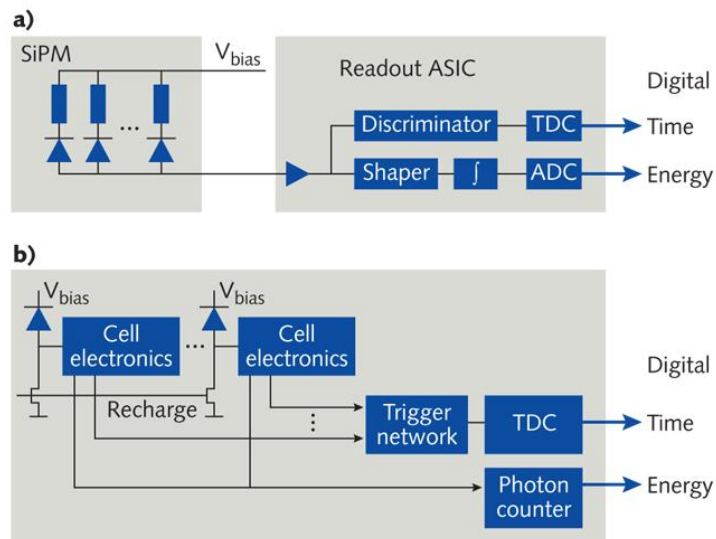


**Figure 4.3:** Schematic layout of a conventional analog SiPM (a) and of the Philips DPC (b). Reprinted from Ref. [3].

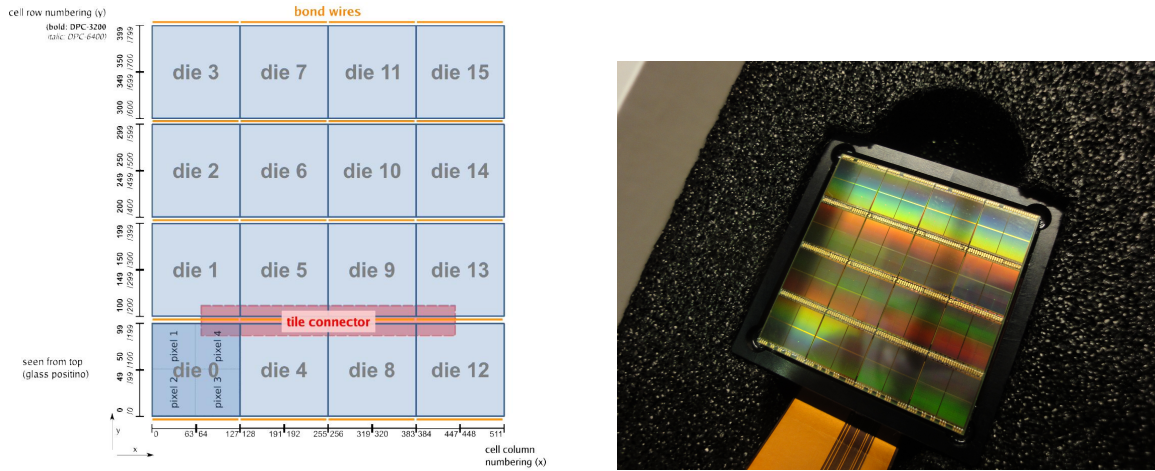


**Figure 4.4:** Left: DPC tile layout [36]. The tile consists of 16 individual dies with 4 pixels each. Each pixel is composed of 3200 (DPC-3200) or 6400 (DPC-6400) cells. Right: photo of a DPC tile seen from the top. The tile is mounted in a frame together with a FPGA at the back and a flat read-out cable.

is added to actively quench and recharge the microcells after breakdown.

This new approach by Philips conserves the digital nature of photon detection with SiPMs and the advantages are quite evident: reduction of dark counts by addressing each microcell and by enabling/disabling specific cells, fast recovery due to active quenching and recharging, conservation of excellent intrinsic timing performance of SiPMs, which may be degraded by large parasitic capacitances in conventional SiPMs.

#### 4.4.1 Sensor layout

The basic unit of the DPC sensor is a so-called die. In the current design 16 dies are arranged in a 4x4 matrix and form the DPC tile with a total area of about  $32 \times 32 \text{ mm}^2$ . A die consists of  $2 \times 2$  pixels with about  $3.2 \times 3.9 \text{ mm}^2$  active area and 3200 (DPC3200-22-44) or 6400 (DPC6400-22-44) microcells each, resulting in a single cell size of about  $59 \times 64 \mu\text{m}^2$  and  $59 \times 32 \mu\text{m}^2$ , respectively. Each pixel is further divided into  $2 \times 2$  sub-pixels. The DPC tile layout is shown in Fig. 4.4. At the backside of the tile there is a FPGA, which allows to control and program the individual dies, collects the events and generates time stamp and photon count values. In this context the photon counts are



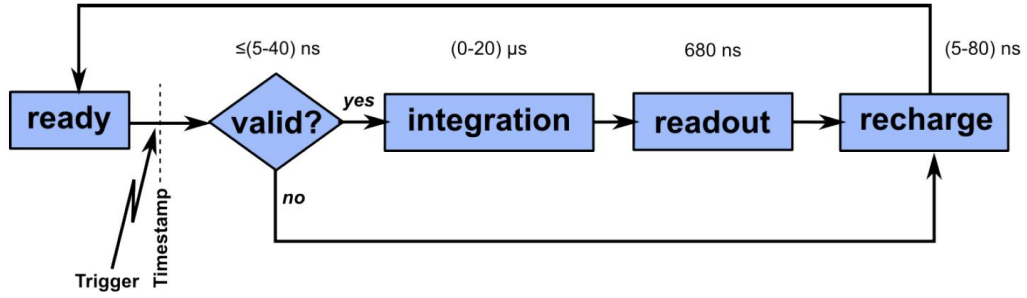


**Figure 4.5:** Data acquisition sequence of the DPC sensor [36], i.e. one event.

summed up on pixel bases, i.e. a single photon count value per pixel (four per die), and the time stamp is generated by a pair of TDCs per die, i.e. a single time stamp per die. The moment of time stamp generation is in turn defined by the configured trigger level. In addition, the sensor contains a validation network which allows to set a photon count value for the validation of an event. The tiles are connected with flat cables to the DPC base unit, which supplies voltage to the tiles and is in turn connected via USB to a computer to allow tile control and access with a dedicated software.

#### 4.4.2 Data acquisition scheme

The data acquisition sequence of the DPC sensor can be explained on the basis of Fig. 4.5. The cycle starts if the photon count reaches the configured trigger threshold, which can be set to 1, 2, 3 or 4 photons. At this moment also the time stamp is generated. If there is a trigger, the validation process starts. The sensor waits for an adjustable time period (5 – 40 ns) if the validation threshold is reached. The validation threshold can be set to 1, 2, 4, 8, 16 or 32 photons. If the photon count exceeds the configured validation threshold, the event is successfully validated and the integration period starts. Within this time window the DPC detects further incoming photons. Finally, the acquired data is read-out (four photon count values and one time stamp per die) and the cells are recharged. If the event is not validated the cells are instantly recharged and the sensor is ready for a new cycle.

It has to be noted that the trigger and validation thresholds do not define exact numbers

of photons that have to be detected in order to trigger or validate an event. In fact, successful triggering/validation depends on the photon distribution on (sub-)pixels. This is because the trigger and validation schemes are based on logic combinations on sub-pixel level, where rows of cells are grouped together to form so-called row-trigger-lines. This leads to statistical trigger and validation thresholds, e.g. a validation threshold set to 4 photons on a DPC-3200 sensor means that on average  $16.9 \pm 6.2$  photons are needed for successful validation [36]. However, a trigger (or validation) threshold of one photon always triggers (or validates) an event if only a single photon is counted and thus gives the time stamp of the first detected photon.

Since the SiPM is the main detector technology used within this work, the next chapter deals with SiPM properties important for later discussion in regard to the SciTil system, and describes the studies that have been done to characterize and understand the functionality and features of the device, as this is the basic ingredient for efficient use of the detector.

## Chapter 5

# Silicon Photomultiplier characterization studies

The Silicon Photomultiplier is the main detector technology used within this work and is also the photodetector of choice for the PANDA SciTil system. This chapter describes detailed SiPM characterization studies and discusses the basic features and parameters of the device, on the basis of various experimental tests carried out in course of this work. During these studies, the focus is mainly put on KETEK SiPMs and MPPCs from Hamamatsu as well as on the Philips Digital Photon Counter, since these detectors have been used for the most part of diverse measurements and because they are also the most promising devices to be used for the SciTil detector.

In this context, the chapter is divided into two parts, the first part dealing with conventional analog SiPMs while the second part concentrates on the digital device. The results of various studies on SiPM characterization and applications performed in course of this thesis are also reported in Ref. [28, 29, 37, 38].

### 5.1 Characterization of analog SiPMs

The SiPM device seems to be the optimal photodetector for the SciTil system. This photodetector is compact in size, fast, insensitive to magnetic fields, offers high PDE and is

considered to be rather radiation hard. The following sections discuss the most important parameters of SiPMs with special emphasis on an application within the PANDA TOF system. Parameters of particular interest for the SciTil detector are the photodetector time resolution, PDE or recovery time as well as their dependency on the operating temperature and applied bias voltage. It is obvious, that the SiPM time resolution directly influences the performance of the whole TOF system. Increasing the PDE of the device leads to a higher number of detected photons and as we will see to improved time precision. Increasing the bias voltage usually leads to improved time resolution and higher PDE but also enforces the influence of noise effects which deteriorate the detector performance. Here, a trade-off has to be found.

### 5.1.1 SiPM gain

The gain of the SiPM defines the charge which is produced by a single pixel after an avalanche breakdown. In good approximation the gain  $G$  is given by:

$$G = \frac{C_{pix}}{q_e} \cdot (V_{bias} - V_{bd}) = \frac{C_{pix}}{q_e} \cdot V_{over} \quad (5.1)$$

with  $C_{pix}$  being the capacitance of the pixel,  $q_e$  the elementary charge and the over-voltage  $V_{over}$  which is defined as the difference between the applied voltage  $V_{bias}$  and the breakdown voltage  $V_{bd}$ . Typical values for the pixel capacitance  $C_{pix}$  are 10 fF up to a few 100 fF, depending on the pixel size. The SiPMs are usually operated a few Volts ( $\leq 5$  V) above the breakdown voltage, resulting in a gain of  $10^5$  to  $10^7$ .

The total output signal of the SiPM is the sum of all single pixel signals. It is proportional to the number of input photons as long as this number is significantly smaller than the total number of pixels of the device. Due to the high gain, a couple of photons can produce a signal of several mV and no further amplification is needed before read-out. However, in order to perform single photon detection the signal is usually amplified using a simple low gain amplifier. For most of the studies presented here, a Photonique AMP-0611 preamplifier [39] was used.

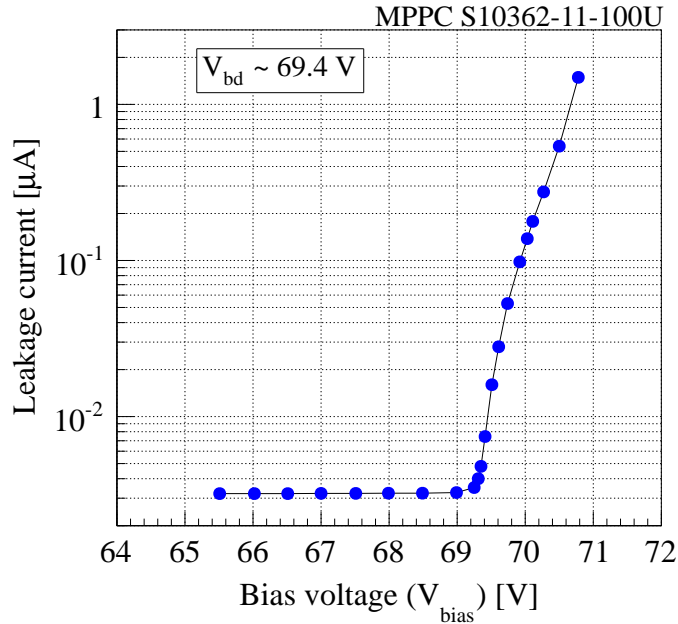


**Figure 5.1:** Dark current of a Hamamatsu MPPC (S10362-11-100U) at an operating temperature of 25°C. When the breakdown voltage is reached the current increases.

Just like the gain, almost all other SiPM parameters, e.g. the PDE, dark count rate (DCR), recovery time, time resolution, are depending on the applied over-voltage. It is therefore of particular interest to study this parameter dependence and to determine the breakdown voltage of the device prior to using it in a dedicated application.

The breakdown voltage can be estimated roughly by measuring the SiPM current in a dark environment as a function of the applied bias voltage, as shown in Fig. 5.1 for a Hamamatsu MPPC with  $1 \times 1 \text{ mm}^2$  sensitive area and  $100 \times 100 \mu\text{m}^2$  pixel size (model number S10362-11-100U). The output current was measured using a Keithley 6517 electrometer. The measurement was done at room temperature (25°C). Below the breakdown voltage the measured current is very small. In this regime thermally generated charge carriers are moving in the electric field, but no uncontrolled avalanche breakdown is happening, resulting in a small leakage current. With increasing the voltage the current stays constant until, at a certain point, the breakdown occurs. An uncontrolled avalanche starts to develop and the current drastically increases. The large change in the SiPM current indicates that the breakdown voltage is reached.

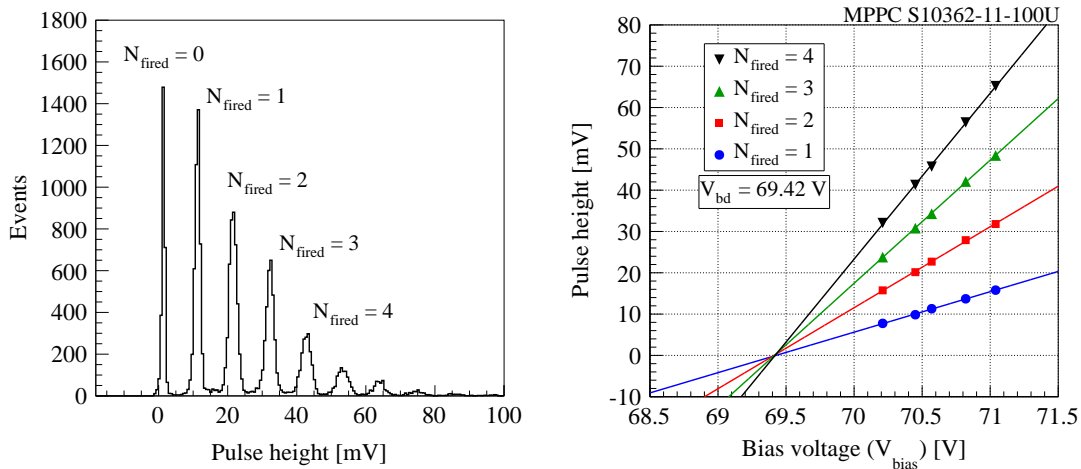


**Figure 5.2:** Left: pulse height spectrum of a Hamamatsu MPPC (S10362-11-100U) operated at  $V_{bias} = 70.45 V$ . The individual peaks in the figure correspond to certain numbers of fired pixels. Measuring the distance between the photo peaks and the pedestal for different bias settings and extrapolating to zero pulse height, i.e. zero gain, allows to determine the breakdown voltage (right). The solid lines show linear fits.

The breakdown voltage can be determined more accurately by using the single photon spectrum of the SiPM, which is received by measuring the output pulse height of the SiPM at low light input and filling the values into a histogram. The result of such a measurement is shown on the left in Fig. 5.2. The low intensity light pulses from a blue laser ( $\lambda = 404 \text{ nm}$ ) with 32 ps pulse width (FWHM) were recorded with a Hamamatsu SiPM operated at  $25^\circ\text{C}$ . Again, the MPPC S10362-11-100U was used. The light intensity was adjusted using a variable optical attenuator. The SiPM signal was amplified using a Photonique AMP-0611 preamplifier and the output pulse height was measured with a LeCroy digital oscilloscope (WavePro 735Zi). The individual peaks in the figure correspond to certain numbers of fired pixels ( $N_{fired}$ ). The peak corresponding to  $N_{fired} = 0$  is the pedestal, i.e. the noise on the signal line. By measuring now at different operating voltages the distance between the photo peaks and the pedestal for each bias setting and extrapolating to zero pulse height i.e. zero gain, the breakdown voltage can be determined as shown on the right in Fig. 5.2.

Since the amplitude of the single photon peak ( $N_{fired} = 1$ ) is proportional to the gain of the SiPM, one can define a relative gain by measuring the distance between two adjacent photo

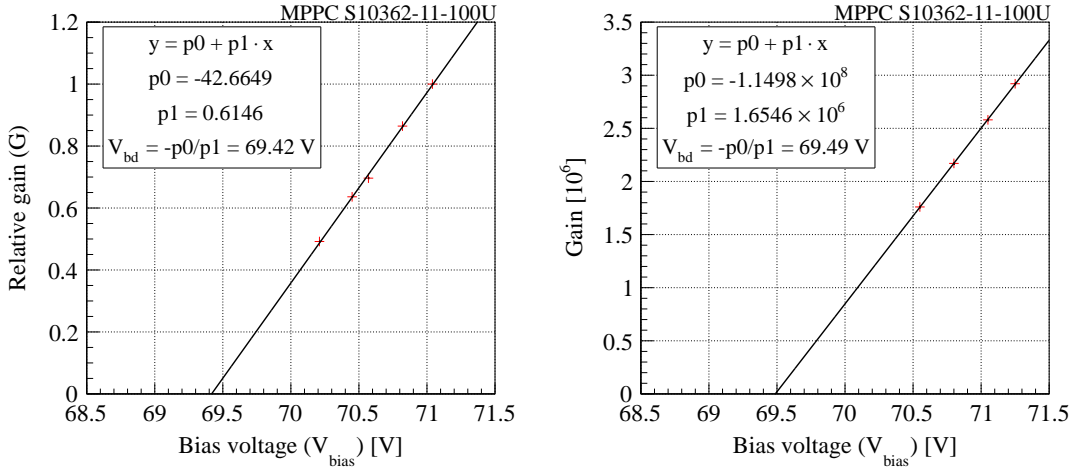


**Figure 5.3:** Left: relative SiPM gain as a function of the bias voltage obtained by measuring the single photon pulse height ( $N_{fired} = 1$ ). Extrapolating to zero gain gives the breakdown voltage. Right: absolute gain vs. bias voltage measuring the output charge for a single fired pixel. The plots show the results for a Hamamatsu MPPC (S10362-11-100U) operated at a temperature of  $25^\circ\text{C}$ .

peaks. Again, the breakdown voltage can be determined by performing the measurement at different bias settings and extrapolating to zero gain (see Fig. 5.3 left). Errors can be minimized by measuring the distance several times using different pairs of adjacent peaks.

Another way to estimate the breakdown voltage is to directly determine the absolute gain of the SiPM at different bias settings, by measuring the output charge (instead of the pulse height) of a single fired pixel ( $N_{fired} = 1$ ) with a Charge to Digital Converter (QDC). The resulting histogram is similar to Fig. 5.2 left but is now representing the output charge (or QDC channels) corresponding to  $N_{fired} = 0$ ,  $N_{fired} = 1$ , etc. The distance between two adjacent photo peaks multiplied by the QDC binning and divided by the elementary charge and the preamplifier gain defines the SiPM gain.

The preamplifier gain was determined by measuring the preamplifier response to input signals of defined pulse height and charge, which were provided by a pulse generator. The signal from the pulse generator was split, one path was connected directly to the oscilloscope as reference and the other was used as input for the preamplifier. The preamplifier output signal was in turn also directed to the oscilloscope. The DC voltage supply for

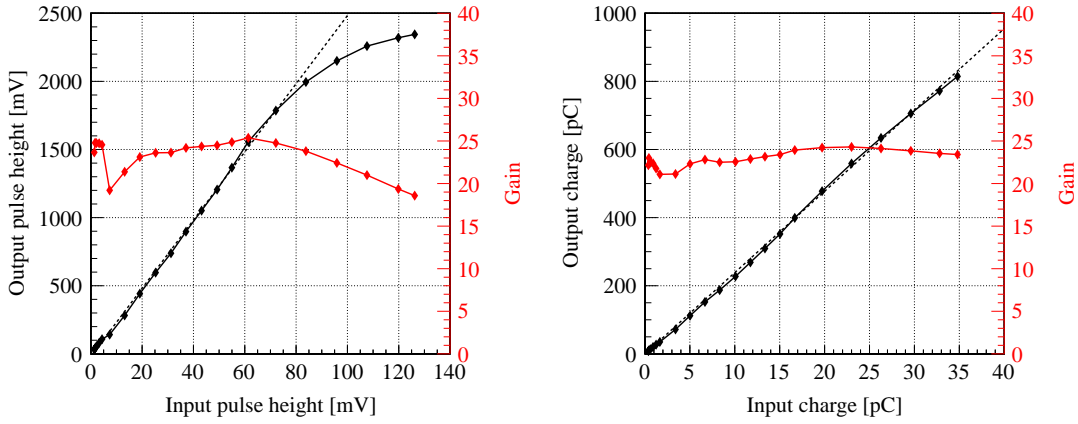


**Figure 5.4:** Preamplifier response in black, obtained by measuring the input/output pulse height (left) and charge (right). The corresponding gain in red. The solid lines are added to guide the eye, the dashed lines to stress the almost linear response over a wide range. The fluctuations for small input signal are due to pick-up noise in the setup.

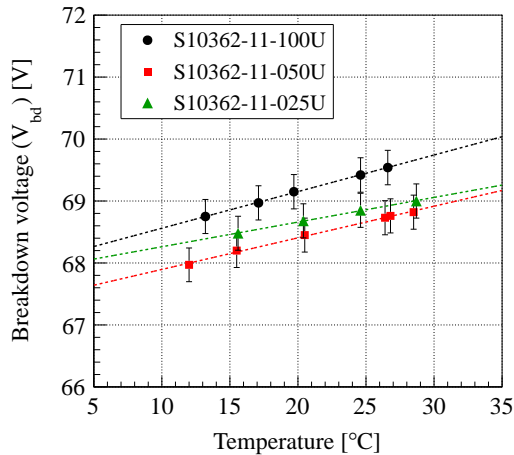
the preamplifier was set to 5 V. The preamplifier gain is defined by determining the ratio between output and input pulse height or charge, respectively.

Fig. 5.4 shows the preamplifier output pulse height (charge) as a function of the input pulse height (charge) and the corresponding gain. The plots show that the preamplifier response is linear within the whole tested range for a charge measurement, while the output pulse height deviates from linearity and saturates around 2.4 V for very high input signals. The charge is measured by integrating the signal within a gate window. In case the signal height is already saturating, the width of the signal and thus the measured charge may still be increasing. Within the linear range, the measurements result in an average gain of  $22.9 \pm 0.2$  for the charge measurement and  $23.8 \pm 0.4$  for the pulse height measurement.

Knowing the gain of the preamplifier, the SiPM gain can be evaluated as described before. On the right of Fig. 5.3 the linear dependence of the gain on the applied bias voltage is shown. Again, the breakdown voltage is defined by extrapolating to zero gain. The different methods described to determine the breakdown voltage show similar results.

In order to evaluate the temperature dependence of the breakdown voltage, the procedure





**Figure 5.5:** Dependency of the breakdown voltage on the operating temperature for three Hamamatsu MPPCs with different pixel sizes.

described above was repeated for different operating temperatures of the SiPM. As the temperature increases, the crystal lattice vibrations become stronger and the probability for interactions of charge carriers with phonons rises. Hence the breakdown voltage increases and thus the gain is reduced if the bias voltage is fixed. In order to operate the SiPM at constant gain either the temperature has to be stabilized or the bias voltage has to be corrected for temperature variations.

Fig. 5.5 shows the linear dependence of the breakdown voltage for three Hamamatsu MPPCs with different pixel sizes of  $100 \times 100 \mu\text{m}^2$  (100U),  $50 \times 50 \mu\text{m}^2$  (050U) and  $25 \times 25 \mu\text{m}^2$  (025U) on the operating temperature. Water- and Peltier cooling was used to stabilize the temperature during the measurement. If the temperature rises by  $1^\circ\text{C}$ , the bias voltage has to be increased by about 59 mV for the 100U, 51 mV for the 050U and 40 mV for the 025U device, respectively, in order to keep the gain constant.

### 5.1.2 Photon Detection Efficiency

The PDE is dependent on three factors: the quantum efficiency (QE), the geometric fill factor  $\epsilon_{fill}$ , defined as the ratio of the sensitive area to total area, and the avalanche trigger probability  $P_{trigger}$ , which is the probability that an incoming photon triggers an

avalanche. Hence, the PDE can be written as:

$$\text{PDE} = \text{QE} \cdot \epsilon_{fill} \cdot P_{trigger} \quad (5.2)$$

The quantum efficiency of the active area is dependent on the wavelength of the incoming light and can reach values up to 90 % [40]. The geometric fill factor can vary between 30 % and 80 % for Hamamatsu and KETEK sensors, depending on the pixel size ( $10 \times 10 \mu\text{m}^2$  to  $100 \times 100 \mu\text{m}^2$ ). It is clear that a high number of pixels per unit area results in larger inactive space needed for resistors and separation lines. Therefore, the pixel size has to be optimized with regard to the application. In case where only few photons are expected, e.g. Cherenkov applications, the PDE should be as high as possible, thus a large pixel size may be used. On the other hand for applications with high light yield, e.g. scintillator read-out or calorimetry, the number of pixels should be large in order to maintain the linearity between the number of input photons and fired cells.

The trigger probability depends on the operating voltage, i.e. the higher the bias voltage, the higher  $P_{trigger}$ . It also depends on the position where the photoelectric effect takes place inside the cell. Since electrons have a higher probability to trigger a breakdown than holes,  $P_{trigger}$  is higher if the photon is absorbed in the p-layer of the p-n junction. By producing different structures (p-on-n or n-on-p structure) the cell is either more sensitive to blue or to red light. This becomes important for applications like scintillator or fiber read-out since these optical materials have characteristic emission spectra. Fig. 5.6 shows the PDE for Hamamatsu and KETEK sensors, as given in the data sheets [41, 42, 43].

### 5.1.3 Dark-noise, cross-talk and after-pulsing

Dark counts are produced by thermal generation or field-assisted generation of free charge carriers inside the depletion layer of the p-n junction. Because of the high electric field, these electron-hole pairs or free electrons can trigger an avalanche breakdown leading to a signal identical to the signal produced by an incoming photon. The DCR is typically in the order of a few 100 kHz to some MHz per  $\text{mm}^2$  at room temperature and strongly

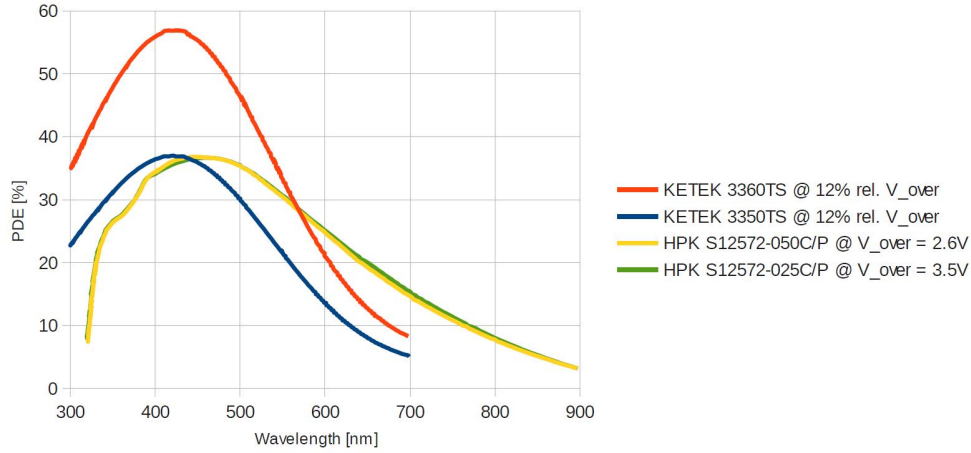


**Figure 5.6:** PDE of various SiPMs from Hamamatsu and KETEK [41, 42, 43]. The PDE is given for typical values of the over-voltage. The breakdown voltage for Hamamatsu devices is typically between 65 V and 70 V, for KETEK sensors it is lower (25 V to 30 V). The relative over-voltage ( $\text{rel. } V_{\text{over}}$ ) is defined as:  $\text{rel. } V_{\text{over}} = (V_{\text{bias}} - V_{\text{bd}}) / V_{\text{bd}}$ . The PDE of the Hamamatsu devices is nearly identical because of the different operating voltages. The figure shows that the KETEK devices are more sensitive to blue light.

depends on the applied bias voltage and temperature. Decreasing the temperature by about 8 °C leads to a reduction of the DCR by a factor of 2 [40].

Furthermore, the threshold of the read-out electronics has a strong influence on the number of detected events triggered by dark counts. If the DCR is in the order of 1 MHz at a threshold of 0.5 p.e. (photoelectrons) equivalent, it is already below 1 kHz setting the threshold higher than the 3 p.e. amplitude [40]. For applications with many photons it is therefore advisable to set the threshold high enough not to trigger on dark count events. However, the first detected photons often provide better time precision and for low light level detection the threshold has to be low enough to be able to detect single photons. Hence dark counts may have a large effect and cooling might be mandatory.

Optical cross-talk in SiPMs is related to the effect that photons which are produced during an avalanche breakdown are reaching neighboring cells, triggering another avalanche there. The cross-talk probability strongly depends on the applied bias voltage and thus on the gain. For a gain of  $10^6$  on average 30 photons are emitted during the avalanche that may cause cross-talk [40]. The effect is unwanted since it limits the photon counting resolution

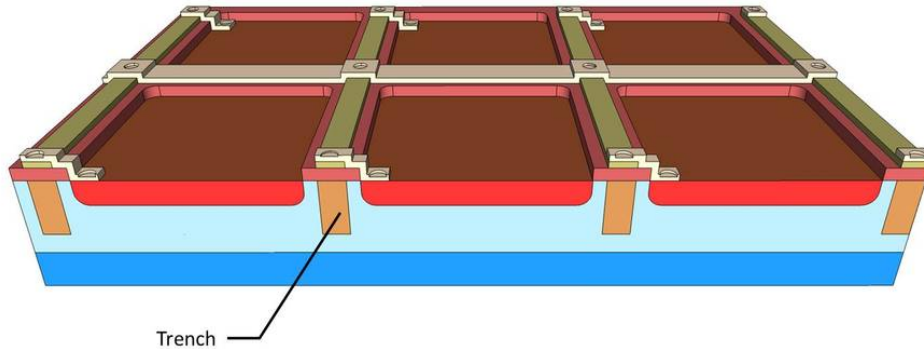


**Figure 5.7:** Cross section of Ketek SiPM with optical trench technology to reduce cross-talk between neighboring microcells. Reprinted from Ref. [44].

of the device, because cross-talk events cannot be distinguished from events coming from external photons. Lowering the bias voltage decreases the cross-talk probability, however with the drawback of decreasing also the PDE. Recently, some vendors started to produce SiPMs with optical trenches in between the microcells in order to reduce the optical cross-talk, as shown in Fig. 5.7. However, this has the disadvantage of slightly reducing the fill factor and thus again the PDE.

After-pulsing happens if charge carriers which are produced during an avalanche breakdown are trapped in the silicon and released at a later time, causing another breakdown. This delayed release can occur a few ns up to several 100 ns to  $\mu$ s after the initial avalanche. Charge carriers which are released within a short delay have small impact if the cell is not yet fully recovered, thus giving only a reduced signal smaller than the 1 p.e. amplitude. After-pulses happening after the recharge of the cell cannot be distinguished from standard 1 p.e. signals and hence reduce the photon counting resolution of the device. Hamamatsu has recently introduced new materials and wafer processing technologies to produce SiPMs with reduced after-pulsing (S12571 series, see Ref. [41]).

#### 5.1.4 Dynamic range

As already mentioned, the SiPM output signal is proportional to the number of incident photons as long as this number is significantly smaller than the total amount of pixels

( $N_{total}$ ) times the PDE. Hence, the two numbers,  $N_{total}$  and the PDE, define the dynamic range of the device. It is obvious that if the number of simultaneously input photons exceeds the total number of pixels, two and more photons start to enter the same cell. However, the output signal of the corresponding cell is always the standard single photon signal, no matter how many photons interact within the pixel at the same time.

It is clear that the device should be preferably operated in a range where a linear response can be expected, otherwise the photon counting capability is lost. For many applications concerned with the detection of high light intensities (several 100 to several 1000 photons), e.g. scintillation detectors, it is therefore important to select devices with sufficiently large dynamic range. In any case it is of great interest to determine the dynamic range and study the response to varying light intensities before using a SiPM device for a specific application. Such response curves could be also used for calibration, allowing the use of SiPMs for high light intensities which are beyond the dynamic range, of course with lower accuracy.

The response of the SiPM (number of fired pixels,  $N_{fired}$ ) to simultaneously incident photons ( $N_{photon}$ ) can be described in good approximation by:

$$N_{fired} = N_{total} \times \left[ 1 - \exp \left( - \frac{N_{photon} \times \text{PDE}}{N_{total}} \right) \right] \quad (5.3)$$

The output linearity lowers with increasing number of input photons and the response saturates at  $N_{fired} = N_{total}$ . If  $N_{photon} \times \text{PDE}$  reaches 50% (80%) of the total number of available cells, the deviation from linearity is already about 20% (more than 30%). Fig. 5.8 shows the response curve given by Eq. 5.3 for  $N_{total} = 100$  and  $N_{total} = 1600$  for two different values of the PDE. Looking at the plots it becomes clear that a SiPM with high number of pixels should be used to maintain the output linearity with increasing light intensity.

Precisely speaking, the above equation is only valid for an ideal photodetector and an infinitely short light pulse. As already discussed, the response of a real SiPM is affected

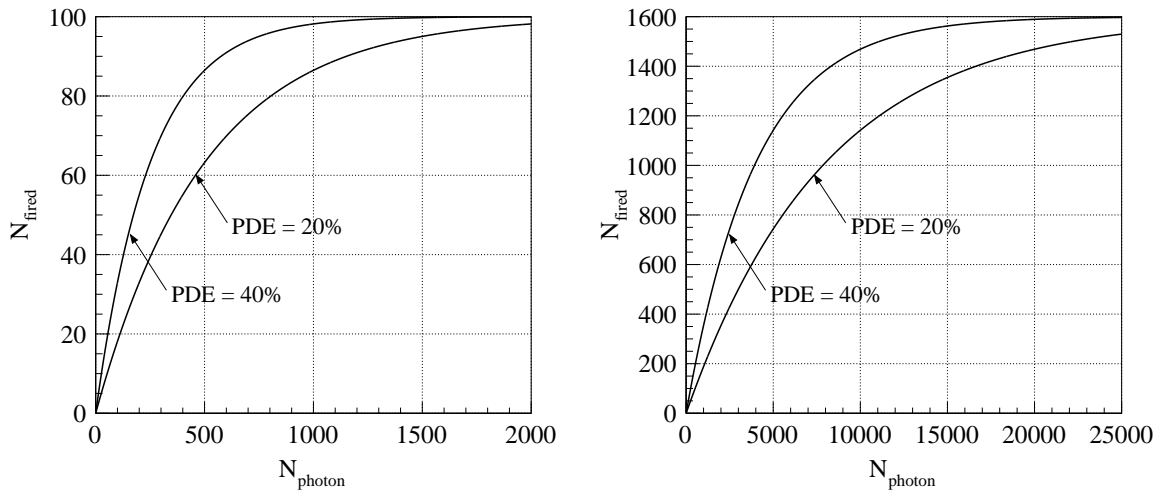


**Figure 5.8:** Theoretical SiPM response curves to simultaneously input photons for 100 pixels (left) and 1600 pixels (right) and different PDE values.

by several effects like dark-noise, cross-talk or after-pulsing, especially at high operating voltage and/or temperature. Furthermore, the response of the device may be influenced by the pixel recovery time if the duration of the light pulse becomes comparable to or larger than the latter. In such a case,  $N_{fired}$  might become even larger than  $N_{total}$ , because pixels could fire several times during one pulse. This can happen when reading out scintillators with long decay time constants. Nevertheless, for moderate operating conditions and short light pulses it can be expected that the SiPM response is well described by Eq. 5.3.

In order to characterize the response of SiPMs, several different devices were tested under laboratory conditions and were exposed to short laser pulses of varying light intensity, ranging from single photon to well above the total number of microcells of the respective detector. The results of this experimental study were published in Ref. [37]. The tests concentrated on SiPMs with  $1 \text{ mm}^2$  sensitive area but with different number of pixels and from various vendors, namely two Hamamatsu MPPCs with 100 pixels (S10362-11-100U) and 400 pixels (S10362-11-050U), respectively, a SSPM from Photonique<sup>1</sup> with 556 pixels (SSPM-0611B1MM-TO18) and a Zecotek MAPD-1 with 560 pixels. Table 5.1 summarizes the main parameters of the tested devices.

<sup>1</sup>Photonique SA has suspended its operations. Product information can be found here: <http://www.photonique.ch/LEGACY>.

**Table 5.1:** Main SiPM parameters. The breakdown voltage,  $V_{bd}$ , has been measured as described before in section 5.1.1. The operating voltage for the measurements of the response curves,  $V_{bias}$ , is typically set  $\sim 1$  V above  $V_{bd}$ . The exact values are stated. The corresponding gain has been calculated using Eq. 5.1. Other parameters are taken from the data sheets [45, 46, 47]. The PDE values given by Hamamatsu include effects from cross-talk and after-pulsing and are therefore overestimating the real PDE. The capacitance values are terminal capacitances of the device. Pixel capacitances can be evaluated using the total number of pixels (ignoring parasitic capacitances).

Parameter	HPK MPPC S10362-11			Photonique SSPM	Zecotek
	-100U	-050U	-025U	0611B1MM-TO18	MAPD-1
Active area [mm <sup>2</sup> ]	1×1	1×1	1×1	1×1	1×1
Number of pixels	100	400	1600	556	560
Pixel size [ $\mu\text{m}^2$ ]	100 × 100	50 × 50	25 × 25	–	–
Fill factor [%]	78.5	61.5	30.8	> 70	–
PDE [% @ 400 nm]	72	47	24	18	15
Capacitance [pF]	35	35	35	40	75.6
Quenching resistor [k $\Omega$ ]	85	105	200	–	–
Breakdown voltage [V]	69.45	68.65	68.85	27.80	34.00
Bias voltage $V_{bias}$ [V]	69.95	69.85	–	29.00	34.70
Gain @ $V_{bias}$	$1.1 \times 10^6$	$6.6 \times 10^5$	–	$5.4 \times 10^5$	$5.9 \times 10^5$

Fig. 5.9 shows a schematic drawing of the measurement setup. “All tests were done at room temperature ( $\sim 25$  °C). As light source we used a pulsed laser with 32 ps pulse width (FWHM) from Advanced Laser Diode Systems. The emission wavelength of the laser head (PIL040) is  $\lambda = 404$  nm. The repetition frequency was set to a level of 20 kHz, to have a time interval between two laser pulses well above the SiPM cell recovery time. After passing a variable optical attenuator, the laser pulses were split using a beam splitter with a splitting ratio of 45:55 (45 % reflectivity, 55 % transmission). One path of the beam is targeted at a Hamamatsu S5971 PIN photodiode for monitoring the light intensity. The current of the PIN photodiode was measured using a Keithley 6517 electrometer. After passing another variable optical attenuator, the second beam was directed to a diffuser in order to homogeneously distribute the light on the SiPM active area. The second attenuator in between beam splitter and SiPM is needed to deal with the different sensitivities of the SiPM and the photodiode.” [37].

The PIN photodiode is operated at low reverse bias ( $V_{bias} = 10$  V) and has no internal

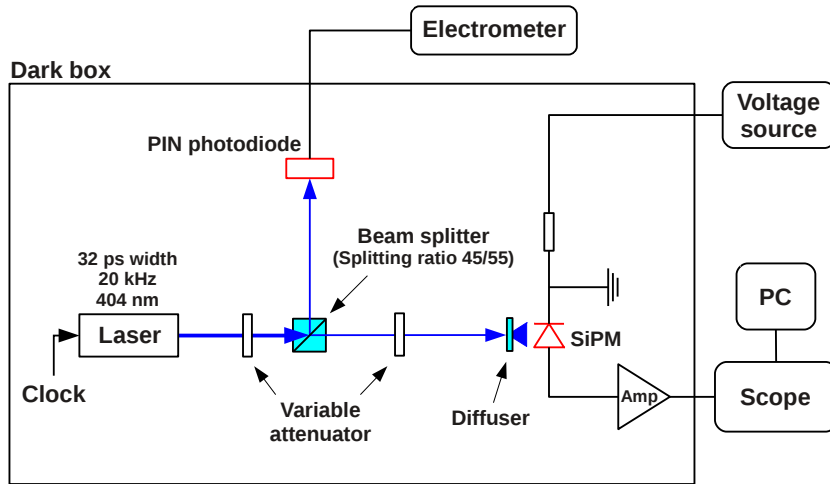


**Figure 5.9:** Schematic of the setup used to measure the SiPM response curve. Reprinted from Ref. [37].

amplification and therefore no sensitivity to low light levels, while the SiPM is sensitive to single photons. However, the photodiode features low noise and a linear response and thus the device is suited for calibration purposes and intensity monitoring. As for the above studies, the SiPM signal was amplified using the Philips AMP-0611 preamplifier. The response of the preamplifier was characterized beforehand and is discussed in Section 5.1.1 (see Fig. 5.4). The gain of the preamplifier is about 23. The operating voltages of the tested SiPMs are listed in Table 5.1. The values were chosen in a way to achieve low to moderate gain of the respective devices, so that the measurand, i.e. the SiPM response, is hardly affected by noise effects like dark-noise, cross-talk or after-pulsing.

In order to quantize the SiPM response and measure the response curve, one needs to determine the number of fired pixels,  $N_{fired}$ , for a defined number of incident photons,  $N_{photon}$ . The former can be estimated by measuring the average output pulse height with the oscilloscope (LeCroy WavePro 735Zi) divided by the single pixel signal ( $N_{fired} = 1$ ), which can be determined as described in Section 5.1.1 by using the single photon pulse height spectrum (see Fig. 5.2). From the spectrum, the output signal of a single fired pixel can be evaluated several times by extracting the horizontal distance between adjacent photo peaks.



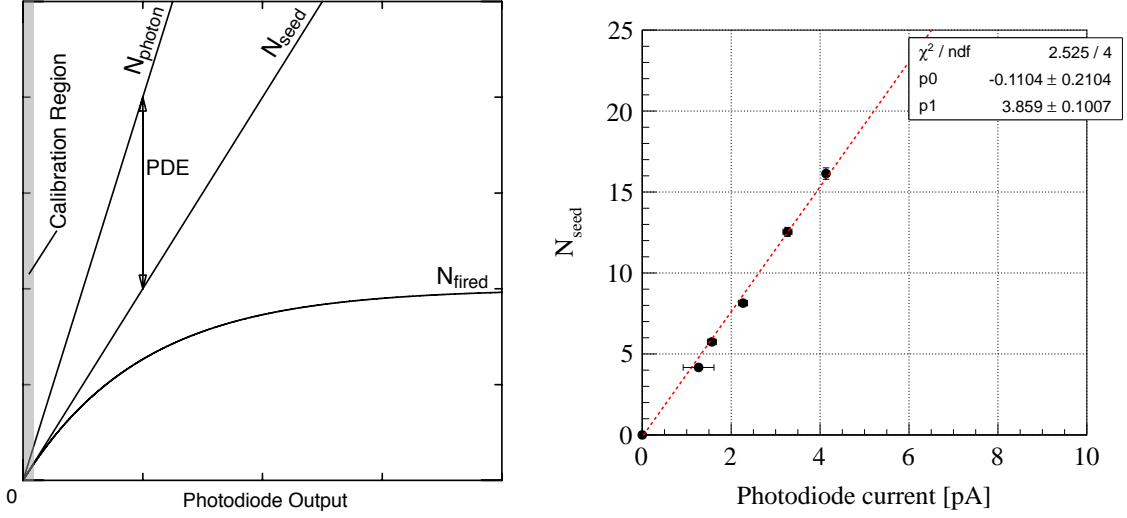


**Figure 5.10:** Left: Schematic of the calibration procedure, reprinted from Ref. [37]. The photodiode was calibrated at low light intensities, where the SiPM response ( $N_{\text{fired}}$ ) is still linear and  $N_{\text{fired}} = N_{\text{seed}}$  (see text). Right: zoom into the calibration region, showing the linear relation between  $N_{\text{seed}}$  and the photodiode output current measured with the Hamamatsu 050U. A linear fit of the form  $y = p0 \cdot x + p1$  was used.

The second variable that must be determined is  $N_{\text{photon}}$ . Therefore, we needed another detector as reference in order to get knowledge about the incident light intensity on the tested device. Here the PIN photodiode was used. However, before the photodiode can be used as a reference detector, it has to be calibrated. The calibration was done at very low light intensities, i.e.  $N_{\text{fired}} < 10$  for the Hamamatsu 100U with 100 pixels and  $N_{\text{fired}} < 20$  for the other devices with more than 400 pixels. Since the input photons were distributed homogeneously on the sensor surface, the SiPM response can be expected to be linear in this regime of very low light input. Fig. 5.10 shows a schematic of the calibration procedure.

“For interpretation of the data, we introduce the average number of “seeds”,  $N_{\text{seed}}$ , which is the average number of photons arriving at the sensitive area of the SiPM, that could trigger an avalanche unless the cells had been fired already. The number of fired pixels,  $N_{\text{fired}}$ , is the main observable of the measurement.  $N_{\text{fired}}$  can be determined by measuring the signal pulse height, as described before. In the calibration region  $N_{\text{seed}} = N_{\text{fired}}$ , thus  $N_{\text{seed}}$  and the linear relation between the photodiode output current and the number of

“seeds” can be determined and in the following extrapolated to higher light intensities. The relation between  $N_{seed}$  and the number of incident photons,  $N_{photon}$ , is given by  $N_{photon} = N_{seed}/PDE$ . In order to avoid the use of a PDE, which depends on the temperature, the operation voltage and the way it is measured, we plot  $N_{fired}$  as a function of  $N_{seed}$  and compare different types of SiPMs. This is a more “natural” representation, because only measured quantities are involved and therefore the actual PDE of the sensor is included a priori.” [37].

Using the above relations, the response curve (Eq. 5.3) changes to:

$$N_{fired} = N_{total} \times \left[ 1 - \exp\left(-\frac{N_{seed}}{N_{total}}\right) \right] \quad (5.4)$$

“As mentioned before, we are determining  $N_{fired}$  by measuring the signal pulse height rather than the output charge. The idea behind is to minimize the influence of delayed correlated noise, like after-pulsing and cross-talk related to this after-pulsing, as well as the influence from dark-noise. In course of the measurements we also monitored the integrated charge and checked that there’s no apparent change in the signal shape for all light intensities that were tested. Since we are operating the SiPM at low gain and therefore low noise, we realized that the measured SiPM response is hardly affected by the method used to determine  $N_{fired}$  (pulse height or charge measurement). The impact of the diverse noise effects on the measurement results is estimated in the following.” [37].

**Dark-noise:** the influence of dark-noise on the measurement result is very small, since it produces signals which are not correlated in time to the “real” signals from the laser pulse. Dark counts are randomly distributed in time and only affect the pulse height measurement if they happen within the rise time of the signal ( $\sim 2-3$  ns). Assuming a DCR below 1 MHz for a SiPM with  $1 \text{ mm}^2$  sensitive area, a dark count may happen within this time span with a probability of a few per mill only. Therefore, the influence of dark-noise on the measurement can be neglected.

**After-pulsing:** as discussed in the previous sections, after-pulsing can be seen as a source of delayed correlated noise, characterized by a certain after-pulse probability and

time constant. Similar to dark-noise, the pulse height measurement can only be affected by after-pulsing, if it happens within a very short time window (during the signal rise time) after the initial avalanche from the laser pulse. If so, it will lead to an overestimation of the SiPM output ( $N_{fired}$ ).

According to Ref. [48], the after-pulse probability is about 10 % for Hamamatsu MPPCs with 1 mm<sup>2</sup> sensitive area at the operating conditions we are using (see Table 5.1). However, on top of this comes the effect of a finite pixel recovery time. An after-pulse happening shortly after the initial breakdown of the cell will only give a certain fraction of the standard single photon pulse height, depending on the recovery status of the pixel. The time needed for a cell to fully recover after a breakdown is in the range of 200 ns for the Hamamatsu 100U and 50 ns for the Hamamatsu 050U [45], so that an after-pulse occurring after 2-3 ns only results in a fraction of about 5-15 % of the standard single cell signal. Combining all the above effects the influence of after-pulsing is therefore only in the range of 1-2 %.

**Cross-talk:** this effect is another form of correlated noise, which occurs almost instantaneously to a breakdown in a neighboring cell with a certain cross-talk probability. This probability is about 5 % at the utilized operating conditions [48]. There are two ways how cross-talk can influence the measurement of the SiPM response. Firstly, it can happen in combination with fast after-pulsing, which was discussed before. However, due to the relatively small effect of after-pulsing itself, this impact is negligible. Secondly, cross-talk can occur in relation to the initial laser pulse. This effect however only plays a role at low light intensities (in the linear range), while for high light input it is suppressed due to the high pixel occupancy. Indeed, in the calibration region cross-talk may influence the measured pulse height, leading to an overestimation of  $N_{fired}$  and thus  $N_{seed}$  ( $N_{fired} = N_{seed}$  in the calibration region) by about 5 %.

“Because of the above considerations, the uncertainty of the SiPM output ( $N_{fired}$ ) due to after-pulsing, cross-talk and dark-noise is < 2 % for most light intensities that were used in the measurements, i.e. beyond the linear region of the response. In this regime, the

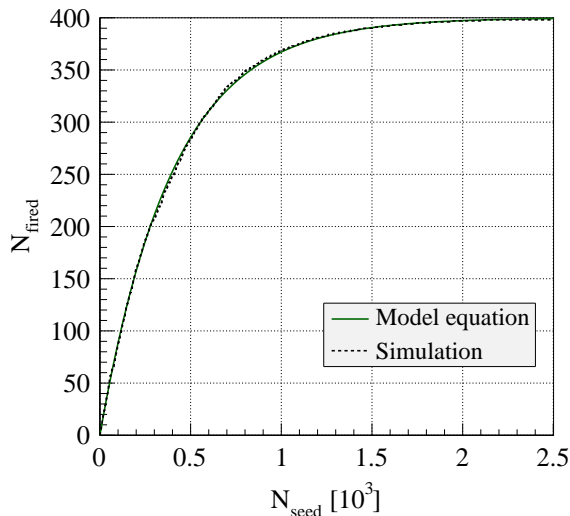


**Figure 5.11:** Comparison between modeled and simulated response curve for an SiPM with 400 pixels ( $N_{total} = 400$ ). Reprinted from Ref. [37]. The model equation is given by Eq. 5.4.

response is mainly influenced by after-pulsing. For low light intensities, also cross-talk starts to play a role and  $N_{fired}$  and  $N_{seed}$ , respectively, may be overestimated by  $\sim 5\%$ . There should be no impact of the recovery process on the measured SiPM response, since the incident light pulse duration is rather short ( $\sim 30$  ps) compared to the pixel recovery time (few 10 ns).” [37].

The model curve given by Eq. 5.4 was compared with a simple Monte Carlo simulation, as shown in Fig. 5.11. The simulation is based on a geometrical consideration, which takes into account that the output of one cell is always the standard single pixel signal, no matter how many photons enter that cell, thus resulting in the expected saturation behavior. The simulation agrees very well with the modeled response curve. Combining all the above considerations, it seems justified to approximate the SiPM response using Eq. 5.3 and Eq. 5.4, respectively.

The following paragraphs concentrate now finally on the presentation, discussion and interpretation of the results obtained from the measurement of the response curve of various SiPMs (Hamamatsu MPPCs with 100 pixels and 400 pixels, Photonique SSPM with 556 pixels and Zecotek MAPD with 560 pixels).

Fig. 5.12 shows the response curves of all tested devices for different ranges of light intensity. As discussed before, the response curves are represented by  $N_{fired}$ , the number of fired pixels, derived from the pulse height measurement, and  $N_{seed}$ , the number of “seeds”, obtained by measuring the photodiode current. It is important to note that both variables are derived from a measurement and hence the actual PDE of the respective SiPM is included. The operating parameters during the measurement are given in Table 5.1.

“For all sensors we tested, the data agree well with the expected response curve at low photon intensity, however, soon start to diverge. It is clearly visible that the pulse height exceeds the maximum expected value. One notices also that the effect of this over saturation behavior varies among the SiPMs tested here. The maximum output we obtained from Hamamatsu 100U (100 pixels) and Hamamatsu 050U (400 pixels) amounts roughly 200 p.e. (photoelectrons) equivalent and 800 p.e. equivalent, respectively, which would be the expected output for a sensor having twice the number of pixels. On the other hand, the Zecotek device with  $N_{total} = 560$  seems less affected and the maximum measured output is  $\sim 650$  p.e. equivalent, that amounts  $\sim 15\%$  larger output than expected. It is also to be noted that within the maximum light intensity ( $\sim 100$  k “seeds”), we see no clear sign of full saturation of the device, especially in the case of the Hamamatsu 100U. Looking at the response curves of the MPPC with 400 pixels and the SSPM with 556 pixels, one can observe an additional enhancement of the dynamic range compared to the model calculation.” [37].

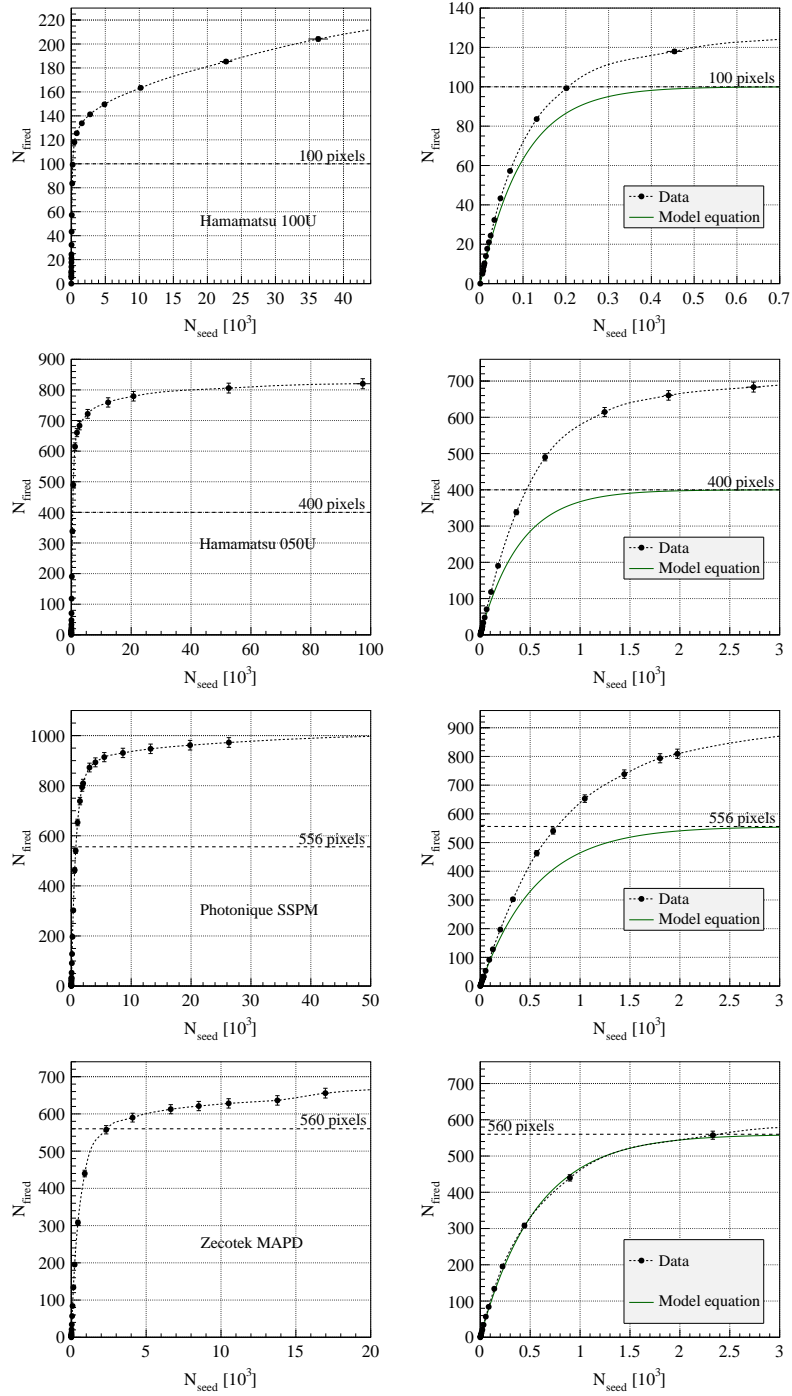


**Figure 5.12:** Response curves of various SiPMs [37] for high light intensities (left) and low to medium light intensities (right). Top to bottom: Hamamatsu MPPC with 100 pixels, MPPC with 400 pixels, Photonique SSPM with 556 pixels and Zecotek MAPD with 560 pixels. A spline curve is added to guide the eye. The expected maxima are indicated by the horizontal dashed lines. The model equation is obtained by inserting the respective values for  $N_{total}$  into Eq. 5.4.

From the above discussion and looking at Fig. 5.12 we see already that the degree of deviation from the expected model curve varies among the different SiPMs. In order to have a better comparison between the tested devices, one may want to put all response curves into a single plot. This can be achieved by normalizing the measured curves with the total number of pixels of the respective devices. By doing so we obtain a universal equation:

$$\frac{N_{fired}}{N_{total}} = 1 - \exp\left(-\frac{N_{seed}}{N_{total}}\right) \quad (5.5)$$

Fig. 5.13 comprises the response curves of all tested devices and the universal equation in the normalized representation. Over a wide range of light intensity the largest effect is seen for the Hamamatsu 050U, where the output even exceeds  $N_{fired}/N_{total} = 2$ . For very high numbers of input photons ( $N_{seed}/N_{total} > 400$ ), the response of the Hamamatsu 100U even increases beyond this value. Looking at Fig. 5.13 right, we notice that the output of the Zecotek MAPD seems to follow the expected model at least up to  $N_{seed}/N_{total} = 4$  before it starts to deviate, however, much less compared to the other devices.

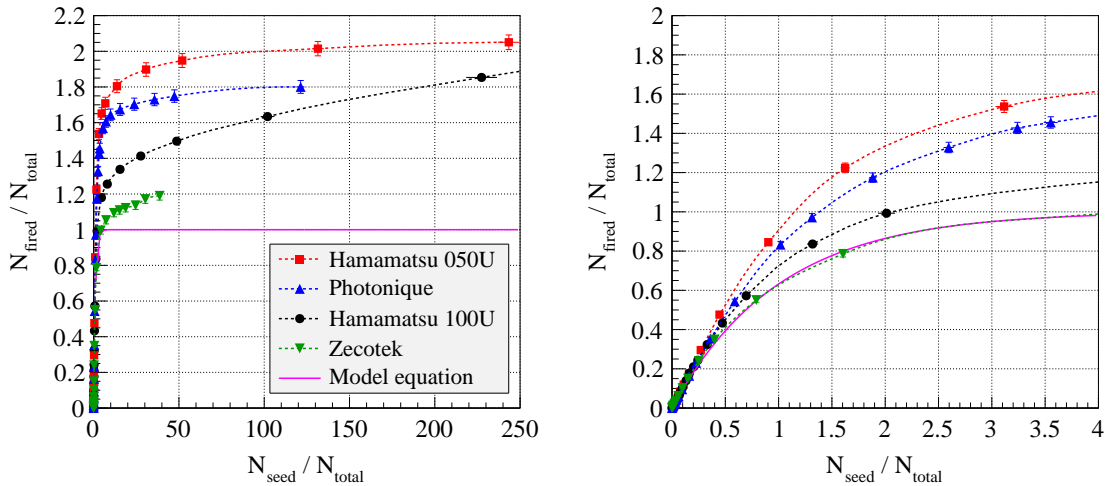


**Figure 5.13:** SiPM response curves, normalized to the total number of pixels of each device,  $N_{total}$ , for high (left) and low to medium light intensities (right). The model curve is given by Eq. 5.5. Reprinted from Ref. [37].

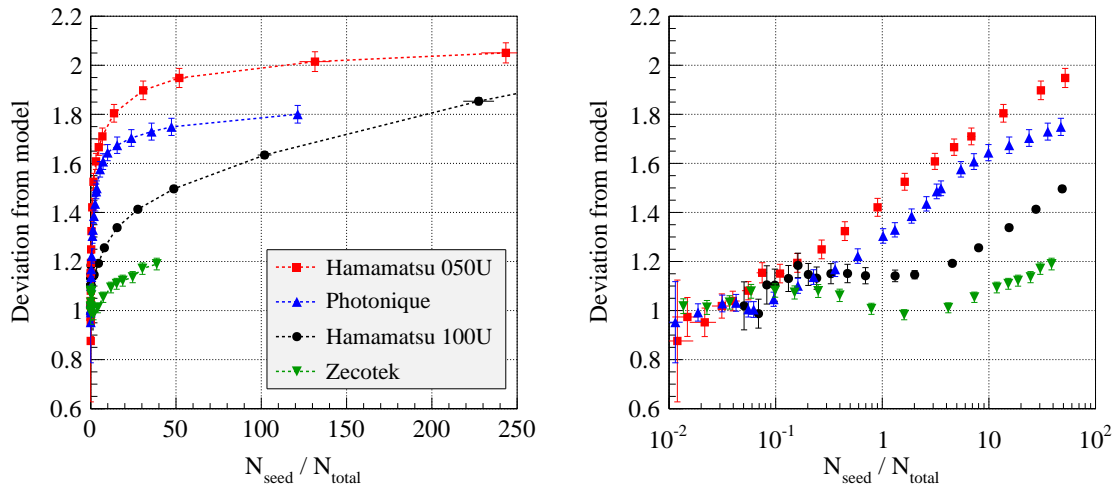


**Figure 5.14:** Deviation of the SiPM response curves from the model curve given by Eq. 5.5. The results are normalized to the total number of pixels of each device,  $N_{total}$ . The deviation is defined as the ratio between measured and calculated values, i.e. 1 means no deviation from the model. Reprinted from Ref. [37].

Fig. 5.14 shows the deviation of the response curves from the model equation. It is achieved by normalizing Fig. 5.13 with the function given by Eq. 5.5. The plot expresses two interesting features. Firstly, a very small and essentially negligible deviation at low light intensities, and secondly, an opposing behavior of the different devices at higher light intensities. The former is true up to about  $N_{seed}/N_{total} = 0.2$ , which is actually the range where the SiPMs are commonly used because one can expect a linear response. Therefore, most applications, where the number of pixels of a device is tuned according to the expected light intensities, might not be affected by the over saturation effect. However, for higher light intensities the deviation is partly drastic.

One should also notice that there are two qualitatively different behaviors among the tested devices. Beyond the linear region, the deviation increases monotonically for the Hamamatsu 050U and the Photonique SSPM. The response curves of the Hamamatsu 100U and Zecotek device follow this trend up to about  $N_{seed}/N_{total} = 0.5$ , but then seem to return to the model expectation before finally increasing again. This is not as expected because one could at least assume that the two MPPCs from the same vendor show comparable behavior.



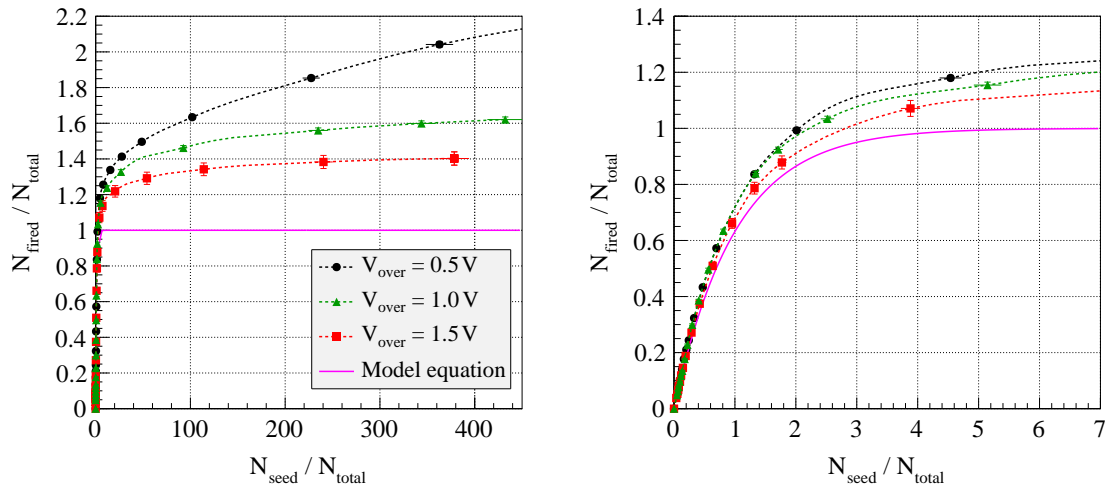


**Figure 5.15:** Dependency of the Hamamatsu 100U response curve on the applied over-voltage. Reprinted from Ref. [37]. The model curve is given by Eq. 5.5. The results are again normalized to the total number of pixels of the device,  $N_{\text{total}}$ .

Another unexpected result is depicted in Fig. 5.15, which shows the response curve of the Hamamatsu 100U for different bias voltages. It is surprising because the over saturation effect seems to be less prominent with increasing over-voltage. Knowing that the after-pulse and cross-talk probabilities are rising with increasing gain [48], and might therefore have a larger effect on the SiPM response, one would naively expect it just the other way round. These results show that the measurement of the response curve based on a pulse height determination is hardly affected by correlated noise, as discussed before in more detail. Otherwise the effect of over saturation would increase for larger over-voltage. Nevertheless, the operating voltage has a large effect on the measured response. Again, there is hardly no deviation from the model curve within the linear range.

Up to now, the SiPM response curve has been described by the number of fired pixels,  $N_{\text{fired}}$ , and the number of “seeds”,  $N_{\text{seed}}$ . This representation has been selected since it includes only direct observables of this measurement. In order to plot the SiPM response as a function of the number of incident photons,  $N_{\text{photon}}$ , as in Eq. 5.3, we have to include the PDE of the respective device and use the relation  $N_{\text{photon}} = N_{\text{seed}}/\text{PDE}$  (see Fig. 5.10).

Since the PDE cannot be derived from this measurement setup, it has to be taken from

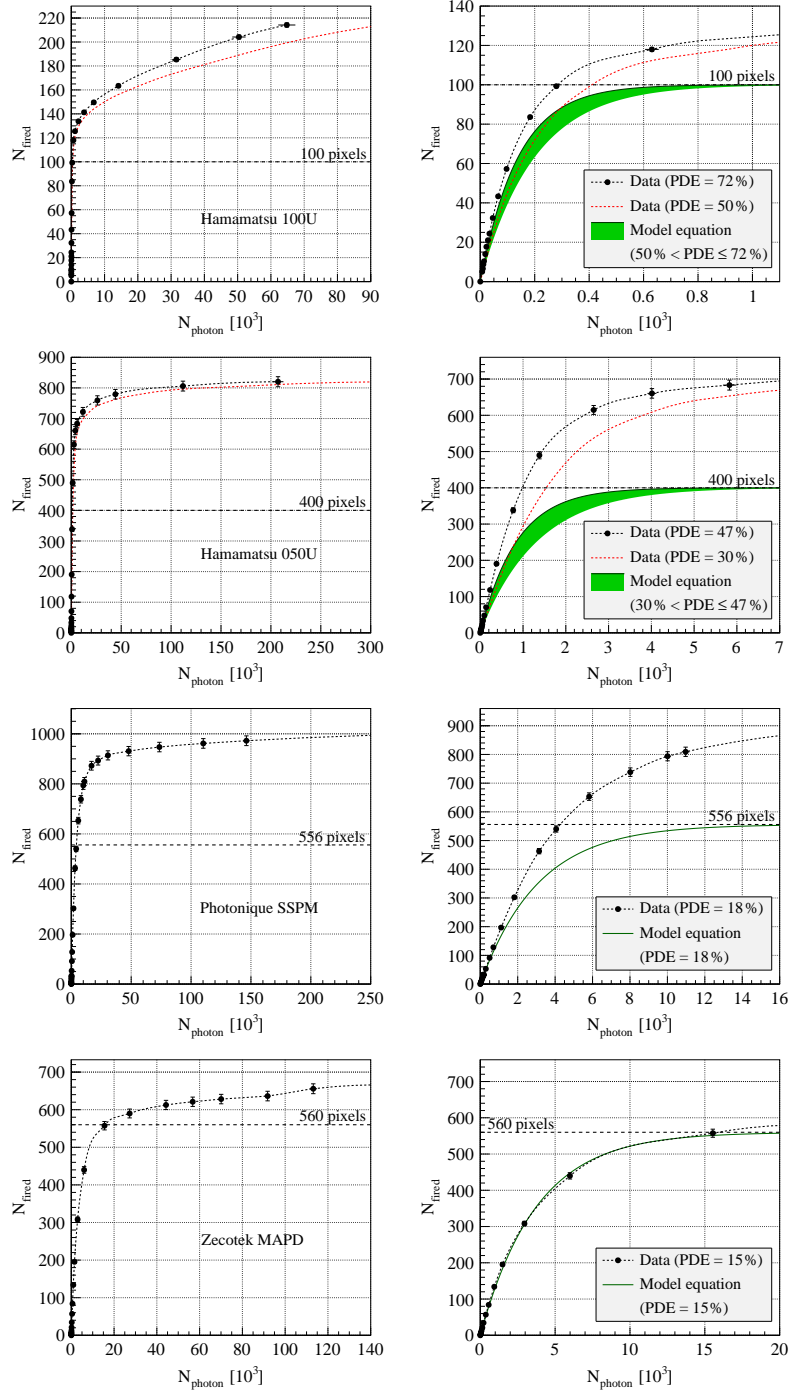


**Figure 5.16:** Response curves represented as  $N_{fired}$  vs.  $N_{photon}$  for high light intensities (left) and low to medium light intensities (right). Top to bottom: MPPC with 100 pixels, MPPC with 400 pixels, SSPM with 556 pixels and MAPD-1 with 560 pixels. The PDE values used to evaluate  $N_{photon}$  are indicated. The model curve is given by Eq. 5.3. The expected values of saturation are indicated by the horizontal dashed lines. Reprinted from Ref. [37].

elsewhere. The PDE values at a wavelength of 400 nm for all tested devices are given in Table 5.1 and were taken from the data sheets [45, 46, 47]. The values for the Hamamatsu MPPCs are known to include after-pulsing and cross-talk effects, which results in an overestimation of the PDE of about 20 % and 10 % [49], respectively.

“There are several other measurements of the PDE available, but the results are also known to depend on the operating conditions, e.g. over-voltage and temperature. Therefore, in order to handle this problem the best, we refer to the PDE values provided by the company and, in case of the Hamamatsu MPPCs, we take those values as an upper boundary of an uncertainty band going down to a  $\sim 30\%$  smaller value. It’s important to stress, that the choice of the PDE value does not affect the measurement result, the PDE is only needed to evaluate  $N_{photon}$ .  $N_{fired}$  and  $N_{seed}$  include the actual PDE already, because they are measured quantities.” [37]. Fig. 5.16 shows now the response curves of various SiPMs, using  $N_{photon}$  instead of  $N_{seed}$ . As it can be seen from the plots, the over saturation effect, which is related to  $N_{fired}$ , is of course not affected by this exchange.

For better comparison, the response curves are again normalized to the total number of pixels,  $N_{total}$ , as shown in Fig. 5.17. In contrast to Fig. 5.13, the response curves are now

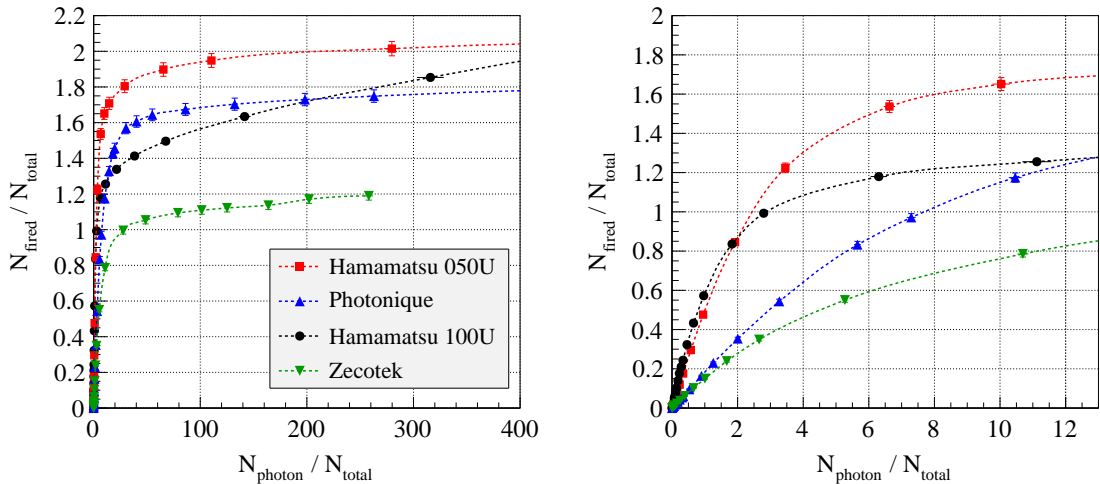


**Figure 5.17:** Response curves represented as  $N_{fired}$  as a function of  $N_{photon}$  for high (left) and low to medium light intensities (right). The curves are normalized to the total number of pixels of each device,  $N_{total}$ . Reprinted from Ref. [37].

crossing because of the different representation and as a consequence the different PDE values used to evaluate  $N_{photon}$  on the one hand, and because of the varying strength of the over saturation effect on the other hand. In the linear range the slope of the curves is given by the PDE, e.g. the Hamamatsu 100U has the steepest slope because of the highest PDE. For higher light intensities the over saturation effect starts to dominate and the curves cross.

The results presented in this section are utterly unexpected since the measured responses exceed by far the expected values of saturation and the dynamic ranges partly seem to be enhanced far beyond the expected range. The former is particularly surprising because from a naive picture one would assume a maximum output of the SiPM being comparable to the total number of pixels times the standard single cell signal. The observation suggests that this naive understanding of the individual pixels acting as digital devices giving always the same output may have to be improved.

Up to now, we could not find any convincing explanation for the measured effects. When looking at measurements of other groups, we find similar observations, however, with much smaller effects and only at high operating voltages, as presented in Ref. [50]. “In this case, however, the number of fired pixels is estimated by integrating the signal using a charge ADC and the result could be explained by the correlated noise (after-pulsing, cross-talk and dark-noise). As discussed, in our case the influence of delayed correlated noise is small, as we are operating the SiPMs at low gain and evaluate the number of pixels from the signal pulse height and not from the collected charge. Cross-talk that occurs almost instantaneously to the initial laser pulse is suppressed for most of the measurements due to high pixel occupancy at high light intensities. Very fast after-pulses occurring within the signal rise time of  $\sim 2-3$  ns, may lead to an overestimation of the SiPM output ( $N_{fired}$ ) by  $\sim 1-2\%$ , and thus cannot explain the large over-saturation we observed.” [37]. Also Fig. 5.15 shows that the measurement is hardly affected by correlated noise, as described before.

As already mentioned, the SiPM response is strongly influenced by the pixel recovery and

therefore by the pulse width of the laser pulses. This is demonstrated in Ref. [51], using pulse widths of several ns and more. In our case, however, we are using a very narrow pulse (32 ps FWHM) and therefore we are not influenced by the recovery process.

Another effect could come from the electronics, especially from a non-linear response of the preamplifier. As explained in Section 5.1.1, we determined the preamplifier gain and its response for a large range of input charge and pulse height (see Fig. 5.4). As one can see from the plots, the preamplifier response is quite linear over a wide range and starts to saturate in case of a pulse height measurement at high input signals. This means that in any case, the pulse height measurement will always underestimate the actual signal because of this saturation. Therefore, we would even underestimate the real over saturation.

“One possible explanation could be that a very high number of input photons per pixel may trigger several avalanches simultaneously, giving rise to a slightly higher output signal compared to the single photon signal. However, the fact that even the two MPPCs do not show the same behavior is in contrast to this assumption and indicates a more complex effect behind.

Another possible reason for the observed effect might be related to the region in-between the microcells. The trenches separating the individual pixels are coated with a thin reflective layer of aluminum and are supposed to be insensitive to incoming light. However, at very high light exposure, some photons may pass the layer, resulting in an additional signal. In order to explain the observed over saturation solely by this effect, one has to assume a gain of at least  $10^3$  for these inactive regions, which is questionable because of the low field there. However, such an effect could explain the discrepancy in the behavior of the two MPPCs. The Hamamatsu 050U has a lower fill factor, i.e. a larger inactive area, than the Hamamatsu 100U.

In general one should note that SiPMs are typically not operated in the regime of very high light exposure since the output linearity is lost, but are preferably used to measure low amounts of light, in the linear, dynamic range, where measurement and model agree

well. Therefore, most cases of application would not be affected by our observation. Nevertheless, understanding this behavior is going to advance the overall understanding of this still relatively new device, and may open a new application, e.g. it may allow to use SiPMs for a wide range of light intensities, using calibration curves, of course with the drawback of decreasing accuracy for increasing intensity.” [37].

### 5.1.5 Recovery Time

The pixel recovery time has a severe impact on the SiPM response to incident light. When measuring the response curve, we discussed already that if the duration of a light pulse (laser pulse, scintillation pulse, etc.) is in the range of or larger than the recovery time, the pixels can fire several times during a single pulse, resulting in a higher output signal than the total number of pixels of the device. On the other hand, if the pulse width is short (well below the recovery time) but the time between two pulses is comparable to the recovery time, the two signals might not be resolved. As a consequence, the recovery time determines the double hit resolution and it is also related to the rate capability of the photodetector, which may be of special interest for HEP experiments.

After a breakdown, the avalanche process is terminated by a quenching resistor  $R_{quench}$  on each pixel, resulting in a drop of the bias voltage  $V_{bias}$  to the breakdown voltage  $V_{bd}$  and a subsequent recovery with a characteristic time constant  $\tau_r$ :

$$V_{bias}(t) = V_{bias}(0) \times [1 - \exp(-t/\tau_r)] \quad (5.6)$$

In good approximation, the recovery time  $\tau_r$  is depending on the value of the quenching resistor and the pixel capacitance,  $\tau_r \sim R_{quench}C_{pix}$ . Typical values are  $R_{quench} \sim 100 \text{ k}\Omega$  and  $C_{pix} \sim 20 - 350 \text{ fF}$ , depending on the pixel size, which translates into recovery times ranging from a few ns up to a few 10 ns. Effects like after-pulsing, cross-talk and dark-noise can prolong the recovery of SiPM pixels since the recharging process starts anew.

In order to study the recovery process and to characterize the rate capability and dou-

ble hit resolution, several MPPCs were exposed to two consecutive laser pulses with a varying relative time difference of a few ns (2-3 ns) up to some 100 ns (1-2  $\mu$ s). In total, three MPPCs with  $25 \times 25 \mu\text{m}^2$ ,  $50 \times 50 \mu\text{m}^2$  and  $100 \times 100 \mu\text{m}^2$  pixel size (S10362-11-025U, S10362-11-050U and S10362-11-100U) were tested. The main parameters are listed in Table 5.1.

Measurements on the MPPC recovery time are also recorded in Ref. [52] and Ref. [53], where the recovery time constant has been extracted by studying after-pulsing and dark-noise, i.e. by recording the amplitude of the after-pulse and the corresponding time it occurs after the initial breakdown. As reported, the method is limited to time differences between after-pulse and initial pulse  $> 10$  ns. The method is in contrast to the one presented here, which is using two real incident light pulses with a defined time difference (down to 2 ns) to determine the recovery curve and is therefore a more realistic situation.

Using such a technique, there are in general two different ways to determine the recovery time. On the one hand, illuminating only one certain pixel of the photodetector results in the determination of the recovery time of this single cell, and on the other hand, illuminating all the pixels allows to evaluate the recovery time of the whole sensor, i.e. the average of the recovery times of all cells.

The first way is demanding a more complicated setup since the laser beam has to be focused onto a single microcell, which is quite challenging at least for the SiPM with  $25 \mu\text{m}^2$  pixel size. Using a small pinhole ( $< 25 \mu\text{m}$  diameter) in front of the photodetector turned out to be difficult due to diffraction of the light. Therefore, a dedicated optical setup combining several lenses would be needed. Finally, the second method was chosen. The constraints for the characteristics of the light pulses are therefore clear. Firstly, the light intensity of each pulse must be high enough to illuminate all the pixels of the sensor in order to ensure that each pixel fires at least once before the second photon hits the cell. As done for the measurements of the response curves in the previous section, a calibrated photodiode (Hamamatsu S5971) was used to measure the light intensity, in order to guarantee that the number of incident photons on the sensor surface is large

enough to achieve full illumination. Secondly, the pulse width should be small compared to the MPPC recovery time in order to ensure that pixels do not fire twice during a single pulse duration.

The measurements were performed using a blue (404 nm) pulsed laser with 32 ps pulse width (FWHM) from Advanced Laser Diode Systems. The laser head (PIL040) was driven by an external control unit, which allowed to set the repetition frequency in the range of 10 Hz to 1 MHz and to tune the laser intensity. The signals of the photodetector were not amplified and were recorded directly with a waveform digitizer from CAEN (V1742, 5 GHz sampling rate). Because of the large MPPC signals due to full illumination, it was not needed to use a preamplifier, which anyway has a limited dynamic range, as shown in Section 5.1.1 (see Fig. 5.4). As a consequence, the impact of the electronics on the measurement results was reduced to a minimum. All measurements were done at room temperature ( $\sim 25^\circ\text{C}$ ).

The two pulses were generated by splitting the laser signal (short and long path), delaying one of the signals and merging again. The delay of the second pulse was either done with multiple reflections using mirrors (up to 5 ns) or for larger delays (up to  $1\ \mu\text{s}$ ) by coupling

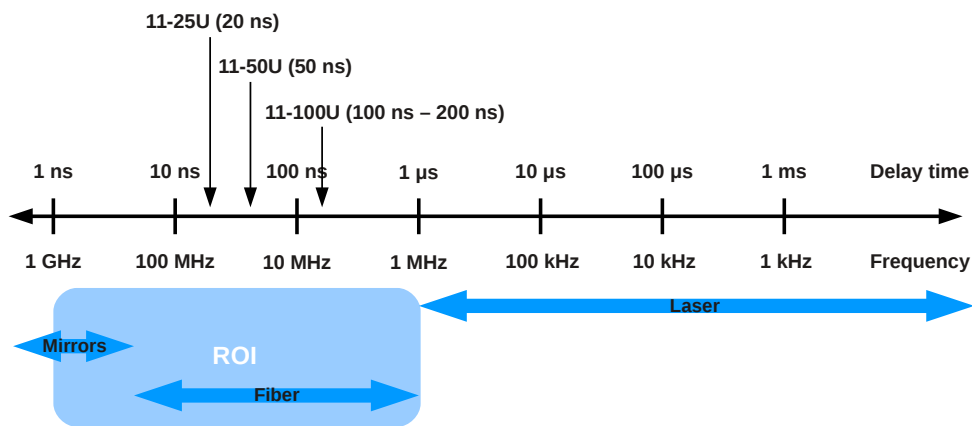


**Figure 5.18:** An illustration of the delay time between two pulses and anticipated recovery time. The blue shaded area indicates the region of interest (ROI), which was covered by using mirrors and optical fibers. Delays of less than 5 ns are essential to study the double hit resolution, longer delays are needed to determine the recovery time and investigate the rate capability. The times needed for 100 % recovery are given. The values are taken from the MPPC data sheet [45].



the light into optical fibers of different lengths (1 m to 200 m). Even larger time intervals between the two pulses could be realized without delay but simply by tuning the repetition frequency of the laser (10 Hz to 1 MHz). Using these three techniques, we were able to cover a wide delay time range. This is illustrated schematically in Fig. 5.18. Since the recovery time is supposed to be in the range of some ns to a few 100 ns depending on the pixel size [45], the most interesting delay time region to measure is below 1  $\mu$ s, so above the maximum repetition rate of the laser. Therefore, most of the measurements were done using mirrors or fibers, respectively, while fixing the laser frequency to 1 kHz. The mirrors were especially needed to provide delays of less than 5 ns, which is essential to investigate the double hit resolution and its limits.

**Setup with mirrors:** in order to study the MPPC double hit resolution at short delays ( $< 5$  ns) we chose a measurement setup based on mirrors, as shown schematically in Fig. 5.19. The dichroic mirrors suitable for our wavelength region and a diameter of 25 mm were mounted on an optical table. The laser signal was split using a beam splitter with 45:55 splitting ratio (45 % reflectivity, 55 % transmission). One of the signals got reflected multiple times before merging again the two signals, using a second beam splitter. An optical diffuser in front of the MPPC ensured that the whole active area of the sensor was evenly illuminated. The maximum path difference between the two signals is defined by the number of mirrors available (9 in total) on the one hand, and by the size of the optical table (60 cm $\times$ 60 cm) on the other hand. However, a delay of 5 ns could easily be established using 4-5 mirrors as shown in Fig. 5.19. The whole measurement was setup inside a light-tight box.

**Setup with optical fibers:** to cover the rest of the interesting delay time region between 5 ns and 1  $\mu$ s, we used multimode optical fibers of different length from Thorlabs GmbH. The short cables, namely 1 m, 2 m and 5 m, have a core diameter of 62.5  $\mu$ m and a numerical aperture of 0.275, while the longer ones (10 m, 25 m and 50 m) have a core diameter of 200  $\mu$ m and a numerical aperture of 0.22. Fibers of any length could be linked together using special fiber connectors. By putting 4 fibers of 50 m length one after another, a maximum delay of 200 m could be established. The setup is shown schematically in

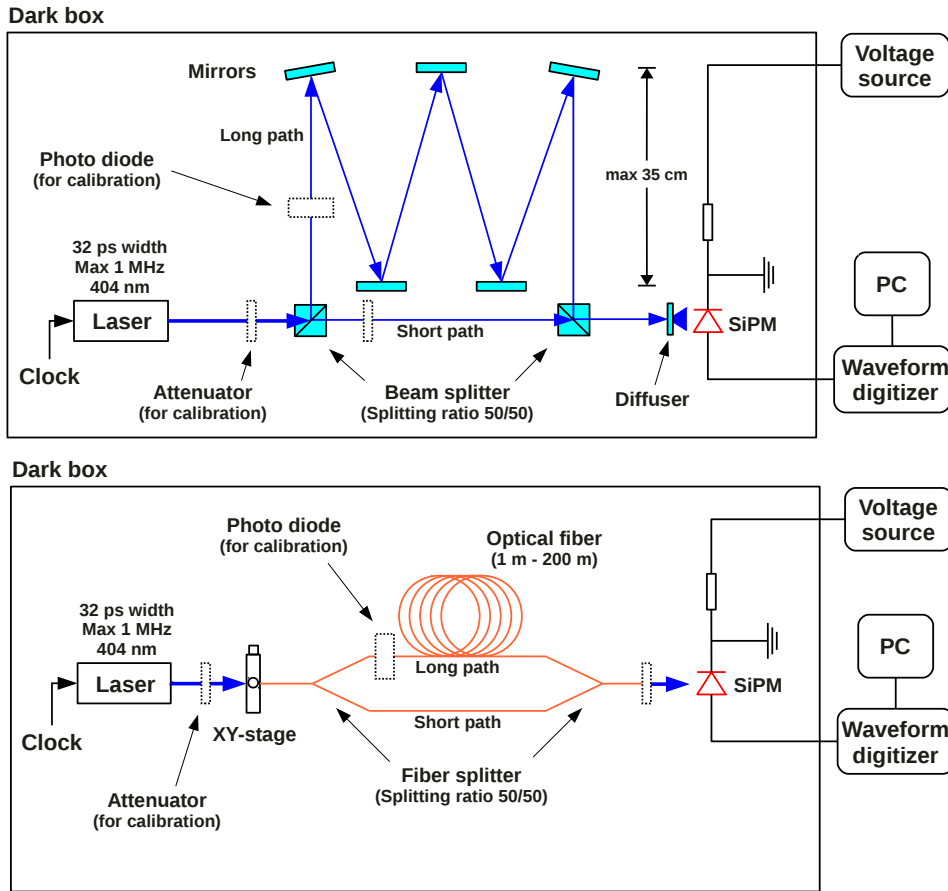


**Figure 5.19:** Schematic drawings of the different setups using mirrors (top) and optical fibers (bottom).

Fig. 5.19. Again, the whole measurement setup was mounted on an optical table inside a dark box. The laser signal was coupled into the fiber by using a lens, which was mounted on a xy-stage for optimal alignment. In the following the signal was split up in a long and short path, using a fiber splitter with 50:50 splitting ratio and 0.275 numerical aperture. Finally, the two signals were merged again and the fiber was placed in front of the MPPC. The optimal distance between fiber and sensor to illuminate the whole sensitive area can be evaluated knowing the numerical aperture of the fiber. In our case the fiber was placed approximately 6 mm in front of the sensor surface.

As mentioned earlier in this section, the light intensity was estimated before data taking by using a PIN photodiode to ensure that the number of photons hitting the MPPC surface

is high enough to achieve full illumination. Therefore, the setup shown in Fig. 5.19 was slightly modified, as indicated in the figure. In the setup with mirrors, two variable attenuators were used to vary the light intensity. One directly after the laser and the other in between the two beam splitters. The second attenuator was needed to be able to deal with the different sensitivities of the MPPC and the photodiode. The photodiode was calibrated by using photon spectra of the MPPC at low light intensities, where the SiPM response is supposed to be linear, just as described in Section 5.1.4. Since the calibration was done at low light levels, the MPPC signal was amplified using a preamplifier from Photonique (AMP-0611). For data acquisition we used a LeCroy oscilloscope (WavePro 735Zi) instead of the waveform digitizer. When using optical fibers, the light intensity was measured in a comparable way (see Fig. 5.19).

In the following the method used to determine the recovery time is explained in more detail. The measurement is based on the extraction of the recovery time from the recovery curve, i.e. from the relation between fraction of recovery and time difference (delay) of two consecutive light pulses. In order to evaluate the recovery fraction, the SiPM signals were interpreted by performing a waveform analysis. The procedure to extract the recovery fraction for fixed over-voltage and delay length (fiber or mirrors) can be divided in three steps, as explained in the following. In each step, a sample of 1000 events is analyzed.

Firstly, a template waveform which is used for fitting the data is created. Therefore, the second (long) path is disconnected (fibers) or blocked (mirrors), respectively, resulting in a single output pulse, as indicated in Fig. 5.20, which actually shows an average of 1000 events. Then, the long path is reconnected or unblocked, while the short path gets interrupted. In the following, each single event is fitted by shifting (vertically and horizontally) and scaling the template waveform obtained before (see Fig. 5.21 left), resulting in three fit parameters. Finally, the short path is reconnected and the obtained double pulse is fitted by adding a second template function properly scaled and shifted, which results in two additional parameters. In the example shown on the right of Fig. 5.21, the second pulse is delayed by 5.5 ns using a fiber of 1 m length. The recovery fraction is estimated by determining the reduction of the second pulse which is estimated by comparing the

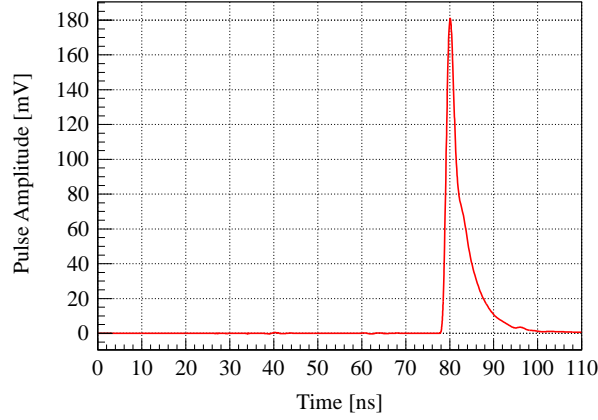


**Figure 5.20:** Template waveform obtained by measuring the signal when the long path is blocked. The figure shows an average of 1000 waveforms.

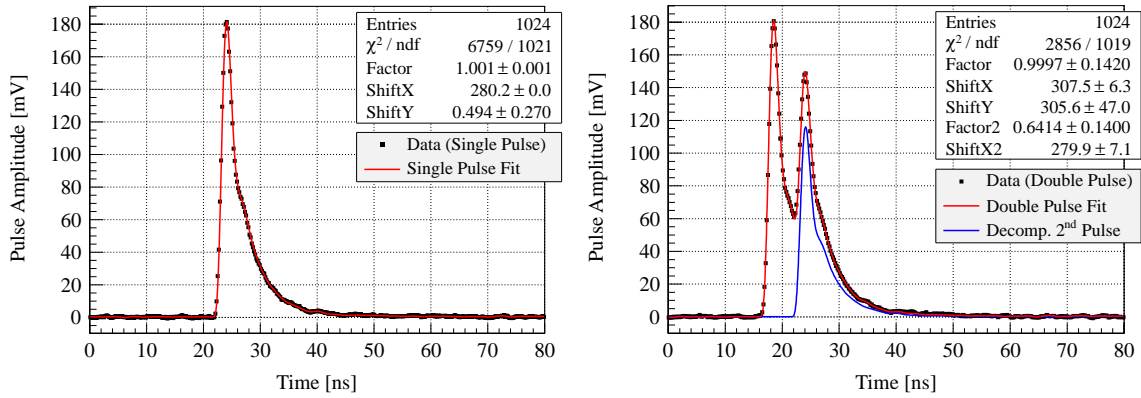


**Figure 5.21:** Example waveforms of a measurement with a MPPC with  $25 \times 25 \mu\text{m}^2$  pixel size operated at  $V_{\text{over}} = 1 \text{ V}$  using a fiber of 1 m length, resulting in a delay time of about 5.5 ns. The figure on the left shows the signal when the short path is blocked, the plot on the right indicates the signal when both paths are connected. In each case, the signals are fitted using a template function, which is scaled by a factor and shifted horizontally and vertically, resulting in three fit parameters for the single pulse and five parameters for the double pulse.

amplitude of the signal when the first (short) path is blocked and the amplitude of the decomposed second pulse.

Steps two and three are applied to 1000 events using the same template function to obtain an average value and corresponding error of the recovery fraction and delay time. The whole procedure is then repeated for different delay lengths in order to obtain the recovery curve and finally extract the recovery time constant of the MPPC. The template function

has to be redefined only when changing the photodetector or the over-voltage.

The recovery curves of all tested MPPCs are shown in Fig. 5.22 for different operating voltages. For low bias voltages ( $V_{over} \leq 1\text{ V}$ ), the influence of noise effects is very small and the recovery curves can be fitted with a simple function of the form:

$$y(\Delta t) = 1 - \exp [-(\Delta t - t)/\tau_r] \quad (5.7)$$

which describes the recovery with the time constant  $\tau_r$ . For a larger gain, the MPPC response is influenced by a multitude of effects and thus the analytical description of the recovery process is rather difficult. However, from the measured curves we can still extract the time which is needed to achieve a certain fraction of recovery, as indicated in the plots. The results of the measurements are summarized in Table 5.2. The measured time constants are compared with the simple approximation  $\tau_r \sim R_{quench}C_{pix}$ . The obtained values roughly agree with the RC time constants.

Looking at the recovery curves at low operating voltages ( $V_{over} = 1\text{ V}$ ), it can be noted that the measured times needed for full recovery are in good agreement with the values given by Hamamatsu, which are listed in Fig. 5.18. From the measurements we obtain values of about 200 ns for  $100 \times 100\ \mu\text{m}^2$  pixel size, 50 ns for  $50 \times 50\ \mu\text{m}^2$  pixels size and 20 ns for  $25 \times 25\ \mu\text{m}^2$  pixels. These values are however drastically increasing if the operating voltages are higher, due to dark-noise, cross-talk and after-pulsing.

Using a waveform analysis technique, two adjacent light pulses could be resolved with the 050U and 025U device down to about 2–3 ns delay between the two pulses. This demonstrates the limit of the double hit resolution. As already noted, the measurements were done with full illumination and without amplifying the MPPC signals. Using a preamplifier will certainly result in reduced double hit resolution because of an increase in signal rise time and width.

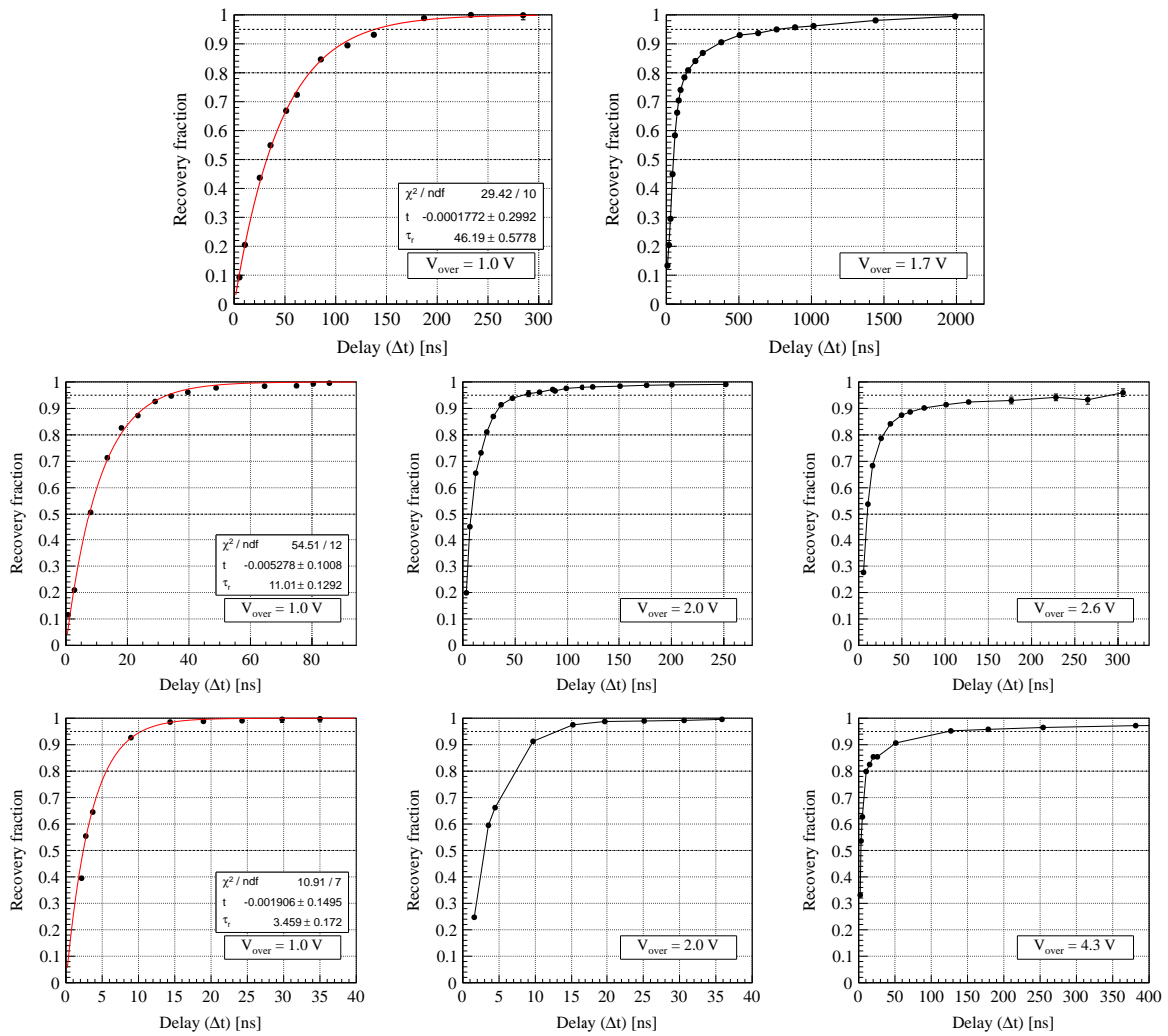


**Figure 5.22:** Recovery curves of various MPPCs, operated at different over-voltages, as indicated in the plots. Top: S10362-11-100U. Middle: S10362-11-050U. Bottom: S10362-11-025U. The black dots are the data points. The solid lines are added to guide the eye. Recovery fractions of 50 %, 80 % and 95 % are indicated by the horizontal dashed lines. For low operating voltages the recovery curves are fitted with a simple function given by Eq. 5.7.

**Table 5.2:** Recovery time constants for the tested MPPCs operated at different bias voltages. Breakdown voltages have been measured and are given in Table 5.1. The time differences between two light pulses ( $\Delta t$ ) needed to achieve a certain fraction of recovery have been extracted from the recovery curves in Fig. 5.22. The recovery time constant ( $\tau_r$ ) can be obtained by fitting the recovery curves measured at low gain. The RC time constants were evaluated by using the values for the pixel capacitances and quenching resistors (see Table 5.1).

MPPC type	S10362-11-100U	
Over-voltage ( $V_{\text{over}}$ )	+ 1.0 V	+ 1.7 V
$\Delta t$ for 50 % recovery [ns]	$\sim 30$	$\sim 50$
$\Delta t$ for 80 % recovery [ns]	$\sim 75$	$\sim 140$
$\Delta t$ for 95 % recovery [ns]	$\sim 140$	$\sim 800$
Recovery time constant ( $\tau_r$ ) [ns]	$\sim 46$	–
RC time constant [ns]	$\sim 30$	–

MPPC type	S10362-11-050U		
Over-voltage ( $V_{\text{over}}$ )	+ 1.0 V	+ 2.0 V	+ 2.6 V
$\Delta t$ for 50 % recovery [ns]	$\sim 8$	$\sim 8$	$\sim 10$
$\Delta t$ for 80 % recovery [ns]	$\sim 18$	$\sim 22$	$\sim 29$
$\Delta t$ for 95 % recovery [ns]	$\sim 33$	$\sim 60$	$\sim 280$
Recovery time constant ( $\tau_r$ ) [ns]	$\sim 11$	–	–
RC time constant [ns]	$\sim 9$	–	–

MPPC type	S10362-11-025U		
Over-voltage ( $V_{\text{over}}$ )	+ 1.0 V	+ 2.0 V	+ 4.3 V
$\Delta t$ for 50 % recovery [ns]	$\sim 2.5$	$\sim 3$	$\sim 3$
$\Delta t$ for 80 % recovery [ns]	$\sim 5.5$	$\sim 7$	$\sim 10$
$\Delta t$ for 95 % recovery [ns]	$\sim 11$	$\sim 13$	$\sim 130$
Recovery time constant ( $\tau_r$ ) [ns]	$\sim 3.5$	–	–
RC time constant [ns]	$\sim 6.5$	–	–

### 5.1.6 Time resolution

After the interaction of the incoming photon in the active layer of silicon within the SiPM, it takes some time for the avalanche to develop and for the creation of a signal at the output. The variation (jitter) in this time defines the intrinsic time resolution of the device. The active layer is usually very thin (few  $\mu\text{m}$ ) and the formation of the avalanche happens quite fast, so that SiPM can be expected to offer excellent timing properties.

When dealing with timing performance of SiPMs, a parameter of particular interest is the single photon time resolution (SPTR), i.e. the time response to single detected photons. A time resolution study using different types of SiPMs has been performed and the results are published in Ref. [38]. Fig. 5.23 shows the SPTR for KETEK and Hamamatsu SiPMs in dependency of the over-voltage and temperature. Looking at the plots it becomes obvious that the time resolution improves with decreasing temperature and increasing bias voltage. At very high over-voltage, dark-noise, cross-talk and after-pulsing start to deteriorate the SPTR. This effect is reduced in case of the KETEK device which uses the trench technology and has a larger operating range. The values shown in Fig. 5.23 are influenced by the time jitter of the electronics and the laser used for the measurements.

Going from single photons to higher light intensities, the signals of all fired SPADs are

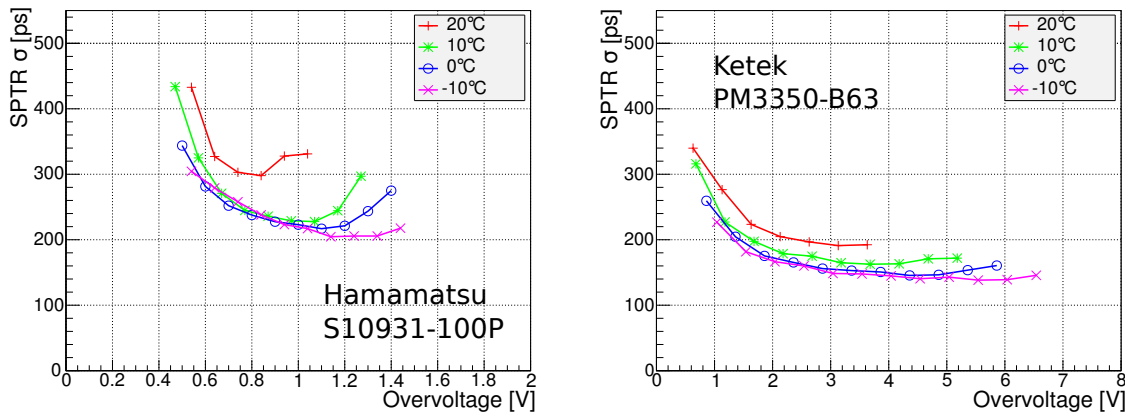


**Figure 5.23:** SPTR of Hamamatsu and KETEK sensors. Reprinted from Ref. [38]. The KETEK SiPM is based on optical trench technology and has a larger operating range.



piled up and the SiPM output signal contains the temporal distribution of the arrival times of the individual detected photons. Hence, the measured SiPM time resolution improves with the number of detected photons  $N$ , following a  $1/\sqrt{N}$  behavior [54, 55, 56]. This is expected from statistics, since the precision of the mean of a Gaussian is inverse proportional to the square root of the number of samples. However, in a real detector the signals of the individual photons are smeared out due to the time response of the SiPM and electronics and thus the behavior can happen to deviate from  $1/\sqrt{N}$ .

Nevertheless, in order to achieve best timing performance of SiPMs in combination with scintillators, it is of particular importance to adjust the spectral sensitivity of the photodetector to the emission spectrum of the scintillator. Detailed studies on the time resolution of scintillation counters with regard to the usage in PANDA have been done in course of this work and are described in the next chapters.

### 5.1.7 Position sensitive SiPM detector

In course of this work, a prototype of a large area photodetector based on a  $8 \times 8$  array of Hamamatsu MPPCs (S10931-100P) was developed and tested. The motivation for such a detector is to overcome the drawback of the small sensitive area of SiPMs by placing several MPPCs side by side, in combination with a suitable light concentrator on top to further increase the detection area. The idea behind was also to provide a candidate for photon detection for the barrel DIRC system of PANDA. The DIRC detector requires efficient collection of low intensity Cherenkov light in a high rate environment within the PANDA target spectrometer. The DIRC system was already described in more detail in Section 2.2.4 of Chapter 2.

Fig. 5.24 shows a picture of the prototype SiPM detector, consisting of 64 MPPCs with  $3 \times 3 \text{ mm}^2$  active area each, the light concentrator, read-out electronics and a cooling system. The light concentrator is composed of 64 pyramid-shaped funnels regularly arranged in a  $8 \times 8$  array, with entrance windows of  $7 \times 7 \text{ mm}^2$  and exit apertures of  $3 \times 3 \text{ mm}^2$ , respectively. It is made out of brass and was coated with either Aluminum or Chromium

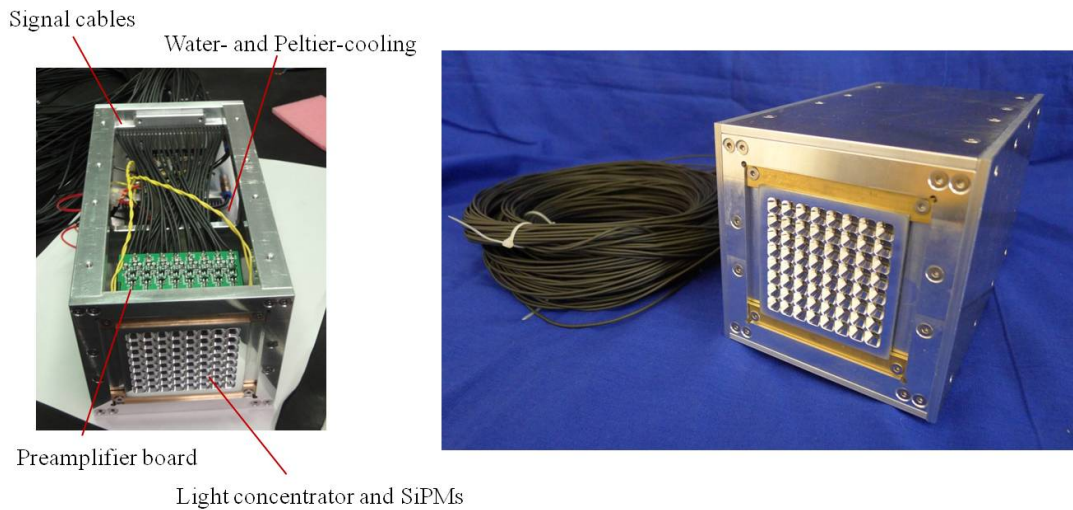


**Figure 5.24:** Pictures of the prototype of a position sensitive SiPM detector [28]. A light concentrator is mounted on top of the SiPM array. The 64 SiPMs are read-out by 4 preamplifier boards.

for efficient reflection of incoming photons onto the sensitive area of the SiPMs. The total detection area of the prototype photodetector is  $5.6 \times 5.6 \text{ cm}^2$ . Each MPPC is read-out separately to provide a position resolution. The SiPM signals are amplified with special preamplifier boards consisting of 16 preamplifiers each, having a gain of about 5 and a shaping time of  $\sim 2 \text{ ns}$ .

Further information about the prototype detector and results of various studies on the performance can be found in Ref. [28] and Ref. [29], where it was shown that the detector works well. For the light concentrator, a collection efficiency of 57% for the Chromium coating and 86% for the Aluminum coating could be measured. There are ideas to further improve the detector and the light concentrator, e.g. by using small plexiglass cones instead of a metal grid. Concerning the capability of using such a detector for the PANDA DIRC system, it was finally concluded that MCP-PMTs are better suited for such an application due to a much lower dark count rate.

## 5.2 Characterization of the Digital Photon Counter

The Philips DPC is certainly interesting as an alternative to the analog SiPM for the SciTil system. One of the biggest advantages of the new device is clearly that the read-out electronics are already integrated into the photodetector and therefore no additional front-end electronics would be needed. However, it is also obvious that the existing DPC layout cannot be used for the SciTil detector. The sensor design would have to be adapted in order to fulfill the space constraints within the PANDA target spectrometer. The following paragraphs aim at the characterization of the DPC device to better understand the functionality and features of this relatively new photodetector technology.

### 5.2.1 Dark count rate

As already mentioned in the previous chapter, the DPC allows to enable/disable single cells in order to reduce the overall DCR of the sensor. This can be done by measuring a dark count map and by creating and uploading an inhibit map to the sensor inhibit memory. The measurement is done in a dark environment while the software enables one cell after the other and measures the corresponding dark counts. Fig. 5.25 shows the measured raw dark count map for one die of a DPC-3200 tile and a combination of the latter with the inhibit map, disabling 20 % of the most active cells. The operating voltage was set to 3 V above breakdown at a temperature of about 12 °C. The temperature was stabilized using water- and Peltier cooling.

Without disabling any cells, the DCR of the die is about 16 MHz. Since the active area of a die is approximately 50 mm<sup>2</sup> this translates in about 320 kHz/mm<sup>2</sup>. At a temperature of 20 °C the DCR is about a factor 2 higher and comparable to the DCR of a conventional SiPM at this temperature [40]. Disabling 20 % of the cells already reduces the total DCR by one order of magnitude.

Using the described setup the dark count maps were acquired for all 16 dies of a DPC tile at several different operating temperatures (see Fig. 5.26 left). The plot shows that the

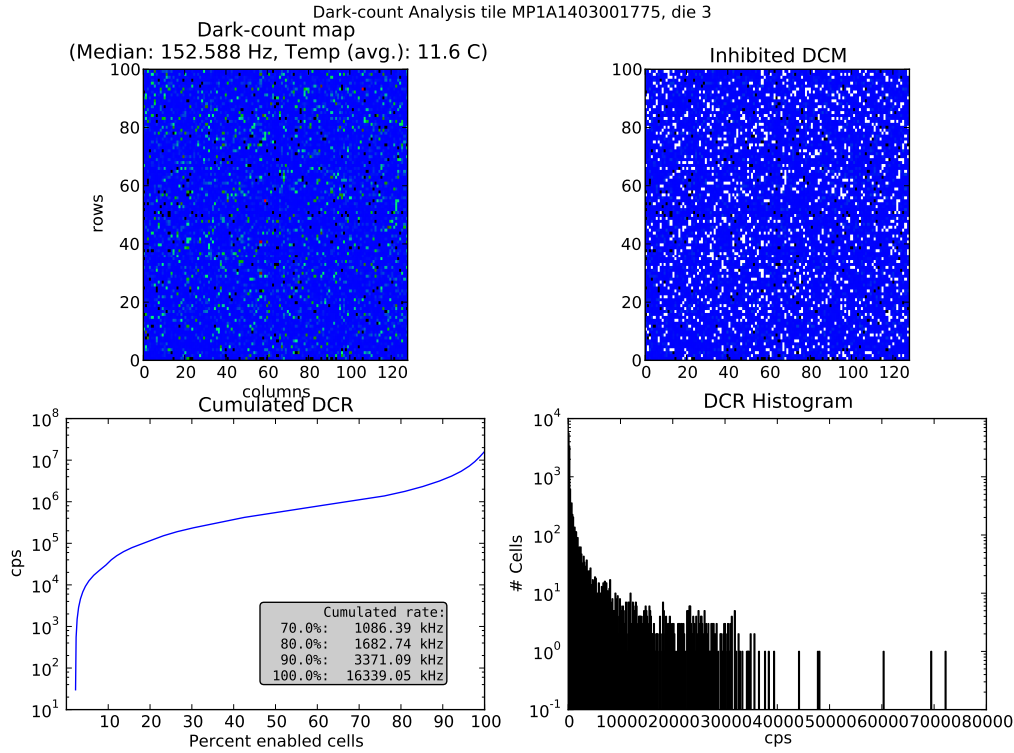


**Figure 5.25:** Results of a dark count measurement for one die of a DPC-3200 sensor. A single die consists of  $4 \times 3200 = 12800$  cells arranged in 128 columns and 100 rows. Top left: raw dark count map. Cells with highest DCR are marked in red, blue cells have very few counts, black cells have zero counts during the acquisition time. Top right: inhibit map disabling 20% of the most active cells. Inhibited cells are marked in white. Bottom left: the overall DCR as a function of the number of enabled cells. Bottom right: DCR histogram.

DCR can vary up to several MHz among dies on the same tile. Furthermore, the DCR shows a strong dependence on the temperature, which is due to the fact that it scales with the charge carrier density  $n(T) \sim T^{3/2} \exp\left(-\frac{E_g}{k_B T}\right)$  in the material.  $E_g$  is the band gap energy in silicon (1.12 eV) and  $k_B$  the Boltzmann constant. Taking the mean of the DCR values allows to define an average DCR per die, which is shown on the right of Fig. 5.26 as a function of the temperature for different amounts of activated cells. The data points were fitted with a function of the form:

$$f(x) = C(x + x_s)^{3/2} \exp\left(-\frac{E_g}{2k_B(x + x_s)}\right) \quad (5.8)$$

with fit parameters  $C$  and  $x_s$ .

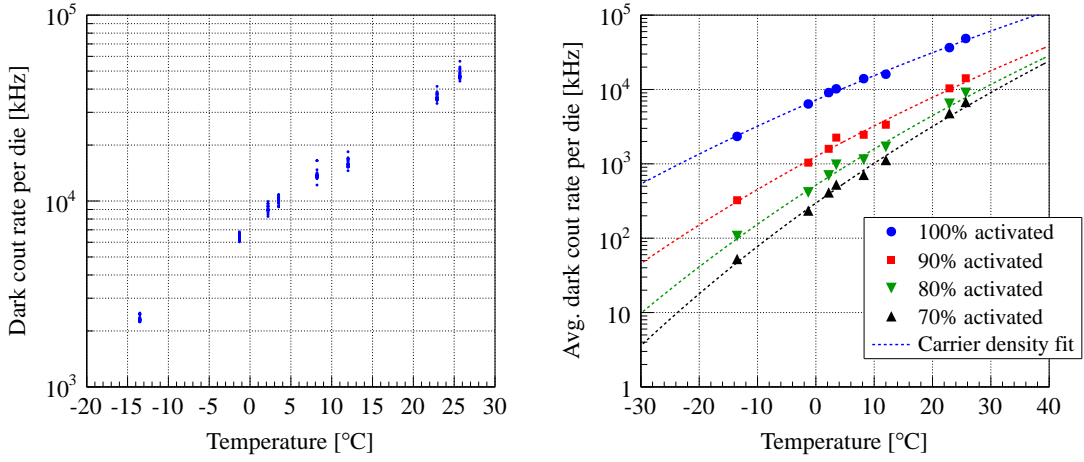


**Figure 5.26:** Temperature dependence of the Philips DPC dark count rate. Left: DCR of all 16 dies of one tile. Right: average DCR per die for different amount of activated cells. The data points were fitted with a function related to the charge carrier density, as given by Eq. 5.8.

### 5.2.2 Time resolution

A femtosecond laser with a wavelength of 400 nm and a pulse width of about 150 fs was used to determine the time resolution of a die of the DPC detector in dependency of the number of detected photons. Detailed analysis and results of the measurements can also be found in Ref. [57]. The light intensity was adjusted by using attenuators of different optical density in front of the photodetector. The active area of the latter was homogeneously illuminated by putting a diffuser into the beam. The DPC was placed inside a light-tight box and the temperature was stabilized using water- and Peltier cooling.

The time resolution for a specific light intensity was determined by measuring the coincidence time spectrum between two dies, demanding the same number of detected photons on both dies, and fitting with a Gaussian function. The time resolution of a single die is then obtained dividing by  $\sqrt{2}$ , assuming that the two dies are identical. Fig. 5.27 shows the photon spectra of the two dies in coincidence at an average light intensity of about 150 detected photons as well as the coincidence time spectrum between the two dies, requiring exactly 150 detected photons on both dies.

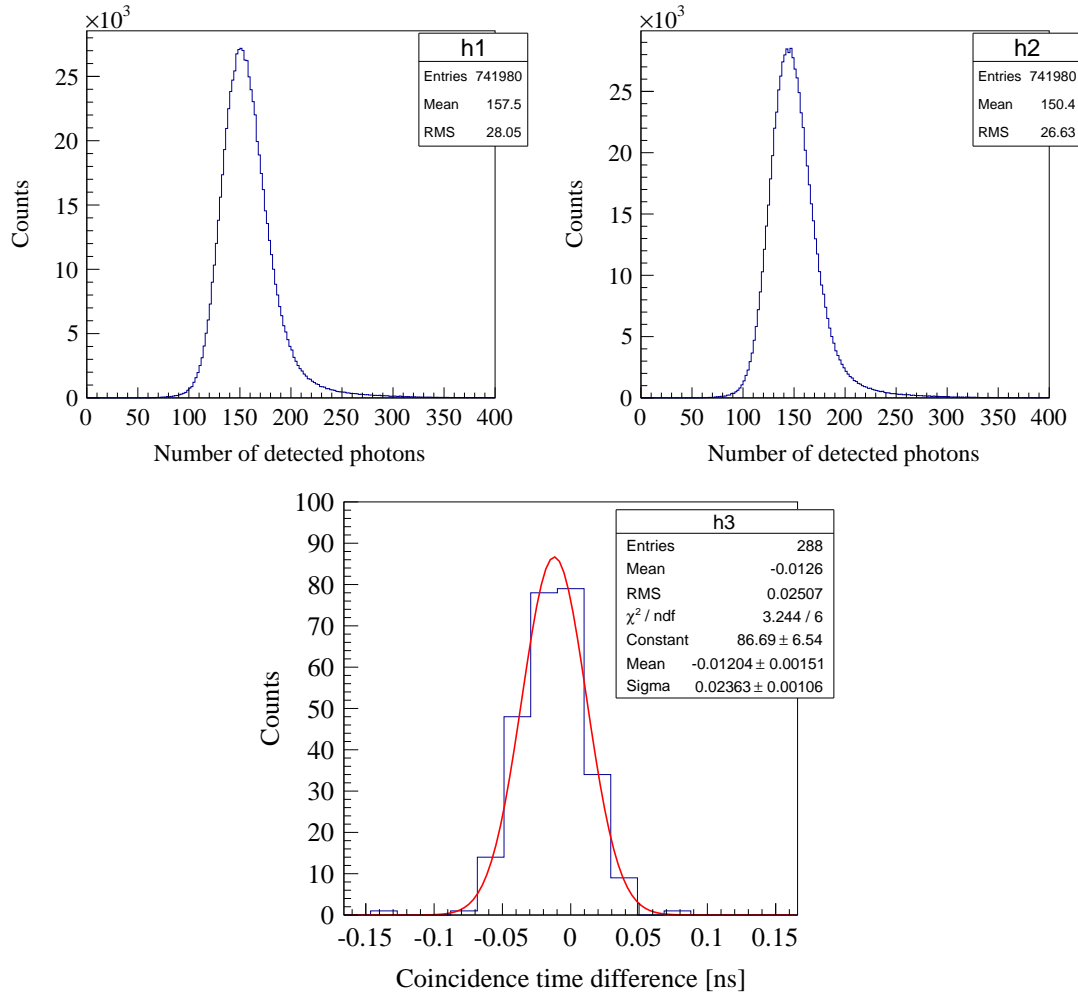


**Figure 5.27:** Top: DPC photon spectra of two neighboring dies exposed to a femtosecond laser pulse. Bottom: coincidence time spectrum between the two neighboring DPC dies. On both dies exactly 150 photons are detected.

Finally, Fig. 5.28 shows the obtained die time resolution as a function of the light intensity. The data points can be fitted with a function of the form  $1/\sqrt{N}$ , with  $N$  being the number of detected photons. It has to be mentioned, that the reason for this behavior is different than in case of the analog SiPM.

Due to the fact that the DPC only provides a single digital time stamp per die, e.g. the time of the first detected photon, and no time information about other detected photons, the time response differs from the one in a conventional SiPM and the die time resolution is essentially not supposed to depend on the number of detected photons. This is however

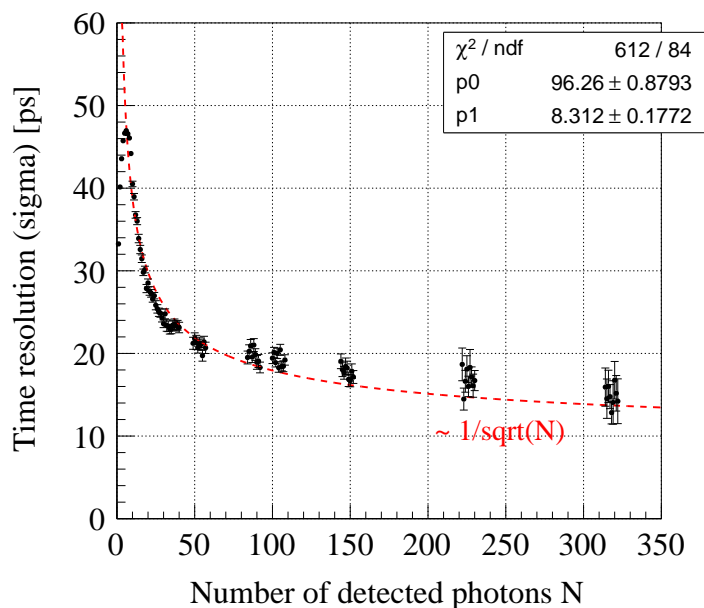


**Figure 5.28:** Time resolution of a single DPC die as a function of the incident light intensity. The time resolution follows a  $1/\sqrt{N}$  behavior down to a few photons, but then starts to deviate, contrary to expectation. As shown in Ref. [57], this is an artifact due to optical cross-talk.

in contrast to what is observed in the measurement, because of the following reasons. Firstly, the time precision of the first photon of some laser or scintillation pulse depends on the number of photons in the pulse. Since we use a laser with a pulse width of about 150 fs, this should be negligible. But secondly, going from high light intensity to lower intensity, the time resolution gets more and more dominated by the trigger network skew of the DPC, which is related to different signal propagation times from the individual cells to the TDC, causing a degradation of the time resolution. The trigger network skew distribution can be roughly described by a Gaussian function [58]. Hence, the measured data can be described in good approximation by  $1/\sqrt{N}$  for most light intensities.

However, at very low numbers of detected photons, the time resolution seems to improve again. This effect has also been reported by Philips in Ref. [3] and is completely contrary to expectation. Monte Carlo simulations indicate that this is related to optical cross-talk between the two neighboring dies [57]. The studies show that the artifact vanishes when investigating two dies which are located far apart from each other.

### 5.3 Discussion of results

Almost all SiPM parameters depend on the applied over-voltage. The PDE, time resolution or gain and related photon counting capability improve with increasing bias voltage. Unfortunately, unwanted noise effects (dark-noise, cross-talk and after-pulsing) are simultaneously also increasing and start to surpass all positive effects at very high operating voltages. In regard to the SciTil system, the intrinsic time resolution and PDE of the photodetectors, both related to the bias voltage settings, are key parameters. In course of the timing studies using a laser setup, we realized already that SiPMs with some technology against after-pulsing and cross-talk show superior performance, not only in terms of absolute values for the time resolution but also concerning the long-term stability during operation with respect to small parameter variations, like temperature or voltage fluctuations.

Among the tested devices, the KETEK PM3350 device with optical trenches in between the  $50 \times 50 \mu\text{m}^2$  pixels showed the best results with a SPTR of  $\sigma \sim 140$  ps. The value includes the time resolution of the measurement system. The device has a larger operating range compared to older models, e.g. Hamamatsu S10931-100P, because of the optical trenches, which make the SiPM more insensitive with respect to noise effects like optical cross-talk. As a result, the device is also not so sensitive to small over-voltage fluctuations due to e.g. temperature changes. This makes it easier to optimize the voltage settings in a large system like the SciTil system.

For the SciTil detector it is also of great importance that the spectral sensitivity of the photodetectors matches the emission spectrum of the plastic scintillators. To achieve excellent time resolution it is necessary to detect as many scintillation photons as possible, because the photodetector time resolution improves with the number of detected photons  $N$ , following a  $1/\sqrt{N}$  behavior, and as we will see in the next chapter also the time precision of the photons itself improves. In this sense the KETEK devices also seem to offer superior characteristics with higher sensitivity in the blue wavelength regime, compared to Hamamatsu MPPCs.



The dynamic range of SiPMs is limited due to a finite number of pixels. By exposing various types of SiPMs to short laser pulses, it has been demonstrated experimentally that the dynamic range as well as the maximum output can be enhanced beyond theoretical expectations at very high incident light intensities. In course of the measurements, SiPM output signals equivalent up to two times the number of total pixels have been observed. Indeed, most applications may not be affected by such an effect due to much lower light intensities, in a regime of linear SiPM response, where measurement and expectation agree well. The same holds for the SciTil detector, where one expects about 100 incident photons per SiPM, so that there is no need to care about any saturation effects.

The recovery time of SiPMs can play an important role for detectors located in high rate environments. In the high luminosity mode of PANDA, the average event rate will be about 20 MHz. If we assume that for every event, there are on average 10 particles leaving the interaction region isotropically and hitting the SciTil barrel located at a radius of about 50 cm, we can roughly estimate the average particle rate per scintillator tile ( $30 \times 30 \text{ mm}^2$ ), i.e. per SiPM. If we approximate the SciTil detector by a sphere with a radius of 50 cm, the calculation yields about  $64 \text{ Hz/mm}^2$  and roughly 60 kHz per tile.

By measuring the recovery time of three Hamamatsu MPPCs with  $1 \times 1 \text{ mm}^2$  active area, it has been shown that the obtained recovery time constants  $\tau_r$  are in good agreement with the approximation  $\tau_r \sim R_{quench} C_{pix}$ , with  $R_{quench}$  being the value of the quenching resistor and  $C_{pix}$  the pixel capacitance. The measurements have been carried out by exposing the SiPMs to two consecutive light pulses of varying delay and performing a waveform analysis on acquired data. At low operating voltages ( $V_{over} = 1 \text{ V}$ ) the values for full recovery are about 200 ns for the 100U device ( $100 \times 100 \mu\text{m}^2$  pixel size), 50 ns for the 050U sensor ( $50 \times 50 \mu\text{m}^2$  pixel size) and 20 ns for  $25 \times 25 \mu\text{m}^2$  pixels. At higher operating voltages, noise effects start to drastically prolong the detector recovery. For MPPC with larger active area ( $3 \times 3 \text{ mm}^2$ ) we can expect comparable values due to similar pixel capacitances. Hence, an event rate in the order of 60 kHz can easily be handled.

The recently introduced DPC by Philips is a promising device for fast timing applications

like the SciTil system. The single die time resolution depends on the number of detected photons because of the trigger network skew, which is associated with different signal path lengths from individual cells to a common TDC. At a light intensity of 150 detected photons a time resolution of about 17 ps sigma was observed. The measured DCR per mm<sup>2</sup> is in the order of about 500 kHz, which is comparable to conventional SiPMs. However, activating larger surfaces requires cooling of the DPC, otherwise the data acquisition is dominated by dark count events. The new detector technology is definitely an option for photon detection in the SciTil system.

## Chapter 6

# Time resolution of plastic scintillators

A scintillation detector as it is proposed for SciTil is composed of several parts contributing to and limiting the achievable time resolution, namely the plastic scintillator, the photodetector and the read-out electronics. After having discussed the characteristics of the photodetector in the previous chapters, we will now concentrate on the scintillator part. As far as the scintillator is concerned, the material properties, i.e. rise-, decay time and light yield, as well as the scintillator geometry are important parameters, as they are directly influencing the time resolution.

In order to understand the impact of the scintillator properties on the time resolution, the statistics of scintillation light emission, often called photostatistics or photon counting statistics, is studied. In this context we will see, that the optimal scintillator should deliver shortest possible time constants and maximum light output. The size of the scintillator tile determines the magnitude of the time jitter introduced by the photon propagation, leading to another time resolution limiting factor.

As shown in Ref. [34], taking into account the individual contributions, the time resolution of a scintillator in terms of the standard deviation  $\sigma_{scintillator}$  can be written as:

$$\sigma_{scintillator} = \sqrt{\sigma_{statistics}^2 + \sigma_{propagation}^2} \quad (6.1)$$

**Table 6.1:** Main parameters of fast plastic scintillators suitable for the SciTil system. These scintillators were used for theoretical considerations and comparative test measurements. All listed scintillators have a refractive index of  $n = 1.58$ . Values are taken from the data sheets<sup>1</sup>.

Scintillator	EJ-232	EJ-228	EJ-204	EJ-200
Commercial equivalent	NE-111A BC-422	Pilot-U BC-418	NE-104 BC-404	Pilot-F BC-408
Light yield [% Anthracene]	55	67	68	64
Light yield [photons/MeV]	8 400	10 200	10 400	10 000
Rise time [ns]	0.35	0.5	0.7	0.9
Decay time [ns]	1.6	1.4	1.8	2.1
Wavelength of max. emission [nm]	370	391	408	425

In Eq. 6.1 one contribution is related to the photon counting statistics,  $\sigma_{statistics}$ , and another contribution is coming from the photon propagation,  $\sigma_{propagation}$ . In the following discussion, the former includes the scintillator rise- and decay time as well as the light yield, while the latter accounts for the different path lengths of the photons. The main properties of fast plastic scintillators suitable for the SciTil system are summarized in Table 6.1. These are also the values used for the following calculations.

## 6.1 The influence of photon counting statistics

The response times of organic and inorganic scintillators are usually very diverse due to different scintillation mechanisms. For many inorganic crystals, the decay time  $\tau_d$  is much larger than the rise time  $\tau_r$  and therefore, the light emission is often modeled by a single exponential function. However, in the case of fast plastic scintillators, the decay time becomes comparable to the rise time and therefore  $\tau_r$  cannot be neglected any more.

Based on Ref. [59] and Ref. [34], the light emission of a scintillator can be described by:

$$y(t) = a \cdot e^{-\frac{t}{\tau_d}} \left( 1 - e^{-\frac{t}{\tau_r}} \right) \quad (6.2)$$

with  $a$ , the maximum amplitude of the scintillation light pulse.

---

<sup>1</sup>Eljen (EJ) Technology, <http://www.eljentechnology.com/>

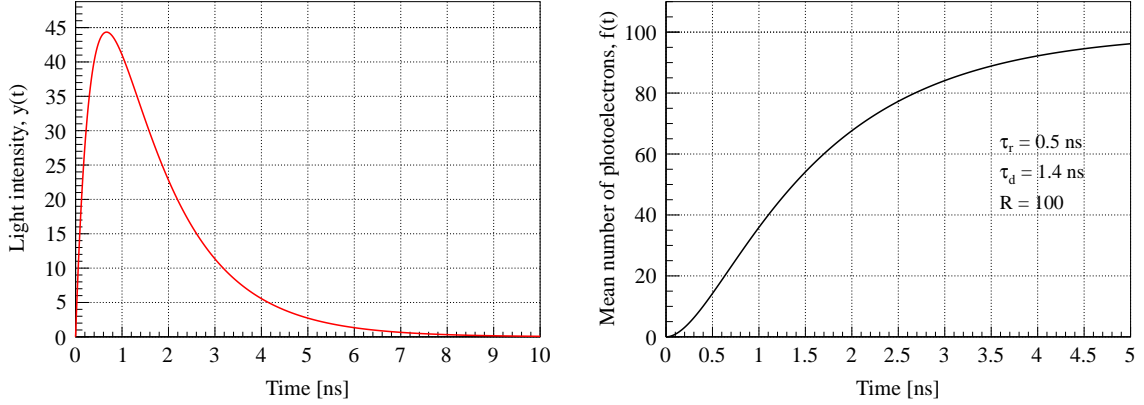


**Figure 6.1:** Light intensity (left) and mean number of photoelectrons (right) as a function of time for a typical plastic scintillator. Parameters are given in the figure.

Integrating  $y(t)$ , one can derive the mean number of emitted photons between time  $t_0 = 0$  and  $t$ ,  $f(t)$ :

$$f(t) = R \left[ 1 - \frac{\tau_r + \tau_d}{\tau_d} e^{-\frac{t}{\tau_d}} + \frac{\tau_r}{\tau_d} e^{-\frac{t}{\tau_r + \tau_d}} \right] \quad (6.3)$$

where  $f(0) = 0$  and  $R = f(\infty) = a \frac{\tau_d^2}{\tau_r + \tau_d}$ , the total photon yield. In reality, only a fraction of all emitted photons is seen by a photodetector and  $R$  usually represents the total number of photons actually detected, i.e. the total number of photoelectrons created by photon-electron conversion in the photodetector, that create a measurable signal. Similarly,  $f(t)$  can be related to the mean number of photoelectrons between  $t_0$  and  $t$ . Fig. 6.1 shows the light output given by Eq. 6.2 as well as  $f(t)$ , for typical values of  $\tau_r = 0.5 \text{ ns}$ ,  $\tau_d = 1.4 \text{ ns}$  and  $R = 100$  for a small plastic scintillator tile read-out with a SiPM.

According to Ref. [60], the probability that  $Q$  photoelectrons are produced between 0 and  $t$  is given by a Poisson distribution as:

$$P_Q(t) = \frac{[f(t)]^Q e^{-f(t)}}{Q!} \quad (6.4)$$

with  $f(t)$  given by Eq. 6.3. Moreover, the probability for the  $Q^{\text{th}}$  photoelectron to be detected between  $t$  and  $t + dt$  is given by:

$$W_Q(t)dt = P_{Q-1}(t) \frac{df(t)}{dt} dt \quad (6.5)$$

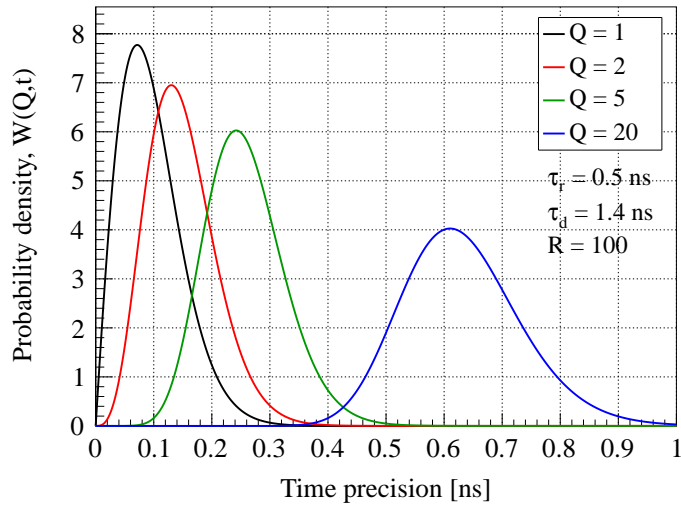


**Figure 6.2:** Probability density  $W(Q,t)$  for the first, second, 5<sup>th</sup> and 20<sup>th</sup> photoelectron. The maximum of  $W(Q,t)$  represents the time precision of the  $Q^{\text{th}}$  photoelectron. Parameters of the scintillator are given in the figure.

with  $P_{Q-1}(t)$ , the probability that  $(Q-1)$  photons are detected at time  $t$ . The maximum of the probability density  $W_Q(t)$  represents the most probable time interval for the detection of the  $Q^{\text{th}}$  photoelectron and thus the time precision of the latter [34]. Fig. 6.2 shows the time precision of different photoelectrons for an EJ-228 scintillator. As one can see from the plot, the best time precision can be achieved when triggering on the first photoelectron ( $Q = 1$ ).

Fig. 6.3 shows the time precision of the first photoelectron ( $Q = 1$ ) as a function of the total number of photoelectrons,  $R$ , for three common plastic scintillators with different rise and decay times. The time precision depends on the scintillator time constants and improves with the number of detected photons.

Studying the photon counting statistics, we can conclude, that the best time precision is achieved when triggering on the first photoelectron ( $Q = 1$ ). The time precision depends on the rise time ( $\tau_r$ ), the decay time ( $\tau_d$ ) and on the total number of detected photons ( $R$ ). The optimal scintillator for best timing performance should have short time constants and high light yield. In a real scintillator, however, one has to find a compromise between these parameters. In addition, one should aim at detecting as many scintillation photons

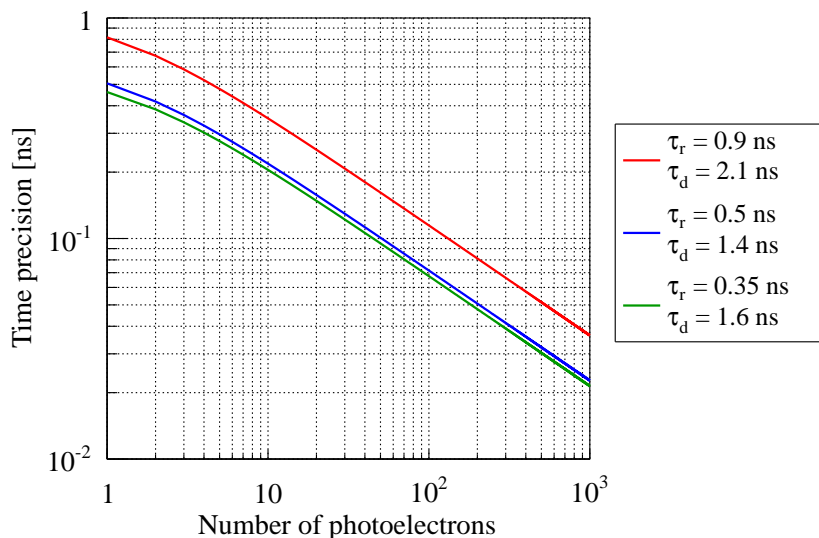


**Figure 6.3:** Time precision of the first photoelectron ( $Q = 1$ ) as a function of the total number of photoelectrons,  $R$ , for common plastic scintillators. Red: EJ-200. Blue: EJ-228. Green: EJ-232.

as possible. It is important to notice, that the above calculations on the time resolution only consider the statistics of the scintillation process and do not include other effects influencing the time performance which can change the above considerations, so that triggering on the first photoelectron do not result in the best time precision any more.

## 6.2 The influence of photon propagation

It was already mentioned that in a real scintillation detector, there are further limitations on the achievable time precision. Concerning the scintillator, there is also an additional time jitter coming from the light propagation inside the material. The contribution to the time resolution can be estimated from the maximum light path difference inside the scintillator [61].

We consider a square shaped scintillator with a side length of 30 mm read-out by a photodetector, detecting two consecutive interactions at different positions  $p_1$  and  $p_2$  at times  $t_1$  and  $t_2$ , as indicated in Fig. 6.4. At position  $p_1$ , the measured travel time  $t_1$  is essentially

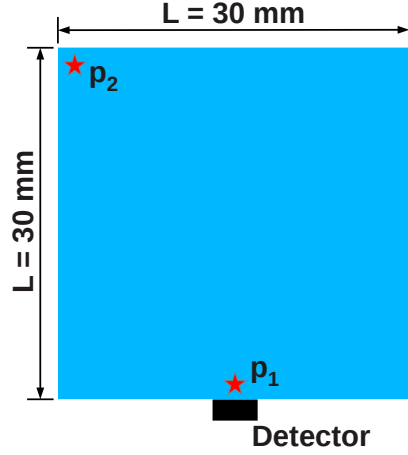


**Figure 6.4:** Square shaped scintillator to estimate the influence of the light propagation inside the material. It is assumed that the scintillation light is emitted from positions  $p_1$  and  $p_2$  to calculate the maximum arrival time difference.

zero, while at position  $p_2$  it is maximal. It is assumed that the photodetector does not add any additional time jitter to the measurement. Considering only photons which are not reflected inside the scintillator, we can estimate the maximum arrival time difference:

$$\Delta t_{max} = t_2 - t_1 = \frac{1}{c_n} \sqrt{L^2 + (L/2)^2} \approx 177 \text{ ps} \quad (6.6)$$

with  $L$  being the length of the scintillator and  $c_n$ , the speed of light in the material. If we assume a Gaussian behavior with a width of  $\sigma_{propagation}$ , then the maximum time difference  $\Delta t_{max}$  can be interpreted as  $6 \cdot \sigma_{propagation}$ , and thus:

$$\sigma_{propagation} = \frac{1}{6} \cdot \Delta t_{max} \approx 30 \text{ ps} \quad (6.7)$$

Combining the discussed contributions, the total time resolution of the scintillator can then be written as:

$$\sigma_{scintillator} = \sqrt{\sigma_{statistics}^2 + \sigma_{propagation}^2} \quad (6.8)$$

with one contribution coming from the photon counting statistics and one originating from the light propagation. However, the total time resolution of a scintillation detector will be affected additionally by the time jitter introduced by the photodetector and read-



out electronics, which has been neglected so far. Besides, there will be an impact from associated electronics noise and, if using SiPMs, from dark-noise and cross-talk.

At this point it is important to mention, that due to electronics noise and due to the response of an SiPM to single photons with an associated single photon time resolution (SPTR), triggering on the first photon will not necessarily result in the best time resolution any more, as presented later in this thesis and also reported by others [62, 63, 64]. In this context, the influence of electronics noise is determined by the slope of the SiPM signal ( $dV/dt$ ) at the time of threshold crossing. For low thresholds,  $dV/dt$  is smaller and thus the impact of electronics noise is higher.

Furthermore, the SPTR influences the time resolution of the scintillation detector as it significantly changes the effect of photon counting statistics. Assuming zero SPTR, triggering on the first photoelectron would still lead to the best time precision, as derived before neglecting the influence of photon propagation, i.e. the scintillator geometry, and other effects. The influence of the electronics (trigger) threshold is going to be discussed also in the next chapter on the basis of examples. It should be also noted that in reality it is usually anyway hardly possible to trigger on the first photoelectron, due to the finite rise time of the SiPM and electronics signals, meaning that until the signal reaches a threshold which is equivalent to a single cell amplitude, a higher number of photoelectrons is piled up already.



## Chapter 7

# Timing performance study for the SciTil detector

In order to reach the required time resolution of  $\sigma \sim 100$  ps for the SciTil system, research on the detector design is needed. As already discussed, the achievable time resolution is influenced by several detector parts, namely the plastic scintillator, the photodetector and the read-out electronics. This work mainly concentrates on the optimization of the first two parts mentioned. Concerning the scintillator, the material properties and the geometry are important parameters. We saw already, that the optimal scintillator should have short time constants and high light yield, while the size of the scintillator tile determines the influence of photon propagation.

Regarding the interplay between photodetector and scintillator, it is crucial to keep in mind the matching between the spectral sensitivity of the photodetector and the emission spectrum of the plastic scintillator, in order to detect as many scintillation photons as possible. Furthermore, a good coupling between scintillator and detector should be accomplished. Additionally, the position to attach the photodetector onto the scintillator has to be optimized. Last but not least, of course also the photodetector with the best intrinsic timing performance has to be found, among a variety of models from different vendors.

In order to evaluate the factors limiting the time resolution and to optimize the detector

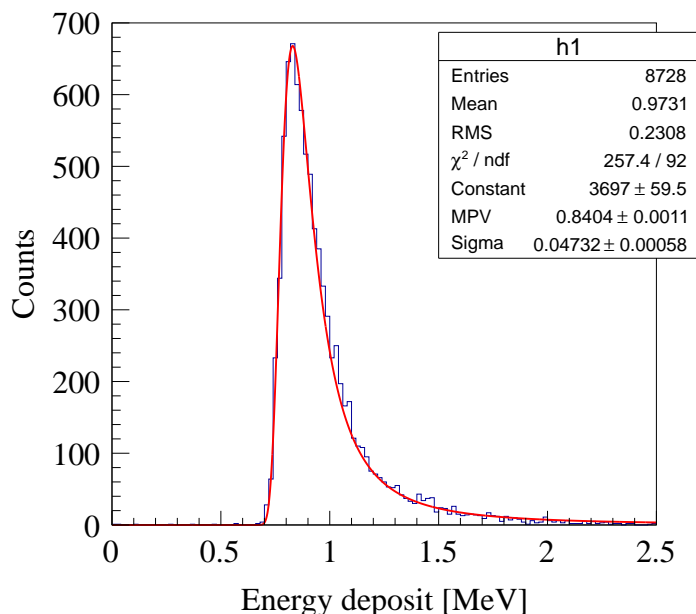


**Figure 7.1:** Simulation of the energy deposit of 1 GeV Kaons in a 5 mm thick plastic scintillator. The histogram is fitted with a Landau distribution.

design, comparative studies using several different plastic scintillators from Eljen<sup>1</sup> read-out with various photodetectors were performed. Different types of photodetectors have been characterized using a laser, as already partly described in the previous chapter. The main properties of all tested scintillators are summarized in Table 6.1. For the tests, square shaped tiles with 20 mm, 28.5 mm, 30 mm and 40 mm side length and 5 mm thickness were available.

A tile geometry of 28.5 mm  $\times$  28.5 mm  $\times$  5 mm was originally proposed for the SciTil detector [9], expecting a time resolution in the order of 100 ps as well as a reasonable spatial resolution, while keeping the total number of channels at an acceptable level. A thickness of 5 mm seems to be optimal concerning space constraints and influence on other detectors in the PANDA barrel region, as well as efficient scintillation photon production. A MIP depositing on average about 1 MeV in 5 mm plastic will produce about 10 k scintillation photons. Detecting about 100 of these photons, we saw already in the previous chapter that a time resolution in the order of 100 ps can be expected.

<sup>1</sup>Eljen Technology, <http://www.eljentechnology.com/>

Fig. 7.1 shows the energy deposit of a 1 GeV  $K^-$  in an EJ-200 plastic scintillator of 5 mm thickness, obtained from a simulation using Geant4 [10]. The energy deposit is well described by a Landau distribution with a most probable energy loss of about 0.85 MeV. The mean energy deposit is about 1 MeV. The results of the experimental studies are presented and discussed in the following sections. Part of this work has already been published in Ref. [38].

## 7.1 Test measurements using the Philips Digital Photon Counter

Due to its large sensitive area with position resolution, the Philips DPC is well suited to study the time resolution of a scintillator tile and its dependency on various parameters described above. Apart from that, the DPC might be an alternative to conventional SiPMs for the SciTil detector.

### 7.1.1 Setup

In order to study the time resolution of a plastic scintillator tile read-out with a Philips DPC, a simple setup as shown in Fig. 7.2 was used. Electrons originating from a  $^{90}\text{Sr}$  source were collimated using two steel plates of 3 mm thickness with holes of 2 mm diameter in the center. The plates were separated by about 8 mm. The source and the collimator plates were mounted on a xy-stage, allowing a positioning with  $\mu\text{m}$  precision to define the beam position.

Two plastic scintillators were attached to a DPC (DPC-3200-22\_C) using BC-630<sup>2</sup> optical grease for good optical coupling, avoiding air gaps between scintillator and photodetector. Unless otherwise noted, the DPC was operated 3 V above the breakdown voltage at a stabilized temperature of  $18 \pm 1^\circ\text{C}$  using water- and Peltier cooling for all measurements.

---

<sup>2</sup>BC-630 silicone optical grease, index of refraction  $n = 1.465$ , Saint-Gobain Crystals, <http://www.crystals.saint-gobain.com/>

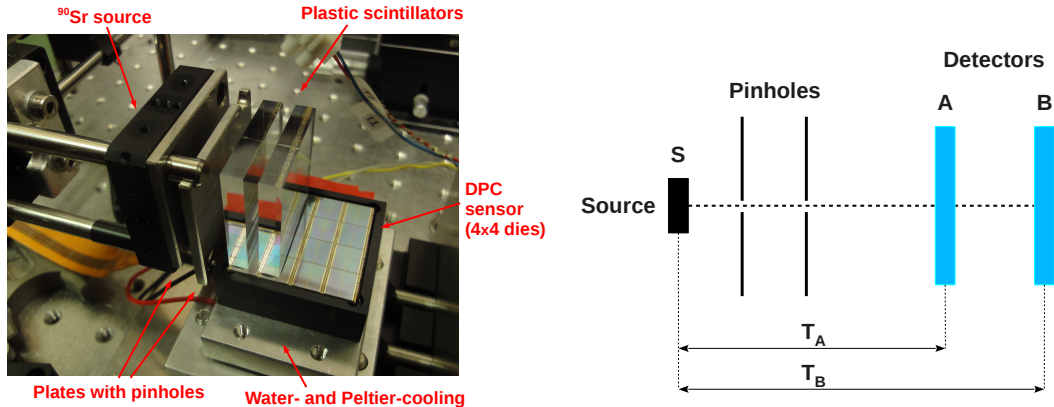


**Figure 7.2:** Picture and schematic of the test setup used to study the time resolution of a plastic scintillator tile. The scintillators are attached to the Philips DPC with large active area, segmented in 16 dies arranged in a  $4 \times 4$  matrix.

The whole setup was mounted inside a light-tight dark box to avoid unwanted exposure to light which could disturb the measurement or even destroy the detector.

### 7.1.2 Optimization of parameter settings

Prior to using the DPC to evaluate the time resolution of scintillator tiles and to perform comparative studies, the detector settings have to be optimized and adapted to the application. As already described in Section 4.4 of Chapter 4, the acquisition sequence of the DPC consists of several consecutive stages. The behavior of the detector and the duration of each stage is defined by the parameter settings done by the user.

The most important settings that can be set by the user are the trigger threshold, the validation threshold, the validation interval, the integration interval and the coincidence time window. The trigger can be set to 1, 2, 3 or 4 photons and defines the moment of triggering, i.e. the begin of an event sequence and the moment of time stamp generation. For the first version of the DPC-3200, which was used in this study, the validation threshold can be either set to 1, 2, 4 or 8 photons or disabled. In the new release of the detector also higher values are possible. This parameter determines if an event is successfully validated or not. The validation interval defines how long the sensor is waiting for suc-

cessful validation. Values ranging from 5 ns to 40 ns are possible. If an event is validated, finally the integration, i.e. the collection and counting of breakdown events, starts. Here, the integration interval (0 to 20  $\mu$ s) specifies the duration of the integration stage. Since we would like to do also coincidence measurements between scintillator tiles, also the coincidence time window has to be adjusted. All these settings influence the performance of the detector, thus all parameters have to be carefully adapted to the application, i.e. efficient and fast detection of scintillation light emitted by a small plastic scintillator tile.

The trigger threshold directly influences the time resolution since it defines which detected scintillation photon determines the trigger time. From photon counting statistics describing the light emission of scintillators it can be expected, that the best time resolution can be achieved when triggering on the first arriving photon.

It is obvious that the validation threshold and interval determine the number of validated events in a given time. However, increasing the validation threshold and decreasing the validation interval will lower the rate of unwanted events, triggered by dark counts. Since the light emission in plastic scintillator is fast and light yields are high, a high validation threshold and a short validation interval are appropriate.

The same holds for the integration interval. Increasing this parameter leads to a higher number of collected photons per event as well as detected dark counts. If the integration interval is set to high values, two consecutive scintillation events may not be resolved but counted as one single event. Decreasing the integration interval lowers the total number of detected photons per event and also the collection of randomly occurring dark counts. Since most plastic scintillators have decay times in the order of a few ns, most of the photons will be emitted in a very short time interval. Therefore, the integration interval should be set at maximum to a few 10 ns, allowing also the detection of late or reflected photons.

Performing coincidences and demanding that two events are detected within a short time window will further reduce the collection of events triggered by dark counts. Since the scintillators are small and flight paths are short, a coincidence window of a few ns should

be applied.

In order to select the optimal parameter settings and determine the influence of different parameters, the  $^{90}\text{Sr}$  spectrum was measured several times with an EJ-228 scintillator ( $30\text{ mm}\times 30\text{ mm}\times 5\text{ mm}$ ), varying one of the parameters while keeping all the other settings constant. The scintillator was read-out with 2 die sensors of the DPC array, demanding a coincidence within 2 ns between the two. Since the thin plastic scintillator covered only about half of the sensitive area of the dies (see Fig. 7.2), only 2 pixels per die were activated and used for read-out.

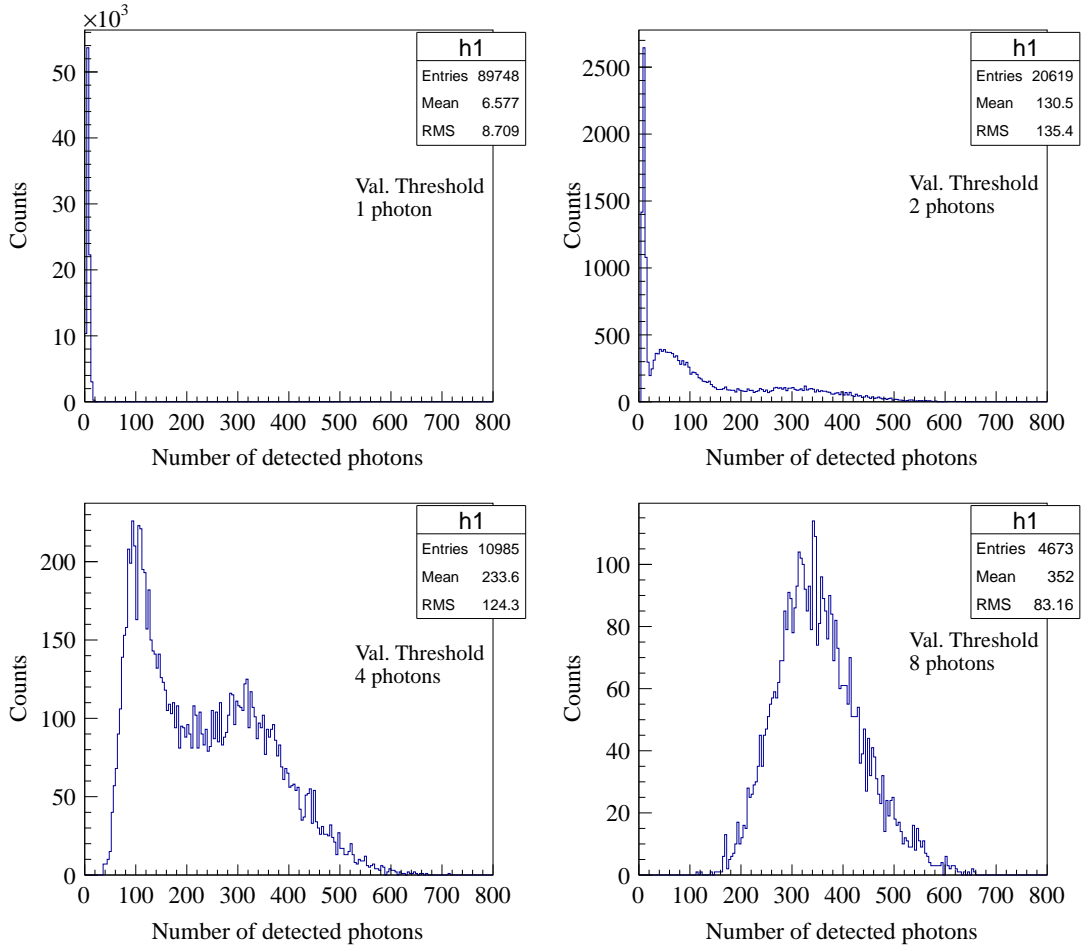
### Validation threshold

Fig. 7.3 shows the measured spectra, setting the trigger threshold to 1 photon, the validation and integration interval to 10 ns and 45 ns, respectively, and varying the validation threshold from 1 photon to 8 photons. The measurement time for each setting was about 65 s. For low validation thresholds the spectra are dominated by dark count events. Increasing the validation threshold reduces the amount of collected events (see histogram entries and maximum counts). Setting the threshold to 4 photons, a nice  $^{90}\text{Sr}$  spectrum can be obtained, indicating that this value is optimal.

With a total of about 11 000 events collected in 65 s, the trigger rate can be estimated to about 170 Hz. Knowing that the use of a validation threshold will not only cut on dark count events but will also reduce the number of events originating from  $^{90}\text{Sr}$  decays, this is in good agreement with the estimated value of about 270  $\beta^-$ -decays per second in the solid angle covered by the pinholes.

At the maximum threshold, the spectrum is cut, which is due to the fact that the validation logic of the DPC requires on average a much higher number of photons being detected for successful validation than given by the set threshold value [36]. Therefore, a validation threshold of 4 photons or 8 photons does not mean that 4 or respectively 8 photons need to be detected for validation, but many more. The same holds for the trigger threshold.





**Figure 7.3:**  $^{90}\text{Sr}$  spectrum measured with an EJ-228 plastic scintillator read-out with the DPC-3200, varying the validation threshold while keeping other settings constant. The plots show the photon counts detected with 2 die sensors (2 pixels each). For low values of the validation threshold the measurement is dominated by events triggered by dark counts. At maximum threshold the spectrum is cut due to the high number of detected photons needed for successful validation. Setting the validation threshold to 4 photons, a nice spectrum can be measured. One can identify the two competing decays of  $^{90}\text{Sr}$  and  $^{90}\text{Y}$  with maximum decay energies of 0.546 MeV and 2.28 MeV, respectively.

**Table 7.1:** Average photon numbers for successful triggering and validation in a DPC-3200. Values are taken from Ref. [36].

Trigger threshold	Avg. number of photons to trigger	Validation threshold	Avg. number of photons to validate
1	1	1	1
2	2.333	2	$4.6 \pm 2.1$
3	3	4	$16.9 \pm 6.2$
4	8.333	8	$52.2 \pm 15.0$

A trigger threshold set to 4 photons does not imply that the 4<sup>th</sup> detected photon defines the trigger time stamp, but rather the 8<sup>th</sup> collected photon on average. However, with a trigger threshold set to 1 photon, it is really the first detected photon that determines the moment of trigger time stamp generation, being of course still not the first scintillation photon due to a finite probability of loss in the scintillator and PDE of the photodetector. The average number of photons to be detected for successful triggering and validation of a DPC-3200 are given in Table 7.1.

From the measurements it becomes clear that the validation threshold should be set to 4 photons in order not to lose too many “real” events on the one hand and to keep the accumulation of dark count events low on the other hand. Employing coincidences between a larger number of dies or multiple scintillators the number of dark count events will be further reduced, thus, the validation threshold can optionally be set to 2 photons.

### Validation interval

Since the scintillation light is emitted fast, it can be expected that the validation interval can be set rather short. In order to determine the impact of the validation interval, the validation threshold was set to the optimal value of 4 photons and the length of the validation stage was varied from 5 ns to 40 ns. Other parameters stayed unchanged.

Fig. 7.4 left shows the number of validated events during the measurement time of 65 s, in dependency of the validation interval. Since we are demanding a coincidence between two dies within a short time window, events validated within a short validation interval

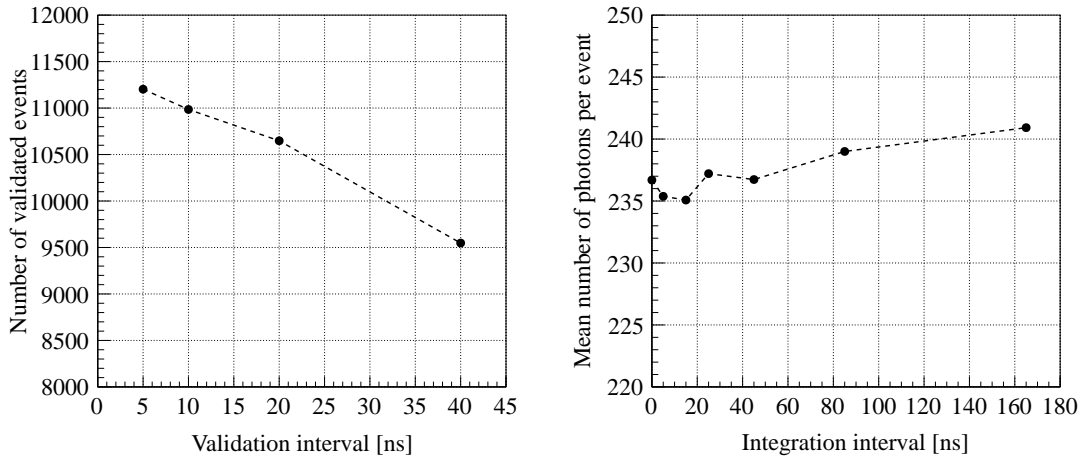


**Figure 7.4:** Left: influence of the validation interval on the total number of validated events within a given measurement time of 65 s. The validation interval can be set as short as possible. Right: average number of detected photons per event as a function of the integration interval. If the integration length becomes longer, more dark counts are accumulated. The dashed lines are added to guide the eye.

will have a higher probability to show coincidence. Therefore, the number of validated events is decreasing with increasing validation interval length. Without coincidence it would be the other way round, mainly due to the increase of events triggered by dark counts for long validation intervals. In any case, the validation interval should be set as low as possible, i.e. to 5 ns.

### Integration interval

The integration interval can be set in the range of  $0 \mu\text{s}$  up to  $20 \mu\text{s}$  and determines the time period the DPC collects breakdown events, hence, it directly influences the number of detected photons per event. If set to large values, the integration interval also limits the double hit resolution and rate capability of the detector, since it is the last stage before read-out and recharging.

Fig. 7.4 right shows the average number of detected photons per event as a function of the integration interval. The plot shows that the influence of short integration intervals of a few 10 ns is marginal. With longer integration times, the detected number of ran-

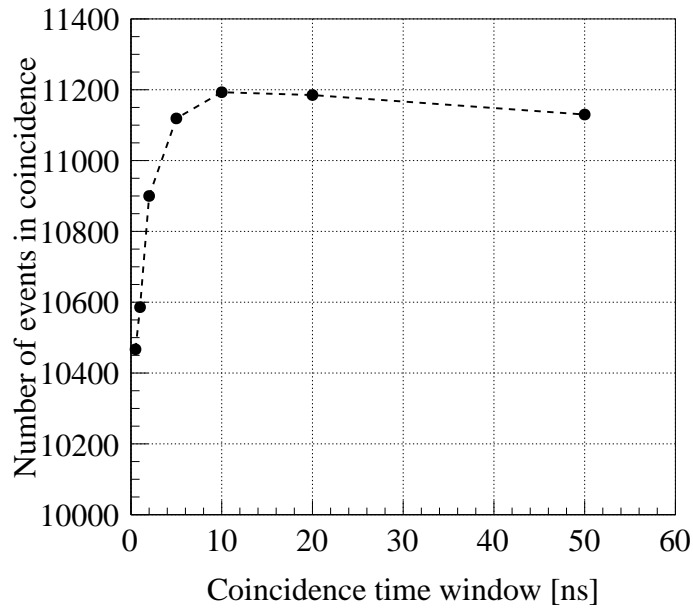


**Figure 7.5:** Influence of the coincidence time window on the number of collected events within a measurement time of 65 s. The dashed line is added to guide the eye.

domly occurring dark counts increases. In order to minimize this number and to keep the acquisition cycle short, it was finally decided to set the integration interval to 45 ns.

### Coincidence time window

Another parameter that can be set by the user is the length of the coincidence time window. Since light emission and arrival of the first photons at the detector is fast, a short coincidence window of a few ns is favorable to avoid random coincidences. However, too short coincidence windows cause loss of “true” events.

Fig. 7.5 shows the number of collected events in 65s in dependency of the length of the coincidence window. The number of coincidence events quickly rises and reaches a plateau with increasing coincidence time length. It is optimal to adjust the length of the coincidence time window just to the beginning of the plateau, i.e. to 10 ns, where the number of collected events starts to saturate.

## Skew correction

Each die of the DPC provides a time stamp signal at the moment of trigger generation. Since the internal signal runtimes are different between individual dies of a DPC tile due to varying lengths of signal lines, there is a small time offset (skew) between these time stamps. In order to achieve optimal timing performance one should correct for these time offsets by applying a skew correction. This can be done by uploading a skew correction table to the DPC tile memory, including the offsets of all dies, or performing an offline correction on the measured data. The skew was measured by exposing the tile to short laser pulses and measuring the time differences between individual dies. This type of skew has nothing to do with the trigger network skew concerning the individual cells on a die, which cannot be corrected and has been discussed in Chapter 5, Section 5.2.

### 7.1.3 Measurement of the time resolution

With optimal DPC parameter settings, the time resolution of a scintillator tile can be estimated by measuring the time-of-flight between the two tiles shown in Fig. 7.2. Each tile was read-out with two adjacent die sensors. Again, only 2 pixels per die were activated. Two identical EJ-228 plastic scintillators ( $30 \times 30 \times 5 \text{ mm}^3$ ) were used. Following the results from the parameter optimization in the previous section, the trigger threshold was set to 1 photon, the validation and integration intervals to 5 ns and 45 ns, respectively, and the coincidence time window to 10 ns. Since a coincidence was now done between two scintillator tiles (4 dies in total), the validation threshold could be set to 2 photons.

It has to be noted that in our setup we are almost not affected by the influence of photon propagation, because of the scintillation photon production happening always almost at the same position and the location of the 2 read-out dies side by side.

Unless otherwise noted, for all measurements only events with a detected photon number corresponding to an approximate energy loss of  $\Delta E \geq 0.8 \text{ MeV}$  in a scintillator tile were selected for data analysis. This is also the expected energy loss for MIPs. In order to

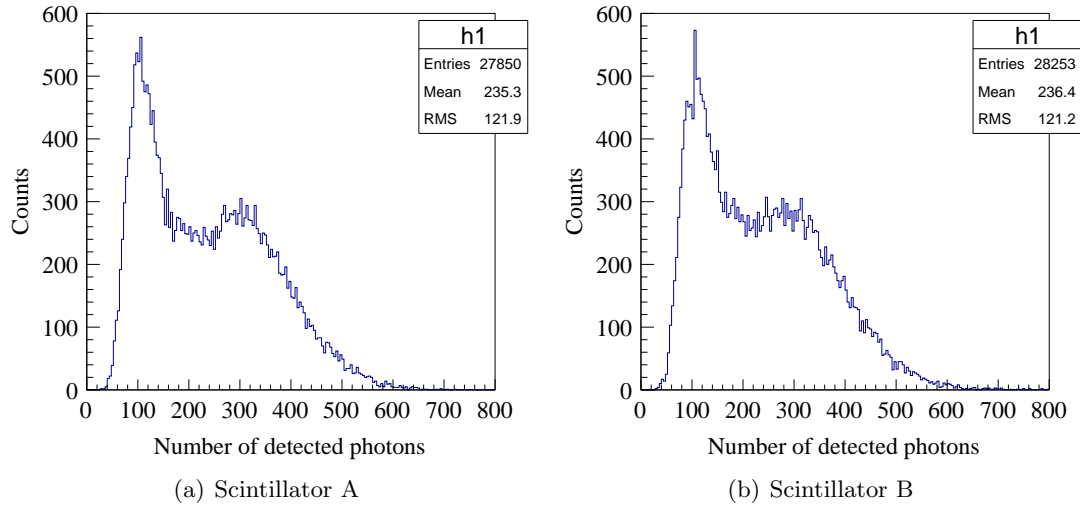


**Figure 7.6:**  $^{90}\text{Sr}$  photon spectra measured with two EJ-228 scintillator tiles at different positions (A and B) to determine the photon number corresponding to an energy loss of about 0.8 MeV. For both scintillators the spectra were cut at 240 detected photons for further analysis.

determine the correct values for this cut, the following calibration procedure was applied.

First, one of the scintillator tiles was removed (scintillator A in Fig. 7.2) and a photon spectrum was acquired using the remaining tile B. Such a spectrum is shown in Fig. 7.6(b). Knowing the maximum decay energies of  $^{90}\text{Sr}$  and  $^{90}\text{Y}$  a rough cut on the photon number corresponding to  $\Delta E \geq 0.8 \text{ MeV}$  could be made. In a second step, scintillator A was put back on top of the DPC and the previous step was repeated also for this tile (see Fig. 7.6(a)). Finally, the two tiles were measured in coincidence applying the cuts for the respective scintillator position. Whenever the setup was modified (change of beam position, scintillator size, position or material, etc.), or any other parameter affecting the detected photon number was changed (DPC settings), the setup was recalibrated. It should be noted, that the scintillator tile B always stayed in place and was never changed, acting as a reference detector. Only the first tile (scintillator A) was exchanged to test different scintillator materials and geometries.

Using such a setup, we got in total four individual time stamps (one per die, two per scintillator tile) at the moment of trigger generation, i.e. the detection of the first photon

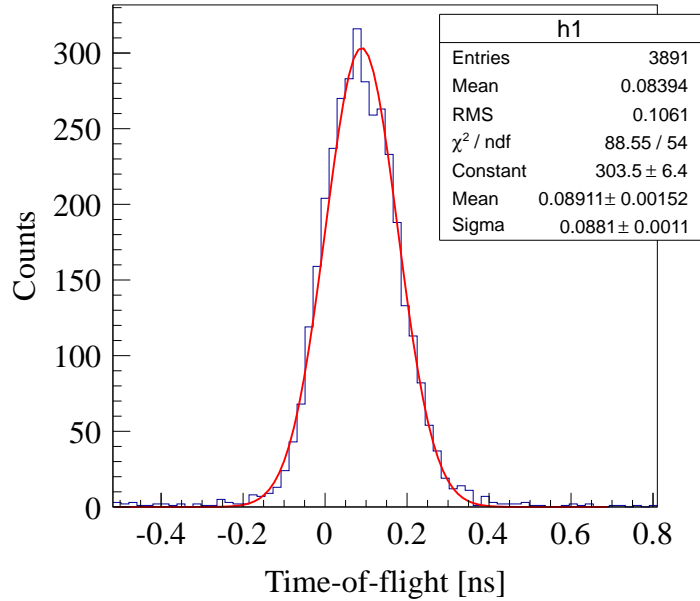


**Figure 7.7:** TOF spectrum between two EJ-228 plastic scintillators A and B with a size of  $30 \times 30 \times 5 \text{ mm}^3$ . The spectrum was fit with a Gaussian function.

on a die. Accordingly, a mean time stamp of two single die time stamps belonging to the same scintillator tile can be generated to improve results. In our setup we can assume that the two scintillation detectors A and B are identical and as shown in Appendix A.1, the intrinsic time resolution of each tile ( $\sigma_A$  and  $\sigma_B$ ) can be calculated from the TOF measurement between the two scintillator detectors A and B and the corresponding TOF resolution  $\sigma_{AB}$ :

$$\sigma_A = \sigma_B = \frac{1}{\sqrt{2}} \sigma_{AB} \quad (7.1)$$

Fig. 7.7 shows the measured TOF  $T_{AB}$  between the two EJ-228 plastic scintillators A and B with a size of  $30 \times 30 \times 5 \text{ mm}^3$ . The TOF resolution  $\sigma_{AB} = 88.1 \pm 1.1 \text{ ps}$  is obtained by fitting the histogram with a Gaussian function. Thus, the time resolution of a single scintillator tile is given by:

$$\sigma_A = \sigma_B = 62.3 \pm 0.8 \text{ ps} \quad (7.2)$$

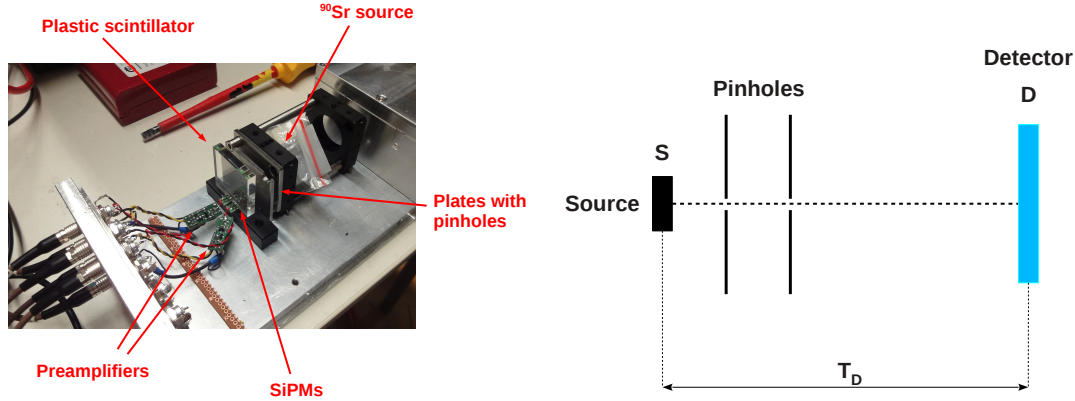


**Figure 7.8:** Picture and schematic of the test setup used to study the time resolution of a plastic scintillator tile. The scintillator is attached to two Hamamatsu SiPMs with  $3 \times 3 \text{ mm}^2$  active area each.

## 7.2 Test measurements using conventional SiPM

In order to study the time resolution of a plastic scintillator tile read-out with conventional analog SiPM, an experimental setup similar to the one described before employing the Philips DPC was used. A picture and schematic of the setup is shown in Fig. 7.8. An EJ-228 plastic scintillator with a size of  $30 \times 30 \times 5 \text{ mm}^3$  was attached to two Hamamatsu SiPMs with  $3 \times 3 \text{ mm}^2$  active area and  $100 \times 100 \mu\text{m}^2$  pixel size (MPPC S10931-100P), using BC-630 optical grease.

Electrons from a  $^{90}\text{Sr}$  source were directed slightly below the center of the scintillator by using two steel plates of 3 mm thickness with centered holes of 2 mm diameter. The SiPM signals were amplified using a preamplifier with a layout based on the AMP-0611 from Photonique, which was already described in Section 5.1.1 of Chapter 5. The DC supply voltage for the preamplifier was set to 5 V. The two SiPMs were operated at room temperature ( $\sim 25 \text{ }^\circ\text{C}$ ) and at bias voltages of 70.1 V and 70.3 V, respectively, in order to achieve the same gain for both detectors. At these conditions, the single photon pulse height was measured to be about 4.5 mV. The amplified signals were recorded with a LeCroy WaveRunner 625Zi digital oscilloscope with a bandwidth of 2.5 GHz and 40 Gs/s for offline waveform analysis. In order to minimize the accumulation of random events,



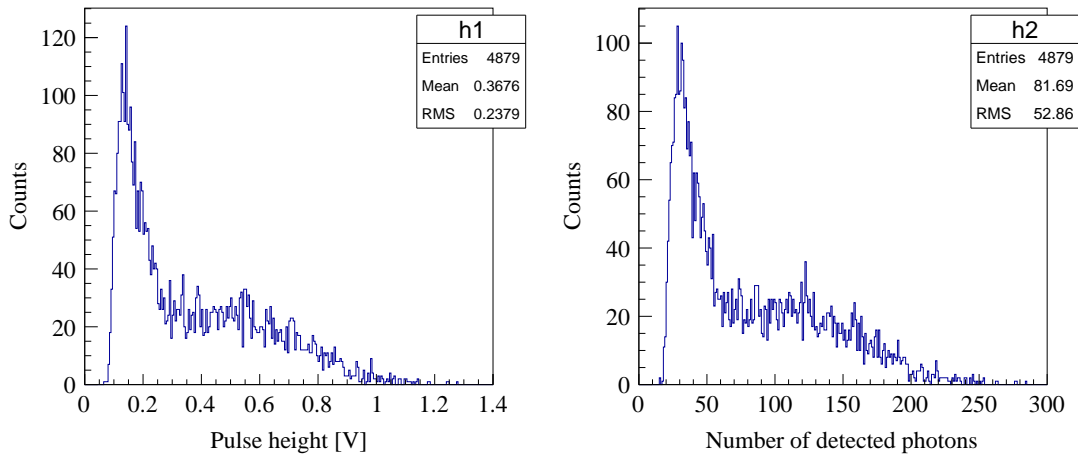


**Figure 7.9:** Left:  $^{90}\text{Sr}$  spectrum measured with an EJ-228 plastic scintillator read-out by two Hamamatsu SiPMs. Since we know the pulse height corresponding to a single fired cell, we can roughly estimate the detected number of photons from the measured signal amplitude (right). For further analysis only events with 90 or more detected photons were accepted. Due to the relatively small sensitive area, the detected number of photons is about a factor 3 less than the number of photons seen with the DPC setup (see Fig. 7.6).

only coincidences between the two SiPMs where both signals exceeded a threshold of 20 mV were accepted.

Compared to the DPC setup, this configuration has the drawback that the sensitive area for photon detection is much smaller. Therefore, one can expect that the number of detected photons is well below the value measured with the DPC and thus also the results concerning the time resolution are expected to be worse. However, by estimating the actual number of detected photons from the measured pulse height spectra, we can compare the results obtained with different setups.

Fig. 7.9 shows the  $^{90}\text{Sr}$  spectrum measured with an EJ-228 plastic scintillator read-out by two Hamamatsu SiPMs. Looking at Fig. 7.9 and Fig. 7.6, we realize that we could detect about 3 times more photons with the DPC compared to the two SiPMs. This is expected due to the 3 times larger sensitive area. Again, a cut on the photon number corresponding to an energy loss of about 0.8 MeV was applied for further analysis. From the measured spectrum, a value of 90 photons was found.

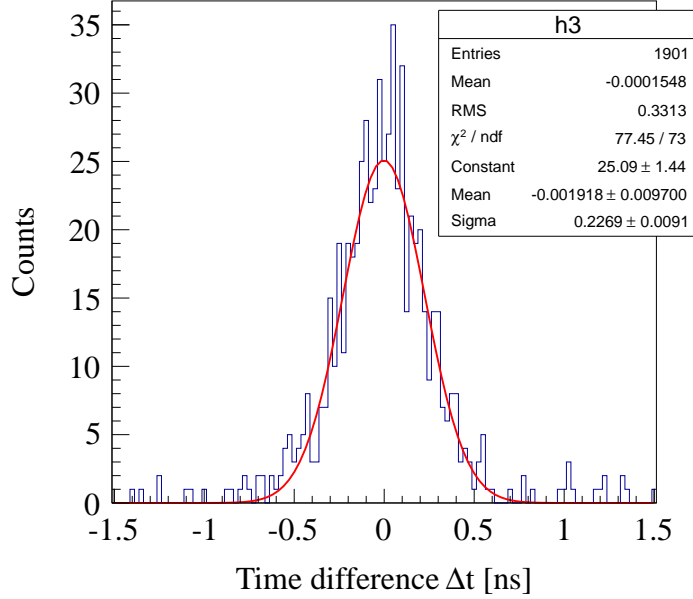


**Figure 7.10:** Threshold crossing time difference between two Hamamatsu SiPMs in coincidence. By fitting with a Gaussian function one can obtain the coincidence time resolution.

As shown in Appendix A.1, the time resolution of a scintillator tile (D) read-out with two photodetectors (D1 and D2) can be estimated by calculating the time difference between the time signals of the two detectors. These time stamps are determined by the time of threshold crossing. Since the data were analyzed offline using a waveform analysis, the threshold could be freely adjusted. In order to avoid time-walk, the threshold was not fixed for all events but set to a constant fraction of the pulse amplitude for each event. The best result was obtained by setting the threshold to 6 % of the pulse amplitude.

Fig. 7.10 shows the time difference ( $\Delta t$ ) between the two SiPM signals. By fitting with a Gaussian function, we can obtain the coincidence time resolution  $\sigma_D^{\text{CTR}} = 226.9 \pm 9.1$  ps. The time resolution of a single detector D1 (or D2) is then given by:

$$\sigma_{D1} = \sigma_{D2} = \frac{\sigma_D^{\text{CTR}}}{\sqrt{2}} = 160.4 \pm 6.4 \text{ ps} \quad (7.3)$$

In order to compare the results with the measurements using the DPC, we can analyze the DPC data in the same way, using only a single scintillator A (or B) (see Fig. 7.2), read-out with 2 dies, to evaluate the coincidence time resolution (CTR) between the two detectors.

Determining the time difference between the two dies and fitting with a Gaussian, a CTR of  $\sigma_A^{\text{CTR}} = 93.3 \pm 0.8$  ps could be found. Thus the time resolution of the single detector A1 (or A2) is:

$$\sigma_{A1} = \sigma_{A2} = \frac{\sigma_A^{\text{CTR}}}{\sqrt{2}} = 66.0 \pm 0.5 \text{ ps} \quad (7.4)$$

This value is only slightly worse than  $\sigma_A$  from Eq. 7.2, which was obtained by using the mean of the two die time stamps and estimating the tile time resolution from a TOF measurement. This shows that in our setup, the photon propagation is hardly affecting the time resolution. In a more realistic setup with the point of interaction and associated scintillation photon production distributed over the whole scintillator surface and photodetectors located at different sides, the CTR  $\sigma_A^{\text{CTR}}$  obtained from the time difference between two detectors will be much worse than  $\sigma_A$ .

To account for the 3 times higher number of detected photons in case of the DPC, one may divide  $\sigma_{D1}$  by another  $\sqrt{3}$ , resulting in  $\sigma_{D1} = 92.6 \pm 3.7$  ps. Although this is a very rough approximation, this value can now be compared to  $\sigma_{A1}$  obtained with the DPC, in order to get a feeling when using different types of detectors.

### 7.3 Detector optimization

We discussed already, that the time resolution of a scintillation detector is influenced by several parts, namely the scintillator, the photodetector and the read-out electronics. In order to achieve the optimal timing performance each part has to be optimized.

Studying photon counting statistics, it was shown that the scintillator rise- and decay times as well as the light output combined with the photodetector efficiency limit the time resolution. The influence of photon propagation is defined by the size of the scintillator. The photodetector and electronics add additional time spread due to intrinsic time jitter, finite signal rise time and bandwidth. The optimal electronics threshold has to be found considering photon counting statistics, the type of photodetector and electronics noise.

Concerning the photodetector, not only the intrinsic time resolution is important but also the PDE and its wavelength dependency. The maximum of the spectral sensitivity should match the maximum of the emission spectrum of the scintillator. Furthermore, the position of the photodetector onto the scintillator and the optical coupling between scintillator and detector can affect the number of detected photons and the time resolution. In the following, the most important factors influencing the time resolution of the scintillator tiles are discussed and studied.

### 7.3.1 Optical coupling between scintillator and photodetector

In order to increase the number of photons reaching the photodetector, the latter is usually attached to the plastic scintillator using some optical grease or cement. For all measurements, we used BC-630 optical grease with an index of refraction of  $n = 1.465$ , which is similar to the refractive indices of the scintillator ( $n = 1.58$ ) and the glass window of the SiPM, which is usually some epoxy resin ( $n = 1.55$ ). Without optical grease there is an air gap between scintillator and detector, which increases the number of photons totally reflected inside the scintillator, thus decreases the number of photons reaching the SiPM. By using optical grease, the critical angle for total internal reflection is increased from  $\Theta_c = \arcsin\left(\frac{n_{\text{air}}}{n_{\text{scint}}}\right) = 39.3^\circ$  to  $\Theta_c = \arcsin\left(\frac{n_{\text{grease}}}{n_{\text{scint}}}\right) = 68.0^\circ$ . In order to test the influence of optical grease, a  $^{90}\text{Sr}$  spectrum was measured in a simple setup, using a BC-408 plastic scintillator with a size of  $25 \times 25 \times 5 \text{ mm}^3$  attached to a DPC-3200 with and without grease. Using optical grease about a factor 1.4 more photons could be detected.

### 7.3.2 Photodetector position

It can be assumed, that the time resolution of a scintillator tile is depending on the position of the photodetector on the scintillator, since the number of photons that can be detected and also light path variations from the point of photon creation to the photodetector are determined by the position of the latter.

Using two SiPMs with a sensitive area of  $3 \times 3 \text{ mm}^2$  and a square shaped scintillator

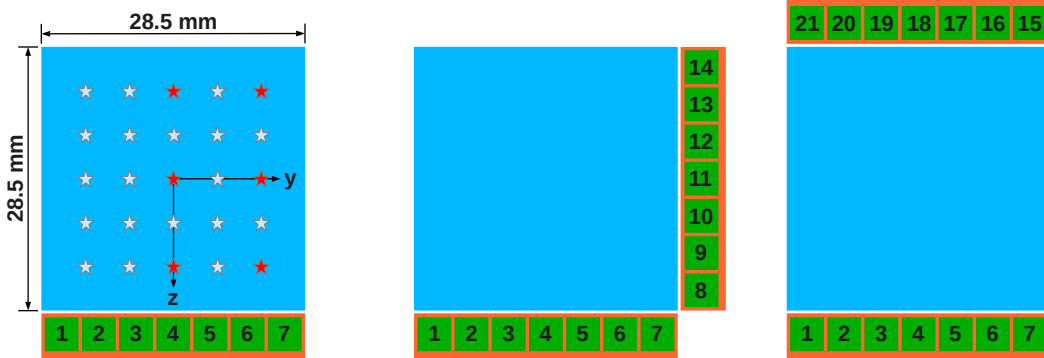


**Figure 7.11:** Possible photodetector positions on a scintillator tile. Two photodetectors can be placed on the same side (left), on different sides (middle) or opposing each other (right), in the center of the rim, e.g. position 4, or on the edge, e.g. position 1. In order to determine the ideal photodetector position, 25 different beam positions were recorded, as indicated by the stars on the left. The measurement results for six beam positions (marked in red) are discussed and shown in Fig. 7.12 and Fig. 7.13. The best time resolution can be achieved by placing the photodetector in the center of the scintillator rim.

with  $28.5 \text{ mm}^2$  side length, there are several combinations possible, as shown in Fig. 7.11. The two photodetectors may be positioned on the same side, on different sides, opposing each other, in the center of the scintillator rim or on the edge, etc. In order to find the optimal position, an EJ-228 scintillator tile ( $28.5 \times 28.5 \times 5 \text{ mm}^3$ ) was placed on top of the DPC using BC-630 optical grease and read-out by 7 pixels (pixel number 1 to 7 in Fig. 7.11). The number of detected photons as well as the time resolution were determined for different beam positions by moving the  $^{90}\text{Sr}$  source in two dimensions in steps of 4.75 mm across the whole scintillator surface, as indicated on the left of Fig. 7.11. Taking the mean of all 25 single measurements gives the optimal pixel position in order to achieve the best time resolution. Again, the data are analyzed by cutting on the photon spectra, considering only events corresponding to an energy loss of  $\Delta E > 0.8 \text{ MeV}$ .

Fig. 7.12 shows the average number of detected photons per event on the individual DPC pixels for six selected beam positions (indicated in Fig. 7.11 left) as well as the mean of all 25 measured positions. The plot shows that the number of detected photons on a specific pixel is related to the point where the photons are created. For beam positions close to the detector array, this relation becomes most evident. In this case, pixels which

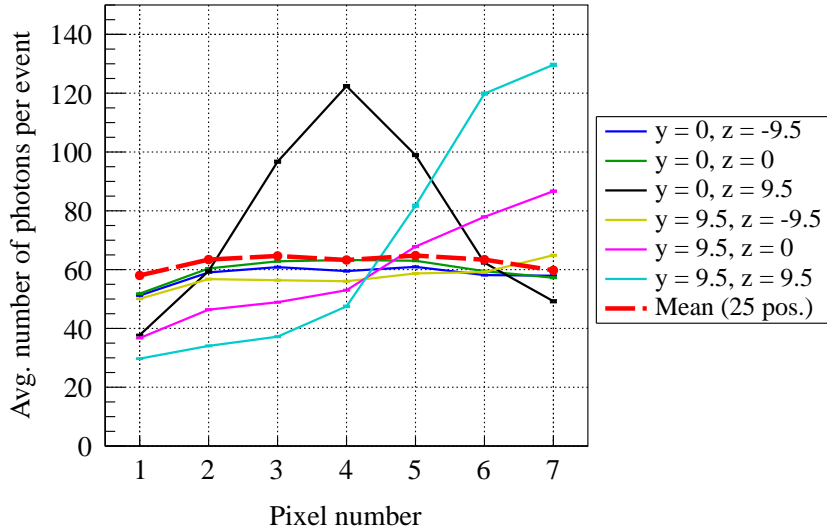


**Figure 7.12:** Average number of detected photons per event in dependency of the photodetector position on the scintillator. The pixel numbers correspond to pixels of the DPC at a certain position, which is shown in Fig. 7.11. Pixel numbers 1 and 7 correspond to pixels at the edge of the scintillator, pixel number 4 is located in the center of the scintillator rim. The different colors belong to different measurements at certain beam positions (see Fig. 7.11). The lines are added to guide the eye. The dashed line shows a mean value of 25 measurements (beam positions). Essentially, the scintillation light is distributed rather equally on the scintillator rim.

are very close to the point of photon creation detect more than three times the number of photons compared to pixels located farthest, due to photon losses and reflections. On the other hand, for beam positions far away from the detectors, the photons are rather equally distributed among the individual pixels. Taking a mean value of all 25 beam positions shows indeed that the scintillation light is rather uniformly distributed on the rim of the scintillator. Slightly less photons could be detected at the edges.

In order to determine the time resolution of the individual pixels, each of the 25 measurements was divided into two steps, for the following reason. The DPC provides a digital time stamp for each die at the moment of trigger occurrence. Since the trigger threshold is set to one photon, this happens when the first photon is detected. However, the scintillator covers 7 adjacent pixels, pairwise belonging to the same die, resulting in a common time stamp for two pixels. In order to get the right time stamp for a single pixel, in each measurement step only 4 pixels belonging to different dies were activated.

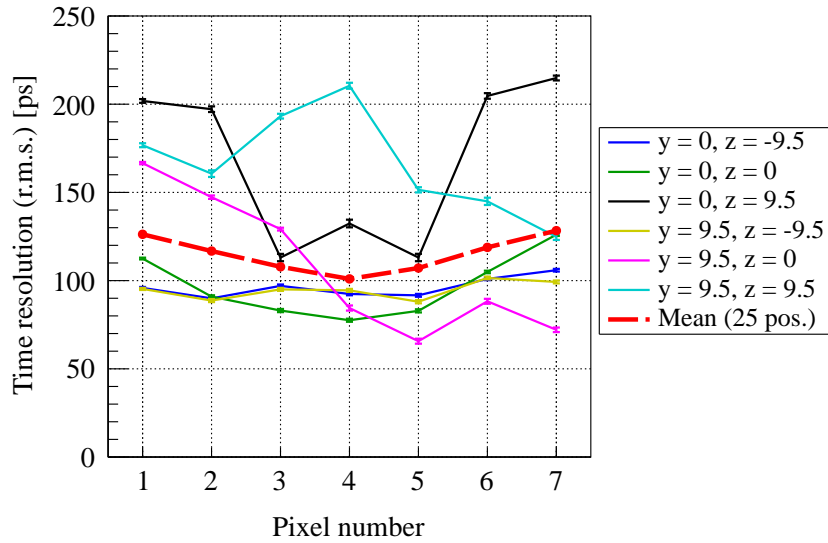


**Figure 7.13:** Time resolution of a scintillator tile in dependency of the photodetector position on the scintillator. The pixel numbers correspond to pixels of the DPC at a certain position, which is shown in Fig. 7.11. Pixel numbers 1 and 7 correspond to pixels at the edge of the scintillator, pixel number 4 is located in the center of the scintillator rim. The lines are added to guide the eye. The dashed line shows mean values of 25 different measurements (beam positions). The best time resolution can be achieved by placing the detector in the center of the scintillator rim.

By measuring the coincidence time spectra between pairs of pixels, the time resolution of single pixels could be extracted.

Fig. 7.13 shows the time resolution of the individual pixels for six selected beam positions (indicated in Fig. 7.11 left) and the mean time resolution for all 25 different beam positions. The time resolution is given as the r.m.s. of the arrival time distribution and has been calculated from the data. From the plot it is obvious, that the best time resolution can be achieved by placing the photodetector in the center of the scintillator rim (pixel number 4). This means that on average the light path variations from the point of photon creation to the photodetector and thus the arrival time jitter is smallest if the detector is placed in the center.

Looking again on Fig. 7.11, it is now clear that the best time resolution can be expected by choosing a combination of pixel numbers 4 and 11 (configuration A) or 4 and 18

(configuration B), respectively. The former might be advantageous because of a higher detection efficiency for photons which are not reflected inside the scintillator but directly hitting the photodetector. Choosing configuration A, the probability for detecting photons created in the corner of the scintillator (e.g.  $y = 9.5$ ,  $z = 9.5$ ) with at least one of the two detectors is higher than for configuration B, where these photons may be totally reflected. The results qualitatively agree with the findings presented in Ref. [38]. The quantitative values for the time resolution do not agree because of different setups (scintillator material, number and position of dies/pixels used for read-out) and analysis (energy cut on photon spectra).

### 7.3.3 Photodetector type

In order to exploit the good intrinsic timing properties of the plastic scintillator tiles, the photodetector with the smallest intrinsic time resolution and highest efficiency to detect scintillation light has to be found. The figures of merit are the SPTR and the PDE.

#### Time resolution

Several types of SiPMs from different vendors (AdvanSiD, Hamamatsu, KETEK) were exposed to pulsed laser light to evaluate the SPTR in dependency of the operating voltage and temperature. The results of this experimental study are presented in Ref. [38]. Among the tested devices, the KETEK SiPM with  $50\ \mu\text{m}$  pixel size and optical trenches for cross-talk reduction shows the best performance. At a temperature of  $20\ ^\circ\text{C}$ , a SPTR of  $\sigma \sim 190\ \text{ps}$  could be achieved, at  $-10\ ^\circ\text{C}$  a value of  $\sigma \sim 140\ \text{ps}$  was obtained.

It has to be noted that this value is limited by the time resolution of the whole setup, consisting of the test device, a trigger detector, the laser and the electronics. Furthermore, this value represents the time resolution for single detected photons. Exposing the SiPM to higher light intensity, the time resolution improves approximately with  $1/\sqrt{N}$ ,  $N$  being the number of detected photons. Assuming that one can detect roughly 60 (100) photons, a time resolution of about 25 ps (20 ps) sigma can be expected at a temperature of  $20\ ^\circ\text{C}$ .



Since it is known that effects like cross-talk and after-pulsing are influencing the photodetector performance, it is not surprising that the SiPMs with optical trenches show the best results. It is therefore advisable to use SiPMs with some technology against such effects. This will also allow higher operating voltages and thus improved time resolution. KETEK as well as Hamamatsu have recently integrated such technology in their products [41, 42].

It is also to be noted that among the tested devices, the SiPM with the smallest pixel size showed the best time resolution. This can be related to a smaller single cell capacitance and thus faster signal rise time. However, going to smaller pixel size decreases the fill factor and therefore the PDE. This can be partly compensated by increasing the bias voltage, especially for the latest devices by Hamamatsu and KETEK. Nevertheless, a tradeoff has to be found.

In a comparable way, the Philips DPC was tested using a femtosecond laser in order to characterize its timing performance. The measurement procedure and some results have been presented already in Section 5.2.2 of Chapter 5. The tests show a die time resolution below 20 ps sigma for more than 100 detected photons. A more detailed description and analysis can be found in Ref. [57].

### **Photon detection efficiency**

In order to achieve the optimum time resolution it is also important to detect as many scintillation photons as possible. Therefore, the photodetector needs a high PDE, that matches the emission spectrum of the scintillator in the best case. Fig. 7.14 shows the PDE of various SiPMs as well as the light output of two common plastic scintillators in dependency of the wavelength. Since the absolute PDE is very much depending on the operating voltage, the PDE is normalized to the maximum of the respective device, in order to be able to compare the spectral sensitivities of the different photodetectors.

The emission spectra of the scintillators are peaked in the blue light range. The new KETEK device with optical trenches is optimized for this wavelength range and covers

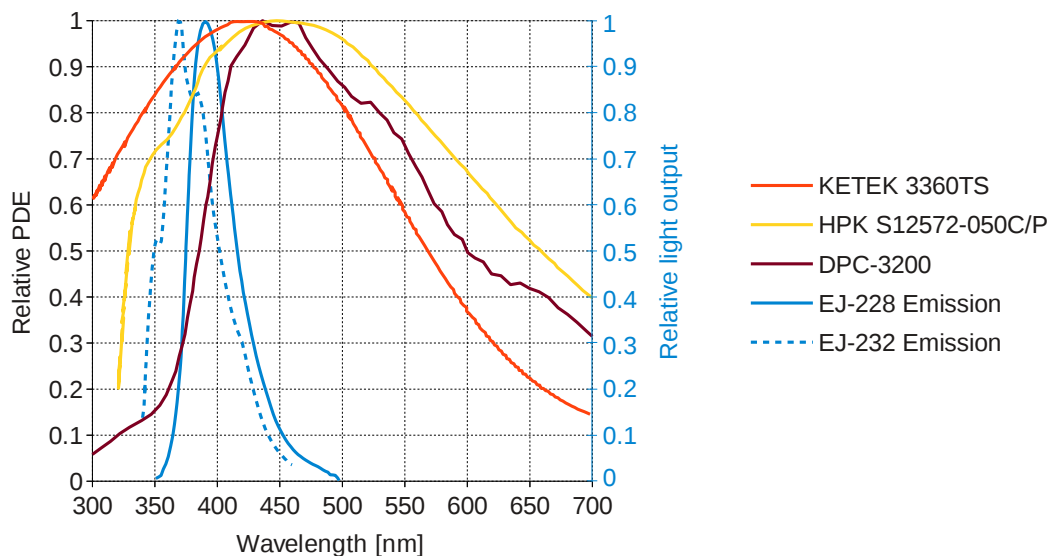


**Figure 7.14:** Spectral sensitivity of various SiPMs. Since the absolute PDE is strongly depending on the operating voltage, the PDE is normalized to the maximum of the respective device to compare between different detectors. The emission spectra of common plastic scintillators are also shown. The curves are taken from the data sheets [41, 43, 65].

this spectral region quite well, whereas the peak sensitivity of the Hamamatsu MPPC and the Philips DPC is shifted slightly towards higher wavelengths.

### 7.3.4 Number of photodetectors

It was originally proposed to use two conventional SiPMs per scintillator tile for photon detection, in order to reach the required time resolution while keeping the total number of read-out channels in the SciTil detector at an acceptable level. First test measurements presented in this work showed that a time resolution in the order of 100 ps sigma should in principle be feasible with an optimized setup using two photodetectors.

Increasing the number of detectors primarily leads to an increase in the number of the detected photons and available time stamps and thus to improved time resolution. By using a setup with four detectors placed symmetrically on a scintillator tile, one could further improve the time resolution by making use of additional pulse height information

to correct for photon propagation from the point of interaction to the photodetector. In this case, one may even think of increasing the size of the scintillator tile to an acceptable level in order to compensate for the higher number of read-out channels. Here, a tradeoff between the spatial resolution of the SciTil system and the total number of channels has to be found. On the other hand, decreasing the number of detectors will also decrease the number of read-out channels by a factor of 2 compared to the proposed layout, but also to a degradation of time resolution, which makes it hardly possible to reach the required performance.

Increasing the number of photodetectors does not necessarily mean to end up with a larger number of read-out channels. One may think of connecting several SiPMs in series or in parallel in order to increase the sensitive area while keeping the total amount of channels constant. A serial connection might be preferred because of smaller capacitance and therefore shorter pulse widths. Usually the breakdown voltage is different from SiPM to SiPM, also among different samples of the same model type. Today, however, new technologies allow to produce a large number of samples with nearly identical characteristics and as already discussed, new devices have large operating ranges. Hence, several SiPMs can be operated with a common voltage source.

Using the Philips DPC offers the possibility to cover larger surfaces, thus improve the number of detected photons and acquire more time stamps to improve time resolution. Test measurements showed that a time resolution well below  $\sigma = 100$  ps can easily be reached. The increase in dark-count rate due to larger sensitive area can be partly compensated by switching off highly active cells. However, extensive cooling is still needed. Considering the whole SciTil system with about 12k scintillator tiles, the fully digital detector may also be a question of cost.

### **7.3.5 Electronics threshold**

By studying the statistics of light emission in a scintillator, we saw that triggering on the first detected scintillation photon, i.e. the first photoelectron, gives the best time precision.

This result, however, only considers and demonstrates the influence of the scintillator on the time resolution. In other words, the photodetector and electronics are assumed to produce a signal without adding any time spread. In a real scintillation detector this assumption is of course not appropriate any more and the question of the optimal threshold setting arises. By investigating the threshold dependence of the time resolution for conventional SiPMs and the Philips DPC, we obtain two qualitatively different answers to this question, as the following examples show.

### **The Philips DPC**

For the DPC, the threshold which is relevant for the time precision is defined by the trigger threshold, which defines the point in time when the time stamp is generated. In order to study the time resolution and its dependency on the electronics threshold, i.e. the trigger threshold, a setup as shown in Fig. 7.2, using two identical EJ-228 scintillators attached to a DPC was used. Each scintillator tile was read-out by two die sensors, resulting in two individual time stamps per tile.

If the trigger threshold is set to 1 photon, each time stamp separately corresponds to the time of detection of the first photon on the respective die. By sorting the two time stamps, one can define the first detected and second detected photon on the total active area and the corresponding time resolution using only one of the two for time stamp generation. In a next step, the trigger threshold can be set to 2 photons and the procedure can be repeated. In this case, however, we do not know the exact number of detected photons to create a trigger due to the DPC trigger network (see also Table 7.1), but only an average value. By sorting the two time stamp we therefore get the time when on average 2.333 photons and 4.666 photons are detected, respectively. This can be repeated for higher trigger thresholds. Fig. 7.15 shows the time resolution of a scintillator tile read-out by the DPC as a function of the number of detected photons used for trigger time generation, i.e. as a function of the electronics threshold.

The plot shows that the best time resolution can be achieved by simply triggering on the

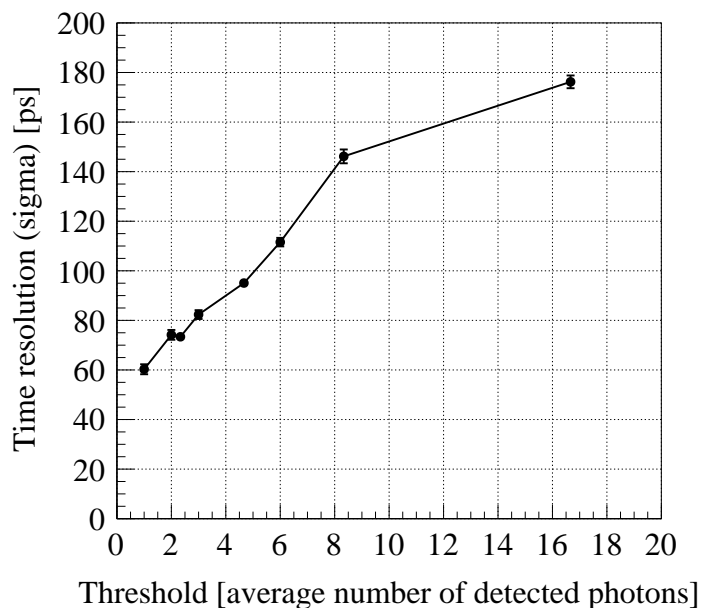


**Figure 7.15:** Time resolution of a scintillator tile read-out by the DPC as a function of the electronics threshold, given as an average number of detected photons defining the trigger time.

first detected photon, as it was derived from photon counting statistics. The best value that could be obtained is  $\sigma = 60.28 \pm 2.0$  ps. The reason for this behavior is that the trigger time stamp is always defined by a single firing cell, resulting in a single digital time stamp. No time information of other detected photons is available. Since the first emitted scintillation photon or respectively the first photoelectron delivers the best time precision, it is best to take the time stamp provided by the first firing cell.

As we will see, in case of an analog SiPM, this situation is different since the trigger time stamp is determined by the time the SiPM signal crosses a certain threshold, whereupon the signal itself is the analog sum of all single firing cell signals and thus carrying the information of all detected photons. Apart from that also electronics noise plays a major role.

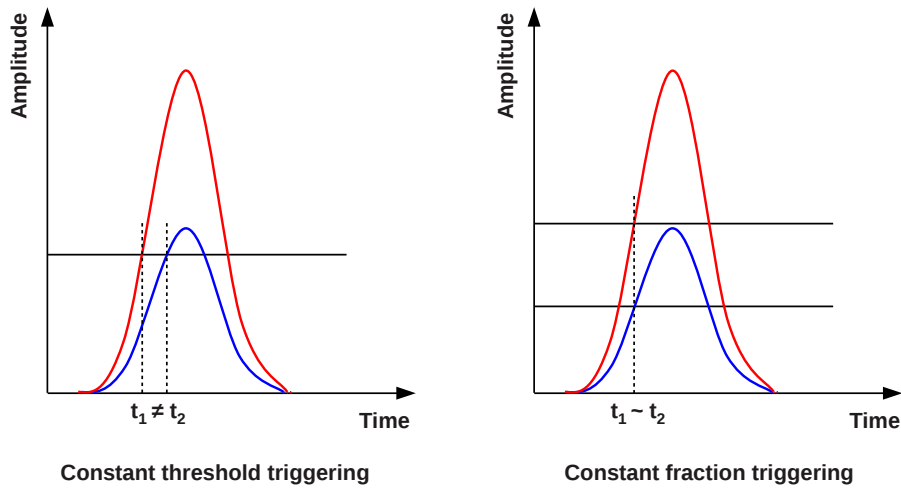


**Figure 7.16:** Trigger time stamp generation using a constant (leading edge) threshold (left) or a constant fraction threshold (right). Constant fraction triggering reduces the time walk effect.

### The conventional SiPM

When using an analog SiPM the time stamp generation is done by applying a threshold to the analog signal and determining the threshold crossing time. This can be done for example with a simple leading edge (constant) threshold or a constant fraction threshold, as shown in Fig. 7.16. Using a constant fraction threshold usually reduces the time walk effect.

In order to study the threshold dependency of the time resolution of a scintillator tile read-out with SiPMs, the same setup as shown in Fig. 7.8 was used. The two SiPM signals were recorded with a LeCroy WaveRunner 625Zi digital oscilloscope with a bandwidth of 2.5 GHz and 40 Gs/s and stored for offline waveform analysis, so that the threshold could be freely adjusted after data taking.

The time resolution can be estimated by performing a coincidence between the two detectors and by calculating the threshold crossing time difference between the two signals. The width of this distribution is a measure for the time resolution. The best coincidence time resolution of  $\sigma_{\text{CTR}} = 226.9 \pm 9.1$  ps could be obtained when using a constant frac-

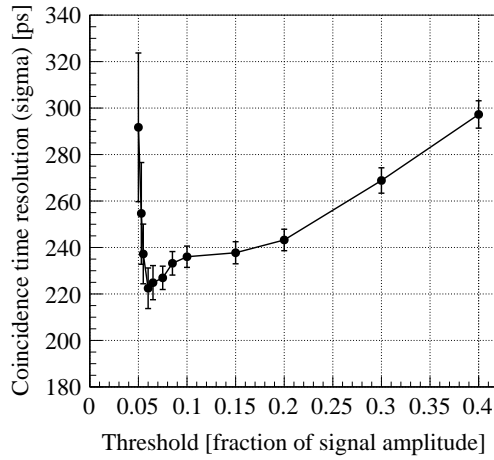


**Figure 7.17:** Coincidence time resolution as a function of the threshold fraction. The time resolution is obtained by fitting the threshold crossing time difference distribution with a Gaussian function.

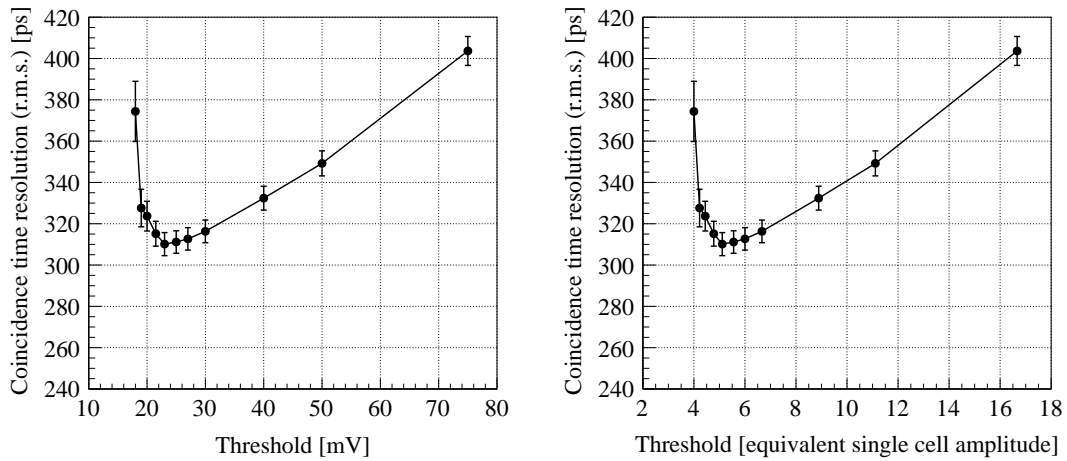


**Figure 7.18:** Coincidence time resolution as a function of the electronics threshold (left). The threshold can be translated into an equivalent single cell amplitude (right). The time resolution is defined as the r.m.s. of the threshold crossing time difference distribution.

tion threshold set to 6% of the signal height, as shown in Fig. 7.17. As explained in Appendix A.1 and Section 7.2, the time resolution of a single detector can be estimated by dividing  $\sigma_{\text{CTR}}$  by  $\sqrt{2}$ . However, here the prior interest is not the absolute value of the tile time resolution but rather the qualitative trend depending on the threshold fraction.

Fig. 7.18 shows the coincidence time resolution when using a leading edge threshold

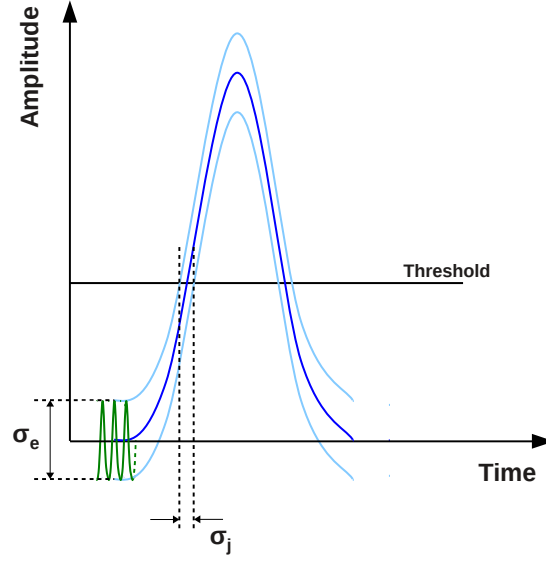


**Figure 7.19:** *Electronics noise time jitter.*

instead of the constant fraction method. A similar behavior as demonstrated before can be seen. Comparable results are also presented in Ref. [62, 63, 64].

The observed minimum and the rise of the time resolution at low thresholds is mainly due to the influence of electronics noise, which can be explained on the basis of Fig. 7.19. The electronics time jitter at the point of threshold crossing  $\sigma_j$  can be approximated by using the slew rate of the signal  $(dV/dt)$  and the input signal noise  $\sigma_e$  [34]:

$$\sigma_j = \frac{\sigma_e}{(dV/dt)_{threshold}} \quad (7.5)$$

Decreasing the threshold leads to lower slew rate and the influence of electronics noise increases. Secondly, the SiPM SPTR drastically changes the influence of photon counting statistics and starts to dominate at low thresholds.

One can conclude that the electronics threshold has to be optimized depending on the type of SiPM and scintillator that is used, since this will influence the interplay between photon counting statistics and the SPTR. The choice of SiPM will also affect the impact of electronics noise because a lower or higher SPTR will also change the slew rate. In



general one can say that triggering on the first photon will not necessarily lead to the best time resolution. On the other hand, for the DPC it can be expected that the best timing performance can be achieved by taking the time stamp of the first detected photon.

For the SciTil system one could think of setting a double threshold, i.e. a high threshold well above the noise to serve for event validation and clean trigger condition and a second threshold for time stamp generation optimized for best timing performance. In case of the Philips DPC such a feature is already implemented with the possibility to set a validation threshold for event validation and a trigger threshold for time stamp generation. For the conventional SiPM one can simply use some proper read-out electronics.

### 7.3.6 Scintillator material

As already discussed, the scintillator properties, i.e. rise time, decay time and light yield, limit the achievable time resolution. In order to study the time resolution for different scintillator materials, a setup as shown in Fig. 7.2 was used. In the figure, scintillator B was used as a reference detector. Its time resolution was determined beforehand by using two identical scintillators A and B and measuring the TOF. Then scintillator A was exchanged by other scintillators of the same size ( $28.5 \times 28.5 \times 5 \text{ mm}^3$ ) but with different physical properties. Table 7.2 summarizes the results obtained with various scintillator materials. The scintillator properties are listed in Table 6.1.

As expected from photon counting statistics, the scintillators with the shortest time constants deliver the best timing performance. EJ-232 and EJ-228 show practically the same results, which indicates that the choice of the scintillator material is a tradeoff between rise (and decay) time and light yield. The EJ-232 material has the shortest rise time but roughly 18% lower light yield compared to EJ-228. As shown in Fig. 7.20, this is reflected in the number of detected photons. Of course, this number is also affected by the characteristic emission spectra of the different materials, as discussed in Section 7.3.3.

**Table 7.2:** Time resolution of plastic scintillator tiles with a size of  $28.5 \times 28.5 \times 5 \text{ mm}^3$  for different scintillator materials. The scintillator properties are listed in Table 6.1.

Scintillator	Time resolution (sigma) [ps]
EJ-232	$59.4 \pm 1.7$
EJ-228	$60.5 \pm 1.7$
EJ-204	$66.5 \pm 1.5$
EJ-200	$81.0 \pm 1.5$

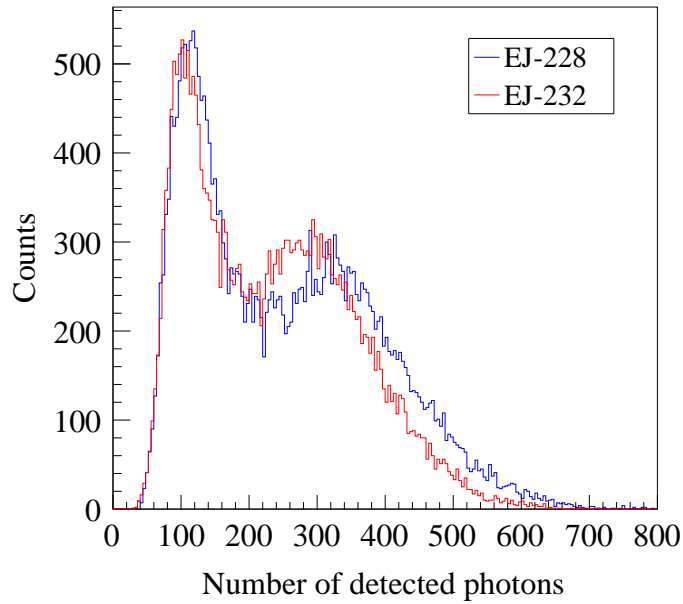


**Figure 7.20:**  $^{90}\text{Sr}$  photon spectra measured with two different scintillator materials. The EJ-232 material features a lower light yield compared to EJ-228, thus the number of detected photons is slightly smaller.

### 7.3.7 Scintillator geometry

The size of the scintillator tile affects the time resolution as it determines the influence of photon propagation inside the scintillator and the number of detected photons. Decreasing the scintillator size leads to smaller time jitter due to photon path variations and larger ratio between photodetection area and scintillator surface, and thus to a higher number of detected photons.

Four square shaped EJ-228 scintillator tiles with different side lengths (20 mm, 28.5 mm,

**Table 7.3:** Time resolution of square shaped EJ-228 plastic scintillator tiles with different sizes.

Dimensions [mm <sup>3</sup> ]	Avg. nb. of detected photons	Time resolution (sigma) [ps]
40 × 40 × 5	271.8	67.6 ± 1.6
30 × 30 × 5	322.4	62.3 ± 1.8
28.5 × 28.5 × 5	350.6	61.8 ± 1.5
20 × 20 × 5	469.7	52.4 ± 2.0

30 mm and 40 mm) and 5 mm thickness were tested in a setup as shown in Fig. 7.2, using the DPC. The tile thickness is basically determined by the spatial constraints within the PANDA barrel region. The measured time resolutions are given in Table 7.3. If we plot the time resolution as a function of the number of photons detected with the respective tile size,  $N$ , we realize that the time resolution improves as  $N$  increases, following roughly a  $1/\sqrt{N}$  behavior, as shown on the left of Fig. 7.21. This is mainly due to photon counting statistics and the trigger network skew of the DPC.

Varying the active area of the DPC by switching on/off a certain amount of cells, while keeping the size of the scintillator constant (30×30 mm), also influences the number of detected photons and therefore the time resolution, as shown on the right of Fig. 7.21. But it also affects the impact of the trigger network skew. If the sensitive area is larger, the trigger network skew has a different, i.e. larger influence on the total time resolution than for smaller number of active cells. Hence, the data deviate from  $1/\sqrt{N}$ .

In Table 7.4 one can look up the total number of scintillator tiles and SiPMs needed to cover the whole SciTil barrel, with a total area of about 4.7 m<sup>2</sup>, depending on the tile size.

**Table 7.4:** Total number of scintillator tiles and SiPMs needed to cover the whole SciTil barrel. It is assumed that two SiPMs are attached to a single tile.

Dimensions [mm <sup>3</sup> ]	Number of tiles	Number of SiPMs
40 × 40 × 5	2924	5848
30 × 30 × 5	5198	10396
28.5 × 28.5 × 5	5760	11520
20 × 20 × 5	11696	23392

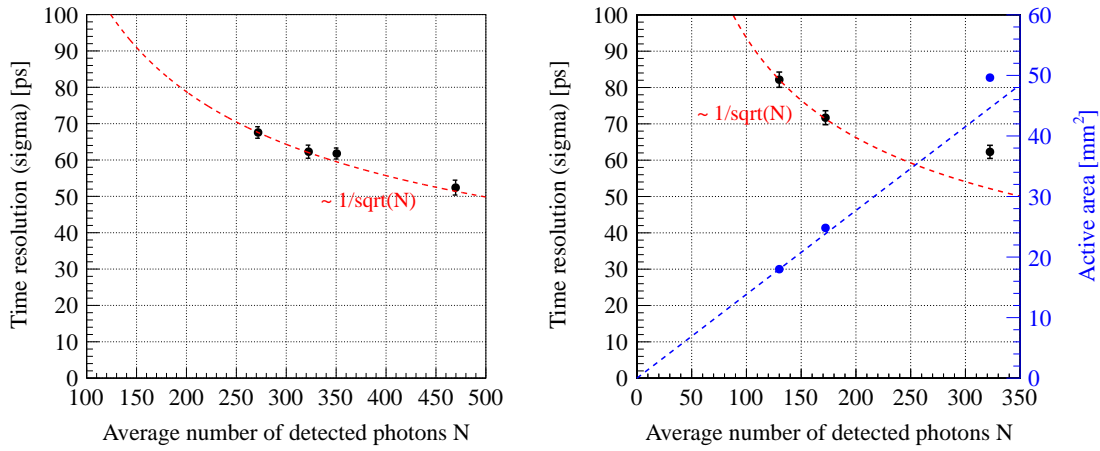


**Figure 7.21:** Left: time resolution as a function of the number of photons detected with different scintillator tile sizes. The time resolution follows  $1/\sqrt{N}$  due to photon counting statistics and the trigger network skew of the DPC. Right: time resolution varying the DPC sensitive area instead of the scintillator size and thus the number of detected photons. The number of detected photons is not strictly proportional to the sensitive area because the photons are not completely equal distributed on the scintillator surface. The data deviate from  $1/\sqrt{N}$  since the influence of the trigger network skew is changed.

### 7.3.8 Scintillator wrapping

A wrapping of the plastic scintillator tiles has not yet been considered in this work and a time resolution below 100 ps sigma has been achieved without wrapping. Nevertheless, it is very likely that some sort of wrapping material is going to be used for the final SciTil detector, in the first instance to shield the scintillator tiles against light from the surrounding. During the experimental tests this has been avoided by performing the measurements inside light tight boxes. For SciTil it may be however difficult to implement large modules consisting of many scintillator tiles in completely dark environment.

The wrapping material will influence the light propagation inside the scintillator tiles and as one can imagine also the time resolution. A reflective material (Teflon, Aluminum) will increase the number of photons reaching the photodetectors but also the time jitter due to many reflections, while for an absorptive material (black tape) one can expect the opposite. In order to find the best suited material, it will be part of upcoming studies to test the influence of different sorts of wrapping by simulation and experiment.

## 7.4 Discussion of results

The time resolution of a scintillator is limited by two factors, namely the statistics of the scintillation process and the photon propagation inside the scintillator. By studying the photon counting statistics, it was shown that the most accurate time precision is given by the first scintillation photon. The achievable time resolution is depending on the scintillator time constants and the light yield. The optimal scintillator for fast timing applications therefore needs short rise and decay times and high light output. The influence of photon propagation is defined by the photon travel path from the point of photon creation to the photodetector. A small scintillator and/or a large number of photodetectors arranged all-over the scintillator surface will reduce the effect.

In a real scintillation detector the time resolution will be further limited by the time jitter introduced by the photodetector and the read-out electronics. Using the Philips DPC the best timing performance could be obtained by triggering on the first detected photon, as expected from statistics. In this case a TOF resolution of  $\sigma_{\text{TOF}} = 88.1 \pm 1.1$  ps could be achieved with two EJ-228 plastic scintillator tiles ( $30 \times 30 \times 5$  mm<sup>3</sup>), thus a time resolution of  $\sigma = 62.3 \pm 0.8$  ps for a single tile read-out with two die sensors.

Reading out the same scintillator with conventional SiPMs and associated electronics, the influence of photon counting statistics is changed and triggering on the first photons does not give the best time resolution any more. In the special case of employing two Hamamatsu MPPCs with  $3 \times 3$  mm<sup>2</sup> sensitive area each, the minimum time resolution for leading edge triggering was measured setting the threshold equivalent to about 5 single fired cell amplitudes. Using a constant fraction threshold set to 6% of the pulse height, a coincidence time resolution of  $\sigma_{\text{CTR}} = 226.9 \pm 9.1$  ps was achieved between the two detectors, hence a time resolution of  $\sigma = 160.4 \pm 6.4$  ps for a single tile read-out with one SiPM.

A detector optimization study has been performed. The time resolution limiting parameters such as scintillator material, scintillator geometry, photodetector type, photodetector

position and electronics threshold have been studied separately. Concerning the scintillator, the best results could be achieved with the fastest scintillators. EJ-228 and EJ-232 scintillators showed nearly the same timing performance. Since the EJ-228 emission spectrum is shifted slightly towards higher wavelength where most common photodetectors are more sensitive and due to lower cost, the EJ-228 might be favored for the SciTil system. Decreasing the size of the scintillator increases the number of detected photons,  $N$ , and decreases the influence of photon propagation. Thus, the time resolution improves and follows roughly  $1/\sqrt{N}$ . The same statements hold for increasing the sensitive area for photodetection. For the SciTil detector it seems optimum to use a scintillator size of about  $30 \times 30 \times 5 \text{ mm}^3$  read-out with minimum two SiPMs, which should be placed in the center of the scintillator rim on opposing sides.

Several types of photodetectors have been tested using a pulsed laser beam. Among the tested devices, the Philips DPC and the KETEK SiPMs with optical trenches showed the best timing performance. Furthermore, the spectral range of the PDE for the KETEK SiPM seems to match best the emission spectra of the used plastic scintillators.

## Chapter 8

# Beam test at COSY

Based on the optimization studies presented in the previous chapters, a SciTil prototype detector has been built and finally tested in a particle beam. Though many experimental tests and characterizations can be done with ionizing sources like  $^{90}\text{Sr}$ , it is however of great importance to test the detector performance in a particle beam of high energy, as expected in the PANDA experiment. In our case, the main intention of the beam test is to check if it is feasible to reach a time resolution in the order of 100 ps sigma with an optimized prototype detector, not only in the laboratory but also in a test beam environment.

The beam test has been carried out at Forschungszentrum Jülich (FZJ), Germany, in January/February 2014. During 2 weeks of beam time lots of data have been taken. Different detector and read-out solutions have been tested, including the Philips DPC as well as conventional SiPMs. It has to be mentioned that detailed analysis of data is still ongoing. This chapter describes the test beam setup and summarizes the most important results.

### 8.1 The JESSICA beam line at COSY

The Cooler Synchrotron (COSY) [66] is an accelerator and storage ring for protons and deuterons located at FZJ. With a total circumference of 184 m, the synchrotron deliv-

## Cooler Synchrotron COSY

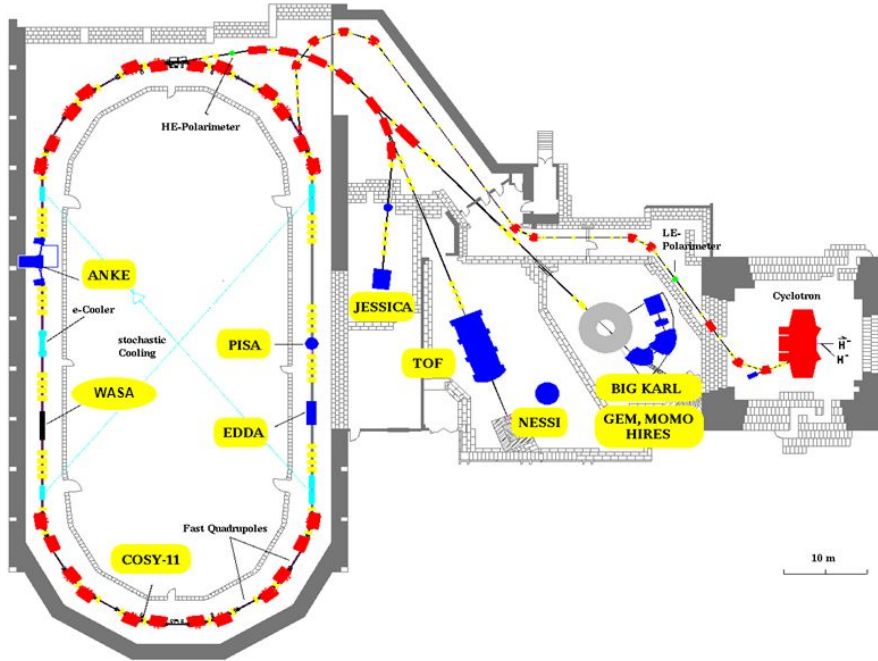


**Figure 8.1:** The COSY facility at FZJ [66]. The beam tests have been carried out at the JESSICA external beam line.

ers proton and deuteron beams with momenta ranging from 300 MeV/c to 3400 MeV/c. COSY is a very versatile particle accelerator that can run in different modes of operation to provide particle beams for several experiments in the circulating beam (internal) as well as for external experiments with extracted beam. The COSY facility is shown in Fig. 8.1 with various internal and external experiments.

The beam tests of the SciTil prototype have been carried out at the JESSICA external beam line [67]. JESSICA stands for Jülich Experimental Spallation Target Set-up in COSY Area and has been originally designed for prototyping experiments for the European Spallation Source (ESS). Besides, the area permits to perform all kinds of other prototyping experiments. For the SciTil beam test we could use a defocused beam of protons ( $\sim 5\text{ cm} \times 5\text{ cm}$ ) with a momentum of about 1.5 GeV/c and 2.7 GeV/c, respec-



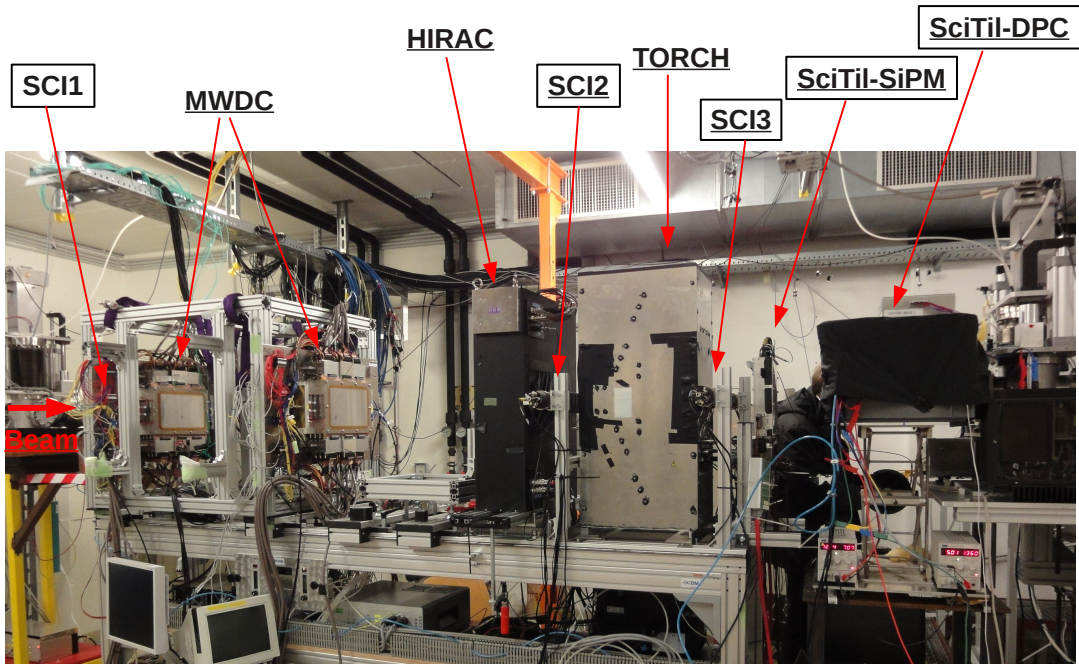


**Figure 8.2:** *The actual beam line at JESSICA. The proton beam is entering from the left. We tested two SciTil prototypes (SciTil-SiPM and SciTil-DPC). Three large plastic scintillators (SCI1, SCI2 and SCI3) were used as trigger detectors for the data acquisition. SCI1 served also as a reference detector for TOF measurements.*

tively, and an intensity of  $10^4 - 10^5$  per second. During the 2 weeks of beam time, several experiments from different collaborations were running in parallel at JESSICA, so that one could partly share the infrastructure.

Fig. 8.2 shows a picture of the actual beam line at JESSICA, showing all the detector systems that have been investigated by different experimental groups. Our setup was located at the end of the beam line and was composed of two SciTil prototypes, one using the Philips DPC for read-out (SciTil-DPC) and one using different types of conventional SiPMs (SciTil-SiPM) with associated electronics. In addition, we could make use of three large plastic scintillators (SCI1, SCI2 and SCI3) located further upstream, each read-out with two PMTs. These scintillation counters served as trigger detectors for our acquisition. Additionally, the scintillation counter SCI1 was used as a reference detector for TOF measurements. Other groups tested some Cherenkov counters (HIRAC and

**Table 8.1:** Main parameters of photodetectors tested at FZJ beam test. Values are taken from data sheets [41, 42, 43, 65].

Photodetector type	HPK MPPC S10372-33		KETEK PM		Philips DPC
	-050C/P	-025C/P	-3360TS	-3350TS	-3200-22-44
Active area [mm <sup>2</sup> ]	3×3	3×3	3×3	3×3	32.6×32.6
Number of cells	3600	14400	2500	3600	3200 per pixel
Cell size [μm <sup>2</sup> ]	50×50	25×25	60×60	50×50	59.4×64
Fill factor [%]	65	62	68	63	74
Peak sensitivity [nm]	450	450	420	420	420
Bias voltage [V]	~ 70	~ 70	~ 28	~ 28	~ 27
Optical trench	no	no	yes	yes	no
Comments	low after-pulse	low after-pulse	low cross-talk	low cross-talk	large active area

**Table 8.2:** Main parameters of plastic scintillators tested at FZJ beam test. These scintillators had shown already the best performance in previous test measurements. All listed scintillators have a refractive index of  $n = 1.58$ . Values are taken from the data sheets<sup>1</sup>.

Scintillator	EJ-232	EJ-228
Light yield [% Anthracene]	55	67
Light yield [photons/MeV]	8 400	10 200
Rise time [ns]	0.35	0.5
Decay time [ns]	1.6	1.4
Wavelength of max. emission [nm]	370	391
Dimensions [mm <sup>3</sup> ]	28.5×28.5×5	28.5×28.5×5 30×30×5

TORCH) and two Multi-wire Drift Chambers (MWDC).

The primary intention of the beam test was to check the feasibility of reaching a time resolution in the order of 100 ps sigma in an ionizing particle beam with a prototype SciTil detector, based on the optimization studies presented in the previous chapters. Secondly, it was intended to quantitatively compare different detector solutions and concepts to further optimize the final design. Therefore, two independent setups were used, one based on conventional SiPMs and the other one based on the Philips DPC. The two setups could be tested in parallel. Several types of SiPMs were tested in combination with different plastic scintillators. The decision on the choice of photodetectors and materials was made on the basis of previous measurement results. A list of all tested devices and associated parameters can be found in Table 8.1 and Table 8.2.

<sup>1</sup>Eljen Technology, <http://www.eljentechnology.com/>

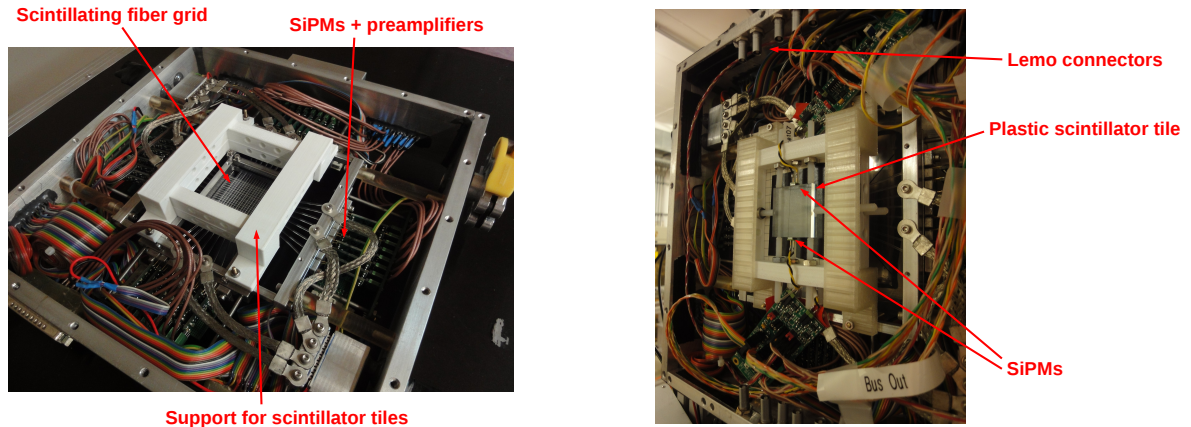


**Figure 8.3:** Left: picture of the scintillating fiber detector with support structure for the plastic scintillator tiles on top of the fiber grid. Right: plastic scintillator tiles mounted on top of the fiber grid with  $3 \times 3 \text{ mm}^2$  SiPMs attached. A black sheet is inserted between the two tile layers to avoid cross-talk.

## 8.2 The SciTil-SiPM prototype

The SciTil-SiPM prototype was integrated into a scintillating fiber detector [68], which had been designed originally as a prototype for beam profile monitoring and tracking in FOPI [69] and AMADEUS [70] experiments. The fiber detector consists of 32 square shaped scintillating fibers (Saint-Gobain<sup>2</sup> BCF-12) with an area cross-section of  $1 \text{ mm}^2$ , arranged in two planes of 16 fibers each for x-y position resolution. With 2 mm fiber pitch, a total area of  $3.2 \text{ cm} \times 3.2 \text{ cm}$  is covered. The fibers are read-out with Hamamatsu MPPCs with  $1 \times 1 \text{ mm}^2$  sensitive area (S10362-11-050U). Fig. 8.3 shows a picture of the scintillation fiber detector. During the beam test we used only 16 fibers (8 in x-direction, 8 in y-direction), disregarding every second fiber, resulting in a pitch of 4 mm.

On top of the fiber grid, two plastic scintillator tiles were mounted and read-out with two  $3 \times 3 \text{ mm}^2$  SiPMs each. The scintillators and photodetectors were fixed with small plastic screws, so that they could be easily exchanged. The SiPMs were coupled to the scintillator tiles using BC-630 optical grease. A thin black sheet was inserted between the two tile layers to avoid optical cross-talk between the two scintillators. Fig. 8.3 shows a

<sup>2</sup>Saint-Gobain Crystals, <http://www.crystals.saint-gobain.com>

picture of the scintillator tiles mounted inside the scintillating fiber detector, on top of the 2-dimensional fiber grid.

The SiPM signals were amplified with Photonique Amp-0604 preamplifiers [39] with a rise time of about 2 ns. The DC supply voltage was set to 5 V. The whole detector was enclosed in a light tight Aluminum box with LEMO feedthroughs, as shown in Fig. 8.3. We did not include cooling for the photodetectors, the temperature inside the JESSICA hall was about 12°C during night when the data were taken.

### 8.2.1 Data acquisition

For the SciTil-SiPM setup the analog waveforms were digitized with a CAEN V1742 Waveform Digitizer (32 channels, 5 Gs/s) and stored for offline data analysis. In total, we recorded 16 channels of the beam profile monitor, 4 channels of the SciTil tiles and 6 channels of the trigger scintillators. The trigger for the V1742 was realized by performing a coincidence logic between the logic signals of the three large plastic scintillators SCI1, SCI2 and SCI3. The individual signals were delayed in a way that the trigger time was always defined by SCI3. A veto signal of 1 ms length was used to protect the trigger. The trigger rate with the V1742 was typically 200 Hz. The data were analyzed by performing a full waveform analysis, as described in the next section.

### 8.2.2 Data analysis

The V1742 data were analyzed by performing a waveform analysis, which permits a lot of freedom in analysis since all parameters, e.g. threshold settings, can be easily changed during analysis and basically all necessary information can be extracted from the digitized waveforms. The raw data were converted and stored into so-called ROOT Trees, that can easily be accessed and handled within ROOT [71]. In the following, it will be discussed how the necessary information is extracted from the data and what kind of information is used to finally determine the time resolution of the plastic scintillator tiles. This will

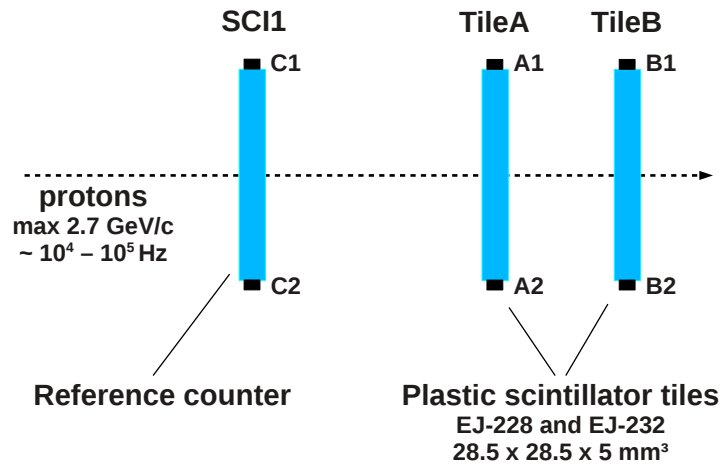


**Figure 8.4:** Schematic of the SciTil-SiPM test beam setup. The two scintillator tiles were read-out with two SiPMs each (A1, A2 and B1, B2). The scintillator SCI1 was read-out with two PMTs (C1 and C2). In reality, the scintillator tiles and the reference counter do not have the same size. SCI1 was much larger.

be done on the basis of an example run, i.e. a special condition during a night of beam time.

The setup as it has been used during the beam test can be drawn schematically as illustrated in Fig. 8.4. For discussion, we choose a run condition where the scintillation counter A was composed of an EJ-228 scintillator read-out with two Hamamatsu MPPCs (S12572-050P), and counter B of two KETEK SiPMs (PM3350TS) attached to an EJ-232 scintillator. Both tiles had a size of  $28.5 \times 28.5 \times 5 \text{ mm}^3$ .

The MPPCs were operated 1.3 V above the breakdown voltage, which corresponds to bias voltages of 64.6 V and 64.7 V, respectively, resulting in a single cell amplitude of 6.7 mV. The KETEK devices were operated 2 V above breakdown, corresponding to 28.8 V and 29.3 V, respectively, resulting in a single cell amplitude of about 3.6 mV. The proton beam momentum was 2.738 GeV/c and the intensity about 40 kHz.

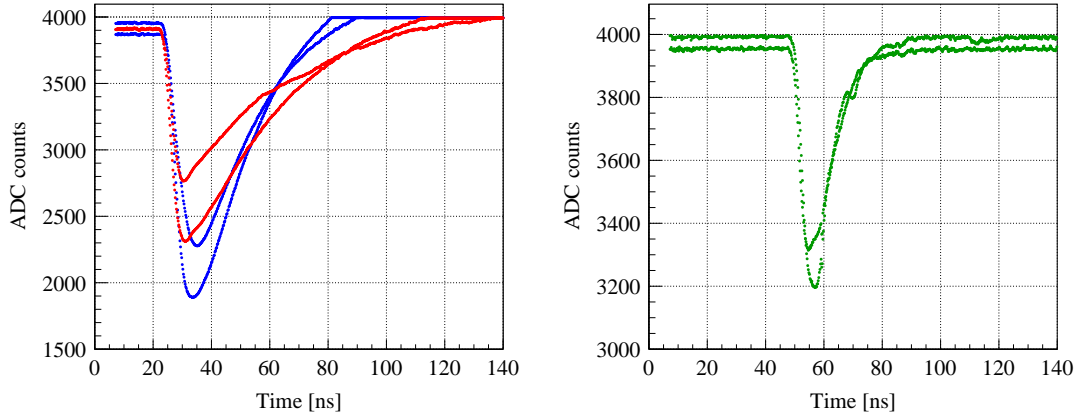


**Figure 8.5:** Photodetector output signals for a single trigger acquired with the V1742 waveform digitizer. Left: signals of two Hamamatsu S12572-050P MPPCs (blue) and two KETEK PM3350TS SiPMs (red) attached to EJ-228 and EJ-232 plastic scintillator tiles, respectively. Right: PMT output signals of the reference counter SC11.

### Signal pulse height and number of detected photons

Fig. 8.5 shows an example of the photodetector signals for a single trigger acquired with the V1742 waveform digitizer using the above settings. The left plot in Fig. 8.6 shows the corresponding pulse height spectra after baseline correction and analyzing a large number of events. Although the amplified photodetector output signals are negative, the pulse height is given by convention as a positive number. The distributions are quite broad due to statistical fluctuations of the energy loss in the plastic scintillators. For the SiPM signals, one can observe a peak at 950 mV and no events with higher pulse heights. This is due to the finite input range of the V1742 which is limited to 1 Vpp. However, the start value can be adjusted by the user between  $\pm 1$  V, for positive and negative signals. In our case, the range was set between +50 mV and -950 mV, meaning that for signals larger than 950 mV there is no pulse height information available.

Looking at the average number of detected photons (Fig. 8.6 right), one can see that about a factor 1.3 more photons could be detected with the KETEK SiPM. The number of detected photons depends on the PDE of the photodetectors within the wavelength range emitted by the scintillators. The KETEK SiPMs are optimized for maximum efficiency in

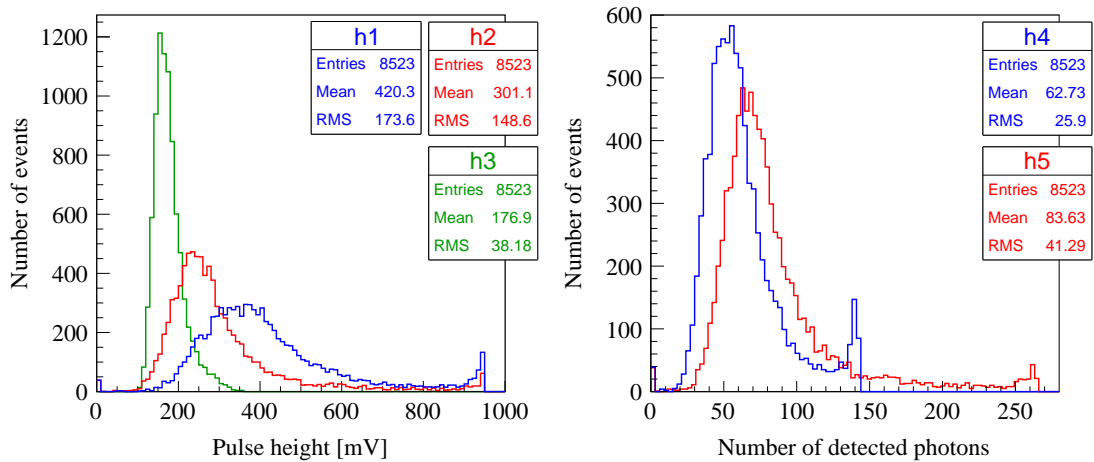


**Figure 8.6:** Left: pulse height spectra measured with photodetectors A1 in blue (Hamamatsu MPPC), B1 in red (KETEK SiPM) and C1 in green (PMT). Due to the finite input range of the V1742, the maximum measurable pulse height is limited to 950 mV. The entries below 20 mV correspond to dark-count and noise events. Right: photon spectra measured with photodetectors A1 in blue (Hamamatsu MPPC) and B1 in red (KETEK SiPM). Knowing the single cell amplitude we can convert the measured pulse heights into an approximate number of detected photons.

the blue wavelength range, while the spectral sensitivity of Hamamatsu MPPCs is shifted more towards higher wavelengths. It is difficult to compare absolute PDE values of the two devices since these values are strongly depending on the operating parameters.

### Threshold crossing time

The time resolutions of the individual scintillation detectors can be determined from multiple TOF measurements, as discussed in detail in Appendix A.2. In order to measure the TOF, we need the trigger time stamps of the three individual counters, which are given by the threshold crossing times of the photodetector signals ( $T_{A1}$  and  $T_{A2}$ ,  $T_{B1}$  and  $T_{B2}$ ,  $T_{C1}$  and  $T_{C2}$ ) as:

$$\begin{aligned}
 T_{\text{TileA}} &= \frac{1}{2}(T_{A1} + T_{A2}) \\
 T_{\text{TileB}} &= \frac{1}{2}(T_{B1} + T_{B2}) \\
 T_{\text{SCI1}} &= \frac{1}{2}(T_{C1} + T_{C2})
 \end{aligned} \tag{8.1}$$

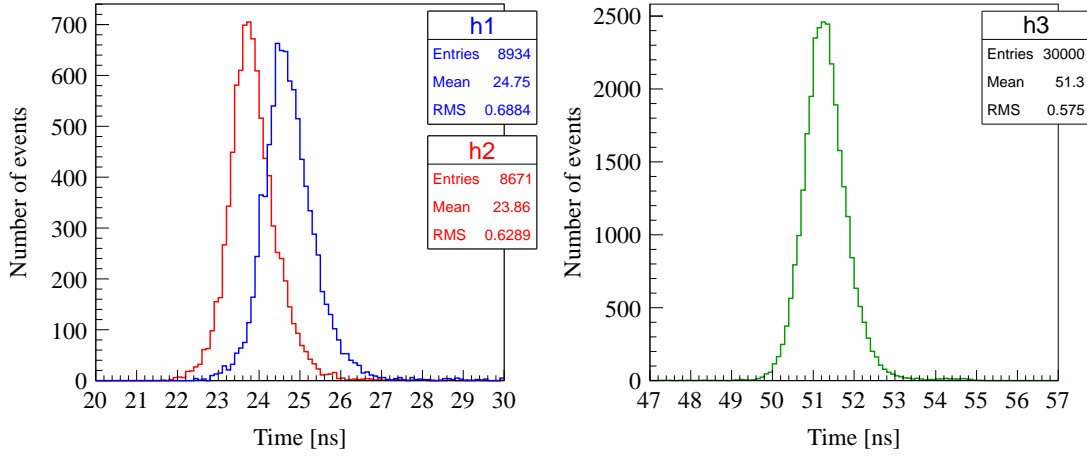


**Figure 8.7:** Threshold crossing times  $T_{A1}$  (blue),  $T_{B1}$  (red) and  $T_{C1}$  (green) at 40 mV level of photodetectors A1 (Hamamatsu MPPC), B1 (KETEK SiPM) and C1 (PMT).

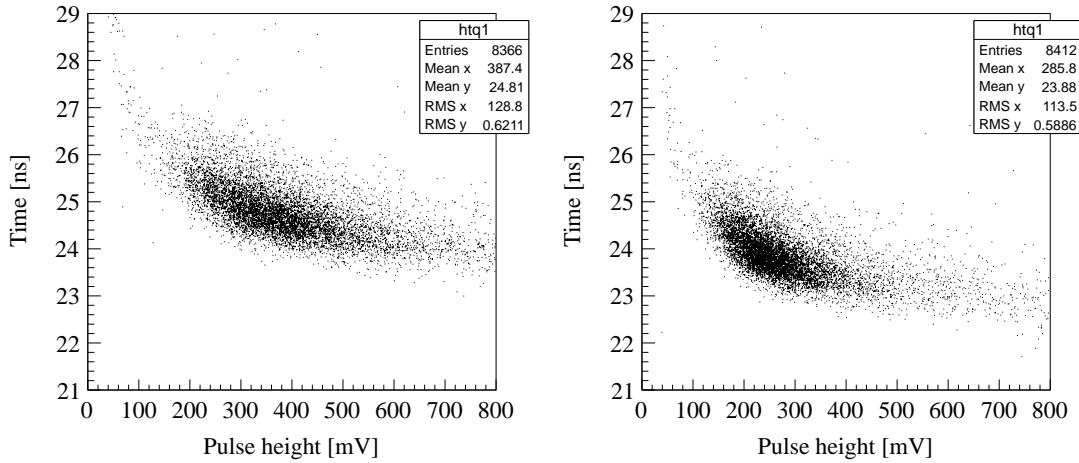


**Figure 8.8:** Correlation between threshold crossing time and pulse height at 40 mV threshold level for detectors A1 (left, Hamamatsu MPPC) and B1 (right, KETEK SiPM). Due to the simple LE triggering there is a strong correlation (time walk).

In a first analysis, a simple leading edge (LE) triggering was used. The threshold was set to 40 mV, which is well above the noise level and equivalent to about 6 single cell amplitudes in case of the MPPCs, and about 11 single cell amplitudes for the KETEK SiPMs. Fig. 8.7 shows the corresponding threshold crossing times of the photodetector signals ( $T_{A1}$ ,  $T_{B1}$  and  $T_{C1}$ ).

We can plot now the threshold crossing time as a function of the pulse height in order to



see the correlation between the two observables, as shown in Fig. 8.8 for Hamamatsu and KETEK devices. Due to the simple LE triggering there is a strong correlation, i.e. time walk. One can notice that the effect is increased in case of the KETEK SiPM due to the higher threshold, relative to the pulse height. Therefore, the time walk is enhanced. In any case, one should aim for correcting the time walk in order to achieve the best possible time resolution.

### **Time walk correction**

In order to correct for the time walk effect one can simply use the pulse height information and its relation to the threshold crossing time. Fig. 8.9 and Fig. 8.10 show the correction for Hamamatsu and KETEK detectors, respectively. Looking at the RMS of the threshold crossing time histograms before and after correction one can see a drastic improvement in time precision.

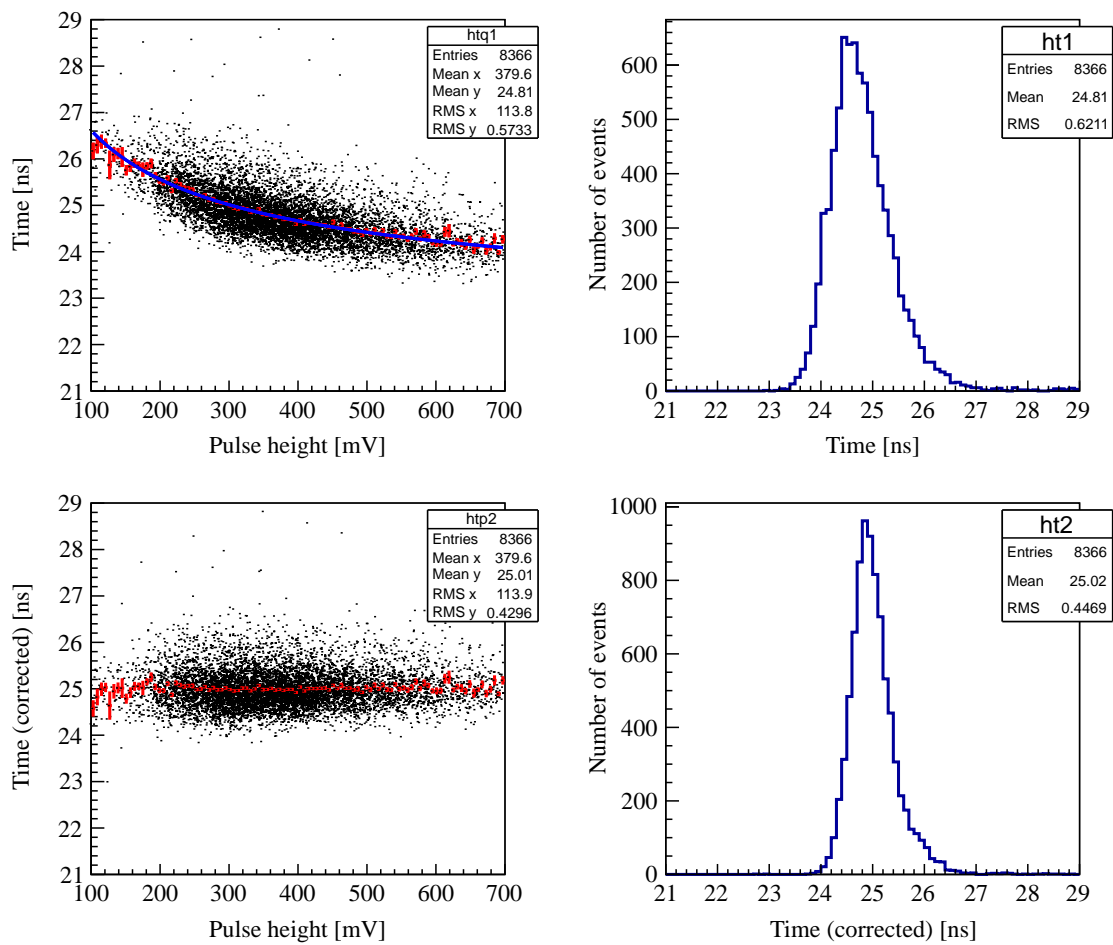


**Figure 8.9:** Time walk correction for Hamamatsu MPPC using pulse height information. Top: uncorrected histograms. Bottom: corrected histograms.

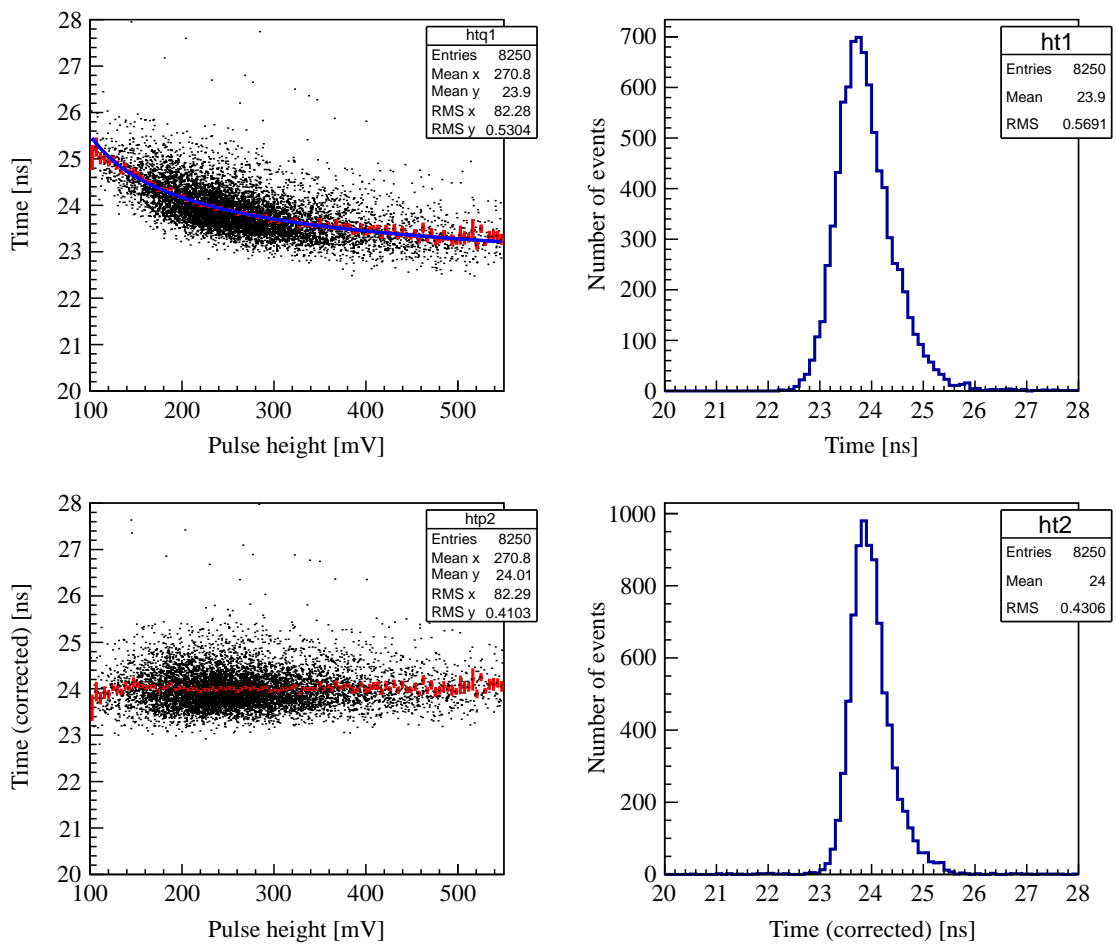


**Figure 8.10:** Time walk correction for KETEK SiPM using pulse height information. Top: uncorrected histograms. Bottom: corrected histograms.

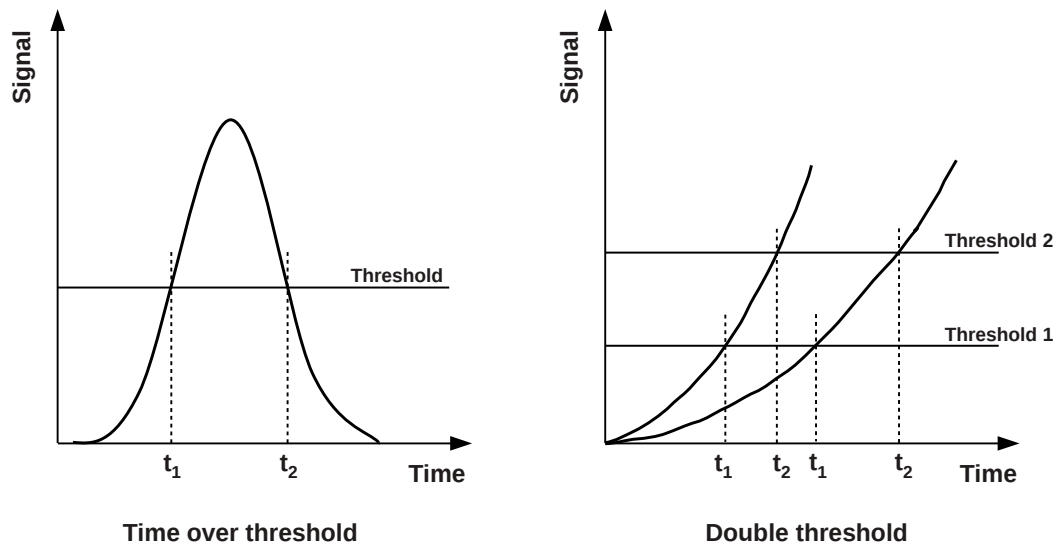
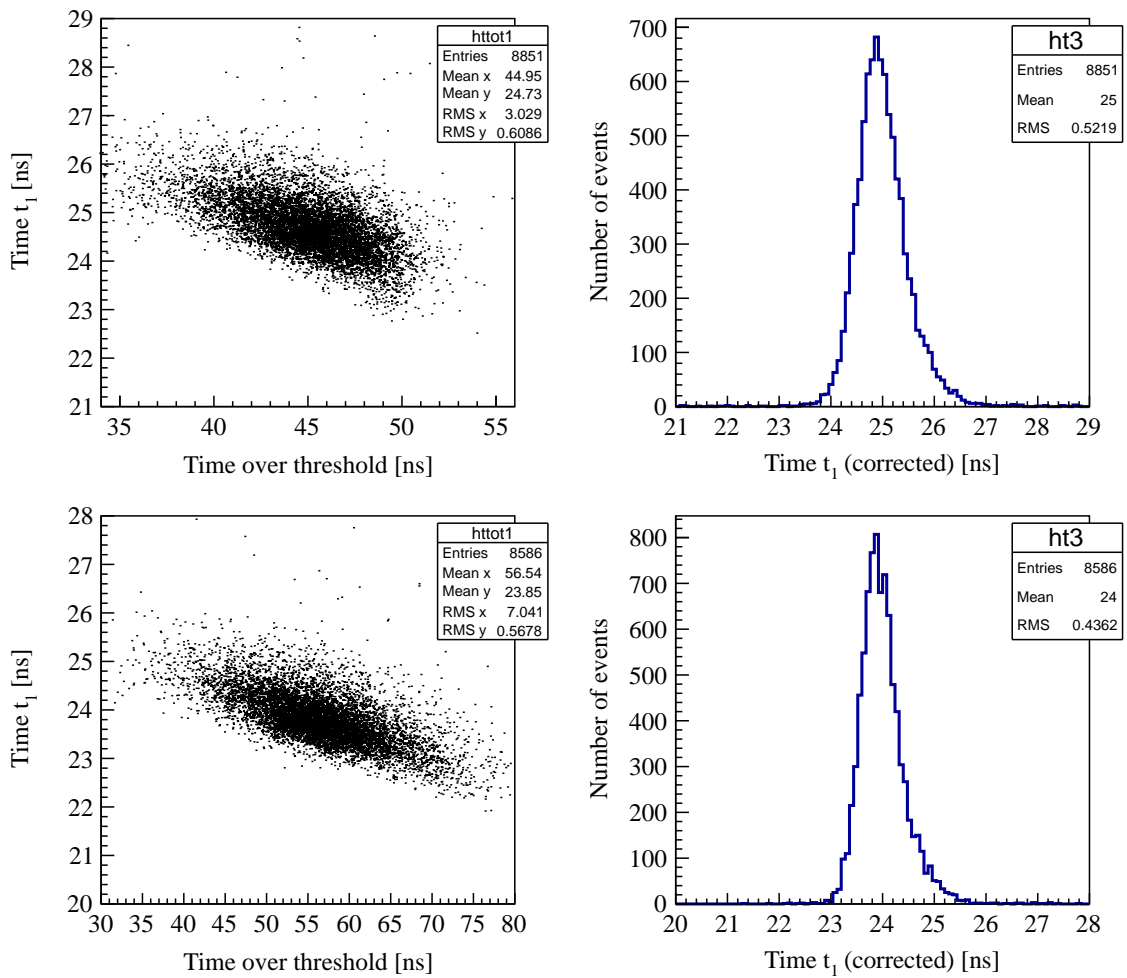


**Figure 8.11:** Left: Time-over-threshold technique. The TOT  $t_2 - t_1$  is proportional to the pulse height. Right: double threshold technique. The threshold crossing time difference  $t_2 - t_1$  is a measure for the signal rise time.

Since the pulse height information might be not available due to the limited range of the V1742 digitizer, one could think of other ways to correct for the observed time walk. Firstly, one could measure the time-over-threshold (TOT) to determine the pulse width, which is usually proportional to the pulse amplitude and signal charge. A schematic of the TOT technique is illustrated on the left in Fig. 8.11. The correlation between TOT and threshold crossing time  $t_1$  can be used to correct for time walk.

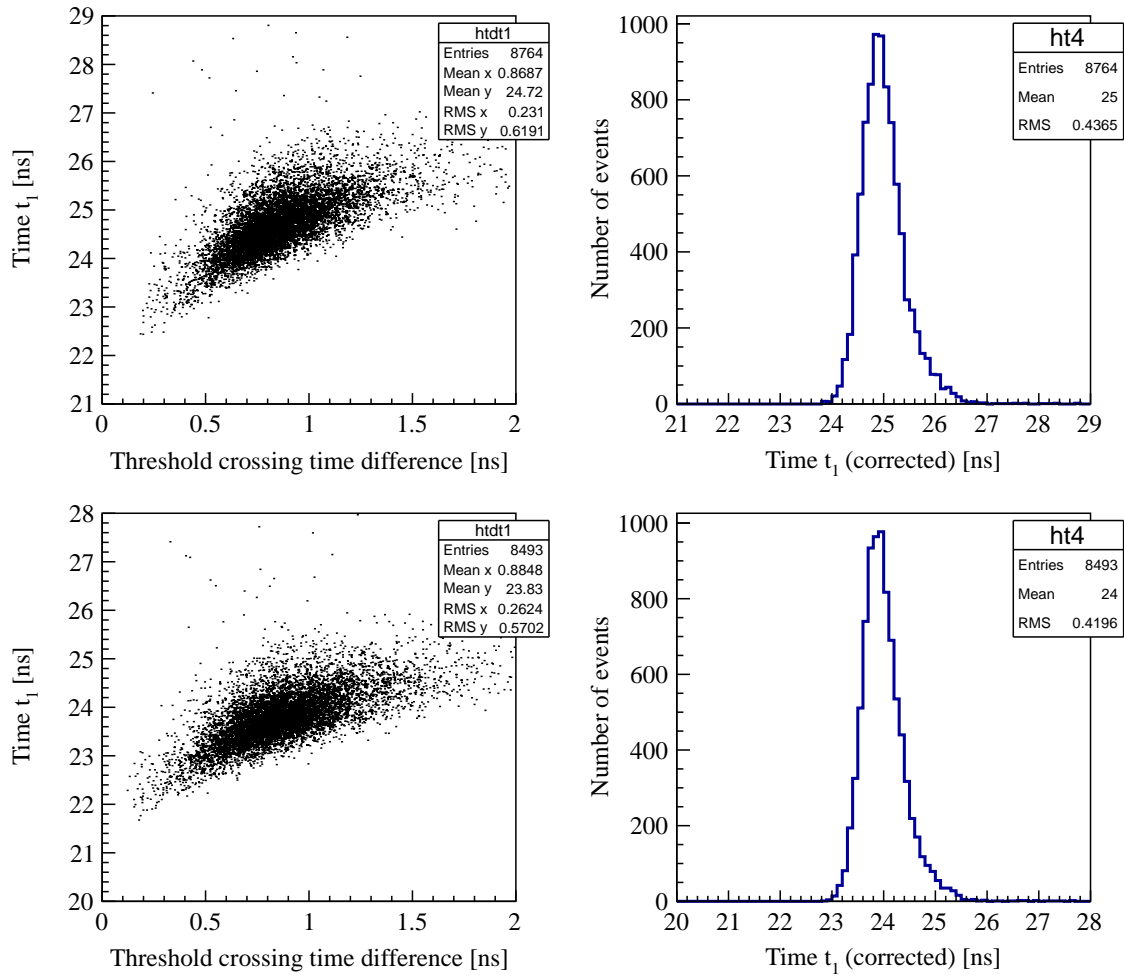
Another way to correct for the time walk is to apply a double threshold to the signal and determine the threshold crossing time difference to evaluate the signal rise time. The idea is shown schematically on the right of Fig. 8.11. In our case Threshold 1 = 40 mV and Threshold 2 =  $2 \times$  Threshold 1. For the correction, the correlation between the difference in threshold crossing times  $t_2 - t_1$  and the threshold crossing time  $t_1$  is used.

Fig. 8.12 and Fig. 8.13 show the correlations that were used to correct for time walk as well as the corrected threshold crossing time histograms for Hamamatsu and KETEK devices. The results show that the time walk correction drastically improves the RMS of the timing



**Figure 8.12:** Time walk correction using Time-over-Threshold information for Hamamatsu MPPC (top) and KETEK SiPM (bottom). Left: uncorrected correlation between  $TOT\ t_2 - t_1$  and threshold crossing time  $t_1$ . Right: corrected threshold crossing time histograms.

histograms, i.e. the time precision, compared to the uncorrected values in Fig. 8.9 and Fig. 8.10. The best results can be achieved using pulse height information or applying a double threshold. Especially for the Hamamatsu MPPC signals, the TOT technique shows the least improvement. Using a double threshold an improvement of about 30% and 26% can be achieved for Hamamatsu MPPCs and KETEK SiPMs, respectively.



**Figure 8.13:** Time walk correction using a double threshold for Hamamatsu MPPC (top) and KETEK SiPM (bottom). Left: uncorrected correlation between the difference in threshold crossing times  $t_2 - t_1$  and the threshold crossing time  $t_1$ . Right: corrected threshold crossing time histograms.

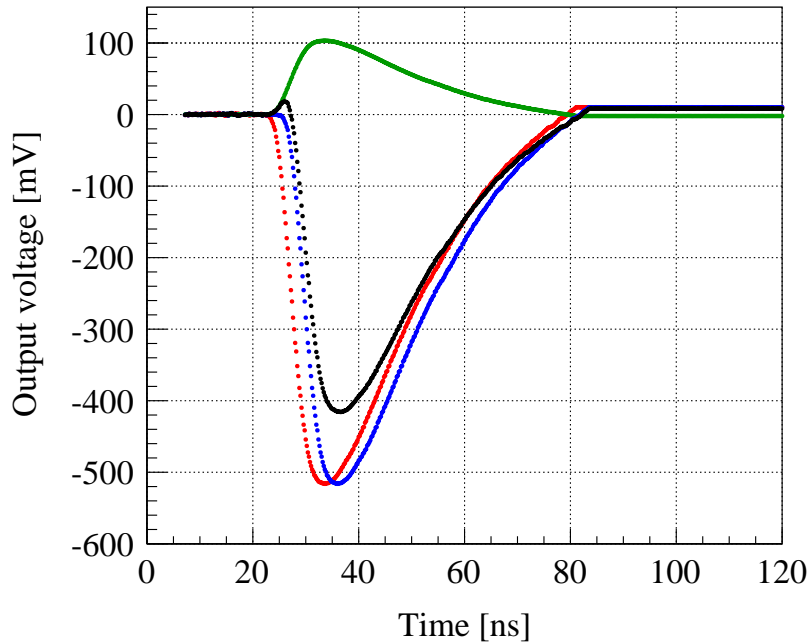


**Figure 8.14:** Constant fraction discriminator input and output pulses. The red input signal is delayed (blue curve) and added to an attenuated inverted signal (green), resulting in a bipolar output pulse (black). The zero crossing defines the CFD timing. In this example, the input signal is delayed by 2.4 ns and attenuated by multiplying with a factor 0.2.

As another option we can consider to use constant fraction triggering in order to avoid time walk at all. Not to be dependent on the pulse height, we can implement the basic functionality of a CFD by software as explained in the following. The input signal is split into two parts. One signal is delayed, the other signal gets attenuated and inverted. Finally, the two signals are summed up again, resulting in a bipolar output pulse. The CFD timing  $t_{CFD}$  is defined by the point of zero crossing of this pulse. Fig. 8.14 shows the CFD signals corresponding to a single event acquired with the waveform digitizer.

In order to compare this method with the time walk correction, we apply the constant fraction triggering to the run that has been analyzed before. Fig. 8.15 shows the resulting threshold crossing time histograms. The improvements are similar to the best results obtained before. For the Hamamatsu MPPCs the improvement in time precision is about 28 %, for the KETEK SiPMs about 25 %.

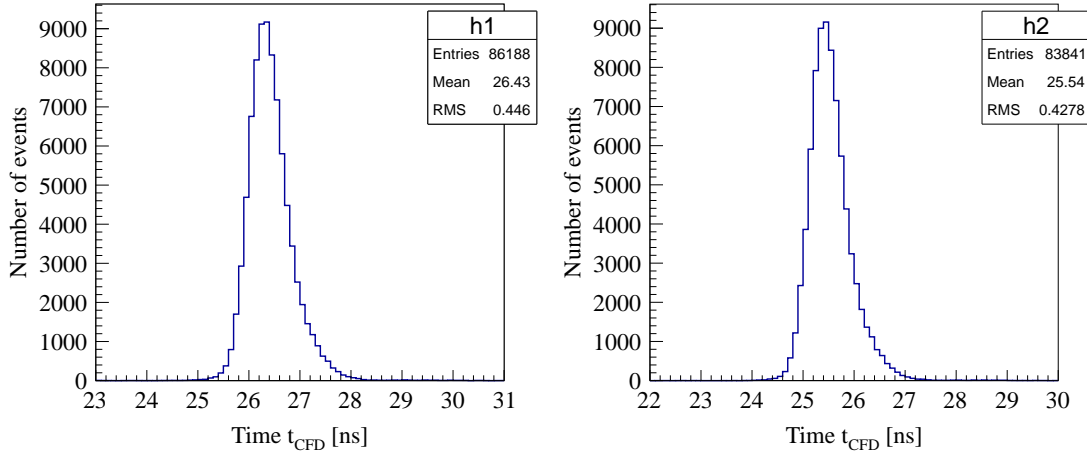


**Figure 8.15:** CFD threshold crossing time  $t_{CFD}$  for Hamamatsu MPPC (left) and KETEK SiPM (right). For the Hamamatsu device the CFD delay was set to 2.2 ns and the attenuation factor to 0.15. In case of the KETEK SiPM, a delay of 2 ns and an attenuation factor of 0.2 was used.

Unless otherwise noted, the CFD method is used for further analysis. The CFD parameters (delay and attenuation) are optimized for different run conditions (SiPM type, operating parameters, etc.) by performing parameter scans. Typical parameter values are delays of 1 ns–2 ns and attenuation factors between 0.1 and 0.25. The constant fraction triggering simplifies the analysis since an additional step for time walk correction can be skipped. The method is also working in case the pulse height information is not available.

### Time resolution

Having determined the threshold crossing times of the individual photodetector signals, we can now evaluate the trigger times in Eq. 8.1 and consequently the three TOFs given by:

$$\begin{aligned}
 T_{\text{TileA-TileB}} &= T_{\text{TileB}} - T_{\text{TileA}} \\
 T_{\text{TileA-SCI1}} &= T_{\text{SCI1}} - T_{\text{TileA}} \\
 T_{\text{TileB-SCI1}} &= T_{\text{SCI1}} - T_{\text{TileB}}
 \end{aligned}
 \tag{8.2}$$

The corresponding TOF resolutions with associated errors can then be determined by fitting the TOF distributions with a Gaussian function, as demonstrated in Figure 8.16.



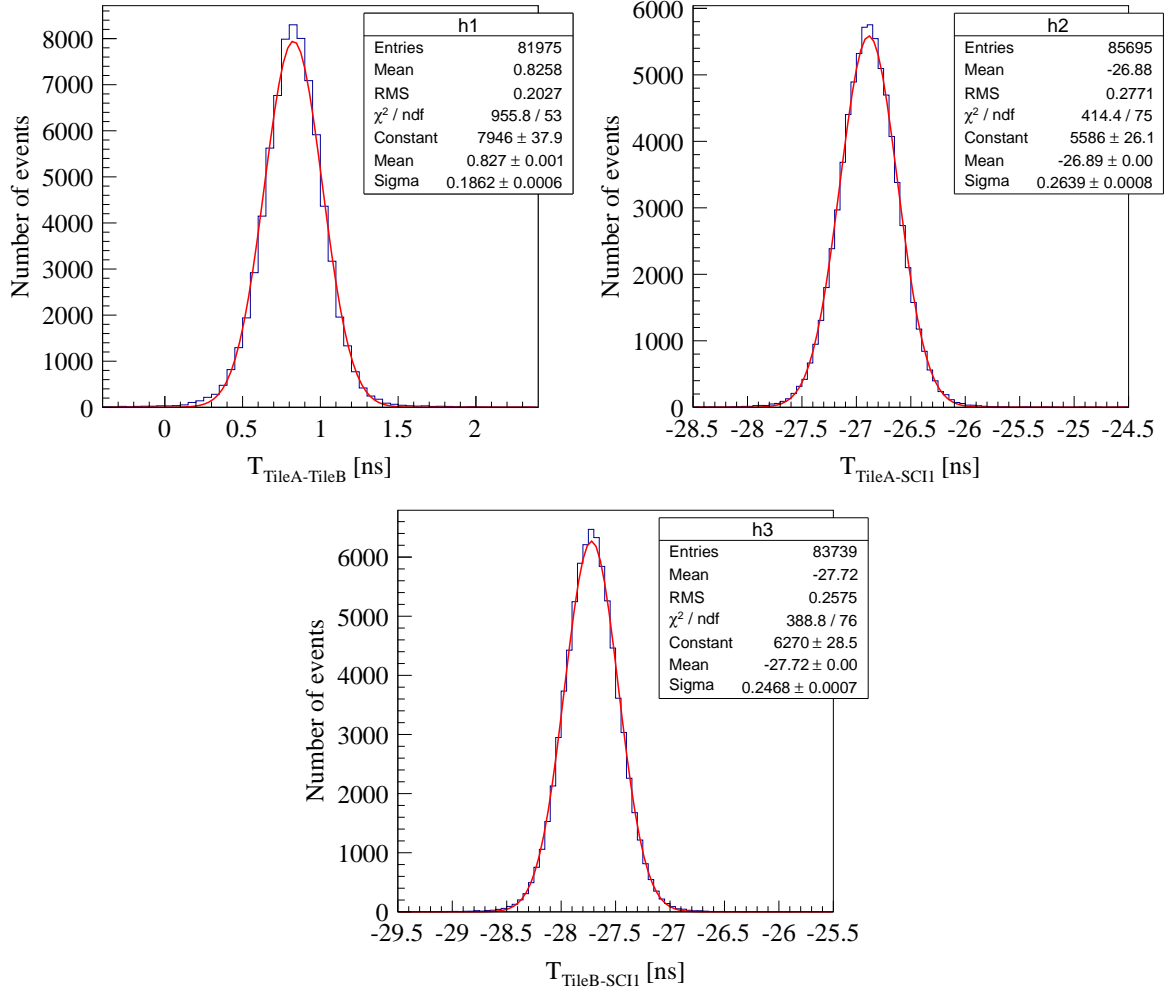


**Figure 8.16:** Time-of-flight measured between different scintillation counters.

The three TOF resolution are given by:

$$\begin{aligned}
 \sigma_{\text{TileA-TileB}} &= 186.2 \pm 0.6 \text{ ps} \\
 \sigma_{\text{TileA-SCI1}} &= 263.9 \pm 0.8 \text{ ps} \\
 \sigma_{\text{TileB-SCI1}} &= 246.8 \pm 0.7 \text{ ps}
 \end{aligned}
 \tag{8.3}$$

As shown in Appendix A.2, the intrinsic time resolution of the individual scintillation counters can be determined by performing a  $\chi^2$  minimization. With the above values as input for the minimization, we obtain the following time resolutions for the two scintillator tiles read-out with two Hamamatsu MPPCs (TileA) and two KETEK SiPMs (TileB),

respectively, and the scintillation counter SCI1:

$$\begin{aligned}
 \sigma_{\text{TileA}} &= 147.3 \pm 1.0 \text{ ps} \\
 \sigma_{\text{TileB}} &= 113.9 \pm 1.3 \text{ ps} \\
 \sigma_{\text{SCI1}} &= 219.0 \pm 0.7 \text{ ps}
 \end{aligned}
 \tag{8.4}$$

### 8.2.3 Results

The data analysis procedure described in the previous section has been applied to the whole data set, including varying beam conditions and operating parameters, different photodetector types, different scintillator tile configurations, etc. The final results on the time resolution of the scintillator tiles are summarized in Fig. 8.17 and Fig. 8.18.

Looking at the two figures, one can realize that the tile time resolution is strongly depending on the operating voltage applied to the photodetectors, while the scintillator material has only less influence. Using Hamamatsu MPPCs for read-out (see Fig. 8.17), a time resolution slightly below 100 ps sigma could be achieved employing the S12572-025C type

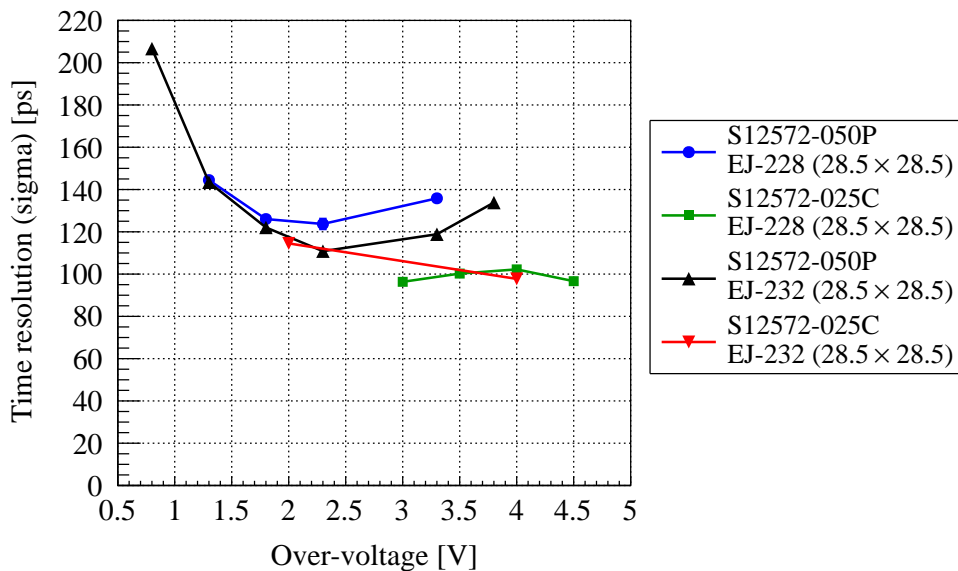


**Figure 8.17:** Final results on the time resolution of various plastic scintillator tiles read-out with two Hamamatsu MPPCs of different type. The lines are added to guide the eye.

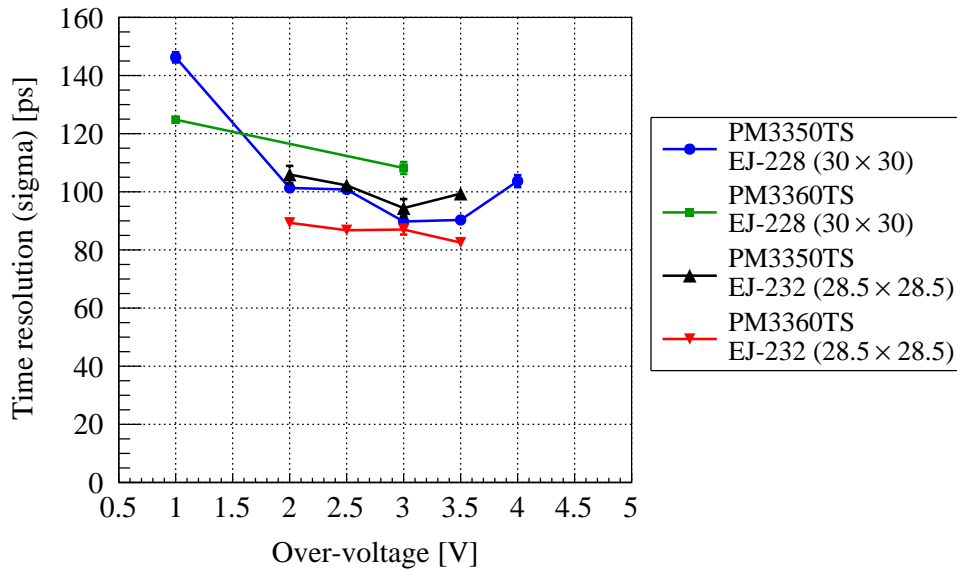


**Figure 8.18:** Final results on the time resolution of various plastic scintillator tiles read-out with two KETEK SiPMs of different type. The lines are added to guide the eye.

with  $25 \times 25 \mu\text{m}^2$  cell size. The best value that could be reached is  $\sigma = 96.3 \pm 0.9 \text{ ps}$  with an EJ-228 scintillator. Using an EJ-232 scintillator shows a nearly identical result. In case of the S12572-050P a characteristic trend of the time resolution as a function of the applied over-voltage can be seen. Increasing the bias voltage raises the gain and improves the time resolution, but on the other hand increases the influence of dark-noise, cross-talk and after-pulses, which deteriorate the time resolution. For the S12572-25C type there are not enough data points to confirm this behavior.

Fig. 8.19 shows the PDE of the tested MPPCs. According to the data sheet, the PDEs of the two types are quasi identical at a certain operating voltage, which is indicated in the plot. Therefore, it seems that the difference in performance between the two MPPC types originates from the intrinsic timing resolution of the devices. The detector type with smaller pixel size can be expected to be faster due to a smaller cell capacitance.

The scintillator tiles read-out with KETEK SiPMs show in general a better time resolution (see Fig. 8.18). For larger variations in the operating voltage one can see again the same characteristic behavior of the time resolution as discussed before. Except for the

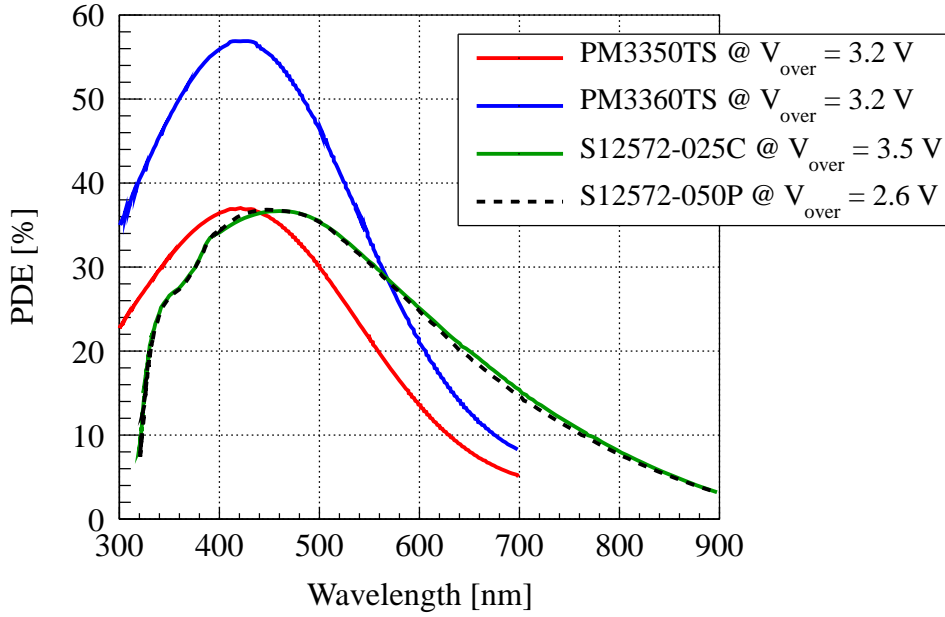


**Figure 8.19:** PDE curves of Hamamatsu MPPCs and KETEK SiPMs at typical operating voltages. The curves are taken from the data sheets [41, 42, 43].

PM3360TS type in combination with an EJ-228 scintillator all configurations show a time resolution below 100 ps sigma. The best value that could be achieved is  $\sigma = 82.5 \pm 1.7$  ps with PM3360TS sensors attached to an EJ-232 plastic scintillator.

The difference in timing performance between the two SiPM types is rather small and may be also related to the PDE of the two devices at the used operating voltages, which is shown in Fig. 8.19. The reason for the large variation in time resolution among the same type of SiPM (PM3360TS) attached to different scintillators is not quite clear, however, especially in case of the configuration using the EJ-228 scintillator there are too few data points available to draw a conclusion from that.

The above results have been obtained using constant fraction triggering. In this case, the threshold crossing time is defined as the time of zero crossing of the bipolar output signal, leading to reduced time walk. In order to achieve the best time resolution, the CFD parameters, i.e. delay time and attenuation factor, were optimized, which can be seen as a sort of threshold optimization. It has been shown already in Chapter 7 how

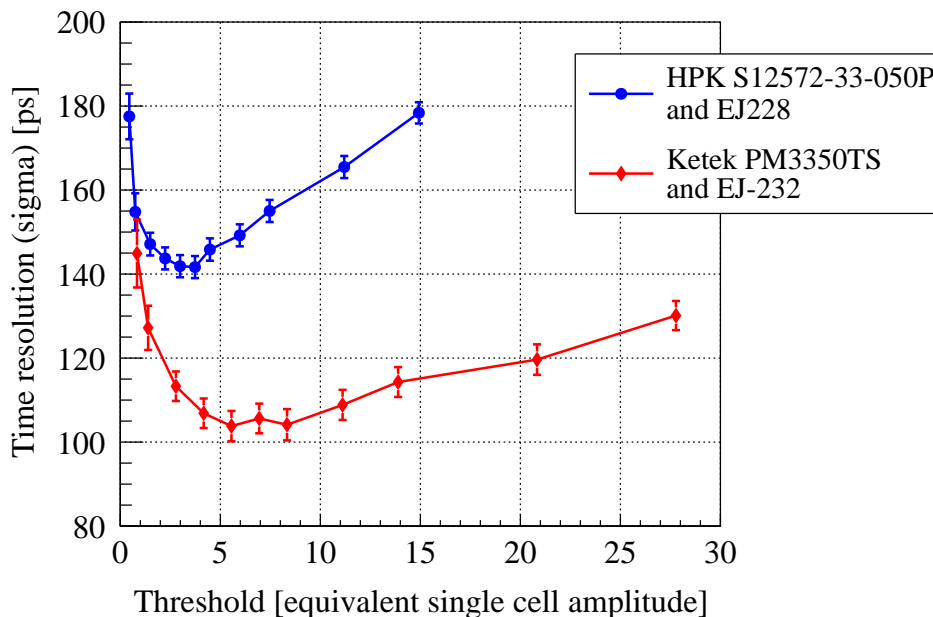


**Figure 8.20:** Dependency of the tile time resolution on the applied threshold. Results have been obtained with LE triggering and subsequent time walk optimization using pulse height information.

the threshold settings can influence the time resolution and that such an optimization is a crucial point to achieve ultimate timing performance. In order to illustrate again the impact of the threshold settings, the run discussed in Section 8.2.2 has been analyzed, using LE triggering in combination with a time walk correction and varying the threshold. Fig. 8.20 shows the tile time resolution as a function of the applied threshold.

The plot shows that the threshold has to be optimized in order to achieve the best time resolution. It also depicts that oftentimes triggering on the first photons does not provide the best time resolution in a scintillation detector, as it is also presented in Ref. [62] or Ref. [64]. As already discussed in more detail in the previous chapter, the observed trend of the tile time resolution is a consequence of the interplay between the scintillator time resolution, the SiPM and electronics time response and electronics noise. In this context, the locations of the minima in Fig. 8.20 depend on the photon counting statistics, which is not the same for the two used scintillators, as well as on the time response of the two different photodetectors.

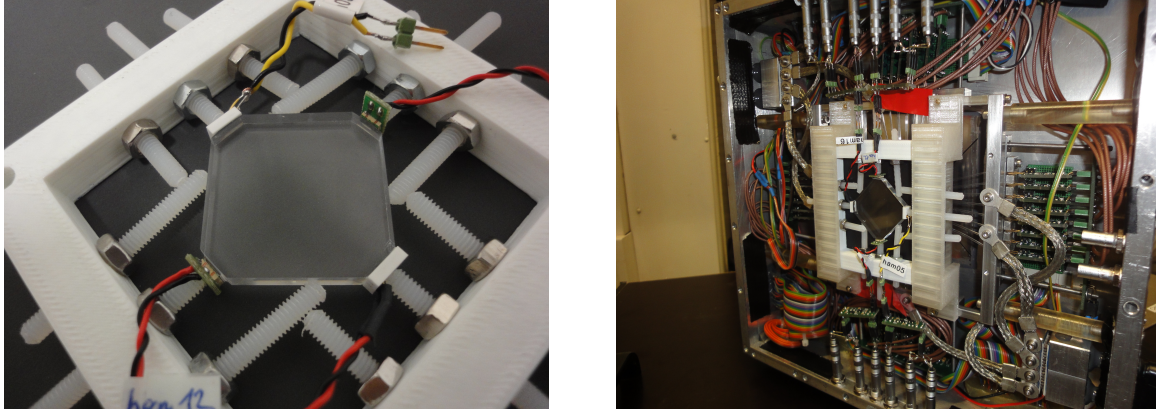


**Figure 8.21:** Pictures of a modified *SciTil-SiPM* setup, using four SiPMs attached to an EJ-228 plastic scintillator. Left: Hamamatsu MPPCs with read-out cables attached to the scintillator and mounted in the support frame. The scintillator edges were cut to attach the photodetectors. Right: the plastic scintillator tile mounted inside the Aluminum box.

The deterioration of the time resolution at low thresholds is due to electronics noise and secondly due to the SPTR of the SiPM. On the other hand, the rise in time resolution at high thresholds is caused by the scintillator time resolution. Comparing the minimum time resolution in Fig. 8.20 with the values obtained before using a CFD (see Eq. 8.4), one can realize once again that the two methods show nearly identical results. As already noted, one should keep in mind that a threshold which is equivalent to e.g. 5 single cell amplitudes does not imply that we are triggering on the fifth detected photon. Due to a certain rise time of the signal, a higher number of photons is already piled up until the signal reaches the 5 p.e. threshold. Furthermore, the number of photons detected prior to the time of threshold crossing fluctuates from event to event and is not unique.

In the analysis, the tile trigger times have been defined by using the threshold crossing times of the respective photodetector signals, as given by Eq. 8.1. In order to study the influence of the number of used time stamps, i.e. threshold crossing times, on the time resolution, a setup as shown in Fig. 8.21, attaching four SiPMs to a single scintillator tile, was used. Four Hamamatsu MPPCs with  $50 \times 50 \mu\text{m}^2$  pixel size (two S12572-050P and two S12572-050C) were attached to an EJ-228 scintillator with a size of  $28.5 \times 28.5 \times 5 \text{ mm}^2$ . The scintillator edges were cut in order to attach the photodetectors. The idea behind this symmetric arrangement was also to study the possibility of estimating the proton

hit position from the photon intensity measured with the SiPMs, which in turn could be used to correct for photon propagation. However, due to the limited range of the V1742 digitizer, pulse height information was rarely available and therefore the correction turned out to be more difficult. If one can efficiently use the TOT information or a double threshold instead is still under investigation.

With the modified setup we obtained in total four threshold crossing times for a single tile. The individual threshold crossing times were determined as usual by applying the CFD method. In the former setup, the tile trigger time was determined by calculating the mean of the two threshold crossing times of the respective photodetector signals (see Eq. 8.1). In order to investigate the effect of a multiple time stamp approach with the new setup, we sort the four threshold crossing times in ascending order and take either a single time stamp or an average of multiple time stamps to define the tile trigger time. Fig. 8.22 shows the obtained tile time resolution as a function of the number of time stamps used to estimate the tile trigger time. In the plot, a number of e.g. three used

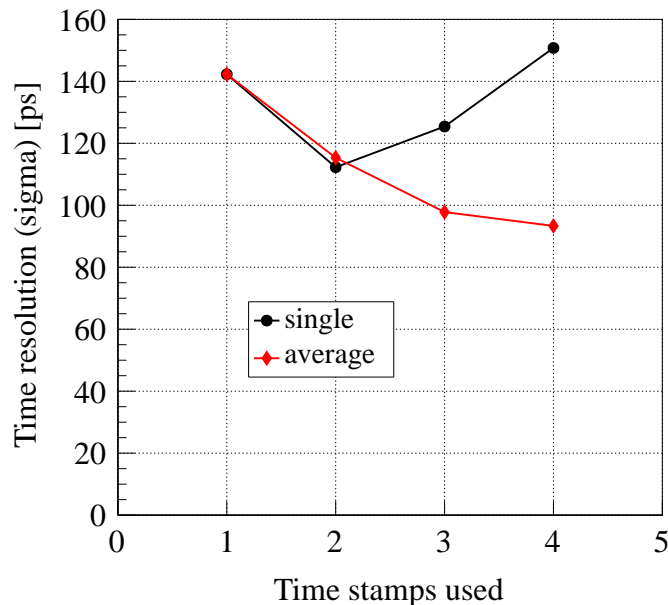


**Figure 8.22:** Tile time resolution as a function of the number of used time stamps. The tile trigger time can either be defined by using a single time stamp (*single*) or an average of multiple time stamps (*average*).

time stamps means that either the third (single) or a mean of the first three (average) threshold crossing times was used to evaluate the tile trigger time.

At first view, the plot shows that the multiple time stamp method allows to achieve better time resolution, which indicates that such a scintillation detector dedicated to fast timing should preferably make use of multiple time stamps. It is also noted, that the first order time stamp does not provide the best timing precision, as also reported in Ref. [63] and Ref. [72]. In case of the single time stamp approach, triggering on late photons leads to reduced time resolution due to the influence of photon counting statistics and photon propagation.



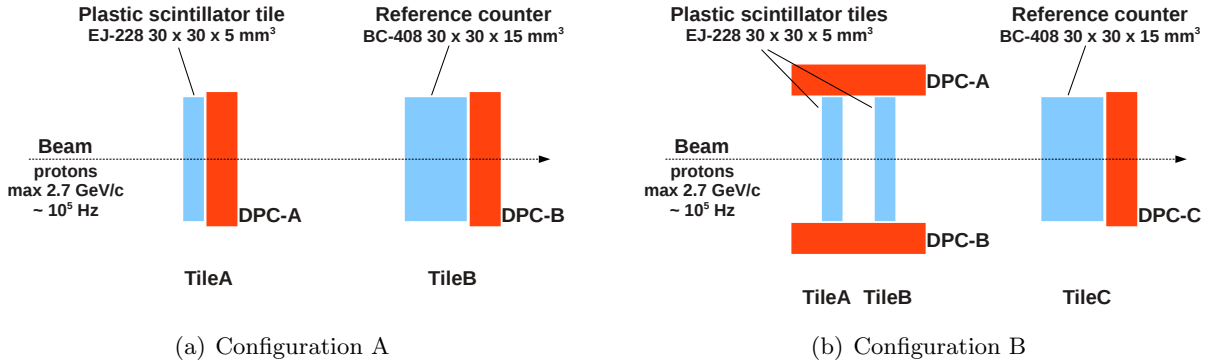


**Figure 8.23:** Schematic of the different DPC setups using either a single DPC to read-out the entire scintillator front side (configuration A) or two DPCs to read-out the rim of the scintillator (configuration B).

### 8.3 The SciTil-DPC prototype

Due to its large sensitive area, the Philips DPC allows to cover not only the whole rim of the plastic scintillator tile but also the entire front side. To exploit this advantage, we used two different setups employing the DPC. The two configurations are shown schematically in Fig. 8.23. Both configurations may be practicable for SciTil, when using the DPC as photodetector, however with a different layout fulfilling the spatial constraints in PANDA.

For both options we used a BC-408 plastic scintillator with a size of  $30 \times 30 \times 15 \text{ mm}^3$ , attached to a DPC-3200, as a reference detector. As shown in Fig. 8.24, the geometry of the scintillator was adapted to the regular die layout of the DPC by segmentation of the monolithic block, in order to get position information. The position can be roughly determined by calculating the centroid of the photon distribution measured with the DPC.

The EJ-228 tiles ( $30 \times 30 \times 5 \text{ mm}^3$ ) were either read-out from one side using a single detector (configuration A) or from two sides using two DPC-3200 sensors (configuration B), as shown in Fig. 8.23. The photodetectors were coupled to the scintillator tiles utilizing BC-630 optical grease. The DPCs were connected with flat cables to the TEK base unit and via USB to a PC. The whole setup was mounted inside a light tight box with an integrated cooling system. A combination of air-, water- and Peltier cooling was used



**Figure 8.24:** Pictures of the segmented BC-408 plastic scintillator attached to a DPC-3200. The geometry of the scintillator has been adapted to the layout of the DPC to achieve position resolution. The slits are 1 mm wide and 10 mm deep and fit the regular die pattern of the DPC. This scintillation detector was used as a reference counter.

to keep the detectors at a temperature of  $12 \pm 1^\circ\text{C}$  during operation. The DPCs were operated at 3 V over-voltage. Some pictures of the different setups are shown in Fig. 8.25.

### 8.3.1 Data acquisition

In case of the SciTil-DPC detector, we simply used the DPCshell control software [36] running on a standard Linux PC, to control, configure and operate the DPC setup and to acquire the data. As output, the DPC delivers digital photon count values and trigger time stamps for each event. The raw data were stored in text format, converted to ROOT files and further analyzed employing the ROOT framework [71].

The DPC parameter settings were done on the basis of the parameter optimization presented in the previous chapter. For most measurements and unless otherwise noted, the trigger threshold was set to 1 photon, the validation threshold to 4 photons, the validation and integration intervals to 5 ns and 45 ns respectively, and the length of the coincidence time window to 50 ns. The coincidence time was set that long to account for skew between dies, which has been corrected only afterward on acquired data. A fraction of 10 % of cells was deactivated to lower the overall dark count rate.

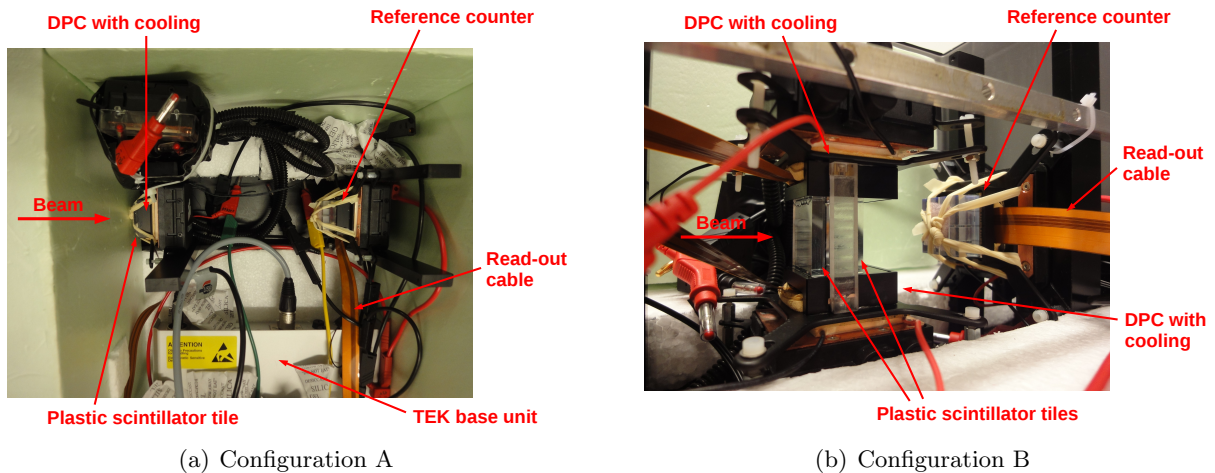


**Figure 8.25:** Pictures of the different DPC setups using either a single DPC to read-out the entire scintillator front side (configuration A) or two DPCs to read-out the rim of the scintillator (configuration B). The beam is entering from the left.

In case of configuration A in Fig. 8.23(a) all dies of both DPCs (DPC-A and DPC-B) were activated, demanding a coincidence between the two tiles (TileA and TileB) and in addition only events with coincidence hits on four or more dies were accepted. For configuration B (see Fig. 8.23(b)), only coincidences between all three tiles (TileA, TileB and TileC) with hits on three or more dies were acquired. On DPC-C all dies were activated, on DPC-A and DPC-B only two rows of pixels were activated, where the scintillator tiles were placed.

### 8.3.2 Data analysis

As a reminder, the DPC-3200 tile consists of 16 die sensors arranged in a  $4 \times 4$  matrix. Each die is further divided into 4 pixels. For every event, the DPC provides a photon count value per pixel and a time stamp per die, i.e. in total 64 photon count values and 16 time stamps, if all dies/pixels are activated. The time stamps are generated at the moment of trigger generation. The trigger is generated at the moment the photon count reaches the required trigger threshold. Thus, the time stamps can be seen in analogy to the threshold crossing times of SiPM signals studied in the previous section, and can be

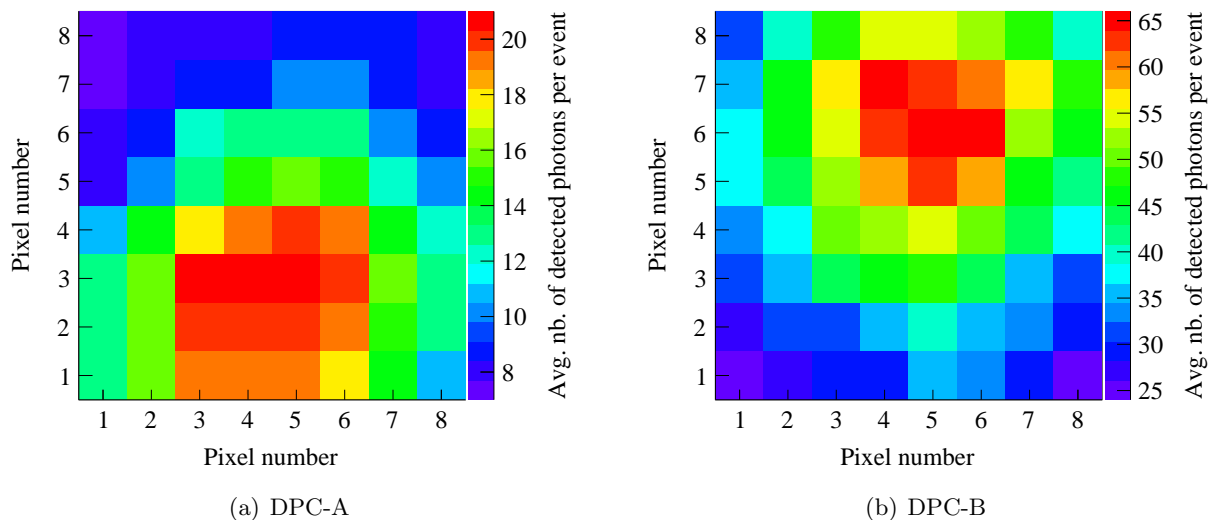


**Figure 8.26:** Average number of photons detected on individual pixels of DPC-A and DPC-B used in configuration A (see Fig. 8.23(a)).

used to determine the time resolution. Now, the difference is however that all parameters have to be adjusted before data taking and cannot be set during data analysis as before. In Chapter 7, we saw that setting the trigger threshold of the DPC to the first detected photon results in the best time resolution. Hence, this setting was used for most of the measurements.

### Number of detected photons

Fig. 8.26 shows the average number of photons detected on the individual pixels of the two DPCs used in configuration A (see Fig. 8.23(a)). The hit patterns show that the setup was slightly misaligned with respect to the beam axis by a few mm. As expected, the DPC-B detected about a factor 3 more photons than DPC-A, due to the three times thicker scintillator attached to this detector.

The total number of photons detected with the two tiles (TileA and TileB) is depicted in Fig. 8.27. The double peak structure observed with TileB is due to the segmentation of the scintillator. The second large peak corresponds to photons generated by protons hitting

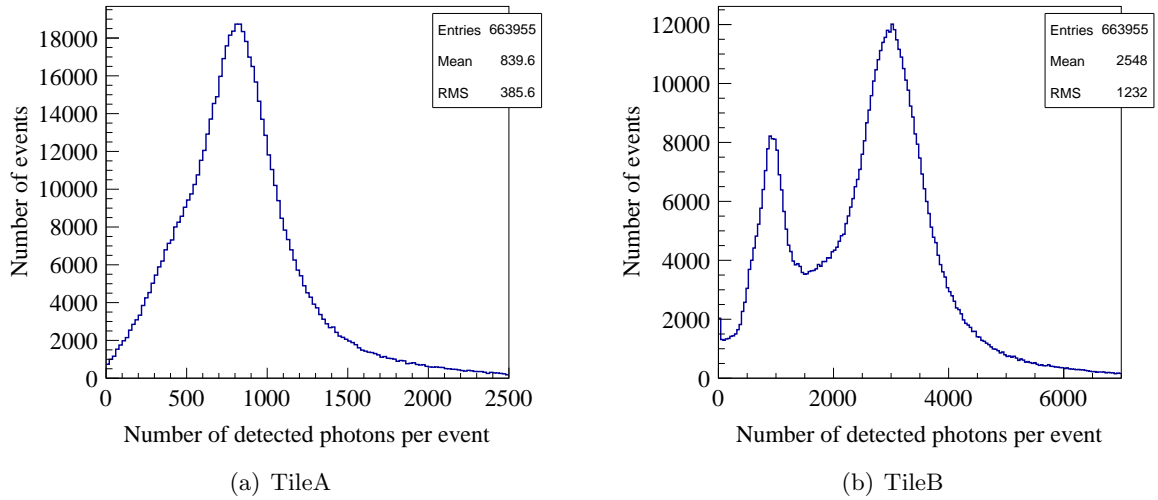
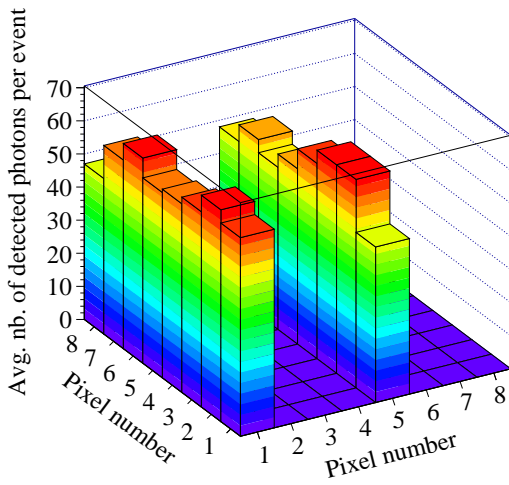


**Figure 8.27:** Total number of detected photons per event with TileA and TileB used in configuration A (see Fig. 8.23(a)). The double peak structure on the right is due to the segmentation of the scintillator. The small peak at low photon numbers is due to dark count events.

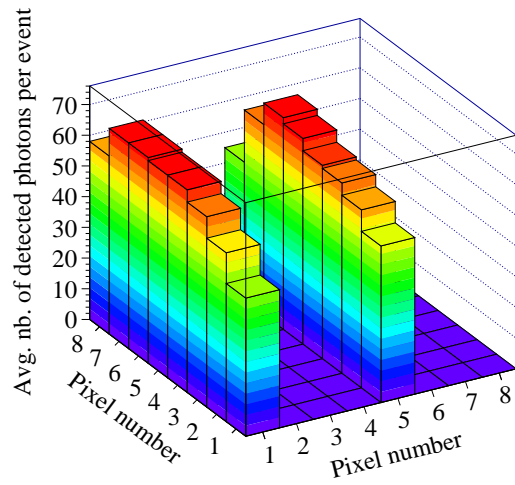
the segments of the scintillator, while the smaller peak is related to protons entering the 1 mm wide and 10 mm deep slits of the scintillator. The latter are interacting effectively in only 5 mm thick plastic, thus depositing about three times less energy and producing three times less photons. The third small peak at very low photon numbers is due to dark count events.

The hit pattern observed with configuration B (see Fig. 8.23(b)) is depicted in Fig. 8.28. About 50–60 photons per pixel could be detected on average per event by placing the DPCs (DPC-A and DPC-B) at the rim of the scintillator tiles, which is less than observed in a comparable setup using conventional  $3 \times 3 \text{ mm}^2$  SiPMs (see Fig. 8.6), although the area of a DPC pixel is larger ( $3.2 \times 3.9 \text{ mm}^2$ ). The difference can be explained by the different PDEs and spectral sensitivities of the two devices.

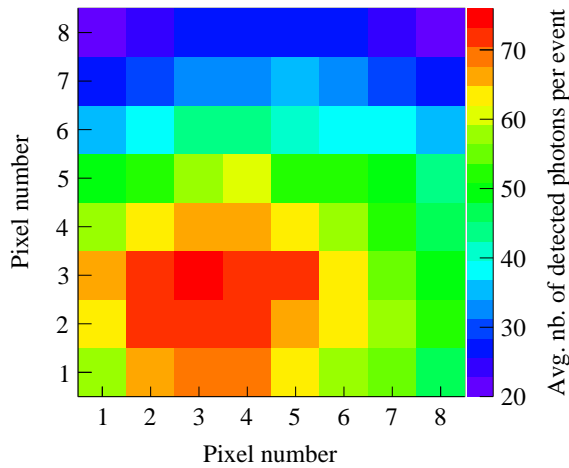
Fig. 8.29 shows the total number of photons detected with the three tiles (TileA, TileB and TileC) used in configuration B (see Fig. 8.23(b)). One can notice again the double peak structure in the photon spectrum measured with the reference counter TileC, which is due to the segmentation of the scintillator. The small peaks at very low photon counts



(a) DPC-A



(b) DPC-B



(c) DPC-C

**Figure 8.28:** Average number of photons detected on individual pixels of DPC-A, DPC-B and DPC-C used in configuration B (see Fig. 8.23(b)).

are related to dark count events. For TileA and TileB the photon spectra are nearly identical.

For later analysis only events with protons interacting in the full thickness of the reference scintillator were selected. This was done by applying cuts on the photon spectra in Fig. 8.27(b) and Fig. 8.29(b), e.g. at about 2000 detected photons.

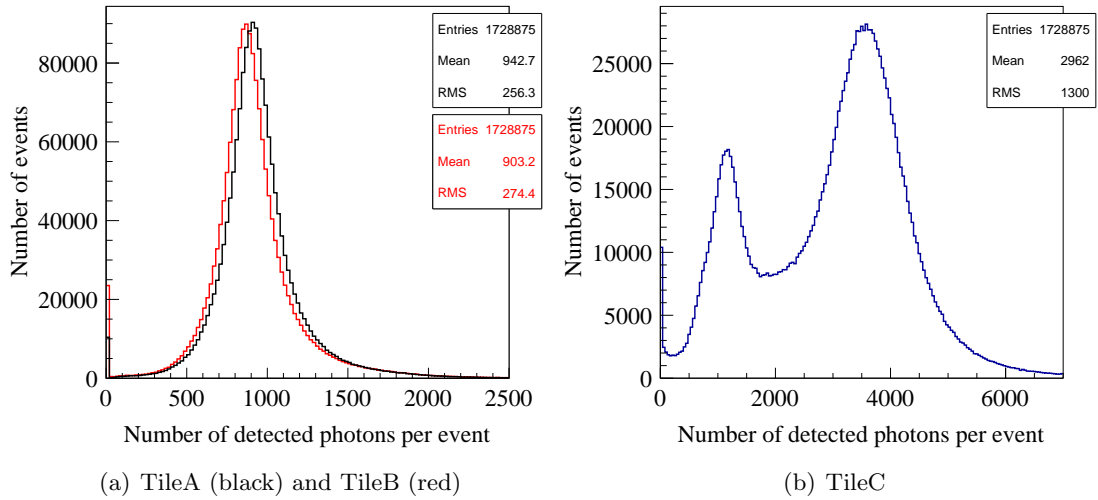


**Figure 8.29:** Total number of photons detected per event with TileA, TileB and TileC used in configuration B (see Fig. 8.23(b)). The double peak structure on the right is due to the segmentation of the scintillator. The small peak at low photon numbers is due to dark count events.

## Time resolution

Similar to the SciTil-SiPM setup, the tile time resolution can be evaluated by performing multiple TOF measurements between the individual scintillation counters. The trigger times of the counters are given by the digital die time stamps of each DPC. For both configurations, many dies of the DPC are activated and usually more than one die triggers, resulting in multiple time stamps per DPC for each event. As a result, the corresponding trigger time can be defined by one or more time stamps, e.g. by the first die triggering ( $t_{first}$ ) or by the mean of multiple die time stamps of all dies triggering ( $t_{mean}$ ). Both options will be discussed.

In case of configuration A, we can perform only a single TOF measurement between the two scintillation counters TileA and TileB, given by:

$$T_{\text{TileA} - \text{TileB}} = T_{\text{TileB}} - T_{\text{TileA}} \quad (8.5)$$

with trigger times  $T_{\text{TileA}}$  and  $T_{\text{TileB}}$ . Due to the different plastic scintillators one cannot assume that the two counters are identical and therefore it is only possible to determine

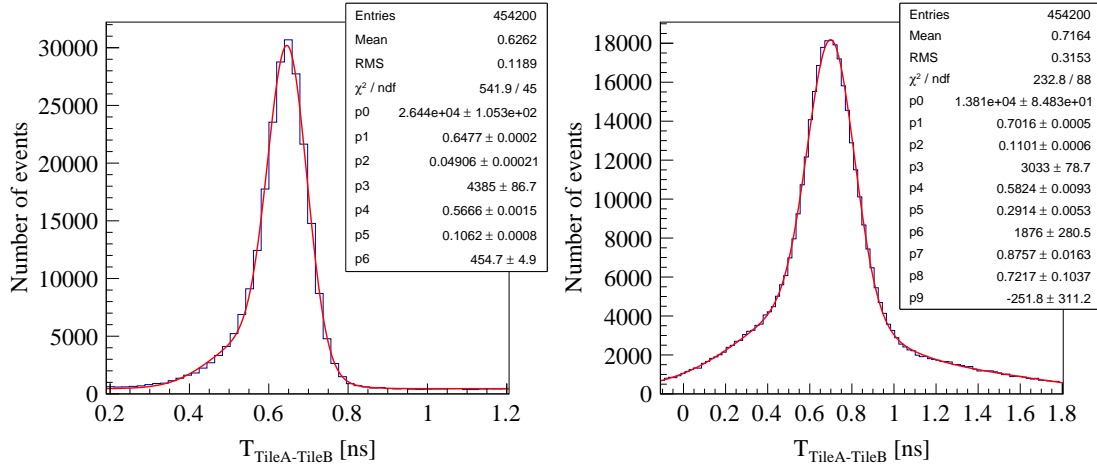


**Figure 8.30:** Time-of-flight between the two scintillation counters TileA and TileB in configuration A (see Fig. 8.23(a)) using either  $t_{first}$  (left) or  $t_{mean}$  (right) to define the trigger times.

the corresponding TOF resolution  $\sigma_{\text{TileA-TileB}}$ , and not the intrinsic time resolutions of the individual counters. Fig. 8.30 shows an example of the TOF measured between the two scintillation counters TileA and TileB using either  $t_{first}$  or  $t_{mean}$  to determine the trigger times.

Due to the quite different geometries of the two scintillator tiles, the photon travel times from the point of photon creation to the photodetector can be expected to vary among the different tile geometries from event to event. As a consequence, also the measured TOF can be different depending on the path of the photons. Especially for the reference scintillator, photons may be reflected inside the scintillator segments, before reaching the sensitive area of the DPC. This is reflected in the measured TOF distributions depicted in Fig. 8.30.

The distributions are asymmetric because of the above reasons. In case of using  $t_{first}$  for trigger time determination, the histogram was fit using a sum of two Gaussian functions and a constant for the background of random events. The Gaussian distributions are related to direct and reflected components, respectively. The TOF resolution was extracted from the fit using only the component related to direct photons, being also the dominating one, thus  $\sigma_{\text{TileA-TileB}} = 49.1 \pm 0.2$  ps.



When using  $t_{mean}$  to define the trigger time, a third Gaussian component has to be introduced, which might be related to the time skew between individual die sensors, having an effect only if multiple time stamps are utilized. Although the skew has been corrected offline on acquired data, it appears that there is still a small effect. Extracting the TOF resolution from the dominant component results in  $\sigma_{\text{TileA-TileB}} = 110.1 \pm 0.6$  ps.

Studying the timing performance of configuration B, we will see that the asymmetric behavior is mainly introduced by the reference detector, i.e. the segmented scintillator tile. Evaluating the TOF between the two identical tiles in configuration B (TileA and TileB in Fig. 8.23(b)), we do not observe such an effect.

For configuration B, one can measure three TOFs between the three scintillation counters TileA, TileB and TileC:

$$\begin{aligned}
 T_{\text{TileA-TileB}} &= T_{\text{TileB}} - T_{\text{TileA}} \\
 T_{\text{TileA-TileC}} &= T_{\text{TileC}} - T_{\text{TileA}} \\
 T_{\text{TileB-TileC}} &= T_{\text{TileC}} - T_{\text{TileB}}
 \end{aligned}
 \tag{8.6}$$

with trigger times  $T_{\text{TileA}}$ ,  $T_{\text{TileB}}$  and  $T_{\text{TileC}}$ . The TOF resolutions and associated errors can be obtained by fitting the corresponding TOF distributions. From the three TOF resolutions one can evaluate the intrinsic time resolutions of the individual counters by performing a  $\chi^2$  minimization (see Appendix A.2).

Fig. 8.31 shows examples of measured TOF distribution between the three scintillation counters using either  $t_{first}$  or  $t_{mean}$  to define the trigger times. Looking at the plots it becomes obvious that the asymmetry in the timing spectra is introduced by the reference counter TileC. In order to extract the corresponding TOF resolutions, the histograms were fit using a sum of two Gaussian functions and a constant, to account for direct and reflected photons as well as for the background. The skew seems to have less influence in this setup configuration, maybe because of less dies activated on DPC-A and DPC-B (less time stamps to form  $t_{mean}$ ), or simply because of the exchange of DPC tiles and more accurate skew correction.

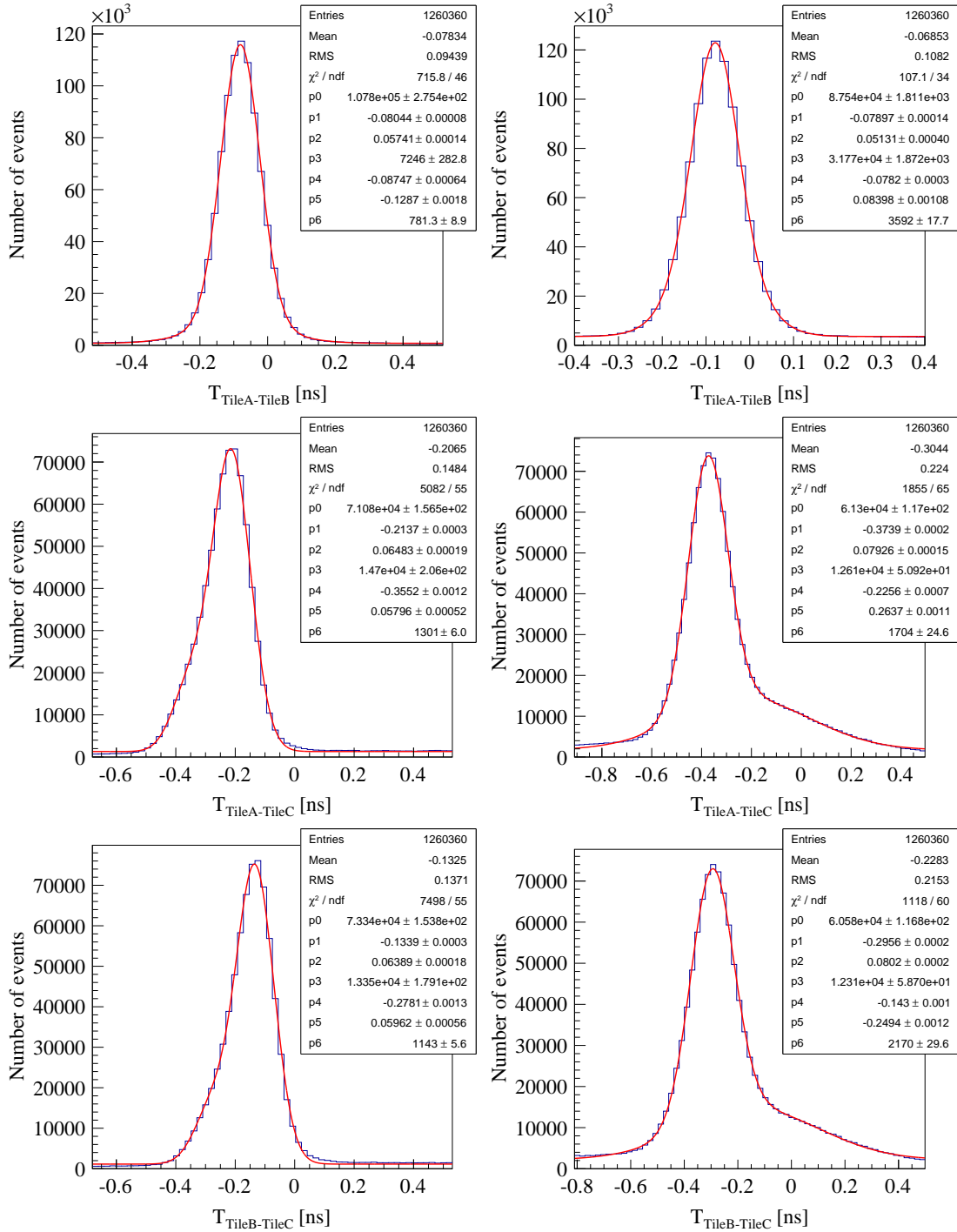


**Figure 8.31:** Time-of-flight between the three scintillation counters TileA, TileB and TileC in configuration B (see Fig. 8.23(b)) using either  $t_{first}$  (left) or  $t_{mean}$  (right) to define the trigger times.

From the fit parameters it was assumed that the dominant components define the TOF resolutions. Performing a  $\chi^2$  minimization as explained in Appendix A.2, the time resolutions of the individual counters could be determined. Using  $t_{first}$  to evaluate the trigger times, the following results could be extracted:

$$\begin{aligned}\sigma_{\text{TileA}} &= 41.3 \pm 0.2 \text{ ps} \\ \sigma_{\text{TileB}} &= 39.8 \pm 0.2 \text{ ps} \\ \sigma_{\text{TileC}} &= 49.9 \pm 0.2 \text{ ps}\end{aligned}\tag{8.7}$$

To cross-check, one could assume that the counters TileA and TileB are identical and evaluate  $\sigma_{\text{TileA}}$  and  $\sigma_{\text{TileB}}$  directly, using the TOF resolution  $\sigma_{\text{TileA-TileB}}$ .

$$\sigma_{\text{TileA}} = \sigma_{\text{TileB}} = \frac{1}{\sqrt{2}} \sigma_{\text{TileA-TileB}} = 40.6 \pm 0.1 \text{ ps}\tag{8.8}$$

The value is comparable with the results obtained from the  $\chi^2$  minimization.

Analyzing the TOF spectra based on  $t_{mean}$ , one can obtain the following time resolutions:

$$\begin{aligned}\sigma_{\text{TileA}} &= 35.4 \pm 0.4 \text{ ps} \\ \sigma_{\text{TileB}} &= 37.1 \pm 0.4 \text{ ps} \\ \sigma_{\text{TileC}} &= 70.9 \pm 0.2 \text{ ps}\end{aligned}\tag{8.9}$$

The determination of  $\sigma_{\text{TileA}}$  and  $\sigma_{\text{TileB}}$  directly from  $\sigma_{\text{TileA-TileB}}$  yields  $\sigma_{\text{TileA}} = \sigma_{\text{TileB}} = 36.3 \pm 0.3 \text{ ps}$ .

### 8.3.3 Results

The following paragraphs summarize the best results that could be obtained with the Philips DPC using two different setups (configuration A and configuration B in Fig. 8.23). The trigger times of the scintillation counters ( $T_{\text{Tile}}$ ), which are needed to determine the time resolution, were defined either by the time stamp of the first triggering die ( $t_{first}$ ) or by the mean of multiple die time stamps of all triggering dies ( $t_{mean}$ ).

## Configuration A

Reading out the whole front side of a plastic scintillator tile with the Philips DPC and using  $t_{first}$  for time stamp definition, a TOF resolution of  $\sigma_{TOF} = 49.1 \pm 0.2$  ps could be measured between a thin EJ-228 plastic scintillator ( $30 \times 30 \times 5$  mm<sup>3</sup>) and a BC-408 reference counter. Using instead  $t_{mean}$  to evaluate the trigger time stamps, the TOF resolution increases by more than a factor two, which is mainly caused by the degradation of the time resolution of the reference counter. Due to long photon travel paths inside the segmented scintillator, the time jitter between individual die time stamps is increased.

## Configuration B

On the basis of this setup we will now discuss in more detail the gain of using multiple time stamps to determine the tile trigger time and time resolution, and also the dependency of the tile time resolution on the hit position of the proton, i.e. the position of photon generation in the scintillator. In the previous sections it was shown that by placing the DPC at the rim of the EJ-228 plastic scintillator tiles, an intrinsic tile time resolution of  $\sigma = 39.8 \pm 0.2$  ps and  $\sigma = 35.4 \pm 0.4$  ps using  $t_{first}$  and  $t_{mean}$ , respectively, could be obtained. In any case, better results could be achieved by defining the tile trigger times out of multiple die time stamps ( $T_{Tile} = t_{mean}$ ). Usually the DPC trigger threshold is set to one photon and so the individual die time stamps are generated when the first photon is detected on the respective die. According to previous studies from Chapter 7, setting the trigger threshold to larger photon numbers leads to reduced tile time resolution.

Fig. 8.32 shows the tile time resolution obtained with Configuration B using either  $t_{first}$  or  $t_{mean}$  to define the tile trigger time, as a function of the DPC trigger threshold. As it can be seen, the results confirm the above statement and the findings from the previous chapter, i.e. the time resolution worsens with increasing trigger threshold. Apart from that, it is interesting to notice that for the highest trigger threshold the time stamp taken from the first triggering die delivers better time precision than  $t_{mean}$ , while for lower

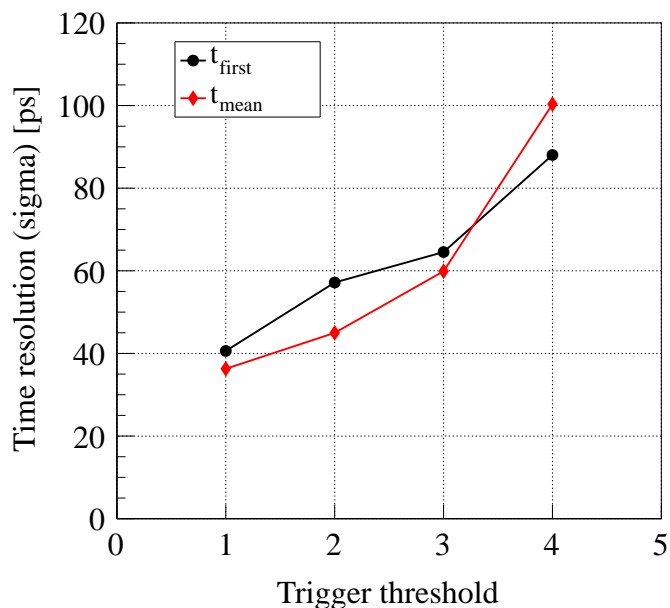


**Figure 8.32:** Tile time resolution in dependency on the DPC trigger threshold. At the highest trigger threshold,  $t_{\text{mean}}$  gives better results due to the DPC trigger logic.

thresholds it is the other way round. This effect is coming from the working principle of the DPC trigger logic.

As explained, trigger thresholds larger than 1 do not define the actual number of photons that have to be detected, but the required number of photons depends on the photon distribution on a die. For a trigger threshold set to 4 photons, the average number of required photons for triggering is about 8 photons. Since the photon distribution on the die is different for every event and die position, the actual number of photons needed for successful triggering fluctuates of course around the average values, resulting in a time spread in trigger time stamps from event to event and also among different dies. The higher the trigger threshold, the larger these fluctuations as well as the the associated time jitter can be. At the highest trigger threshold, these fluctuations and the corresponding time jitter become so large, that using a single time stamp from the first triggering die is superior than a mean of multiple time stamps from all triggering dies.

We can take a closer look at the influence of the number of available time stamps by

investigating the individual die time stamps in greater detail. In configuration B each scintillator tile is read-out by eight dies, four at the bottom and four at the top. Each die provides a time stamp at the moment of trigger occurrence. This happens when the first photon is detected on the respective die, since the trigger threshold is usually set to 1 photon. In total we therefore receive at maximum eight individual time stamps of a single event. By sorting these time stamps in ascending order and taking the first value,  $t_{first}$  is defined, whereas  $t_{mean}$  is determined by simply calculating the average of all available time stamps.

The total number of available time stamps is in most cases eight, but can also be less if one or more dies do not trigger. However, since the time information of all triggering dies is available, one can also perform other combinations of time stamps to provide the tile trigger time. Using a single time stamp ( $t_{single}$ ), we may also use the second ( $t_{single} = t_{second}$ ), third, fourth, etc., time stamp instead of the first ( $t_{single} = t_{first}$ ). On the other hand, the average ( $t_{average}$ ) can be also calculated from a subset of available time

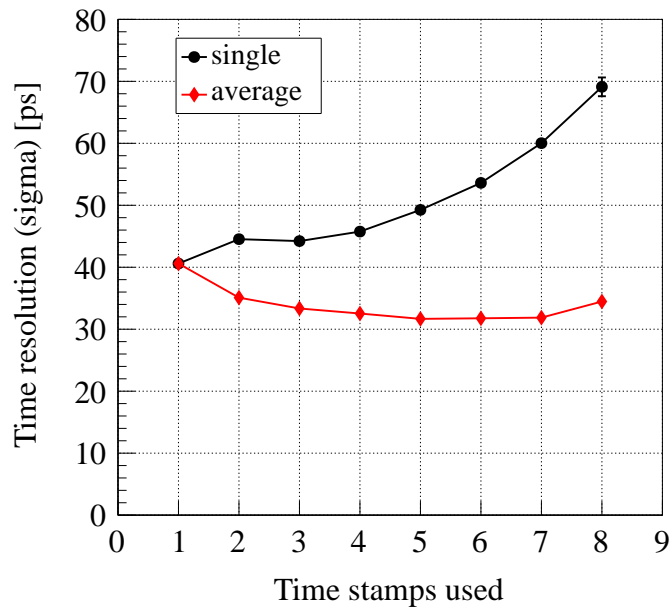


**Figure 8.33:** Tile time resolution as a function of the number of used time stamps to visualize the advantage of having multiple time stamps. The tile trigger time can either be defined by using a single time stamp (*single*) or an average of multiple time stamps (*average*).

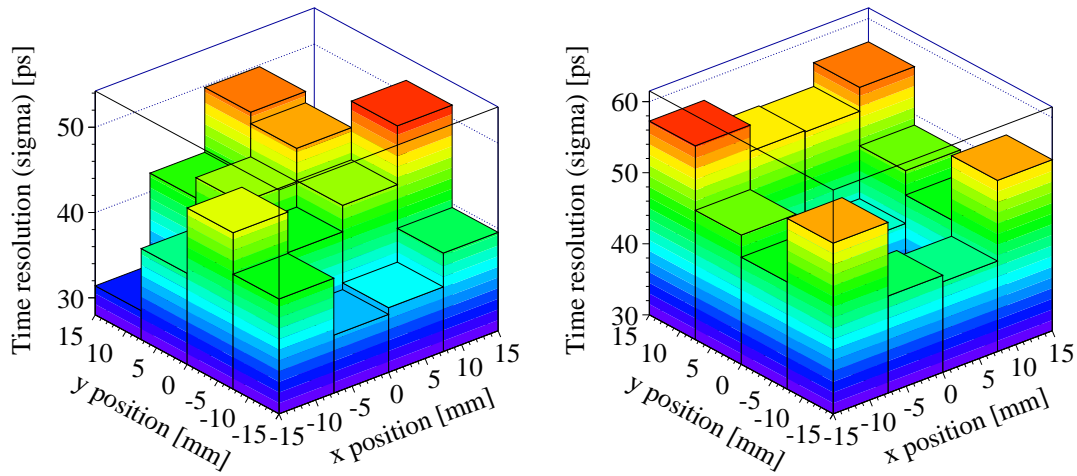
stamps, e.g. taking the average value of the first four die time stamps. Fig. 8.33 shows the measured time resolution of a single tile as a function of the time stamp order used to determine  $t_{single}$  or  $t_{average}$ . The tile time resolution has been determined by measuring the TOF between the two scintillator tiles ( $T_{TileA}$  and  $T_{TileB}$ ) and dividing by  $\sqrt{2}$ .

As expected, the plot shows that the multiple time stamp approach delivers better time resolution than a single time stamp. In case of using the single time stamp method, the first registered photon provides the best time precision, as expected from photon statistics. This confirms the findings from the previous chapter. Apart from that it is interesting to notice that the multiple time stamp approach provides the best results when taking an average of the first 5–6 acquired time stamps, whereas for higher numbers of used time stamps the time resolution worsens. This can be also understood by the statistics of the scintillation process. Late photons show less time precision and do not provide valuable input for the multiple time stamp method.

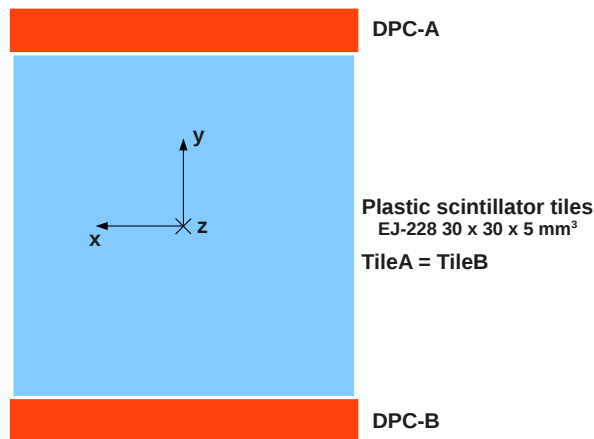
In order to study the position dependency of the tile time resolution, we can use the photon distribution measured with the segmented reference detector (TileC). By calculating the centroid of the DPC hit pattern, one can determine the hit position, i.e. the scintillator segment that was most likely hit by a proton. Since the three detectors (TileA, TileB and TileC) are located close together and aligned properly, it can be assumed that this represents also the hit position on TileA and TileB.

Fig. 8.34 shows the tile time resolution  $\sigma_{TileA} = \sigma_{TileB}$  for different hit positions using either  $t_{first}$  or  $t_{mean}$  to define the tile trigger times. The time resolution was calculated from the TOF resolution  $\sigma_{TileA-TileB}$ , assuming that the two tiles are identical. For better understanding, Fig. 8.35 shows a schematic of the setup when looking in beam direction.

Looking at the two plots in Fig. 8.34, one can see that the time resolution is strongly depending on the hit position. In case of using  $t_{first}$  for trigger time generation, the time resolution is better for interactions at the border of the scintillators, close to the DPC active area. The time precision of  $t_{first}$  is determined by the time jitter of the first detected photon, which is smallest for photon creation close to the detector, where the



**Figure 8.34:** Tile time resolution for different hit positions in configuration B (see Fig. 8.35) using either  $t_{first}$  (left) or  $t_{mean}$  (right) to define the trigger times.



**Figure 8.35:** Schematic of the configuration B setup looking in beam direction ( $z$ -direction).

photon travel paths are short.

When making use of  $t_{mean}$ , it is exactly the other way round and the time resolution is best for hits in the center of the scintillator tile. Since  $t_{mean}$  is defined by multiple die time stamps, the best time precision can be achieved if the photon path variations from the point of photon creation to the individual dies are small, which is the case if the scintillation light is created in the center of the tile.



## 8.4 Discussion of results

Various SciTil prototypes consisting of small plastic scintillator tiles read-out with SiPMs have been tested in a proton beam with a maximum momentum of 2.7 GeV/c at FZJ. Various SiPMs with  $3 \times 3 \text{ mm}^2$  sensitive area from Hamamatsu and KETEK, as well as the Philips DPC have been employed in combination with different types of fast plastic scintillators from Eljen.

It was shown that in case of photon detection with conventional SiPMs, the tile time resolution is strongly depending on the operating voltage of the respective device. A time resolution below 100 ps sigma is only feasible if the bias voltage is properly adjusted. With KETEK SiPMs the best results could be obtained at 12 % to 13 % relative over-voltage, for Hamamatsu MPPCs optimal performance could be observed around 5–6 % relative over-voltage. The relative over-voltage is defined as  $V_{over}/V_{bd}$ .

The large variations of signal heights from event to event led to a strong time walk effect when using simple LE triggering. In order to achieve the envisaged time resolution of 100 ps sigma, a time walk correction has to be applied, which can be done by using pulse height information, a double threshold or a CFD. The different methods show similar results.

The measurements showed that the time resolution is depending on the threshold settings, indicating that the optimization of threshold levels is another crucial point. In this context, it was illustrated that triggering on the first detected photons is usually not associated with the best timing performance in a scintillation detector using SiPMs. The time resolution could be improved by applying a multiple time stamps approach to estimate the proton interaction time, which led to the conclusion that a scintillation detector dedicated to optimum timing should preferably make use of a multitude of time stamps.

After optimization, a tile time resolution of  $\sigma = 82.5 \pm 1.7 \text{ ps}$  could be obtained, using two KETEK PM3360TS sensors attached to an EJ-232 plastic scintillator with a size of

$28.5 \times 28.5 \times 5 \text{ mm}^3$ . Employing two Hamamatsu S12572-025C MPPCs, a time resolution of  $\sigma = 96.3 \pm 0.9 \text{ ps}$  could be reached with an EJ-228 scintillator. Using an EJ-232 scintillator tile instead shows a nearly identical result.

Due to its large sensitive area, the Philips DPC offers the possibility to cover a larger fraction of the scintillator tile surface. The increased number of detected photons and the multitude of available trigger time stamps result in improved time resolution. Reading out two opposite sides of the plastic scintillator tiles with the DPC led to a tile time resolution of  $\sigma = 35.4 \pm 0.4 \text{ ps}$ .

The obtained results are very encouraging and demonstrate that a time resolution well below  $\sigma = 100 \text{ ps}$  is feasible with the proposed SciTil layout, employing either conventional  $3 \times 3 \text{ mm}^2$  SiPMs or the DPC. Therefore, both detector options can be seen as candidates for photon detection in the PANDA TOF system.

## Chapter 9

# Simulation of the timing properties of a scintillator tile detector

The results obtained from the test beam data analysis proved that the required time resolution of  $\sigma \sim 100$  ps can be achieved with the proposed tile layout. However, in order to sustain for the whole SciTil system with thousands of channels a time resolution constantly below 100 ps over a long period of operation, it is of course beneficial to reach a single tile time resolution considerably below the required system value. As already shown, ways to further improve the time resolution are to increase the number of detected photons or the number of available time stamps. As a more sophisticated method one could think of using the detected photon distribution or difference in photon arrival times to estimate the position of the primary interaction in the scintillator and to correct for the photon propagation.

In order to raise the number of detected photons without increasing the photodetection area one can simply modify the geometry of the scintillator tile. Recently, it has been proposed to replace the tile geometry by a bar-shaped scintillator geometry [73], which has been called SciRod instead of SciTil. A single rod with a cross section of e.g.  $5 \text{ mm} \times 5 \text{ mm}$  and a length of 120 mm could be read-out from both sides by two SiPMs, just as for the tile geometry. Compared to the scintillator tile, however, a larger number of photons will be totally internally reflected and guided onto the sensitive area of the photodetectors.

Furthermore, a measure of the time difference between the two SiPM signals can be used to roughly determine the point of interaction and to correct for photon propagation. In case of the tile geometry such a position correction is more complicated and may also require to measure the photon intensities. First measurements using the proposed layout showed that about a factor 1.7 to 1.8 more photons could be detected with SciRods compared to SciTils and that a time resolution of about 50–60 ps can be achieved [74].

Covering the whole TOF barrel with SciRods of the above dimensions instead of SciTils, the total number of scintillators and photodetectors, respectively, would increase by one third compared to the tile geometry. Another consequence would be that the spatial resolution changes, i.e. improved resolution in azimuthal direction but reduced resolution in  $z$ -direction. Resulting impacts on the performance have not yet been studied.

This chapter presents the first results obtained with a simulation tool that is currently being developed in order to further optimize the SciTil detector and fully understand its timing properties and the results obtained from experiment. The simulation is based on the Geant4 toolkit [10] using version 9.4.04. The final aim is to use the output from simulation as input for the experiments to push the time resolution towards its limits. Furthermore, the simulation will also provide valuable input for the comparison between SciTils and SciRods in order to finalize the detector geometry. The here presented results are not meant to give absolute values of the time resolution but in this first stage the simulation is used to compare between different geometries and configurations. In a later stage the simulation is going to be compared with measurements in order to be sure that the simulation can reproduce a realistic experimental situation, and to be able to give more accurate predictions on the absolute value of the time resolution.

## 9.1 Detector construction

As a first step we consider two different detector geometries, one using the tile layout with a size of  $28.5 \times 28.5 \times 5$  mm<sup>3</sup>, and one using the rod-shaped geometry with dimensions

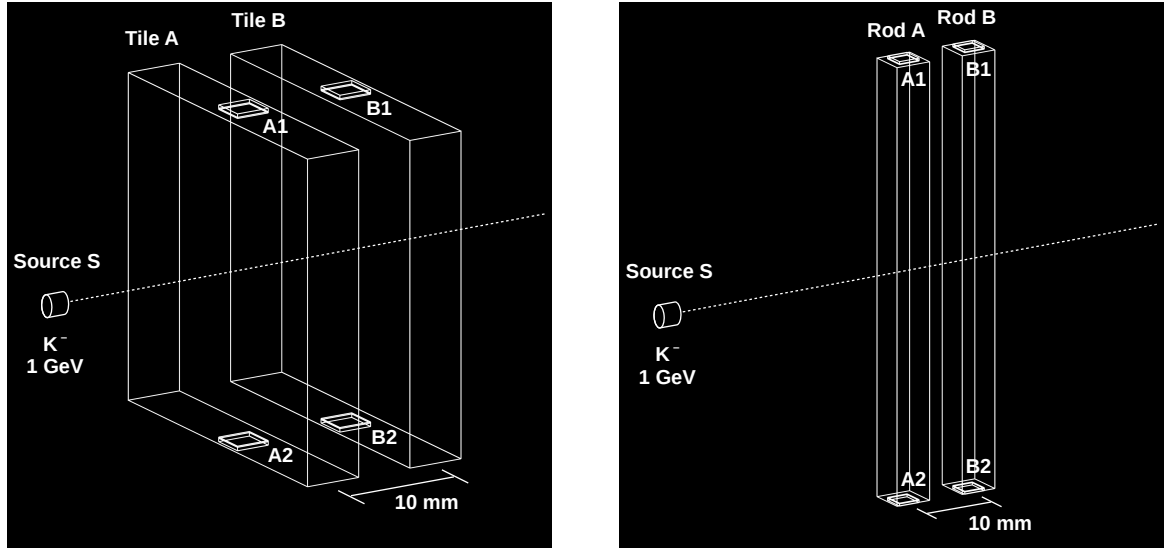


**Figure 9.1:** Simulation of SciTil (left) and SciRod (right) detector geometries. Each scintillator is read-out by two photodetectors (A1, A2 and B1, B2) with  $3 \times 3 \text{ mm}^2$  active area each.

of  $5 \times 120 \times 5 \text{ mm}^3$ , as shown in Fig. 9.1. Just as for the experiments, we use two EJ-228 scintillators separated by 10 mm and read-out by two  $3 \times 3 \text{ mm}^2$  photodetectors each. In-between the scintillators and detectors a  $100 \mu\text{m}$  thick layer of optical grease is simulated. The scintillation rise- and decay times as well as the light yield and refractive index are taken from the data sheet<sup>1</sup> (see also Table 6.1). The wavelength of emitted photons is simulated following the characteristic emission spectrum of the scintillator. The scintillator surface is assumed to be perfectly flat and polished and surrounded by air. In the simulation the optical cross-talk between the two adjacent scintillators is found to be less than 1%. For the beginning, the photodetectors are assumed to be ideal, i.e. having an infinite time resolution and a PDE of 1.

The primary particles are  $\text{K}^-$  with an energy of 1 GeV, emitted from a point source. The position of the source is distributed randomly across the whole scintillator surface for subsequent events. For each geometry 10 000 events are simulated. In each event, the moment of creation of the primary particle determines the time  $t = 0$  in the simulation. For every event we record the number of scintillation photons reaching the surface of the

<sup>1</sup>Eljen Technology, <http://www.eljentechnology.com/>

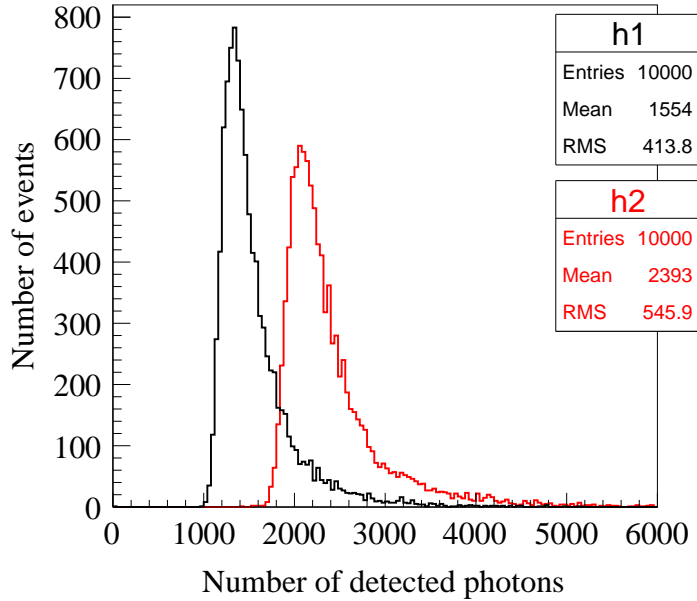


**Figure 9.2:** Simulated number of detected photons with a single scintillator tile (black) and a scintillator rod (red) read-out with two SiPMs. With the SciRod geometry about a factor 1.6 more photons are detected.

photodetectors and the arrival times  $t_i$  of all detected photons. In analogy to experiment, the tile time resolution is determined by using the TOF between the two scintillation counters. Since the two counters are identical in the simulation we can estimate the tile time resolution from the TOF resolution divided by  $\sqrt{2}$ . By making use of a multitude of arrival times  $t_i$  we can study again the gain of a multiple time stamp approach.

## 9.2 Number of detected photons

By counting the number of scintillation photons hitting the surface of the photodetectors we can compare the light collection efficiencies of the two geometries. Fig. 9.2 shows the number of photons detected with a single scintillator rod or tile, respectively, read-out with two SiPMs. As already mentioned, the simulation does not yet provide absolute numbers but allows to compare between the different configurations. The plot shows that the number of detected photons with the SciRod geometry is about a factor 1.6 larger

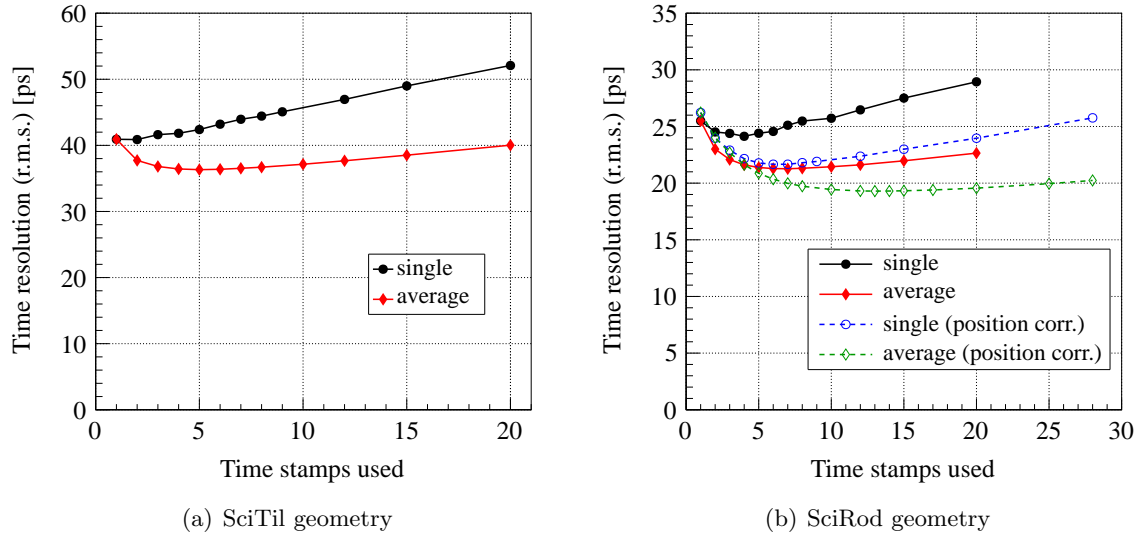
compared to the SciTil layout, which is also in agreement with first measurements [74]. Considering only this result one can expect already an improvement in the measured time resolution roughly by a factor  $\sqrt{1.6}$ .

### 9.3 Time resolution

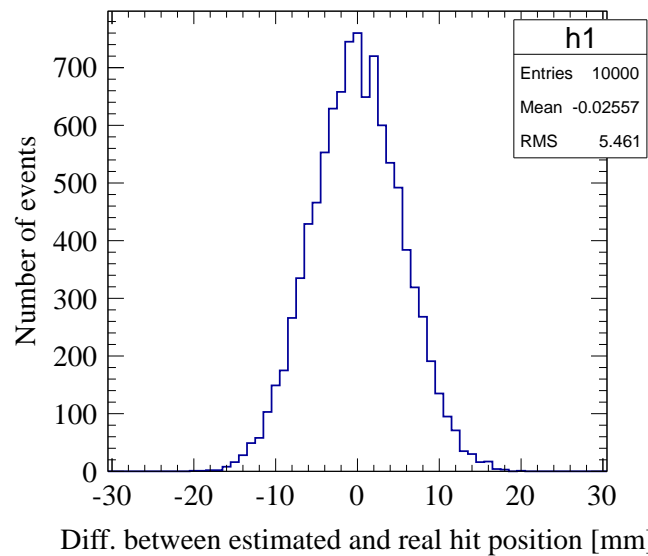
The time resolution for both, the SciTil and the SciRod geometry, has been determined using a single time stamp method as well as a multiple time stamp approach, by sorting the photon arrival times  $t_i$  in ascending order. By doing so, order statistics gets involved. For the single time stamp approach, the trigger time is defined by a single photon arrival time rank, while for the multiple time stamp method, the trigger time gets determined by calculating an average of a certain number of arrival times. In case of the SciRod layout, the time resolution has been additionally corrected for fluctuations of the position of photon creation, by using the arrival time difference between the two opposing photodetectors.

Fig. 9.3 shows the obtained time resolution for a single scintillator tile and rod, respectively. At first sight it is noted that the use of multiple time stamps improves the time resolution for both geometries compared to the single time stamp method. This has already been demonstrated by experiment in the previous chapter and is also reported in Ref. [63]. Apart from that we can observe the influence of photon propagation on the time resolution, which appears to be different for the two cases, as expected due to the diverse scintillator geometries.

For the SciTil detector, the single time stamp method still gives the best results using the lowest time stamp ranks as predicted by photon counting statistics. Using a multiple time stamp approach, the best time resolution can be achieved when averaging among the arrival times of the first five detected photons, while the usage of time stamps of late photons reduce the time precision, as also shown by experiment in the previous chapter. In case of the SciRod geometry, however, the minimum of the time resolution is shifted



**Figure 9.3:** Simulated time resolution as a function of the number of used time stamps, for SciTil (left) and SciRod (right) geometries. Results of single and multiple (average) time stamp methods are shown. In case of the SciRod, the time resolution has been corrected for fluctuations of the position of photon creation, by using the arrival time difference between the two opposing photodetectors. The lines are added to guide the eye.



**Figure 9.4:** Difference between estimated and real hit position along the SciRod.



towards higher time stamp ranks due to the impact of photon propagation. The best values can be achieved using the single time stamp of the fourth detected photon or an average of the arrival times of the first seven detected photons. Using the difference of the arrival time of the first photons detected with two opposing SiPMs attached to a SciRod, as an estimate for the position of the primary interaction of the  $K^-$  along the scintillator rod, the time resolution could be further improved by about 10%. Fig. 9.4 shows the deviation of the estimated hit position from the real hit position along the SciRod. The standard deviation is about 5.5 mm.

In order to demonstrate that the different trends of the time resolution as a function of the number of used time stamps are originating from the influence of photon propagation, we shrink the scintillator to a size of  $3 \times 3 \times 3 \text{ mm}^3$  and fix the source position to the center of the scintillator. In this case, the impact of photon propagation on the time resolution is minimized. The results are presented in Fig. 9.5. As expected from pure photon counting statistics, using a single time stamp, triggering on the first detected photon leads to the best time precision. Comparing this plot with Fig. 9.3, one can see how the change of

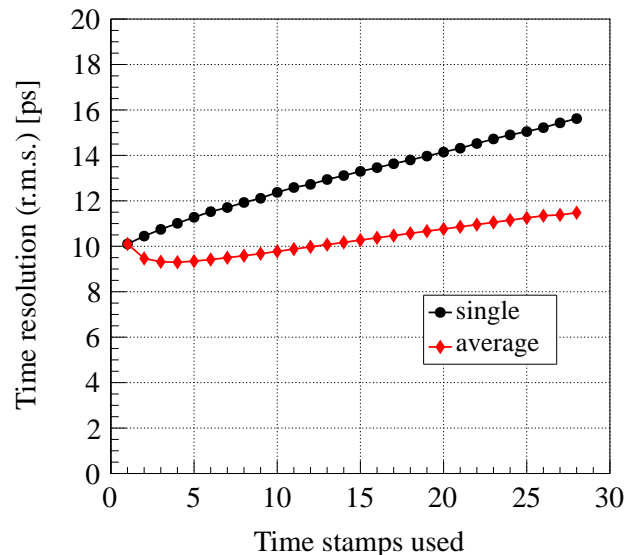


**Figure 9.5:** Simulated time resolution as a function of the number of used time stamps for a small scintillator with a size of  $3 \times 3 \times 3 \text{ mm}^3$ . With this geometry the influence of photon propagation is reduced to a minimum.

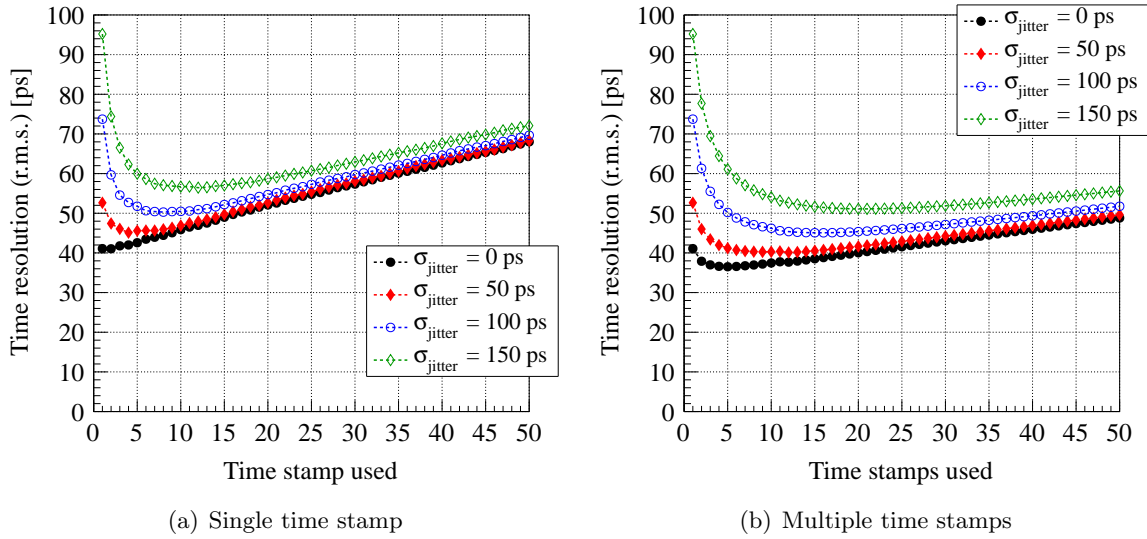


**Figure 9.6:** Simulated SciTil time resolution as a function of the number of used time stamps, using a single time stamp (left) and multiple time stamp (right) approach. A Gaussian jitter is added to the photon arrival times to simulate the single photon time resolution of the photodetector. The lines are added to guide the eye.

geometry and thus the influence of photon propagation affects the time resolution and optimum time stamp ranks.

Going back to the SciTil geometry, we introduce a more realistic situation by including a single photon time resolution (SPTR) of the photodetector, simply by adding a Gaussian jitter  $\sigma_{jitter}$  to the photon arrival times. Fig. 9.6 shows the resulting time resolution of a SciTil for the single and multiple time stamp approach and different values of  $\sigma_{jitter}$ . The plot demonstrates how the single photon time jitter changes the influence of the photon counting statistics. For values of  $\sigma_{jitter} > 0$  and using the single time stamp method, triggering on the first photon does not give the best time precision any more. This is actually what we have also seen in the experiments presented in the previous chapters and has been also reported in Ref. [63] and Ref. [72]. Also in case of the multiple time stamp approach, the minimum of the time resolution is shifted to higher time stamp ranks as the jitter increases.

## 9.4 Discussion of results

A simulation tool based on Geant4 has been developed to further improve the time resolution of the scintillation detectors for the PANDA TOF system. In this context, the currently foreseen tile-shaped scintillator geometry (SciTil) with a size of  $28.5 \times 28.5 \times 5 \text{ mm}^3$  has been compared with a newly proposed rod-shaped scintillator layout (SciRod) with a cross section of  $5 \text{ mm} \times 5 \text{ mm}$  and a length of 120 mm. In a first stage a perfectly flat and polished scintillator surface as well as an ideal photodetector recording the individual arrival times of all photons reaching the detector have been assumed. Preliminary results show that the number of detected photons using the SciRod geometry is about a factor 1.6 higher compared to the SciTil layout, which is in agreement with first measurements [74].

The time resolution of the scintillation detectors has been determined by using either a single or multiple time stamp approach, meaning that either the arrival time of a single photon or an average of multiple photon arrival times has been used to evaluate the trigger times. For both scintillator geometries the multiple time stamp method resulted in improved time resolution. In case of the SciTil the minimum of the time resolution could be found when using the time information of the first five detected photons, for the SciRod geometry averaging among the first seven photon arrival times gave the best value.

Comparing the two diverse scintillator geometries it becomes obvious how the photon propagation influences the achievable time resolution and the time stamp ranks for optimum triggering. With a single time stamp method triggering on the first photon gives the best result for the tile layout, indicating that the influence of photon propagation is rather small and photon counting statistics is dominating the overall time resolution. However, in case of the rod-shaped scintillator the optimum trigger threshold is shifted to higher photon ranks due to the impact of photon propagation. Measuring the time difference between the two opposing photodetectors to correct for the variations of the primary hit position led to an improvement of the SciRod time resolution by about 10%.

Adding a time jitter to the photon arrival times in order to simulate the single photon time resolution of the photodetector, triggering on the first arriving photon does not result in the best time precision anymore, as the SPTR starts to significantly affect the influence of photon counting statistics. The smearing of the scintillation signal with the single photon time jitter of the photodetector leads to a rise of the time resolution at low trigger thresholds, and shifts the optimum trigger level to higher values. Such a trend has been also observed in the experiments presented in this work. In a real photodetector, however, this behavior is additionally affected by the finite rise time and slew rate of the analog signals and by the noise of the electronics.

The presented simulation can already partly reproduce the trend of the time resolution of the scintillation detectors observed in the experiments and can be used to compare different detector configuration. In order to make predictions about absolute values for the time resolution, the simulation has to be further adapted to the realistic experimental situation. In this context, the scintillator surface will be simulated as an irregular surface allowing also diffuse reflection. Concerning the photodetector, the PDE will be considered and the detector response will be simulated by modeling a realistic output signal as the analog sum of the individual SPAD signals.

## Chapter 10

# Summary and outlook

This work concentrated on the investigation and optimization of the time resolution of scintillator based detectors for high energy physics (HEP) applications, in particular for the barrel time-of-flight (TOF) detector of the PANDA experiment. Such a detector consists of several parts, usually a scintillator, a photodetector and dedicated read-out electronics, that need to be optimized and adapted to the demands of the application. In the special case of PANDA an area of about  $5.2\text{ m}^2$  will be covered by 5760 individual scintillation detectors to form the Scintillator Tile (SciTil) Hodoscope. Small plastic scintillator tiles will be read-out with compact Silicon Photomultipliers (SiPMs) in order to fulfill the spatial constraints within the PANDA target spectrometer and to reach the required time resolution in the order of 100 ps sigma.

The intention of the first part of the thesis was to fully understand the SiPM device, its functionality and features and to find the optimum settings of operating parameters for the utilization in a fast scintillator based TOF detector. Therefore, a detailed characterization study has been carried out. For the tests we used commercially available SiPMs from different vendors. Both, conventional analog devices, mainly from Hamamatsu and KETEK, as well as the first fully digital SiPM, called Digital Photon Counter (DPC) from Philips, were tested. In TOF applications the intrinsic time resolution of the photodetector is one of the key parameters. Among the tested analog SiPMs, the PM3350TS model with optical trenches from KETEK with  $50\times 50\ \mu\text{m}^2$  pixel size showed the best

time performance when exposed to short picosecond laser pulses. In general, SiPMs with some technology against after-pulsing and cross-talk delivered superior performance not only in terms of time resolution but also concerning the long-term stability, mainly due to larger optimum operating ranges.

Other important parameters of a photodetector for HEP applications are the dynamic range and the recovery time. Both parameters were determined experimentally for several kinds of SiPMs. The dynamic range can be estimated by measuring the response curve of the photodetector, i.e. the output signal as a function of the number of incident photons on the detector. We found an unexpected enhancement of the dynamic range in most tested devices, and with increasing light intensities the output signal started to exceed by far the theoretical expectations, namely a maximum output comparable to the total number of pixels multiplied with the single cell amplitude. This observation was found among all tested SiPMs from Hamamatsu, Photonique and Zecotek. In case of the S10362-11-050U model from Hamamatsu an output signal equivalent up to two times the total number of pixels was measured. Up to now, no explanation for the observation could be found and it has to be mentioned that most application may not be affected due to much lower light intensities, in the regime where the SiPM response is linear and models and measurements showed good agreement. Nevertheless, the results indicate that the current understanding of the device may not be complete.

The recovery time of three Hamamatsu MPPCs was determined by exposing the photodetectors to two consecutive light pulses with varying relative time differences. It was shown that the recovery time constant  $\tau_r$  can be approximated by the simple relation  $\tau_r \sim R_{quench}C_{pix}$ , with  $R_{quench}$  being the value of the quenching resistor and  $C_{pix}$  the pixel capacitance. At low operating voltages ( $V_{over} = 1$  V) we found full recovery after about 200 ns for the 100U device ( $100 \times 100 \mu\text{m}^2$  pixel size), 50 ns for the 050U sensor ( $50 \times 50 \mu\text{m}^2$  pixel size) and 20 ns for  $25 \times 25 \mu\text{m}^2$  pixel size. Increasing the operating voltages, led to an increase of noise effects which drastically prolonged the detector recovery, so that full recovery was observed after  $1 - 2 \mu\text{s}$ .

The Philips DPC is a relatively new photodetector technology which is becoming more and more interesting also for HEP applications. One of the biggest advantages of this new device is that the read-out electronics are already included into the detector and placed very close to the individual cells. Although the measured dark count rate (DCR) is in the order of about 500 kHz per mm<sup>2</sup> and comparable to conventional SiPMs, the device usually needs extensive cooling in order to avoid that the data acquisition is dominated by dark count events, especially if the whole sensitive area of about 32×32 mm<sup>2</sup> is activated. However, disabling 20 % of the cells already led to a reduction of the total DCR by one order of magnitude.

The time resolution of the DPC was evaluated by exposing the detector to femtosecond laser pulses of varying intensity. The time resolution as a function of the number of detected photons  $N$  is roughly following a  $1/\sqrt{N}$  behavior, which is related to the trigger network skew that dominates the time resolution at low photon numbers. At a light intensity of 150 detected photons a time resolution of  $\sigma \sim 17$  ps was found. With an adapted sensor layout the DPC can be definitely considered as a candidate for photodetection in the SciTil system.

The goal of the second part of this work was to develop a prototype scintillation detector based on the SciTil design, reaching a time resolution below 100 ps sigma. Starting from theory and studying the statistics of light emission in a plastic scintillator showed that scintillators for high time resolution should provide short rise- and decay times as well as high light output. In this context, it was shown that triggering on the first photoelectron leads to the best time precision. However, in a real scintillation detector the influence of photon counting statistics is changed due to photon propagation, the photodetector response and electronics noise. As a consequence, triggering on the first detected photon does not necessarily provide the best time resolution, as shown by simulation and experiment.

In the following, a detector optimization study was carried out using radioactive sources. The time resolution limiting parameters such as scintillator material, scintillator size,

photodetector position and type and electronics threshold were investigated. For the experimental tests we used different types of plastic scintillators from Eljen. In general, the best results could be obtained with the fastest scintillators, i.e. EJ-228 and EJ-232. The best time resolution could be achieved by placing the photodetectors in the center of the scintillator rim. Using an EJ-228 plastic scintillator with a size of  $30 \times 30 \times 5 \text{ mm}^3$  read-out with two Hamamatsu MPPCs (S10931-100P) with  $3 \times 3 \text{ mm}^2$ , it was found that the best time resolution could be achieved by setting the electronics threshold equivalent to about five single cell amplitudes. Employing the DPC instead, the response of the photodetector is different and setting the trigger threshold to the first detected photon resulted in the best time resolution. Using this setup a time resolution of  $\sigma = 62.3 \pm 0.8 \text{ ps}$  was obtained. Using an EJ-232 scintillator nearly identical results were achieved.

To finally proof the feasibility of reaching a time resolution below 100 ps sigma with the proposed detector, a test beam experiment was carried out, using a beam of protons with a maximum momentum of  $2.7 \text{ GeV}/c$  at the COSY accelerator located in Jülich, Germany. We investigated conventional analog SiPMs from KETEK and Hamamatsu as well the Philips DPC. In case of using the analog devices, the operating voltages had to be carefully adjusted in order to reach the required time resolution. With KETEK SiPMs the best results could be obtained at 12 % to 13 % relative over-voltage, for Hamamatsu MPPCs optimal performance could be observed around 5–6 % relative over-voltage. The relative over-voltage is defined as  $V_{over}/V_{bd}$ . The breakdown voltage for KETEK sensors was in the order of 27 V, while for Hamamatsu devices it was found around 64 V.

The large variations of signal heights from event to event led to a strong time walk effect, which was avoided by using a constant fraction discriminator (CFD), leading to an improvement in time resolution of up to 28 % compared to leading edge triggering. Using other methods for time walk correction, e.g. pulse height information, double threshold, showed similar effects. After correction, a tile time resolution of  $\sigma = 82.5 \pm 1.7 \text{ ps}$  could be obtained, using two KETEK PM3360TS sensors attached to an EJ-232 plastic scintillator with a size of  $28.5 \times 28.5 \times 5 \text{ mm}^3$ . Employing two Hamamatsu S12572-025C MPPCs, a time resolution of  $\sigma = 96.3 \pm 0.9 \text{ ps}$  could be reached with an EJ-228 scintillator. Using



an EJ-232 scintillator tile instead showed a nearly identical result.

Due to its large sensitive area, the Philips DPC allowed to cover a larger fraction of the scintillator tile surface. This resulted in an increased number of detected photons and a multitude of available trigger time stamps and led to a tile time resolution of  $\sigma = 35.4 \pm 0.4$  ps.

The results demonstrated that the envisaged time resolution of 100 ps sigma is feasible with the proposed detector design. In the experiment, it was shown that the most precise estimate of the time of the primary interaction can be obtained by using multiple time stamps. Analyzing the test beam data, the best values for the time resolution could be found by using an average of a certain number of available trigger time stamps. This was also confirmed by simulation and indicates that a scintillation detector aiming at highest time resolution should preferably make use of a set of multiple time stamps.

In order to fully understand the experimental results and to further optimize the SciTil detector a simulation tool based on Geant4 was developed. The simulation will allow to push the single tile time resolution towards the limits, which will help to sustain a time resolution for the whole SciTil system constantly below 100 ps sigma. Furthermore, it will be used to decide on the final scintillator geometry, by investigating a recently proposed rod-shaped scintillator layout. The simulation could already reproduce experimental trends of the time resolution and showed how different geometries affect the time resolution due to the influence of photon propagation. It was also shown that an estimate of the position of the primary interaction can be used to correct for different photon path lengths and improve the time resolution. However, the simulation will be further adapted to be able to model a realistic scintillation detector including scintillator, photodetector and electronics. Finally, a time resolution in the order of 50 ps sigma and below should be possible with analog SiPMs, considering also the constant improvements in the field of photodetectors.



## Appendix A

# Time-of-flight resolution and intrinsic time resolution

The following paragraphs deal with the estimation of intrinsic detector time resolutions in a detector system composed of two or more scintillation counters, by using time-of-flight measurements. We use here the terminology scintillation counter instead of scintillation detector, not to confuse with the individual (photo-)detectors and associated time resolutions. The derivations are based on the work presented in Ref. [75].

### A.1 Time-of-flight with two identical detectors

As a first case, we assume to have a detector system as illustrated in Fig. A.1, composed of a particle source S and two scintillation counters A and B, each consisting of a scintillator read-out with two photodetectors A1, A2 and B1, B2, respectively.

The trigger times  $T_A$  and  $T_B$  of the two scintillation counters A and B can then be written as:

$$T_A = \frac{1}{2}(T_{A1} + T_{A2}) \quad \text{and} \quad T_B = \frac{1}{2}(T_{B1} + T_{B2}) \quad (\text{A.1})$$

However, we cannot measure  $T_A$  and  $T_B$  directly since usually we do not know the time  $T=0$  when a particle is emitted from the source. But one can measure the time-of-flight

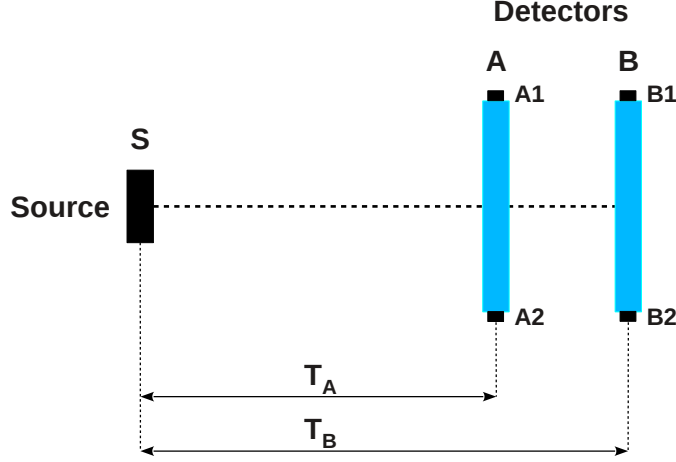


**Figure A.1:** Schematic measurement setup consisting of a particle source ( $S$ ) and two identical scintillation counters ( $A$  and  $B$ ), each composed of a scintillator and two photodetectors ( $A1$  and  $A2$ ,  $B1$  and  $B2$ ).

$T_{AB}$  between the two counters, which is given by:

$$T_{AB} = T_B - T_A + \Delta T_{AB} \quad (\text{A.2})$$

with an associated measurement error  $\Delta T_{AB}$ . The error can be written as a function of random variables  $\Delta T_A$  and  $\Delta T_B$ , belonging to the counters  $A$  and  $B$ :

$$T_{AB} = T_B - T_A + \Delta T_{AB} = (T_B + \Delta T_B) - (T_A + \Delta T_A) \quad (\text{A.3})$$

and thus:

$$\Delta T_{AB} = \Delta T_B - \Delta T_A \quad (\text{A.4})$$

If  $\Delta T_A$  and  $\Delta T_B$  are independent, we can calculate the variance of  $\Delta T_{AB}$ :

$$\sigma_{AB}^2 = \sigma^2(\Delta T_{AB}) = \sigma^2(\Delta T_B) + \sigma^2(\Delta T_A) = \sigma_A^2 + \sigma_B^2 \quad (\text{A.5})$$

If we now assume that in our measurement setup the two scintillation counters  $A$  and  $B$  are identical and have the same resolution, we can calculate the intrinsic time resolution of each counter ( $\sigma_A$  and  $\sigma_B$ ) from the TOF measurement and corresponding TOF resolution  $\sigma_{AB}$ :

$$\sigma_A = \sigma_B = \frac{1}{\sqrt{2}} \sigma_{AB} \quad (\text{A.6})$$

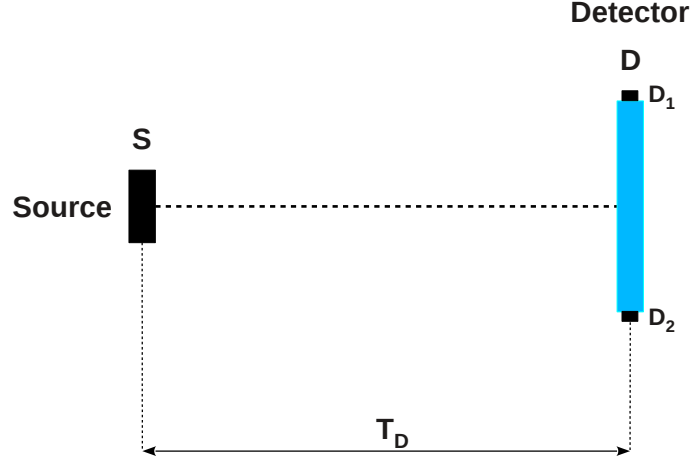


**Figure A.2:** Schematic measurement setup consisting of a particle source ( $S$ ) and a single scintillation counter ( $D$ ), which is composed of a scintillator and two photodetectors ( $D1$  and  $D2$ ).

As another example, we assume a measurement setup consisting of only one scintillation counter with two photodetectors, as shown schematically in Fig. A.2. In order to extract a detector time resolution in such a setup, the only possibility is to measure a time difference between the two detectors  $D1$  and  $D2$ , which can be seen as a form of TOF, ignoring the flight path. In analogy to Eq. A.3 we can write:

$$T_D = T_{D1} - T_{D2} + \Delta T_D = (T_{D1} + \Delta T_{D1}) - (T_{D2} + \Delta T_{D2}) \quad (\text{A.7})$$

and:

$$\Delta T_D = \Delta T_{D1} - \Delta T_{D2} \quad (\text{A.8})$$

The variance can then be calculated by:

$$\sigma_D^2 = \sigma^2(\Delta T_D) = \sigma^2(\Delta T_{D1}) + \sigma^2(\Delta T_{D2}) = \sigma_{D1}^2 + \sigma_{D2}^2 \quad (\text{A.9})$$

and the intrinsic time resolution of a single detector, assuming that the two detectors  $D1$  and  $D2$  are identical, is given by:

$$\sigma_{D1} = \sigma_{D2} = \frac{1}{\sqrt{2}} \sigma_D \quad (\text{A.10})$$

In order to compare this result with the previous example and to estimate the resolution achievable with this intrinsic detector resolution in a system consisting of multiple scintillation counters as before, we can do the following calculation. Looking at the previous example and considering Eq. A.1, the variance of a single scintillation counter A (or B), can be written similar to Eq. A.9:

$$\sigma_A^2 = \sigma^2(\Delta T_A) = \left(\frac{1}{2}\right)^2 [\sigma^2(\Delta T_{A1}) + \sigma^2(\Delta T_{A2})] = \left(\frac{1}{2}\right)^2 [\sigma_{A1}^2 + \sigma_{A2}^2] \quad (\text{A.11})$$

Comparing Eq. A.11 and Eq. A.9 leads to:

$$\sigma_D^2 = 2^2 \sigma_A^2 \quad \text{or} \quad \sigma_D = 2\sigma_A \quad (\text{A.12})$$

## A.2 Time-of-flight with three detectors

In a more realistic detector system, the individual sub-detectors will usually not have the same time resolution, but in some case quite different resolution, such that above estimations are no longer applicable. In the following we will show two methods to estimate the intrinsic time resolution of each detector in such a system from multiple TOF measurements. We start from a detector system as treated before and introduce a third scintillation counter C, as illustrated in Fig. A.3. Each counter is consisting of a scintillator read-out with two photodetectors.

### A.2.1 Calculation of intrinsic time resolution

The following derivations are again based on the work presented in Ref. [75]. With the presented setup, we can measure three TOFs:

$$\begin{aligned} T_{AB} &= T_B - T_A + \Delta T_{AB} \\ T_{AC} &= T_C - T_A + \Delta T_{AC} \\ T_{BC} &= T_C - T_B + \Delta T_{BC} \end{aligned} \quad (\text{A.13})$$

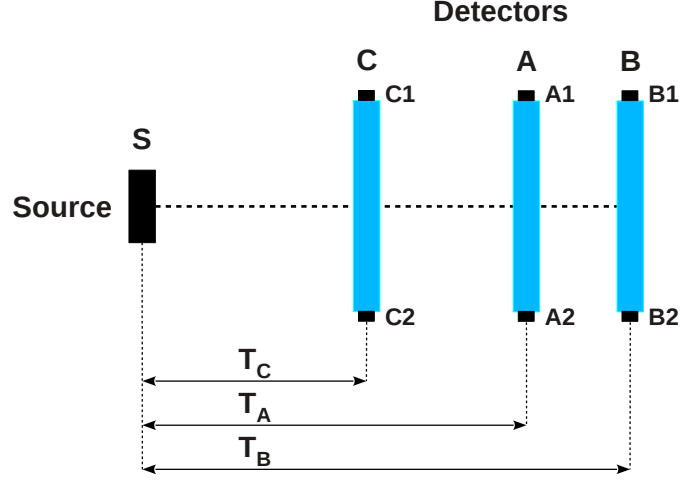


**Figure A.3:** Schematic measurement setup consisting of a particle source ( $S$ ) and three scintillation counters ( $A$ ,  $B$  and  $C$ ), each composed of a scintillator and two photodetectors ( $A1$  and  $A2$ ,  $B1$  and  $B2$ ,  $C1$  and  $C2$ ).

with associated measurement errors  $\Delta T_{AB}$ ,  $\Delta T_{AC}$  and  $\Delta T_{BC}$ .  $T_A$ ,  $T_B$  and  $T_C$  are the trigger times of the scintillation counters and can be defined similar to Eq. A.1. In analogy to Eq. A.4, we can write the measurement errors as functions of random variables associated with each detector:

$$\begin{aligned}
 \Delta T_{AB} &= \Delta T_B - \Delta T_A \\
 \Delta T_{AC} &= \Delta T_C - \Delta T_A \\
 \Delta T_{BC} &= \Delta T_C - \Delta T_B
 \end{aligned}
 \tag{A.14}$$

If  $\Delta T_A$ ,  $\Delta T_B$  and  $\Delta T_C$  are independent, we can calculate the variances:

$$\begin{aligned}
 \sigma_A^2 &= \sigma^2(\Delta T_A) = \frac{1}{2} [\sigma^2(\Delta T_{AB}) + \sigma^2(\Delta T_{AC}) - \sigma^2(\Delta T_{BC})] \\
 \sigma_B^2 &= \sigma^2(\Delta T_B) = \frac{1}{2} [\sigma^2(\Delta T_{AB}) + \sigma^2(\Delta T_{BC}) - \sigma^2(\Delta T_{AC})] \\
 \sigma_C^2 &= \sigma^2(\Delta T_C) = \frac{1}{2} [\sigma^2(\Delta T_{AC}) + \sigma^2(\Delta T_{BC}) - \sigma^2(\Delta T_{AB})]
 \end{aligned}
 \tag{A.15}$$

Hence, we can evaluate the intrinsic time resolution of each detector,  $\sigma_A$ ,  $\sigma_B$  and  $\sigma_C$ , from the TOF measurements and corresponding TOF resolutions  $\sigma_{AB}$ ,  $\sigma_{AC}$  and  $\sigma_{BC}$ . The errors  $\Delta\sigma_A$ ,  $\Delta\sigma_B$  and  $\Delta\sigma_C$  can be calculated using error propagation.

### A.2.2 Chi-square minimization

During this work, we used also another method to determine the detector time resolutions and associated errors in a TOF hodoscope, which shall be presented in the following. The method is based on a  $\chi^2$  minimization using the MINUIT package within ROOT [71, 76]. The basic idea is, that MINUIT searches for a set of parameters that minimize a given function,  $FCN$ , which is usually defined as a  $\chi^2$ :

$$\chi^2(\alpha) = \sum_{i=1}^n \frac{(f(x_i, \alpha) - e_i)^2}{\Delta e_i^2} \quad (\text{A.16})$$

with  $\alpha$  being the vector of free parameters to fit, and  $e_i$  the individual measurements with associated uncertainties  $\Delta e_i$ .

From the three TOF measurements, we obtain the TOF resolutions and the corresponding errors as our measurement observables  $e_i$  and  $\Delta e_i$ . As shown in Eq. A.5, the TOF resolutions can be written as:

$$\begin{aligned} \sigma_{AB}^2 &= \sigma^2(\Delta T_{AB}) = \sigma_A^2 + \sigma_B^2 \\ \sigma_{AC}^2 &= \sigma^2(\Delta T_{AC}) = \sigma_A^2 + \sigma_C^2 \\ \sigma_{BC}^2 &= \sigma^2(\Delta T_{BC}) = \sigma_B^2 + \sigma_C^2 \end{aligned} \quad (\text{A.17})$$

where  $\sigma_A$ ,  $\sigma_B$  and  $\sigma_C$  are the intrinsic time resolutions of the detectors, thus these are the  $f(x_i)$  with the parameters we are looking for. The function to minimize is therefore given by:

$$FCN = \frac{\left(\sqrt{\sigma_A^2 + \sigma_B^2} - e_1\right)^2}{\Delta e_1^2} + \frac{\left(\sqrt{\sigma_A^2 + \sigma_C^2} - e_2\right)^2}{\Delta e_2^2} + \frac{\left(\sqrt{\sigma_B^2 + \sigma_C^2} - e_3\right)^2}{\Delta e_3^2} \quad (\text{A.18})$$

As output of the minimization we obtain the parameters  $\sigma_A$ ,  $\sigma_B$  and  $\sigma_C$  with associated errors.



### A.2.3 Example

In order to compare the two methods, we apply them to a measurement from the latest test beam experiment. Three TOF resolutions have been determined using a trigger scintillator C and two plastic scintillator tiles A and B:

$$\begin{aligned}\sigma_{AB} &= 175.8 \pm 1.5 \text{ ps} \\ \sigma_{AC} &= 250.8 \pm 2.1 \text{ ps} \\ \sigma_{BC} &= 231.4 \pm 2.0 \text{ ps}\end{aligned}\tag{A.19}$$

Applying the first method and using Eq. A.15, we obtain the intrinsic time resolutions of the individual scintillation counters:

$$\begin{aligned}\sigma_A &= 141.9 \pm 2.6 \text{ ps} \\ \sigma_B &= 103.8 \pm 3.6 \text{ ps} \\ \sigma_C &= 206.8 \pm 1.8 \text{ ps}\end{aligned}\tag{A.20}$$

The values given in Eq. A.19 are the  $e_i$  and  $\Delta e_i$  as input for the  $\chi^2$  minimization. Performing a minimization in ROOT gives the following results:

$$\begin{aligned}\sigma_A &= 141.9 \pm 2.6 \text{ ps} \\ \sigma_B &= 103.8 \pm 3.6 \text{ ps} \\ \sigma_C &= 206.8 \pm 1.8 \text{ ps}\end{aligned}\tag{A.21}$$

which are identical to the values obtained before.



# List of Tables

3.1	Time weighted efficiencies and gain for different time resolutions . . . . .	29
3.2	Physics channels with single forward going tracks . . . . .	30
5.1	Main SiPM parameters . . . . .	55
5.2	MPPC recovery time constants . . . . .	79
6.1	Main plastic scintillator parameters . . . . .	92
7.1	Average photon numbers for successful triggering and validation in a DPC- 3200 . . . . .	106
7.2	Time resolution for different scintillator materials . . . . .	130
7.3	Time resolution for different scintillator sizes . . . . .	131
7.4	Total number of scintillator tiles and SiPMs needed for SciTil . . . . .	131
8.1	Photodetectors tested at FZJ beam test . . . . .	138
8.2	Plastic scintillators tested at FZJ beam test . . . . .	138



# List of Figures

2.1	Schematic view of the FAIR accelerator complex . . . . .	6
2.2	Time dependence of the luminosity in the HESR . . . . .	8
2.3	3D-view of the PANDA detector . . . . .	9
2.4	Side view of the PANDA target and forward spectrometers . . . . .	10
2.5	The PANDA solenoid and dipole magnet . . . . .	11
2.6	The PANDA Micro Vertex Detector . . . . .	13
2.7	The PANDA Straw Tube Tracker . . . . .	14
2.8	The PANDA GEM stations . . . . .	14
2.9	The PANDA Forward Tracker . . . . .	16
2.10	The PANDA DIRC detectors . . . . .	17
2.11	The PANDA electromagnetic calorimeter . . . . .	20
3.1	Distribution of the time difference between two successive events in PANDA	26
3.2	Event time distribution for different time resolutions . . . . .	27
3.3	Rate dependence of the event building efficiency . . . . .	28
3.4	Basic layout of the SciTil detector . . . . .	32
3.5	Half barrel of the SciTil detector . . . . .	33
4.1	Schematic of photodiodes . . . . .	36
4.2	Basic layout of SiPM . . . . .	38
4.3	Electronics layout of conventional SiPM and Philips DPC . . . . .	39
4.4	DPC tile layout . . . . .	40
4.5	Data acquisition sequence of the DPC sensor . . . . .	41

5.1	SiPM dark current . . . . .	45
5.2	SiPM pulse height spectrum . . . . .	46
5.3	Breakdown voltage determination measuring the gain . . . . .	47
5.4	Gain curve of Photonique preamplifier . . . . .	48
5.5	Temperature dependency of the breakdown voltage . . . . .	49
5.6	PDE of Hamamatsu and KETEK SiPMs . . . . .	51
5.7	KETEK SiPM with trench technology . . . . .	52
5.8	SiPM response curve to simultaneously input photons . . . . .	54
5.9	Setup for response curve measurements . . . . .	56
5.10	Calibration of the PIN photodiode . . . . .	57
5.11	Simulated SiPM response curve . . . . .	60
5.12	Measured response curves of various SiPMs . . . . .	62
5.13	Normalized SiPM response curves. . . . .	63
5.14	Deviation of the SiPM response curves from the model . . . . .	64
5.15	Over-voltage dependency of the SiPM response . . . . .	65
5.16	Alternative representation of SiPM response curves . . . . .	66
5.17	Normalized alternative SiPM response curves . . . . .	67
5.18	Delay time range for recovery time measurement . . . . .	72
5.19	Setup for recovery time measurements . . . . .	74
5.20	MPPC template waveform . . . . .	76
5.21	Waveform analysis and extraction of the recovery fraction . . . . .	76
5.22	Recovery curves of various MPPCs . . . . .	78
5.23	Single photon time resolution of Hamamatsu and KETEK SiPMs . . . . .	80
5.24	Position sensitive SiPM detector . . . . .	82
5.25	Philips DPC dark count map . . . . .	84
5.26	Philips DPC temperature dependent dark count rate . . . . .	85
5.27	DPC photon spectra and time resolution in response to a femtosecond laser pulse . . . . .	86
5.28	DPC time resolution as a function of the incident light intensity . . . . .	87

6.1	Light emission of a plastic scintillator as a function of time . . . . .	93
6.2	Probability density $W(Q,t)$ versus time precision for different photoelectrons	94
6.3	Time precision as a function of the total number of photoelectrons for different scintillator materials . . . . .	95
6.4	Estimation of the influence of light propagation inside a scintillator on the time resolution . . . . .	96
7.1	Energy deposit of Kaons in a plastic scintillator . . . . .	100
7.2	SciTil test setup using the Philips DPC . . . . .	102
7.3	$^{90}\text{Sr}$ spectrum measured with a DPC-3200 varying the validation threshold	105
7.4	Influence of the validation and integration interval . . . . .	107
7.5	Influence of the length of the coincidence time window . . . . .	108
7.6	DPC photon spectra measured with two scintillator tiles . . . . .	110
7.7	TOF spectrum using two EJ-228 plastic scintillator tiles . . . . .	111
7.8	SciTil test setup using Hamamatsu SiPMs . . . . .	112
7.9	$^{90}\text{Sr}$ spectrum measured with an EJ-228 scintillator read-out by two SiPMs	113
7.10	Coincidence time spectrum of two Hamamatsu SiPMs . . . . .	114
7.11	Possible photodetector positions on a scintillator tile . . . . .	117
7.12	Average number of detected photons in dependency of the photodetector position . . . . .	118
7.13	Time resolution of a scintillator tile in dependency of the photodetector position . . . . .	119
7.14	Spectral sensitivity of various SiPMs . . . . .	122
7.15	DPC time resolution as a function of the electronics threshold . . . . .	125
7.16	Leading edge and constant fraction triggering . . . . .	126
7.17	Coincidence time resolution as a function of the threshold fraction . . . . .	127
7.18	Coincidence time resolution as a function of the electronics threshold . . . . .	127
7.19	Electronics noise time jitter . . . . .	128
7.20	Photon spectra for different scintillator materials . . . . .	130

7.21	Time resolution varying the size of the scintillator and the photodetection area . . . . .	132
8.1	The COSY facility at FZJ . . . . .	136
8.2	The beam line at JESSICA . . . . .	137
8.3	The SciTil-SiPM prototype . . . . .	139
8.4	Schematic of the SciTil-SiPM test beam setup . . . . .	141
8.5	Photodetector output signals . . . . .	142
8.6	Photodetector pulse height spectra . . . . .	143
8.7	Threshold crossing time histograms . . . . .	144
8.8	Correlation between threshold crossing time and pulse height . . . . .	144
8.9	Time walk correction for MPPC using pulse height information . . . . .	146
8.10	Time walk correction for KETEK SiPM using pulse height information . . . . .	147
8.11	Time-over-threshold and double threshold technique . . . . .	148
8.12	Time walk correction using time-over-threshold . . . . .	149
8.13	Time walk correction using double threshold . . . . .	150
8.14	CFD input and output pulses . . . . .	151
8.15	CFD threshold crossing time histograms . . . . .	152
8.16	Time-of-flight distributions . . . . .	153
8.17	Beam test results for Hamamatsu MPPCs . . . . .	154
8.18	Beam test results for KETEK SiPMs . . . . .	155
8.19	PDE of Hamamatsu and KETEK SiPMs . . . . .	156
8.20	Threshold dependency of tile time resolution . . . . .	157
8.21	Modified SciTil-SiPM setup using four SiPMs attached to a single tile . . . . .	158
8.22	Tile time resolution as a function of the number of used threshold crossing time stamps . . . . .	159
8.23	Schematic of the SciTil-DPC prototype . . . . .	161
8.24	Segmented reference scintillator . . . . .	162
8.25	Pictures SciTil-DPC prototype . . . . .	163
8.26	Photon hit pattern with DPC configuration A . . . . .	164



8.27	Number of detected photons with DPC configuration A . . . . .	165
8.28	Photon hit pattern with DPC configuration B . . . . .	166
8.29	Number of detected photons with DPC configuration B . . . . .	167
8.30	Time-of-flight with configuration A . . . . .	168
8.31	Time-of-flight with configuration B . . . . .	170
8.32	Tile time resolution in dependency on the DPC trigger threshold . . . . .	173
8.33	Tile time resolution as a function of the number of used DPC time stamps	174
8.34	Position dependency of the tile time resolution . . . . .	176
8.35	Schematic of the configuration B setup looking in beam direction . . . . .	176
9.1	Simulation of SciTil and SciRod detector geometries . . . . .	181
9.2	Simulated number of detected photons with tile and rod geometries . . . . .	182
9.3	Simulated time resolution for tile and rod geometries . . . . .	184
9.4	Difference between estimated and real hit position along the SciRod . . . . .	184
9.5	Simulated time resolution of a small scintillator . . . . .	185
9.6	Simulated SciTil time resolution including a single photon time jitter . . . . .	186
A.1	Schematic measurement setup with two identical scintillation counters . . . . .	196
A.2	Schematic measurement setup consisting of a single scintillation counter . . . . .	197
A.3	Schematic measurement setup with three scintillation counters . . . . .	199



# List of abbreviations

**ADC** Analog to Digital Converter

**AMADEUS** Antikaon Matter at DaΦne: Experiments with Unraveling Spectroscopy

**APD** Avalanche Photodiode

**APPA** Atomic, Plasma Physics and Applications

**ASIC** Application-Specific Integrated Chip

**CALICE** Calorimeter for Linear Collider Experiment

**CBM** Compressed Baryonic Matter

**CERN** European Organization for Nuclear Research

**CFD** Constant Fraction Discriminator

**CMOS** Complementary Metal-Oxide Semiconductor

**CMS** Compact Muon Solenoid

**COSY** Cooler Synchrotron

**CR** Collector Ring

**CT** Central Tracker

**CTR** Coincidence Time Resolution

**DCR** Dark Count Rate

**DIRC** Detection of Internally Reflected Cherenkov Light

**DPC** Digital Photon Counter

**EMC** Electromagnetic Calorimeter

**ESS** European Spallation Source

**FAIR** Facility for Antiproton and Ion Research

**FNAL** Fermi National Accelerator Laboratory  
**FOPI** Four Pi ( $4\pi$ )  
**FPGA** Field-programmable Gate Array  
**FT** Forward Tracker  
**FWHM** Full Width at Half Maximum  
**FZJ** Forschungszentrum Jülich

**G-APD** Geiger-mode Avalanche Photodiode  
**GEM** Gas Electron Multiplier  
**GSI** GSI Helmholtz Centre for Heavy Ion Research

**HEP** High Energy Physics  
**HESR** High Energy Storage Ring  
**HIRAC** High Refractive Index Aerogel Cherenkov Counter  
**HV-MAPS** High-Voltage Monolithic Active Pixel Sensor

**JESSICA** Jülich Experimental Spallation Target Set-up in COSY Area

**KEK** The High Energy Accelerator Research Organization

**LE** Leading Edge  
**LEAR** Low Energy Antiproton Ring  
**LINAC** Linear Accelerator

**MAPD** Multi-pixel Avalanche Photo Diode  
**MAPMT** Multi-Anode Photomultiplier Tube  
**MCP-PMT** Micro-Channel Plate Photomultiplier Tube  
**MDT** Mini Drift Tube  
**MIP** Minimum Ionizing Particle  
**MPPC** Multi-pixel Photon Counter  
**MRS** Muon Range System  
**MVD** Micro Vertex Detector  
**MWDC** Multi-wire Drift Chamber

**NESR** New Experimental Storage Ring  
**NuSTAR** Nuclear Structure and Astrophysics  
**PANDA** Antiproton Annihilations in Darmstadt  
**PDE** Photon Detection Efficiency  
**PET** Positron Emission Tomography  
**PID** Particle Identification  
**PMT** Photomultiplier Tube  
**QCD** Quantum Chromo Dynamics  
**QDC** Charge to Digital Converter  
**QE** Quantum Efficiency  
**R&D** Research and Development  
**RESR** Recirculation Experimental Storage Ring  
**RICH** Ring Imaging Cherenkov Counter  
**RMS** Root Mean Square  
**SciRod** Scintillator Rod  
**SciTil** Scintillator Tile  
**SiPM** Silicon Photomultiplier  
**SMI** Stefan Meyer Institute for Subatomic Physics  
**SPAD** Single Photon Avalanche Diode  
**SPTR** Single Photon Time Resolution  
**SSPM** Solid State Photomultiplier  
**STT** Straw Tube Tracker  
**T2K** Tokai to Kamioka  
**TAG** Technical Assessment Group  
**TDC** Time to Digital Converter  
**TEK** Technology Evaluation Kit  
**TOF** Time-of-Flight

**TOF-PET** Time-of-Flight Positron Emission Tomography

**TORCH** Time of Internally Reflected Cherenkov Light

**TOT** Time-over-Threshold

**UNILAC** Universal Linear Accelerator

**USB** Universal Serial Bus

# Bibliography

- [1] M. Conti et al., *Focus on time-of-flight PET: the benefits of improved time resolution*, Eur. J. Nucl. Med. Mol. Imaging 38-6, pp. 1147-1157, 2011.
- [2] Dennis R. Schaart et al., *LaBr(3):Ce and SiPMs for time-of-flight PET: achieving 100 ps coincidence resolving time*, Phys. Med. Biol. 55-7, pp. N179-189, 2010.
- [3] T. Frach et al., *The Digital Silicon Photomultiplier - Principle of Operation and Intrinsic Detector Performance*, IEEE Nucl. Sci. Symp. Conf. Rec., 2009.
- [4] The CALICE collaboration, *Construction and commissioning of the CALICE analog hadron calorimeter prototype*, JINST 5 (2010) P05004.
- [5] The T2K Collaboration, *The T2K Experiment*, Nucl. Instrum. Meth. A 659 (2011) 106.
- [6] Benjamin Lutz for the CMS Collaboration, *Upgrade of the CMS Hadron Outer Calorimeter with SiPM sensors*, J. Phys.: Conf. Ser. 404 012018, 2012
- [7] The Belle II Collaboration, *Belle II Technical Design Report*, KEK Report 2010-1, arXiv:1011.0352v1 [physics.ins-det], Oct. 2010.
- [8] PANDA Collaboration, *Physics Performance Report for PANDA: Strong Interaction Studies with Antiprotons*, PANDA Physics Report, arXiv:0903.3905 [hep-ex], Mar. 2009.
- [9] K. Goetzen et al. *Proposal for a Scintillator Tile Hodoscope for PANDA*, PANDA note, Version 1.1, <https://panda-wiki.gsi.de/foswiki/pub/Tof/SciTil/scitil.pdf>, Mar. 2011.
- [10] S. Agostinelli et al., *Geant4 - a simulation toolkit*, Nucl. Instrum. Meth. A 506 (2003) 250-303.
- [11] D. Bettoni, *The PANDA Experiment at FAIR*, Proceedings of CHARM07, Ithaca, NY, August 2007, eConf C070805, arXiv:0710.5664 [hep-ex], 2007.
- [12] H. H. Gutbrod, *FAIR - Baseline Technical Report*, Volume 1, Executive Summary, ISBN 3-9811298-0-6, Sept. 2006.
- [13] V. E. Fortov et al., *European Facility for Antiproton and Ion Research (FAIR): the new international center for fundamental physics and its research program*, Phys.-Usp. 55 (6), 582-602, 2012.
- [14] GSI Helmholtz Centre for Heavy Ion Research GmbH, GSI Webpage, <https://www.gsi.de/en.htm>.

- [15] K. Goetzen, *Influence of Particle Timing on Event Building*, PANDA Note, <https://www-panda.gsi.de/db/notesDBr/KG13-110311.KGoetzen.EventMixingAtPanda.pdf>, Mar. 2011.
- [16] PANDA Wiki, <https://panda-wiki.gsi.de>.
- [17] PANDA Collaboration, *Technical Design Report for the PANDA Internal Targets: The Cluster-Jet Target and Developments for the Pellet Target*, PANDA Technical Design Report, [www-panda.gsi.de/archive/TargetTDR/Targets\\_TDR.pdf](http://www-panda.gsi.de/archive/TargetTDR/Targets_TDR.pdf), Apr. 2012.
- [18] Panda Collaboration, *Technical Design Report for the PANDA Solenoid and Dipole Spectrometer Magnets*, PANDA Technical Design Report, arXiv:0907.0169 [physics.ins-det], Jul. 2009.
- [19] PANDA Collaboration, *Technical Design Report for the PANDA Micro Vertex Detector*, PANDA Technical Design Report, arXiv:1207.6581 [physics.ins-det], Aug. 2012.
- [20] PANDA Collaboration, *Technical Design Report for the PANDA Straw Tube Tracker*, PANDA Technical Design Report, arXiv:1205.5441 [physics.ins-det], Jun. 2012.
- [21] The PANDA Experiment Website, <http://www-panda.gsi.de>.
- [22] K. Föhl et al., *The DIRC detectors of the PANDA experiment at FAIR*, Nucl. Instrum. Meth. A 595 (2008) 88.
- [23] C. Schwarz et al., *Particle identification for the PANDA detector*, Nucl. Instrum. Meth. A 639 (2011) 169.
- [24] C. Schwarz et al., *The Barrel DIRC of the PANDA experiment*, Nucl. Instrum. Meth. A 595 (2008) 112.
- [25] C. Schwarz et al., *The Barrel DIRC of PANDA*, JINST 7 (2012) C02008.
- [26] The PANDA Cherenkov Collaboration, J. Schwiening, *The Barrel DIRC detector for the PANDA experiment at FAIR*, Nucl. Instrum. Meth. A 639 (2011) 315.
- [27] BABAR-DIRC Collaboration, I. Adam et al., *The DIRC particle identification system for the BaBar experiment*, Nucl. Instrum. Meth. A 538 (2005) 281.
- [28] L. Gruber, G. S. M. Ahmed, S. E. Brunner, P. Bühler, J. Marton, K. Suzuki, *Position sensitive SiPM detector for Cherenkov applications*, JINST 6 (2011) C11024.
- [29] M. Rihl, S. E. Brunner, L. Gruber, J. Marton, K. Suzuki, *Efficiency and uniformity measurements of a light concentrator in combination with a SiPM array*, Nucl. Instrum. Meth. A 732 (2013) 419-422.
- [30] A. Gillitzer et al., *Motivation of the Barrel Time-of-Flight Detector for PANDA*, PANDA Note, Version 1.2, <https://panda-wiki.gsi.de/foswiki/pub/ToF/TimingBarrel/barreltof-tag.pdf>, Jan. 2011.
- [31] PANDA Collaboration, *Technical Design Report for PANDA Electromagnetic Calorimeter (EMC)*, PANDA Technical Design Report, arXiv:0810.1216 [physics.ins-det], Oct. 2008.
- [32] G. Schepers et al., *Particle Identification at PANDA*, Report of the PID TAG, [http://www-panda.gsi.de/db/notesDBr/GS14-090310\\_pid-tag.pdf](http://www-panda.gsi.de/db/notesDBr/GS14-090310_pid-tag.pdf), Mar. 2009.



- [33] T. Frach et al., *The Digital Silicon Photomultiplier - System Architecture and Performance Evaluation*, IEEE Nucl. Sci. Symp. Conf. Rec., pp. 1722-1727, 2010.
- [34] F. Powolny, PhD Thesis, *Characterization of time resolved photodetector systems for Positron Emission Tomography*, Université de Neuchâtel, 2009.
- [35] C. Degenhardt et al., *The Digital Silicon Photomultiplier – A Novel Sensor for the Detection of Scintillation Light*, IEEE Nucl. Sci. Symp. Conf. Rec., pp. 2383-2386, 2009.
- [36] Philips Digital Photon Counting, PDPC-TEK User Manual v0.21, <http://www.digitalphotoncounting.com/wp-content/uploads/PDPC-TEK-Manual-v0.21.pdf>.
- [37] L. Gruber, S. E. Brunner, J. Marton, K. Suzuki, *Over saturation behavior of SiPMs at high photon exposure*, Nucl. Instrum. Meth. A 737 (2014) 11-18.
- [38] S. E. Brunner, L. Gruber, J. Marton, H. Orth, K. Suzuki, *Time resolution below 100 ps for the SciTil detector of PANDA employing SiPM*, JINST 9 (2014) C03010.
- [39] Photonique preamplifier, AMP-0611 and AMP-0604, [http://www.photonique.ch/LEGACY/Products\\_amps.html](http://www.photonique.ch/LEGACY/Products_amps.html).
- [40] D. Renker and E. Lorenz, *Advances in solid state photon detectors*, JINST 4 (2009) P04004.
- [41] Hamamatsu MPPC, data sheet, [http://www.hamamatsu.com/resources/pdf/ssd/s12572-025\\_etc\\_kapd1043e03.pdf](http://www.hamamatsu.com/resources/pdf/ssd/s12572-025_etc_kapd1043e03.pdf).
- [42] KETEK PM3350, data sheet, [http://www.ketek.net/downloads/sipm/?eID=dam\\_frontend\\_push&docID=2224](http://www.ketek.net/downloads/sipm/?eID=dam_frontend_push&docID=2224).
- [43] KETEK PM3360, data sheet, [http://www.ketek.net/downloads/sipm/?eID=dam\\_frontend\\_push&docID=2225](http://www.ketek.net/downloads/sipm/?eID=dam_frontend_push&docID=2225).
- [44] KETEK GmbH, KETEK Webpage, <http://www.ketek.net>.
- [45] Opto-Semiconductor Handbook, Hamamatsu Photonics K.K., [http://www.hamamatsu.com/resources/pdf/ssd/e02\\_handbook\\_si\\_photodiode.pdf](http://www.hamamatsu.com/resources/pdf/ssd/e02_handbook_si_photodiode.pdf).
- [46] Photonique SSPM-0611B1MM-TO18, data sheet, <http://www.photonique.ch/LEGACY/DataSheets/SSPM.0611B1MM.TO18.pdf>
- [47] Zecotek Photonics Inc., Zecotek Brochure, 2008.
- [48] P. Eckert et al., *Characterization studies of silicon photomultipliers*, Nucl. Instrum. Meth. A 620 (2010) 217-226.
- [49] Hamamatsu Photonics K.K., Private communication, 2013.
- [50] P. Eckert et al., *Study of the response and photon-counting resolution of silicon photomultipliers using a generic simulation framework*, JINST 7 (2012) P08011.
- [51] S. Uozumi, *Study and Development of Multi Pixel Photon Counter for the GLD Calorimeter Read-out*, PoS(PD07)022, 2007.

- [52] Y. Du, F. Retière, *After-pulsing and cross-talk in multi-pixel photon counters*, Nucl. Instrum. Meth. A 596 (2008) 396-401.
- [53] H. Oide et al., *Study of afterpulsing of MPPC with waveform analysis*, PoS(PD07)008, 2007.
- [54] G. Collazuol et al., *Single photon timing resolution and detection efficiency of the IRST silicon photo-multipliers*, Nucl. Instrum. Meth. A 581 (2007) 461.
- [55] S. Gundacker et al., *SiPM time resolution: From single photon to saturation*, Nucl. Instrum. Meth. A 718 (2013) 569-572.
- [56] Ahmed Gamal, Bühler Paul, Marton Johann, Suzuki Ken, *Silicon photomultiplier timing performance study*, Nucl. Instrum. Meth. A 652 (2011) 528-531.
- [57] S. Brunner, *Fast single photon detection for scintillation and Cherenkov applications using silicon photomultipliers*, PhD Thesis, Vienna University of Technology, 2014.
- [58] T. Frach, *Optimization of the digital Silicon Photomultiplier for Cherenkov light detection*, JINST 7 (2012) C01112.
- [59] Y. Shao, *A new timing model for calculating the intrinsic timing resolution of a scintillator detector*, Phys. Med. Biol. 52 (2007) 1103-1117.
- [60] R. F. Post, L. I. Schiff, *Statistical Limitations on the Resolving Time of a Scintillation Counter*, Phys. Rev. 80, p. 1113, 1950.
- [61] P. Lecoq et al., *Progress on photonic crystals* IEEE Nucl. Sci. Symp. Conf. Rec., pp. 1970-1975, 2010.
- [62] S. Gundacker et al., *Time of flight positron emission tomography towards 100ps resolution with L(Y)SO: an experimental and theoretical analysis*, JINST 8 (2013) P07014.
- [63] S. Seifert, H. van Dam, D. Schaart, *The lower bound on the timing resolution of scintillation detectors*, Phys. Med. Biol. 57 (2012) 1797-1814.
- [64] S. Seifert et al., *A Comprehensive Model to Predict the Timing Resolution of SiPM-Based Scintillation Detectors : Theory and Experimental Validation*, IEEE Trans. on Nucl. Sci., Vol. 59, pp. 190-204, 2012.
- [65] Philips DPC, data sheet, [http://www.digitalphotoncounting.com/wp-content/uploads/dSiPM-Leaflet\\_A4\\_2013-11\\_A4.pdf](http://www.digitalphotoncounting.com/wp-content/uploads/dSiPM-Leaflet_A4_2013-11_A4.pdf).
- [66] D. Prasuhn et al., *Status of the cooler synchrotron COSY Juelich*, IEEE Proceedings of the 2001 Particle Accelerator Conference, PAC 2001, Chicago, June 18-22, 2001, p. 3350-3352.
- [67] H. Stelzer et al., *JESSICA, the Test Facility for an Advanced Cold moderator System for ESS*, Proceedings of the International Conference on Nuclear Engineering, Tokyo, Japan, April 20-23, 2003, ICONE11-36422.
- [68] K. Suzuki, P. Bühler, S. Fossati, J. Marton, M. Schafhauser, J. Zmeskal, *Development of SciFi/CheFi detector with SiPM readout*, Nucl. Instrum. Meth. A 610 (2009) 75-77.
- [69] FOPI Collaboration, *Experimental Proposal to GSI*, 2007.

- [70] AMADEUS Collaboration, *AMADEUS – Letter of Intent*, <http://www.lnf.infn.it/esperimenti/siddharta/LOI.AMADEUS.March2006.pdf>, March 2006.
- [71] Rene Brun and Fons Rademakers, *ROOT - An Object Oriented Data Analysis Framework*, Proceedings AIHENP'96 Workshop, Lausanne, Sep. 1996, Nucl. Instrum. Meth. A 389 (1997) 81-86. See also <http://root.cern.ch/>.
- [72] Matthew W. Fishburn and Edoardo Charbon, *System Tradeoffs in Gamma-Ray Detection Utilizing SPAD Arrays and Scintillators*, IEEE Trans. on Nucl. Sci., Vol. 57, pp. 2549-57, 2010.
- [73] A. Lehmann, S. Motz et al., “*SciRods*”: *An Alternative to SciTils?*, Talk at the PANDA Collaboration Meeting, GSI, June 25, 2013.
- [74] A. Lehmann, S. Motz, A. Britting, F. Uhlig, *Performance Comparison of SciRods and SciTils*, Talk at the SciTil Meeting, Vienna, July 24, 2014.
- [75] J. Pouthas et al., *Intrinsic Time Resolution of Detectors in a Time-of-Flight Spectrometer*, Nucl. Instrum. Meth. A 145 (1977) 445-451.
- [76] F. James, *MINUIT - Function Minimization and Error Analysis*, MINUIT Reference Manual, Version 94.1, CERN, 1998. See also <http://wwwasdoc.web.cern.ch/wwwasdoc/minuit/minmain.html>.



# Curriculum vitae

## Personal Data

---

Name: Lukas Gruber, MSc  
Address: Kaiserstraße 90/24, 1070 Wien, Austria  
office: +43 (0) 1 / 4277 29736  
mobile: +43 (0) 650 / 65 85 000  
e-mail: lukas.gruber@oeaw.ac.at  
Date of birth: May 6<sup>th</sup>, 1985  
Place of birth: St. Pölten  
Citizenship: Austria

## Education

---

since 10/2010 PhD studies of Technical Sciences at the Vienna University of Technology, Austria

since 10/2010 PhD thesis at the Stefan Meyer Institute, Austrian Academy of Sciences, Vienna, Austria  
Thesis title: "Studies of SiPM photosensors for time-of-flight detectors within PANDA at FAIR"  
Supervision: Dr. Johann Marton

10/2003 – 03/2010 Master studies of Technical Physics at the Vienna University of Technology, Austria  
Master of Sciences, March 2010 (with distinction)

01/2009 – 12/2009 Master thesis at CERN, Geneva, Switzerland  
Thesis title: "Optimization of the operating parameters of the LHCb muon system"  
Supervision: Prof. Dr. Christian Fabjan

09/1995 – 06/2003 Grammar school with focus on Natural Sciences, Krems, Austria  
School leaving exam, June 2003 (passed with distinction)

09/1991 – 06/1995 Primary school, Traismauer, Austria

## Professional Career

---

- since 10/2010      Scientific employee at the Stefan Meyer Institute of the Austrian Academy of Sciences, Vienna, Austria
- PhD in experimental particle physics with focus on fast photon detection with semiconductor photosensors for high energy physics and medical applications
  - Participation in research in an international collaboration in the field of experimental particle physics (PANDA at FAIR)
  - Experimental activities at various particle accelerator facilities (CERN, FZ Jülich, INFN-LNF)
  - Presentation of results at international conferences and meetings
- 01/2009 – 12/2009      Technical student at the Physics Department at CERN, Geneva, Switzerland
- Master thesis in experimental particle physics with emphasis on particle detection with gaseous detectors (MWPC)
  - Assistance in optimization, commissioning and installation of the LHCb muon system
  - Participation in research in an international collaboration in the field of experimental particle physics (LHCb at CERN)
- 11/2008 – 12/2008      Project work at the Institute for Quantum Optics and Quantum Information, Vienna, Austria
- 10/2007 – 06/2008      Scientific trainee at the Institute of Atomic and Subatomic Physics, Vienna UT, Austria
- Practical training in reactor physics and reactor instrumentation
  - Experiments with polarized neutrons at the TRIGA Mark-II reactor
- 07/2008 – 07/2008      Trainee at KWI Consultants and Engineers AG, St. Pölten, Austria
- Measurements for noise protection at factories and construction sites
- 07/2007 – 07/2007      Trainee at KWI Consultants and Engineers AG, St. Pölten, Austria
- Training on CAD
- 08/2006 – 09/2006      Technical student in the R&D division at Voith Paper GmbH, St. Pölten, Austria
- Development and testing of a mobile paper press
  - Description of results by corresponding theoretical models

08/2005 – 09/2005      Technical student in the R&D division at Voith Paper GmbH, St. Pölten, Austria

- Installation and commissioning of a test stand for simulation of the dewatering in a paper machine

---

## Awards

2008                      Scholarship for outstanding performance awarded by the Vienna University of Technology ("Leistungsstipendium")

---

## Computer Knowledge

Word processing	MS Word, Latex
Office	LibreOffice, MS Office, OpenOffice
Other software	AutoCAD, Root, Geant4, Garfield
Programming	C, C++, Fortran, LabView, Visual Basic, Perl, HTML
Hardware	Camac, NIM, VME
Operating systems	Linux, Mac OS, Windows

---

## Language Skills

Mother tongue	German
Other languages	English (fluent)
	French (fluent)
	Italian (basic knowledge)

---

## Activities and Interests

Memberships	Member of the Austrian Physical Society
Voluntary work	Lions Club
Hobbies	Cycling, tennis (team), skiing, soccer, hiking, playing the piano (band, choir)

---

## Conference contributions

Annual Meeting of the Austrian Physical Society, September 24-27, 2014, Pöllau, Austria, *Time resolution studies for the PANDA time-of-flight detector using SiPM.*

Joint Annual Meeting of the Austrian Physical Society and Swiss Physical Society, September 4-6, 2013, Linz, Austria, *Over Saturation Behavior of SiPMs at High Photon Exposure.*

DIRC2013: Workshop on fast Cherenkov detectors, September 4-6, 2013, Rauischholzhausen, Germany, *Time resolution studies for the PANDA Scintillation Tile Hodoscope using the Philips digital SiPM.*

Annual Meeting of the Austrian Physical Society, September 18-21, 2012, Graz, Austria, *Recovery Time and Double Hit Resolution Measurements of SiPM Using a Double Pulsed Laser*.

DIRC2011: Workshop on fast Cherenkov detectors, April 4-6, 2011, Giessen, Germany, *Position sensitive SiPM detector for Cherenkov applications*.

Joint Annual Meeting of the Austrian Physical Society and Swiss Physical Society, September 2-4, 2009, Innsbruck, Austria, *Time resolution limits of Multi Wire Proportional Chambers*.

## Publications (peer-reviewed)

---

L. Gruber, S. E. Brunner, J. Marton, K. Suzuki, *Over saturation behavior of SiPMs at high photon exposure*, Nucl. Instrum. Meth. A 737 (2014) 11-18, DOI: 10.1016/j.nima.2013.11.013.

L. Gruber, G. S. M. Ahmed, S. E. Brunner, P. Bühler, J. Marton, K. Suzuki, *Position sensitive SiPM detector for Cherenkov applications*, JINST 6 (2011) C11024, doi: 10.1088/1748-0221/6/11/C11024.

L. Gruber, W. Riegler, B. Schmidt, *Time resolution limits of the MWPCs for the LHCb muon system*, Nucl. Instrum. Meth. A 632 (2011) 69-74, DOI: 10.1016/j.nima.2010.12.131.

S. E. Brunner, L. Gruber, J. Marton, H. Orth, K. Suzuki, *Time resolution below 100 ps for the SciTil detector of PANDA employing SiPM*, JINST 9 (2014) C03010, doi: 10.1088/1748-0221/9/03/C03010.

M. Rihl, S. E. Brunner, L. Gruber, J. Marton, K. Suzuki, *Efficiency and Uniformity Measurement of a light concentrator in combination with a SiPM Array*, Nucl. Instrum. Meth. A 732 (2013) 419-422, DOI: 10.1016/j.nima.2013.05.187.

S. E. Brunner, L. Gruber, J. Marton, K. Suzuki, A. Hirtl, *New Approaches for Improvement of TOF-PET*, Nucl. Instrum. Meth. A 732 (2013) 560-563, DOI: 10.1016/j.nima.2013.05.028.

S. E. Brunner, L. Gruber, J. Marton, K. Suzuki, A. Hirtl, *Studies on the Cherenkov Effect for Improved Time Resolution of TOF-PET*, IEEE Trans. on Nucl. Sci., Vol. 61, pp. 443-447, 2013, doi: 10.1109/TNS.2013.2281667.

S. E. Brunner, J. Marton, K. Suzuki, L. Gruber, A. Hirtl, M. Jankovec, P. Knoll, A. Gamal, *Improving Time-Of-Flight PET using silicon photomultipliers*, Radiotherapy and Oncology, vol. 102, suppl. 1, pp. S137-S138, 2012, [http://dx.doi.org/10.1016/S0167-8140\(12\)70228-1](http://dx.doi.org/10.1016/S0167-8140(12)70228-1).

L. Anderlini, R. Antunes Nobrega, W. Bonivento, L. Gruber, A. Kashchuk, O. Levitskaya, O. Maev, G. Martellotti, G. Penso, D. Pinci, A. Sarti, B. Schmidt, *A new method based on noise counting to monitor the frontend electronics of the LHCb muon detector*, JINST 8 (2013) P06001, doi: 10.1088/1748-0221/8/06/P06001.



M. Anelli, R. Antunes Nobrega, G. Auriemma, W. Baldini, G. Bencivenni, R. Berutti, V. Bocci, N. Bondar, W. Bonivento, B. Botchin, S. Cadeddu, P. Campana, G. Carboni, A. Cardini, M. Carletti, P. Ciambrone, E. Dané, S. De Capua, C. Deplano, P. De Simone, F. Dettori, A. Falabella, F. Ferreira Rodriguez, M. Frosini, S. Furcas, G. Graziani, L. Gruber, A. Kashchuk, A. Lai, G. Lanfranchi, M. Lenzi, O. Levitskaya, K. Mair, O. Maev, G. Manca, G. Martellotti, A. Massafferri Rodrigues, R. Messi, F. Murtas, P. Neustroev, R. G. C. Oldeman, M. Palutan, G. Passaleva, G. Penso, A. Petrella, D. Pinci, S. Pozzi, G. Sabatino, B. Saitta, R. Santacesaria, E. Santovetti, A. Saputi, A. Sarti, C. Satriano, A. Satta, M. Savrié, B. Schmidt, T. Schneider, A. Sciubba, P. Shatalov, S. Vecchi, M. Veltri, S. Volkov, A. Vorobyev, *Performance of the LHCb muon system with cosmic rays*, JINST 5 (2010) P10003, doi: 10.1088/1748-0221/5/10/P10003.

A.A. Alves Jr, L. Anderlini, M. Anelli, R. Antunes Nobrega, G. Auriemma, W. Baldini, G. Bencivenni, R. Berutti, A. Bizzeti, V. Bocci, N. Bondar, W. Bonivento, B. Botchin, S. Cadeddu, P. Campana, G. Carboni, A. Cardini, M. Carletti, P. Ciambrone, E. Dané, S. De Capua, V. De Leo, C. Deplano, P. De Simone, F. Dettori, A. Falabella, F. Ferreira Rodriguez, M. Frosini, S. Furcas, E. Furfaro, G. Graziani, L. Gruber, G. Haefeli, A. Kashchuk, F. Iacoangeli, A. Lai, G. Lanfranchi, M. Lenzi, O. Levitskaya, K. Mair, O. Maev, G. Manca, M. Mara, G. Martellotti, A. Massafferri Rodrigues, R. Messi, F. Murtas, P. Neustroev, R. G. C. Oldeman, M. Palutan, G. Passaleva, G. Penso, D. Pinci, E. Polycarpo, D. Raspino, G. Sabatino, B. Saitta, A. Salamon, R. Santacesaria, E. Santovetti, A. Saputi, A. Sarti, C. Satriano, *Performance of the LHCb muon system*, JINST 8 (2013) P02022, doi: 10.1088/1748-0221/8/02/P02022.

C. Schwarz, A. Britting, P. Bühler, E. Cowie, V. Kh. Dodokhov, M. Düren, W. Eyrich, K. Föhl, L. Gruber, A. Hayrapetyan, M. Hoek, R. Hohler, G. Kalicy, T. Keri, P. Koch, B. Kröck, A. Lehmann, D. Lehmann, B. Lewandowski, J. Marton, O. Merle, R. Montgomery, M. Patsyuk, K. Peters, G. Rosner, G. Schepers, L. Schmitt, J. Schwiening, B. Seitz, C. Sfienti, K. Suzuki, F. Uhlig, A. S. Vodopianov, E. Widmann, *The Barrel DIRC of PANDA*, JINST 7 (2012) C02008, doi: 10.1088/1748-0221/7/02/C02008.

G. Kalicy, H. Kumawat, J. Schwiening, R. Dzhygadlo, A. Gerhardt, R. Hohler, D. Lehmann, B. Lewandowski, M. Patsyuk, K. Peters, G. Schepers, L. Schmitt, C. Schwarz, M. Traxler, M. Zühlsdorf, V. Kh. Dodokhov, A. Vodopianov, A. Britting, W. Eyrich, A. Lehmann, F. Uhlig, M. Düren, K. Föhl, A. Hayrapetyan, P. Koch, B. Kröck, O. Merle, E. Cowie, T. Keri, R. Montgomery, G. Rosner, B. Seitz, P. Achenbach, M. Cardinali, M. Hoek, C. Sfienti, M. Thiel, C. Ugur, P. Bühler, L. Gruber, J. Marton, K. Suzuki, E. Widmann, *The Panda Cherenkov Group, Status of the PANDA Barrel DIRC*, JINST 9 (2014) C05060, doi: 10.1088/1748-0221/9/05/C05060.

A. Lehmann, A. Britting, W. Eyrich, F. Uhlig, R. Dzhygadlo, A. Gerhardt, K. Götzen, R. Hohler, G. Kalicy, H. Kumawat, D. Lehmann, B. Lewandowski, M. Patsyuk, K. Peters, G. Schepers, L. Schmitt, C. Schwarz, J. Schwiening, M. Traxler, M. Zühlsdorf, V. Kh. Dodokhov, M. Düren, K. Föhl, A. Hayrapetyan, B. Kröck, O. Merle, J. Rieke, E. Cowie, T. Keri, R. Montgomery, G. Rosner, P. Achenbach, M. Cardinali, M. Hoek, W. Lauth, C. Sfienti, M. Thiel, P. Bühler, L. Gruber, J. Marton, K. Suzuki, *Improved lifetime of microchannel-plate PMTs*, In Press, 2014, DOI: 10.1016/j.nima.2014.04.005.

M. Hoek, R. Dzhygadlo, A. Gerhardt, K. Götzen, R. Hohler, G. Kalicy, H. Kumawat, D. Lehmann, B. Lewandowski, M. Patsyuk, K. Peters, G. Schepers, L. Schmitt, C. Schwarz, J. Schwiening, M. Traxler, M. Zühlsdorf, V. Kh. Dodokhov, A. Britting, W. Eyrich, A. Lehmann, F. Uhlig, M. Düren, K. Föhl, A. Hayrapetyan, B. Kröck, O. Merle, J. Rieke, E. Cowie, T. Keri, R. Montgomery, G. Rosner, P. Achenbach, M. Cardinali, W. Lauth, C. Sfienti, M. Thiel, P. Bühler, L. Gruber, J. Marton, K. Suzuki, *The PANDA Barrel DIRC detector*, In Press, 2014, DOI: 10.1016/j.nima.2014.04.006.

O. Merle, R. Dzhygadlo, A. Gerhardt, K. Götzen, R. Hohler, G. Kalicy, H. Kumawat, D. Lehmann, B. Lewandowski, M. Patsyuk, K. Peters, G. Schepers, L. Schmitt, C. Schwarz, J. Schwiening, M. Traxler, M. Zühlsdorf, V. Kh. Dodokhov, A. Britting, W. Eyrich, A. Lehmann, F. Uhlig, M. Düren, E. Etzelmüller, K. Föhl, A. Hayrapetyan, B. Kröck, D. Mühlheim, J. Rieke, E. Cowie, T. Keri, R. Montgomery, G. Rosner, P. Achenbach, M. Cardinali, M. Hoek, W. Lauth, C. Sfienti, M. Thiel, P. Bühler, L. Gruber, J. Marton, K. Suzuki, *Development of an Endcap DIRC for PANDA*, In Press, 2014, DOI: 10.1016/j.nima.2014.04.016